

## ABSTRACT

Title of Document:                   LOW AND ATMOSPHERIC PRESSURE  
  PLASMA INTERACTIONS WITH  
  BIOMOLECULES AND POLYMERS.

Elliot Andrew James Bartis, Ph.D., 2015

Directed By:                         Professor Gottlieb S. Oehrlein, Department of  
  Materials Science and Engineering

Cold atmospheric plasma (CAP) sources have emerged as economical and environmentally friendly sources of reactive species with promising industrial and biomedical applications. Many different sources are studied in the literature for advanced applications including surface disinfection, wound healing, and cancer treatment, but the underlying mechanisms for these applications are not well-understood. The overall goals of this dissertation are to 1) identify how plasma treatments induce surface modifications and which plasma species are responsible for those modifications; 2) identify how changes in surface and plasma chemistry contribute to changes in biological activity of biomolecules; and 3) investigate how fluxes of reactive species produced by atmospheric pressure plasma devices can be controlled. As a first step, a well-studied low pressure plasma system was used to isolate the effects of ions, high energy photons, and radicals using Ar and H<sub>2</sub> plasma. The finding that plasma-generated radicals can biodeactivate and modify films with negligible etching motivated further study at atmospheric pressure. Two very different CAP sources were used under mild, remote conditions

to study the biological deactivation of two immune-stimulating biomolecules: lipopolysaccharide (LPS), found in bacteria such as *Escherichia coli*, and peptidoglycan, found in bacteria such as *Staphylococcus aureus*. The surface chemistry was measured to understand which plasma-generated species and surface modifications are important for biological deactivation. To simplify the complex molecular structure of the biomolecules and study specific moieties, model polymer films were studied including polystyrene, poly(methyl methacrylate), polyvinyl alcohol, and polypropylene. The interaction of the plasma plume with the environment was studied as a parameter to tune surface modifications. It was found that increasing ambient N<sub>2</sub> concentrations in an N<sub>2</sub>/Ar ambient decreased surface modifications of LPS, similarly to how adding N<sub>2</sub> to the O<sub>2</sub>/Ar feed gas decreased the plasma-generated O<sub>3</sub> density and O atom optical emission. In this work, we first observed the formation of surface-bound NO<sub>3</sub> after plasma treatment, which had not been reported in the literature. The plasma-ambient interaction was further studied using polystyrene as a model system. This detailed study demonstrated a competition between surface oxidation and nitridation, the latter of which occurs under very specific conditions. It was found that NO<sub>3</sub> formed on all the materials studied in this dissertation after plasma treatment. This NO<sub>3</sub> formed after treatment by both sources, but in different concentrations. The surface-bound NO<sub>3</sub> correlated better with changes in biological activity than general oxidation, demonstrating its importance. Studying model polymers revealed that this surface moiety preferentially forms on –OH containing surfaces. Since the atmospheric pressure plasma jet (APPJ) operates with low N<sub>2</sub>/O<sub>2</sub> admixtures to Ar and the surface microdischarge (SMD) operates with N<sub>2</sub>/O<sub>2</sub> mixtures, the mechanisms that cause biological deactivation must be different, and are discussed.

LOW AND ATMOSPHERIC PRESSURE PLASMA INTERACTIONS WITH  
BIOMOLECULES AND POLYMERS

By

Elliot Andrew James Bartis

Dissertation submitted to the Faculty of the Graduate School of the  
University of Maryland, College Park, in partial fulfillment  
of the requirements for the degree of  
Doctor of Philosophy  
2015

Advisory Committee:

Professor G. S. Oehrlein, Department of Materials Science and Engineering, Chair  
Professor J. Seog, Department of Materials Science and Engineering  
Professor R. M. Briber, Department of Materials Science and Engineering  
Professor R. J. Phaneuf, Department of Materials Science and Engineering  
Professor P. Kofinas, Fischell Department of Bioengineering

© Copyright by  
Elliot Andrew James Bartis  
2015



## **Acknowledgements**

Many people have helped me during my PhD. I would like to start by thanking my advisor, Professor Oehrlein, for helping me become an effective researcher and teaching me valuable skills that will last a lifetime. Your ideas and insights transformed my way of thinking about and approaching problems. Thank you for support, encouragement, and enthusiasm over the course of my PhD. I truly enjoyed discussing our research and the state of the field with you. Most importantly, you taught me to never settle for anything less than the exceptional.

I would also like to thank my co-advisor, Professor Seog. I could not have grasped the entire biology side of this dissertation without you. Thank you for giving me the tools to think about these biomolecules on a molecular level.

I would like to thank the U.S. National Science Foundation and U.S. Department of Energy for financial support over the years.

I would also like to thank my dissertation committee for taking the time to support my dissertation. I hope you enjoy reading this. Thank you, Professor Briber, Professor Kofinas, and Professor Phaneuf. I would like to thank further Professor Phaneuf for nominating me for the Ann G. Wylie Graduate Dissertation Fellowship.

To my collaborators, without the fruitful discussions, your insights and ideas, and your hard work, I would not have progressed so much. Thank you Dr. Ting-Ying Chung, Dr. Ning Ning, Professor Jih-Wei, Chu, and Professor David Graves (University of California, Berkeley), Dr. David Burnette, Professor Igor Adamovich, and Professor Walter Lempert (The Ohio State University).

To my colleagues throughout these past years who have become close friends of mine. I enjoyed our time inside and outside of the lab. Thank you Dr. Nick Lyon, Dominik Metzler,

Andrew Knoll, Chen Li, Pingshan Luan, Adam Pranda, and Dr. Florian Weirnboeck, Amy Lee, Brian Stock, and Eddy Salgado for all the wonderful times and support. I will miss working with you all. To my IREAP pal, Dr. Jane Cornett, there are no words.

I am also grateful to all of my students and interns that helped me with the research, including Connor Hart, Caleb Barrett, Vanessa Rieger, Sivan Sachar, and Brandon Nguyen. Thank you to the many people that helped me and my research. Jay Pyle and Nolan Ballew, I am grateful for all the help in the machine shop and the enthusiasm for my work.

Last, but certainly not least, I would like to thank my parents, Drs. James and Lois Bartis and sister, Aleya Bartis. I fear I will never be able to repay you for everything you've done to help me become the man I am today. Dad, thank you for being a world-class role model and inspiring me to pursue science and engineering. I will never forget your wisdom in *all* things. Mom, thank you for the endless love, positivity, and encouragement. Aleya! Thanks for being my best friend for life! I couldn't have made it through graduate school without all the healthy and not-so-healthy food.

## Table of Contents

Acknowledgements.....	ii
Table of Contents.....	iv
List of Figures.....	vi
List of Tables.....	xi
Chapter 1: Introduction.....	1
1.1. Plasma-Material Interactions and Plasma Medicine.....	1
1.2. Collaborative Research.....	4
1.3. Immunostimulating Biomolecules: Lipopolysaccharide and Peptidoglycan.....	5
1.4. Model Polymers.....	7
1.5. Plasma Treatments.....	8
1.6. Characterization.....	11
1.7. Thesis Outline.....	18
Chapter 2: Deactivation of lipopolysaccharide by Ar and H <sub>2</sub> inductively-coupled low pressure plasma.....	20
2.1. Introduction.....	22
2.2. Experiments and Methods.....	23
2.3. Results and Discussion.....	32
2.4. Conclusion.....	46
Chapter 3: Atmospheric pressure plasma treatment of lipopolysaccharide in a controlled environment.....	49
3.1. Introduction.....	51
3.2. Experiments and Methods.....	52
3.3. Results and Discussion.....	55
Chapter 4: Polystyrene as a Model System to Probe the Impact of Ambient Gas Chemistry on Polymer Surface Modifications Using Remote Atmospheric Pressure Plasma under Well-Controlled Conditions.....	63
4.1. Introduction.....	66
4.2. Materials and Methods.....	68
4.3. Results.....	73
4.4. Discussion.....	85
4.5. Conclusion.....	94
Chapter 5: Biodeactivation of Lipopolysaccharide Correlates with NO <sub>3</sub> Formation after Cold Atmospheric Plasma Treatment.....	96
5.1. Introduction.....	98

5.2. Materials and Methods.....	99
5.3. Results and Discussion .....	104
5.4. Conclusions.....	116
Chapter 6: A Comparative Study of Biomolecule and Polymer Surface Modifications by a Surface Microdischarge and Atmospheric Pressure Plasma Jet .....	118
6.1. Introduction.....	121
6.2. Materials and Methods.....	124
6.3. Results.....	132
6.4. Discussion .....	154
5. Conclusion .....	163
Chapter 7: Conclusions and Future Work.....	165
References.....	172

## List of Figures

### Chapter 1:

- Figure 1.1: Inductively-coupled plasma reactors used in this work with (a) 125 mm substrate diameter and equipped with *in situ* ellipsometry and (b) 300 mm substrate diameter and vacuum transfer to surface analysis.
- Figure 1.2: Photograph of the atmospheric pressure plasma jet showing where certain species are found.
- Figure 1.3: SMD operating in air.
- Figure 1.4: Simplified schematic of an ELISA.

### Chapter 2:

- Figure 2.1. Schematic of lipopolysaccharide highlighting the structure of lipid A. Enclosed is the structure of biotin, which is conjugated to LPS for endotoxicity measurements. Ph = phosphate/pyrophosphate, KDO = 3-deoxy-D-manno-oct-2-ulosonic acid, Hep = heptose, Glc = glucose, Gal = galactose, NGc = N-acetyl-glucosamine, NGa = N-acetyl-galactosamine.
- Figure 2.2: Schematic of the set up (not to scale) used for (a) real-time *in situ* ellipsometry of UV/VUV treatment and (b) radical treatment of LPS films. For UV/VUV treatment, a MgF<sub>2</sub> optical filter sits on top of a housing which prevents ion and electrons from interacting with the sample. The ellipsometer laser probed the sample through small apertures in the housing. For radical treatment, a roof structure sits 0.7 mm above the sample. Plasma is not produced within the gap, so only neutral species that diffuse under the gap (aspect ratio  $\approx 20$ ) can reach the sample.
- Figure 2.3: Representative surface morphology measured by tapping mode atomic force microscopy for untreated LPS films. The film was spin-coated on piranha treated silicon substrate at 100 rpm. Root mean square surface roughness is less than 10 nm.
- Figure 2.4: Absorbance as a function of bLPS concentration as measured by ELISA for various times under vacuum. The inset shows the background signal of the measurement. Vacuum conditions have a negligible effect on the biological activity of the molecule. Furthermore, absorbance begins to saturate starting at  $\sim 0.5$   $\mu\text{g/ml}$ .
- Figure 2.5: The fraction of the original film thickness as a function of treatment time for direct, UV/VUV, and radical treatments.
- Figure 2.6: Normalized biodeactivation of bLPS films as a function of treatment time for direct, UV/VUV, and radical treatments. Plasma conditions: 50 sccm of feed gas, 10 mTorr operating pressure, 150 W source power, no external bias.
- Figure 2.7: High resolution XPS spectra of untreated LPS at (a) shallow probing and (b) deep probing depths. Peak assignments are indicated in the figure.

- Figure 2.8: XPS difference plots (treated-untreated) of P 2p, C 1s, N 1s, and O 1s spectra for H<sub>2</sub> (a) direct, (b) UV/VUV, and (c) radical treatments of LPS collected at shallow probing depths. Peak assignments are indicated on the figure.
- Figure 2.9: XPS difference plots (treated-untreated) of P 2p, C 1s, N 1s, and O 1s spectra for Ar (a) direct, (b) UV/VUV, and (c) radical treatments of LPS collected at shallow probing depths. Peak assignments are indicated on the figure.
- Figure 2.10: Schematic of the modifications to intact LPS/lipid A for the various conditions explored in this work and complementary work by Chung et al.<sup>[1]</sup> Damage to the highlighted functional groups in lipid A would also be found on similar functional groups in the core oligosaccharide and O-chain of LPS as shown for N-acetyl galactosamine.

### Chapter 3:

- Figure 3.1. (a) A schematic representation of the atmospheric pressure plasma jet (APPJ). (b) The APPJ is mounted inside a vacuum chamber where the environment can be controlled during the treatment as shown. After the treatment, the samples are vacuum transferred to XPS for surface analysis.
- Figure 3.2. XPS C 1s, N 1s, and O 1s spectra of lipopolysaccharide (LPS) films after treatment in N<sub>2</sub>/Ar environments for conditions where the plasma is (a) exposed to the environment and (b) confined within the alumina tube. The distance from nozzle to the LPS coated substrate was 4 cm for both conditions.
- Figure 3.3. Normalized biodeactivation vs. treatment time for four different gas chemistries in the confined geometry. The N<sub>2</sub> admixture causes minor deactivation, while O<sub>2</sub>-based discharges show clear deactivation.
- Figure 3.4. (a) Emission due to atomic O and the second positive system of N<sub>2</sub> normalized to the Ar emission at 750 nm for O<sub>2</sub>/N<sub>2</sub> admixtures in the confined geometry. (b) Ozone density measured using UV absorption spectroscopy for 1% O<sub>2</sub> admixture in the confined geometry was monitored as N<sub>2</sub> is added to the feed gas.

### Chapter 4:

- Figure 4.1. Schematic of the atmospheric pressure plasma jet (APPJ) mounted in a vacuum chamber that can be pumped out and refilled with a controlled environment. The distance, *s*, between the source and the nozzle can be adjusted to regulate the interaction of the plasma plume with the environment. The photograph shows an Ar APPJ operating in the exposed geometry.
- Figure 4.2. As a function of APPJ treatment time, (a) C 1s composition and (b) oxygen and NO<sub>3</sub> composition measured by XPS at shallow probing depths. Treatment conditions: 1% O<sub>2</sub>/Ar, confined geometry, N<sub>2</sub> ambient.
- Figure 4.3. As a function of APPJ O<sub>2</sub> admixture (a) C 1s composition and (b) oxygen and nitrogen composition measured by XPS at shallow probing depths. Treatment conditions: Ar carrier gas, confined geometry, N<sub>2</sub> ambient, 3 min treatment.
- Figure 4.4. Tapping mode AFM image of pristine PS and PS treated by 1% O<sub>2</sub> in Ar plasma in N<sub>2</sub> in the confined geometry for 7 minutes. The applied voltage and frequency were 14 kV pk-pk and 24 kHz, respectively.

- Figure 4.5. High resolution XPS C1s, N1s, and O1s spectra of PS films before and after the confined 1% O<sub>2</sub>/Ar treatment in O<sub>2</sub>, air, and N<sub>2</sub> environments.
- Figure 4.6. C1s difference plots (treated-untreated) for Ar and 1% admixtures of N<sub>2</sub>, Air, and O<sub>2</sub> to Ar in O<sub>2</sub> and N<sub>2</sub> ambients. The confined geometry (black solid line) was compared with the exposed geometry (red dashed line) to study how the environment interacts with long-lived and short-lived species.
- Figure 4.7. Integrated peak areas corresponding to (a) C=C/C-C, (b) C-O, (c) O-C-O/C=O, (d) O-C=O, (e) O-CO-O, and (f)  $\pi$ - $\pi^*$  for APPJ treatments in the exposed (left side) and confined (right side) configurations for Ar and 1% O<sub>2</sub>, air, and N<sub>2</sub> admixture to Ar feed gases in the N<sub>2</sub> (red) and O<sub>2</sub> (green) ambients.
- Figure 4.8. High resolution XPS N1s spectrum of PS comparing exposed N<sub>2</sub>/Ar and O<sub>2</sub>/Ar treatments in an N<sub>2</sub> environment.
- Figure 4.9. The O<sub>3</sub> density measured by UV absorption at 254 nm as a function of treatment time for a 1% O<sub>2</sub>/Ar plasma operated at peak-peak voltages of 12 kV, 14 kV, 16 kV, and 18 kV. O/C ratios extracted from XPS analysis are shown for the 12 kV and 18 kV condition.
- Figure 4.10. XPS measured oxygen composition as a function of NO<sub>x</sub> composition for the various experimental conditions used in this work in (a) N<sub>2</sub> ambient and (b) O<sub>2</sub> ambient. Surface nitration is limited by the availability of O<sub>2</sub> to oxidize the surface via NO<sub>x</sub>. For O<sub>2</sub>-deficient situations, if the oxygen composition is plotted against NO<sub>3</sub> instead of NO<sub>x</sub>, the modifications follow an O<sub>2</sub>-rich condition, demonstrating that NO<sub>3</sub> is a key species for feed gases other than O<sub>2</sub>/Ar. A typical error bar is shown in Fig. 10 (a).
- Figure 4.11. The dependence of surface bound NO, NO<sub>2</sub>, and NO<sub>3</sub> on the O composition of PS treated films under a wide range of experimental conditions explored in this work. For the most highly oxidized films, NO and NO<sub>2</sub> are not present.
- Figure 4.12. Possible mechanism for the surface reaction of PS with NO to oxidize the styrene ring and eliminate aromaticity.

## Chapter 5:

- Figure 5.1. N1s spectra of pristine LPS and LPS after SMD treatment (a) on Si and (b) in the well. NO<sub>3</sub> forms on both surfaces.
- Figure 5.2. Angle-resolved XPS N1s spectrum of LPS after treatment by 15% N<sub>2</sub> in O<sub>2</sub> SMD. More NO<sub>3</sub> is found at the surface than in the bulk. Treatment conditions: 7 min, 6 kV<sub>pp</sub>, 41.5 kHz, 3 mm mesh-sample gap.
- Figure 5.3. XPS C1s, N1s, O1s spectra taken before and after APPJ treatment of LPS, PMMA, PP, and PS. NO<sub>3</sub> forms on all the materials, but the accompanying oxygen uptake is material dependent. Treatment conditions: 7 min, 1% O<sub>2</sub> in Ar, 14 kV<sub>pp</sub>, 24 kHz, 9 cm source-to-nozzle gap, 3 cm nozzle-sample gap.
- Figure 5.4. XPS spectra of LPS before and after treatment by the SMD. Treatment conditions: 15% N<sub>2</sub> in O<sub>2</sub>, 7 min, 6 kV<sub>pp</sub>, 41.5 kHz, 3 mm mesh-sample gap.
- Figure 5.5. NO<sub>3</sub> and O composition derived from XPS analysis of SMD-treated LPS for various N<sub>2</sub>/O<sub>2</sub> gas chemistries. For the open circles, the NO<sub>3</sub> contribution to the O composition has been subtracted out. Treatment conditions: 7 min, 6 kV<sub>pp</sub>, 41.5 kHz, 3 mm mesh-sample gap.

- Figure 5.4.
- Figure 5.6. Normalized LPS biodeactivation vs.  $N_2/O_2$  ratio as measured by ELISA compared with (a)  $NO_3$  composition and (b) O composition with and without  $NO_3$  considered. Treatment conditions: 6 kV<sub>pp</sub>, 41.5 kHz, 7 min.
- Figure 5.7. Normalized LPS biodeactivation vs (a)  $NO_3$  and (b) O (without  $NO_3$ ) composition of SMD-treated LPS films.
- Figure 5.8. A Langmuir model of adsorption for LPS biodeactivation following CAP treatment demonstrating the modification of LPS (the antigen) binding sites inhibiting antibody binding.

## Chapter 6:

- Figure 6.1: Chemical structures of the polymers studied in this work. PMMA = poly(methyl methacrylate).
- Figure 6.2: SMD experimental setup enabling controlled environments and sample transport under vacuum to surface analysis for (a) the APPJ and (b) the SMD..
- Figure 6.3: Normalized biodeactivation by the SMD as a function of  $N_2/O_2$  mixture for biotinylated-LPS (bLPS), LPS, and PGN.
- Figure 6.4: After SMD treatment, (a) C1s, (b) N1s, and (c) O1s XPS spectra of LPS. In (d), the  $NO_3$  and O composition vs  $N_2/O_2$  mixture are shown.
- Figure 6.5: (a) Power density vs  $N_2/O_2$  mixture for the surface microdischarge at constant applied voltage and (b) film composition vs power density for the investigated gas chemistries.
- Figure 6.6: (a) LPS  $NO_3$  and O composition of LPS for varying applied voltages after SMD treatment in 15%  $N_2$  in  $O_2$ . (b) LPS  $NO_3$  and O composition after SMD treatment as a function of total generated  $O_3$ . The O composition is divided into total O composition (solid circles) and O composition independent of  $NO_3$  (open circles). The dotted line indicates the O composition of the pristine film.
- Figure 6.7:  $O_3$  density produced by the SMD vs time for (a) varying  $N_2/O_2$  mixtures at constant applied voltage (6 kV) and (b) varying applied voltage for 15%  $N_2$  in  $O_2$  environment.
- Figure 6.8: (a) C 1s XPS spectra of PGN after SMD treatment and (b) PGN  $NO_3$  and O composition as a function of  $N_2/O_2$  mixture. In (b), the dotted line indicates the pristine PGN film O composition.
- Figure 6.9. N1s spectra of (a) PVA, (b) PS, (c) PP, and (d) PMMA before and after SMD treatment. Treatment conditions: 7 min, 6 kV<sub>pp</sub>, 41.5 kHz.
- Figure 6.10: C1s spectra of (a) PVA, (b) PS, (c) PP, and (d) PMMA before and after SMD treatment. Treatment conditions: 7 min, 6 kV<sub>pp</sub>, 41.5 kHz. Peak positions are indicated in the figure.
- Figure 6.11 O1s spectra of (a) PVA, (b) PS, (c) PP, and (d) PMMA before and after SMD treatment. Treatment conditions: 7 min, 6 kV<sub>pp</sub>, 41.5 kHz. Peak positions are indicated in the figure.
- Figure 6.12  $NO_3$  and O compositions vs  $N_2/O_2$  mixture for a) PP, b) PMMA, c) PS, and d) PVA. For PMMA and PVA after SMD treatments. The dotted line shows the O composition of the pristine film. Open circles show the O composition if contributions due to  $NO_3$  are subtracted.



Figure 6.13: Normalized biodeactivation by the APPJ as a function of the 1% N<sub>2</sub>/O<sub>2</sub> admixture chemistry for biotinylated-LPS (bLPS), LPS, and PGN.

Figure 6.14 (a) LPS C1s composition for the virgin LPS film and various 1% molecular gas admixtures to Ar. In (b) the LPS NO<sub>3</sub> and O compositions as a function of the 1% N<sub>2</sub>/O<sub>2</sub> gas admixture chemistry.

## List of Tables

### Chapter 1:

Table 1.1. Organization chart of collaborators and competencies.

Table 1.2. Model polymers studied in this work.

### Chapter 4:

Table 4.1. XPS measured composition of PS films after various APPJ treatments for the standard conditions used in this work.

# Chapter 1: Introduction

## 1.1. Plasma-Material Interactions and Plasma Medicine

Non-thermal low temperature (cold) plasmas are traditionally used at low pressure for surface processes in the microelectronics industry. The wide variety of energetic species including ions, electrons, high energy photons in the vacuum ultraviolet and ultraviolet ((V)UV), and reactive neutrals participate in both gas-phase and surface reactions. In low temperature plasma, the electrons, having low mass and high mobility, can easily gain energy from electric fields compared to the ions. This leads to electron temperatures as high as 10000 K with neutral and ion temperatures only slightly above room temperature. The high energy electrons are responsible for many of the gas-phase reactions (e.g. electron impact ionization, excitation, and dissociation). Low temperature plasma can also be generated at atmospheric pressure. An early example of this is an ozone generator, which is based on a dielectric barrier discharge. In contrast to low pressure plasmas, charged species play a very small role in surface modifications at atmospheric pressure and will only contribute under specific conditions. At atmospheric pressure, reactive neutral species dominate. The past two decades have seen the rise of a new direction for cold atmospheric plasma (CAP): applications in healthcare and biology.

This new field, termed plasma medicine, has many promising applications including decontamination/disinfection of living and non-living surfaces (e.g. skin or medical devices),<sup>[2-8]</sup> cancer treatment,<sup>[9-15]</sup> blood coagulation,<sup>[6, 16]</sup> wound healing,<sup>[17-21]</sup> and also in dentistry.<sup>[22, 23]</sup> Plasma has a well-established medical role in electrosurgery devices for applications including tissue cutting and cauterizing. These devices differ from CAP in that they rely on heating tissue with electric current. The effect is thermal. The worldwide effort to advance this rapidly growing field is very impressive and many reviews are available.<sup>[24-28]</sup> While numerous applications exist,

an atomistic understanding of how CAP interacts with something as complex as living tissue is lacking. It has been speculated that the key species are reactive oxygen species (ROS) and reactive nitrogen species (RNS), which are sometimes collectively referred to as reactive oxygen and nitrogen species (RONS).<sup>[29]</sup> These species include radicals such as O, OH, NO, NO<sub>2</sub>, and nonradicals such as O<sub>3</sub>. RONS have been widely studied in aerobic biology in redox (oxidation-reduction) biology, and have been typically associated with only destructive effects, which is why foods that are rich in antioxidants have become popular. While some of these foods are undoubtedly healthy, the negative connotation associated with radicals is undeserved. In fact, the 1998 Nobel Prize in Physiology or Medicine was awarded for the discovery of the role of nitric oxide (NO) in the cardiovascular system. RONS are also naturally generated by both animal and plant immune systems to fight against microbes, parasites, and tumors and to encourage tissue regeneration.

CAP can also be used for industrial surface processing of polymers such as polystyrene and polypropylene. Common polymeric materials are lightweight, low-cost, easily recyclable, and have excellent mechanical properties. However, some polymers exhibit hydrophobic surfaces, which results in poor wettability or adhesion, which is required for certain applications such as coating and printing. Wet chemical technologies aimed at achieving desirable surface properties are slowly being replaced by plasma treatments at low, medium, and high pressures as plasma treatments can be low-cost and environmentally friendly.<sup>[30]</sup> Additionally, model polymers can be used to simplify the complex molecular structure of cells and biomolecules, as discussed later.

From a plasma medicine perspective, this dissertation focuses on decontamination of surfaces. Specifically, the deactivation of pernicious biomolecules that are found in bacteria cells

such as *Escherichia coli* (*E. coli*) and *Staphylococcus aureus* (*S. aureus*). This is distinguished from sterilization, which refers to the killing of living bacteria cells. There is a dire need for effective cleaning, sterilization, and decontamination of medical instruments in hospitals to ensure patient safety. Traditional cleaning techniques such as autoclaving, ethylene oxide washes, and gamma radiation suffer from several disadvantages: autoclaving cannot be used with heat sensitive materials; ethylene oxide is highly toxic; and gamma radiation requires large assemblies and strict safety precautions. Most importantly, the aforementioned procedures can leave harmful biomolecular residues on instruments after cleaning, which may transfer to the patient during medical procedures through contact with a patient's sterile tissues and bloodstream, causing an immune response. Even if the bacteria cell is killed by, e.g. UV radiation that results in fatal DNA damage in the cell nucleus, biomolecules can still be released from the cell wall, which can lead to generalized sepsis syndrome including fever, hypotension, shock, multiple organ failure, and even death. If the bacteria cell was not killed, this can lead to a hospital acquired infection (HAI).<sup>[31]</sup> A 2005 study found that the primary cause of infections due to surgical implants resulted from bacterial contamination of biomaterial surfaces.<sup>[32]</sup> A 2011 study found that mortality, cost, and length of stay all increase dramatically if the patient has HAIs.<sup>[33]</sup> The odds of mortality were up to 9-fold higher for patients with HAIs while costs and length of stay were at least 2-fold higher. While not all HAIs result from inadequate cleaning, it is clear that new cleaning and sterilization techniques need to be explored. There is also an increasing danger of antibiotic resistant bacteria such as *Methicillin-resistant Staphylococcus aureus* (MRSA), which presents a major public health threat responsible for 19,000 deaths annually in the USA with an increasing economic burden.<sup>[34]</sup>

CAP treatment of has several key advantages over traditional decontamination techniques. CAP devices operate at low temperature, which allows them to be used on heat-sensitive (polymer-based) devices, they consist of non-toxic gases such as argon, oxygen, and nitrogen, and, in contrast to antibiotics, bacterial resistance has yet to be observed.<sup>[35]</sup> Lastly, these devices can be inexpensive and portable. I envision a 3<sup>rd</sup> world country doctor traveling with a portable CAP device to clean her instruments.

The use of CAP is not limited to medicine. Any application requiring clean conditions, such as food and drug packaging or removing biological warfare agents can benefit from this field. There is also extensive research in CAP-based thin film deposition<sup>[36]</sup> and nanoparticle synthesis.<sup>[37, 38]</sup>

## **1.2. Collaborative Research**

This research project was based on world-class cross-disciplinary collaborations with leading experts in academia. A chart of participating institutions and their competencies is shown in Table 1.1.

**Table 1.1.** Organization chart of collaborators and competencies.

<b>Project Member</b>	<b>Members</b>	<b>Collaboration</b>	<b>Task</b>
UMD	Oehrlein, Seog	ICP reactor, atmospheric plasma sources, XPS, ellipsometry, OES, AFM, ELISA	Plasma processing, etch rates, plasma properties, surface analysis, surface morphology, biological testing
UCB	Graves	Low pressure VUV and radical sources, FTIR, QCM	VUV and radical effects, bulk chemical composition
OSU	Lempert, Adamovich	Gas-phase characterization: TALIF, LIF, OES, IROES	ROS/RONS detection
U Antwerp	Bogaerts	MD simulations	Modeling ROS interactions with biomolecules
U Michigan	Kushner	MD simulations	Modeling plasma-water interactions

### 1.3. Immunostimulating Biomolecules: Lipopolysaccharide and Peptidoglycan

As mentioned above, CAP is a promising technology for surface disinfection. Bacteria can be divided into two classes based on the structural characteristics of the cell wall: Gram-negative and Gram-positive.

In Gram-negative bacteria such as *E. coli*, the outermost layer of the cell membrane consists of lipopolysaccharide (LPS). The structure, function, and recognition of LPS are well established in the literature and will be briefly overviewed here.<sup>[39,40]</sup> LPS, also called endotoxin, can be divided into three components: immune-stimulating lipid A, a core oligosaccharide, and an O-antigen. Across different strains and species of LPS, lipid A is the most structurally conserved component. Lipid A consists of a several acyl chains (12-14 carbons each) linked by esters and amides to a diphosphorylated disaccharide backbone. The core oligosaccharide and O-antigen protect the cell and are made up of cyclic carbohydrates and their derivatives, some of which contain amide groups. These latter two regions give the biomolecule a hydrophilic

character, but are not ubiquitous in all Gram-negative strains. The O-antigen is the least conserved structure in LPS and consists of a repeating glycan polymer whose exact structure determines the serotype of LPS for a particular Gram-negative species. Furthermore, a single organism will produce LPS with O-antigen subunit repetitions between 0 and 50. The O-antigen is essential for bacteria survival as it protects that cell from penetration of immune cells. The core oligosaccharide contains an unusual sugar, 3-deoxy-D-manno-octulosonic acid (Kdo), which directly links to lipid A and is the smallest saccharide component naturally seen in LPS. That is, its presence is required for cell viability.

In Gram-positive bacteria such as *S. aureus*, the outermost layer of the cell membrane is composed of peptidoglycan (PGN), wall teichoic acids and lipoteichoic acid.<sup>[41]</sup> PGN, also called murein, is found in Gram-negative bacteria, but is typically less than 10 nm thick between the outer and inner membrane, whereas, in Gram-positive bacteria, it is 20-40 nm thick. This thick layer provides structural rigidity to the cell wall and protects the cell. Peptidoglycan is a large glycan polymer that forms a 3D mesh-like macromolecular structure via peptide crosslinks. The glycan backbone consists of a repeating disaccharide subunit of *N*-acetylglucosamine and *N*-acetylmuramic acid. A carboxyl group on *N*-acetylmuramic acid links the peptide chain to the backbone. While the backbone is highly conserved, the peptide cross-links are variable between different Gram-positive species. For example, *S. aureus* peptides are cross-linked by a pentaglycine interpeptide bridge whereas *bacilli* species peptides are directly cross-linked without the interpeptide bridge. Analogous to LPS, the most conserved part of peptidoglycan, the disaccharide backbone, induces the immune response whereas the variable peptide stem does not.<sup>[41]</sup>

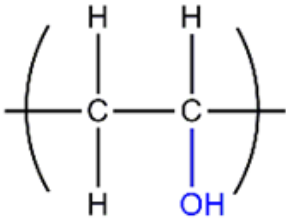
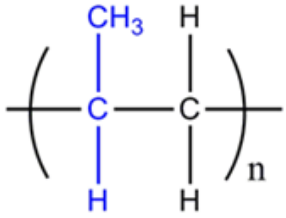
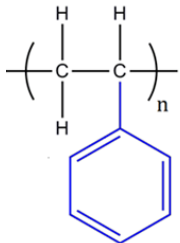
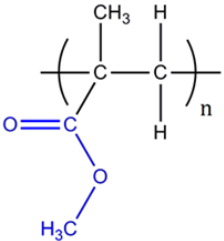


Both of these biomolecules activate the mammalian innate immune system, the body's first response to a pathogen. LPS is recognized when it forms a complex with lipopolysaccharide binding protein. This complex binds to monocytes and macrophages via immune cell surface receptors including Toll-like receptor 4 (TLR-4) and CD14. This recognition initiates the secretion of signaling molecules such as pro-inflammatory and immunomodulating cytokines (small proteins), including interleukin-1 $\beta$  (IL-1 $\beta$ ), IL-6 and tumor-necrosis factor- $\alpha$  (TNF- $\alpha$ ). This response is necessary to activate the immune system, but can lead to a dysregulated, whole-body inflammatory response (cytokine storm) at high LPS concentrations.<sup>[41-46]</sup> The innate immune system recognizes these biomolecules by molecular pattern recognition whereby innate immune system receptors detect microbial motifs that are conserved, such as lipid A. Fortunately, these microbial motifs are essential for the pathogen and not present in host cells. Changes to these microbial motifs i.e. the molecular structure of lipid A decrease the biomolecule's toxicity and thus the immune response. For example, it has been found that monophosphorylated lipid A or lipid A with shorter or fewer aliphatic chains induces a decreased immune response compared to the intact molecule.<sup>[39]</sup> Peptidoglycan behaves similarly. This direct structure-function relationship is promising for mild, CAP treatments that can cause modifications that deactivate the biomolecule.

#### **1.4. Model Polymers**

To simplify the complex molecular structure of the biomolecules and isolate specific functional groups, model polymers were studied as well, as shown in Table 1.2.

**Table 1.2.** Model polymers studied in this work.

Material	Structure	Functional group	Biological relevance
polyvinyl alcohol (PVA)		alcohol	carbohydrates, some amino acids, hormones
polypropylene (PP)		alkyl	lipids, amino acids
polystyrene (PS)		aromatics, rings	amino acids, nucleic acids
poly(methyl methacrylate) (PMMA)		ester groups	fats/oils, DNA backbone

### 1.5. Plasma Treatments

Both low and atmospheric pressure plasma sources were used. The low pressure work was performed in two inductively-coupled plasma (ICP) reactors (125 mm and 300 mm diameter substrates) schematically shown in figure 1.1. These two ICP systems have been described in detail previously.<sup>[47, 48]</sup> In both systems, a planar coil placed on top of a quartz window is powered through an L-type matching network with a 13.56 MHz power supply (0-2000 W). The bottom electrode can be biased to independently control the ion bombardment energy, but this

was not used in this work. The temperature of the bottom electrode is kept constant at 10 °C by a chiller and samples thermally contact the substrate via thermal grease. For the low pressure experiments, Ar and H<sub>2</sub> plasmas were chosen at a gas flow rate of 50 standard cubic centimeters per second (sccm). Before treatments, the base pressure in the chamber was  $2 \times 10^{-3}$  Pa. In these experiments, no external bias was applied, so the ion energy in direct plasma treatments was determined by the plasma potential and floating surface potential and is estimated near ~20 eV. High energy photons and radicals were isolated from the bulk plasma, as described in Chapter 2.

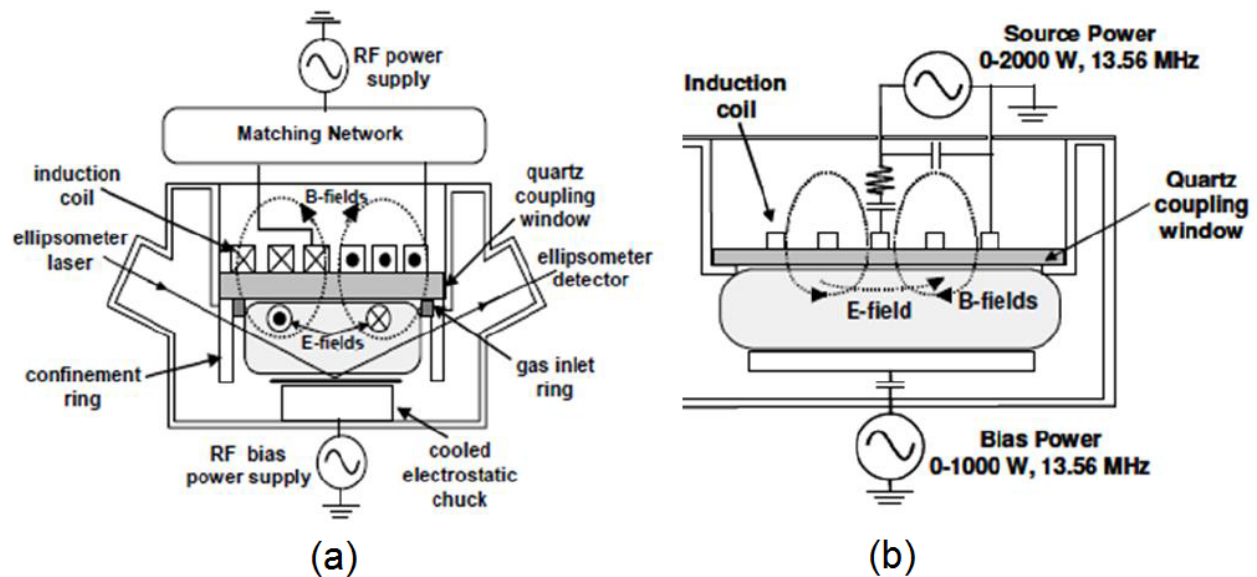


**Figure 1.1:** Inductively-coupled plasma reactors used in this work with (a) 125 mm substrate diameter and equipped with *in situ* ellipsometry and (b) 300 mm substrate diameter and vacuum transfer to surface analysis.

The atmospheric pressure plasma work was performed by an atmospheric pressure plasma jet (APPJ) and surface microdischarge (SMD) that are mounted inside the 300 mm ICP described above, which allows for samples to be transferred under vacuum to surface analysis.

The plasma-ambient interaction can be evaluated by evacuating the chamber and then refilling it with a gas chemistry of choice. The APPJ used in this work is based on a design first described by Teschke *et al.* where two electrodes are wrapped around a dielectric tube (alumina in this work).<sup>[49]</sup> When Ar (or He) flows through the tube and a high voltage is applied across the electrodes, the plasma ignites. To add reactivity to the plasma, up to 2% admixtures of O<sub>2</sub>/N<sub>2</sub> can be added to the Ar carrier gas. As described in detail in Chapters 3 and 4, the plasma-ambient interaction can be regulated by moving the source close to or far from the nozzle. When the source is close to the nozzle, a visible plume extends into the ambient, exciting and interacting with ambient gas molecules. When the source is far from the nozzle, the plume is confined within the tube and plasma-ambient interactions are minimized. Charged species will dominate inside the source and in the plume, metastables and short-lived reactive neutrals will dominate inside and just outside the plume, and long-lived species dominate in the far effluent, as shown in Fig. 1.2.

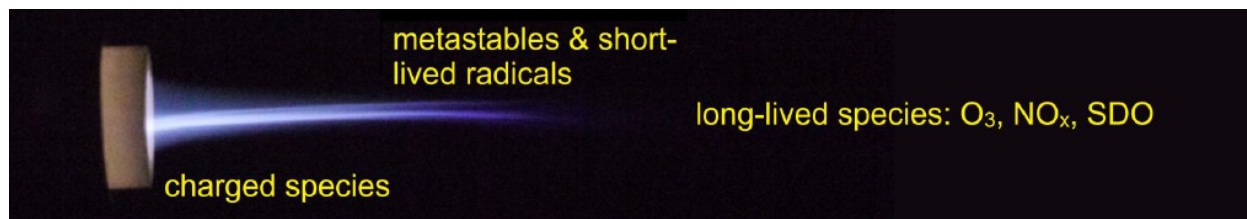


**Figure 1.2:** Photograph of the atmospheric pressure plasma jet showing where certain species are found.

The SMD used in this work is based on the sandwich design by Morfill *et al.* in which a copper electrode and grounded mesh are separated by a thin dielectric.<sup>[50]</sup> When a voltage ( $\sim 6$  kV<sub>pp</sub>) driven at kHz frequencies is applied to the copper electrode, a plasma forms around the

mesh. The SMD operates in  $N_2/O_2$  ambients and does not require a noble carrier gas. A photograph of the SMD used in this dissertation is shown in Figure 1.3.

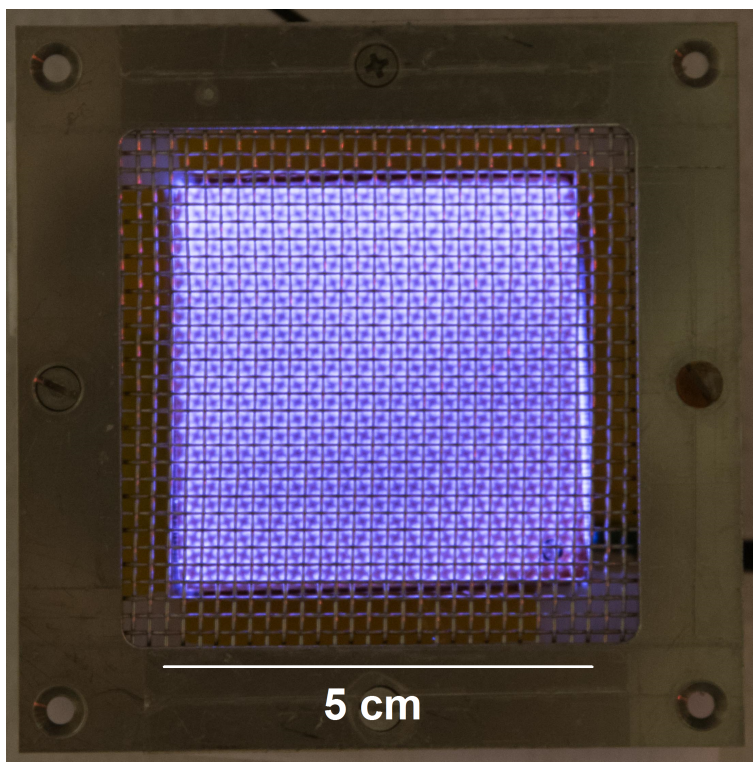


**Figure 1.3.** SMD operating in air.

## 1.6. Characterization

Plasma treatments were monitored in real-time by *in situ* ellipsometry, optical emission spectroscopy (OES), electrical diagnostics, and ultraviolet absorption spectroscopy. Before and/or after processing, materials were characterized by x-ray photoelectron microscopy (XPS), atomic force microscopy (AFM), ellipsometry, and an enzyme linked immunosorbent assay (ELISA). An informal collaboration with the University of Antwerp provided complementary classical molecular dynamic simulations.

**Ellipsometry.** Ellipsometric analysis of films was carried out *in situ* and *ex situ* using an automated rotating compensator SOFIE STE70 ellipsometer in the polarizer-compensator-sample-analyzer (PCSA) configuration using a He-Ne laser ( $\lambda = 632.8$  nm) at a  $\sim 72^\circ$  angle of incidence. Film thickness and modification were extracted with multilayer optical modeling of films on top of a Si substrate with refractive index fixed at  $\tilde{N}=3.886-0.028i$ . Ellipsometry measures  $\Psi$  and  $\Delta$ , which relate to the amplitude ratio and phase shift of the polarized laser components, respectively.

**Optical Emission Spectroscopy.** Plasma emission spectra were measured by a Princeton Instruments SpectraPro 2300i optical emission spectrometer with a grating of 1200 grooves/mm blazed at 300 nm. The optical fiber was oriented along the plasma jet axis to probe into the discharge. An intensified charge-coupled device (iCCD) camera and optical filters available through a collaboration with Profs. Walter Lempert and Igor Adamovich at the Ohio State University allowed for spatially resolved emission measurements perpendicular to the plasma jet.

**Ultraviolet (UV) Absorption Spectroscopy.** UV absorption spectroscopy was used to detect plasma-generated ozone based on ozone's absorption of 254 nm light and Beer's law<sup>[51]</sup>

$$N_{O_3} = -\ln\left(\frac{I_t/I_0}{\sigma L}\right) \quad (1.1)$$

where  $I_t$  is the transmitted light intensity after passing through ozone,  $I_0$  is the intensity of the incident light,  $\sigma$  is the absorption cross section ( $1.15 \times 10^{-17}$  cm<sup>-2</sup> for O<sub>3</sub>), and  $L$  is the path length of the light. An ambient ozone analyzer (Thermo Electron UV Photometric O<sub>3</sub> Analyzer Model 49) generously provided by Prof. Russell Dickerson in UMCP's Department of Atmospheric and Oceanic Science was initially used to measure O<sub>3</sub> densities. With this analyzer, the outlet from

the plasma jet was fed into the analyzer and does not interact with the ambient. Later, a homemade O<sub>3</sub> analyzer was used. The 254 nm light was generated by an Ar/Hg lamp and measured by a photodiode after passing through a band pass filter centered at 254 ± 10 nm.

**X-ray Photoelectron Spectroscopy (XPS).** XPS analysis provided information on chemical changes at the film surface. The analysis was performed with a Vacuum Generators ESCA Mk II surface analysis system employing a Mg-K $\alpha$  source (1253.6 eV) at electron takeoff angles of 90° (deep probing depth  $\approx$  8 nm) and 20° (shallow probing depth  $\approx$  2-3 nm) relative to the surface. Unless otherwise noted, samples were transferred to XPS after treatment under vacuum through an interface between the CAP treatment chamber and the aforementioned vacuum cluster. Vacuum transfer prevents exposure to ambient conditions, which can result in contamination and oxidation. Sample charging was compensated by calibrating the binding energy position of the C-C/C-H peak in the C1s spectra to 285 eV after Shirley background subtraction. Peak assignments were taken from the literature.<sup>[52]</sup>

**Atomic Force Microscopy (AFM).** Surface morphology and roughness was measured before and after treatment by a tapping mode AFM (MFP-3D, Asylum Research). The surface roughness values reported were calculated from the root mean square of the surface profile.

**Enzyme Linked Immunosorbent Assay (ELISA).** ELISA is a powerful technique for detecting a wide variety of biomolecules based on a color change induced by enzyme-tagged antibodies. It is sensitive enough to detect biomolecule concentrations on the order of pg/ml. This technique is commonly used to detect antigens based on antigen-antibody binding and results can be either

qualitative (yes/no) or quantitative. Three different ELISA techniques are generally used and will be briefly overviewed here. In a direct ELISA, an antigen in a buffered solution is directly adsorbed to the bottom of a well in a 96-well plate through nonspecific interactions. This incubation step takes several hours and is typically done overnight. In a second step, a blocking solution is added, typically containing nonreacting proteins such as bovine serum albumin (BSA) or casein. This step is necessary to block any parts of the well that are not covered by the antigen to prevent nonspecific binding of the antibodies to the well. A primary antibody is then added that will specifically bind to the antigen. This antibody can be tagged with an enzyme, which will produce a color change in subsequent steps. If the primary antibody is not tagged with an enzyme, then an enzyme-labeled secondary antibody is used. A substrate is then added which changes color upon reaction with the enzyme. This reaction is then stopped by addition of acid and the optical density is measured at a wavelength that depends on the choice of enzyme/substrate. In between most steps, excess antigen/antibody is removed by washing at least three times. Sandwich ELISA is similar to the direct ELISA, except for the well plate is precoated with an antibody that captures antigens from the solution. The rest of the assay proceeds as described above, although the blocking step is sometimes excluded due to the complete coverage by the capture antibody. This method requires matched pairs of antibodies that will bind to different epitopes of the antigen. The last commonly used type of ELISA is competitive ELISA whereby the binding affinity of different antibodies to an antigen can be measured.

In this dissertation, quantitative, direct ELISA is used and is shown in a simplified schematic in Figure 1.4. The antigens are peptidoglycan from *S. aureus* (PGN), lipopolysaccharide (LPS) from *E. coli*, and biotin, which is bound to LPS (bLPS). A monoclonal



antibody specific to LPS or PGN binds to the antigen followed by a horseradish peroxidase (HRP)-conjugated secondary antibody. In the case of bLPS, antibodies were not used. Instead, streptavidin, a small protein, conjugated with HRP was used. HRP induces a color change (blue) in the substrate that changes to yellow when the reaction is stopped by addition of 2 M H<sub>2</sub>SO<sub>4</sub>. The yellow color can be measured by absorption of 450 nm light by an automatic microplate reader. A detailed protocol can be found in Appendix A. The intensity of the color directly corresponds to the amount of HRP present, which directly relates to the presence of the antigen. Thus, a weak yellow color will appear when low concentrations are present and a strong yellow color will appear at high concentrations. This intensity difference results from Beer's Law, which, alternatively to Equation 1.1, can be written as:

$$A = C\epsilon l \quad (1.1)$$

Where  $A$  is the absorbance,  $C$  is the analyte (HRP-activated substrate) concentration, and  $l$  is the path length the light travels through the absorbing medium. The molar attenuation coefficient,  $\epsilon$ , reflects how well the medium attenuates light of a particular wavelength. The exact surface density of HRP on the antibodies is proprietary, and one cannot expect a 1:1 relation between the analyte concentration and surface density of antigen. However, it is clear that the absorbance directly relates to the amount of antigen in the well.

To measure the plasma-based deactivation, a plasma treatment step is inserted before the blocking step. To analyze the results, the optical density for the negative control (0  $\mu$ g/ml of antigen) was subtracted from all the wells. Treated wells were then compared to untreated wells from the standard curve of the same pretreatment concentration. The biological activity is defined as a ratio of the absorbance of the treated well to the absorbance of the untreated well in

the standard curve of the same initial concentration. We consider this the normalized biological activity (BA):

$$BA = \frac{A_p}{A_0} \quad (1.2)$$

where  $A_p$  is the absorbance of the plasma treated well and  $A_0$  is the absorbance of the untreated well. The normalized biodeactivation (BDA) is unity minus this value:

$$BDA = 1 - BA \quad (1.3)$$

Thus, a normalized biodeactivation of unity would correspond to complete biodeactivation and zero would correspond to zero biodeactivation.

It should be noted that some biomolecules have multiple binding sites for different antibodies/proteins. Based on conversations with the primary antibody manufacturer, the LPS antibody is thought to bind to lipid A's disaccharide backbone. However, LPS binding protein, a protein in human blood, binds to the entire lipid A complex including the aliphatic chains. Thus, the work in this dissertation only describes the biodeactivation of one type of interactions. We expect this biodeactivation to be indicative of a reduction in the overall immunological response based on investigations by collaborators at UCB. This work described by Chung et al. used the human whole blood test to measure the biodeactivation of lipid A by VUV photons, O radicals, and D radicals.<sup>[1]</sup> In this test, human whole blood is incubated on the treated or untreated lipid A-coated Si chip. After incubation, supernatants were collected from the blood by centrifugation and the pro-inflammatory protein IL-1 $\beta$ , which is released in human whole blood in the presence of lipid A, was measured. This test more directly simulates an immune response, though quantification and interpretation of results was difficult due to the differences between human whole blood from different donors. Nevertheless, an overall reduced immune response was measured. Even though the ELISA described in this dissertation only describes one type of

biodeactivation i.e. prevention of one antibody-antigen binding complex, the results are likely generic to many interactions and thus contribute to an overall reduction in immune response.

Chung et al. also found that the human whole blood test and biodeactivation were effectively monitoring the film surface.<sup>[1]</sup> They attributed this to the fact that lipid A films were not readily soluble in blood and from time of flight secondary ion mass spectroscopy (ToF-SIMS) and Fourier transform infrared spectroscopy (FTIR) analysis showing that radicals only impacted the film surface. As will be discussed below, we also find that the ELISA method measures the film surface. In Chapter 2, we show that the lipid A portion of LPS organizes at the air-film interface. In Chapter 5, we show that the film in the well behaves similarly to the film on the Si substrate. The density of lipid A, which is necessary for antibody binding, determines the biological response. In Chapter 5, we show that NO<sub>3</sub> correlates with biodeactivation. Angle resolved XPS measurements show that the NO<sub>3</sub> is also localized at the film surface. With these considerations in mind, biodeactivation indirectly measures the degree of modifications to binding sites at the surface by directly measuring the ability of an antibody to bind.

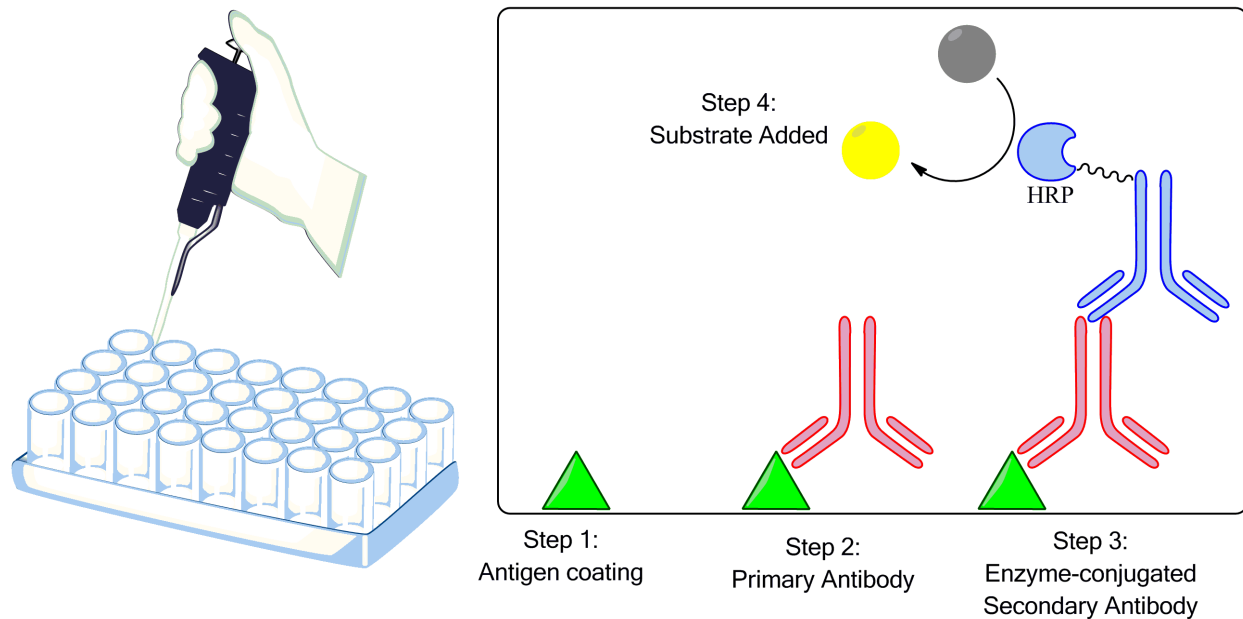


**Figure 1.4.** Simplified schematic of ELISA.

### 1.7. Thesis Outline

The goal of this thesis is to advance society’s understanding of the underlying mechanisms of how low temperature plasma interacts with biological and polymeric surfaces. Only by gaining atomistic understandings like those described in this thesis can the emerging field of plasma medicine safely and effectively grow.

In Chapter 2, we investigated the individual contributions of ions, high energy photons, and reactive neutrals in a low pressure plasma system. We show how each of these species contributes to etching, biodeactivation, and surface modifications. A model of modifications is also proposed that is consistent with complementary work by collaborators. The findings reported there motivated work at atmospheric pressure.

In Chapter 3, the first experiments at atmospheric pressure are performed and the role of plasma-ambient interactions is explored. We find that  $N_2$  present in the ambient can quench

plasma-generated reactive oxygen species. This quenching is consistent with when  $N_2$  is purposely added to the feed gas, reducing oxygen atom emissions and ozone densities.

In Chapter 4, plasma-ambient interactions were further investigated using polystyrene as a model polymer system. By using a variety of environmental and feed gas chemistries and regulating the plasma-ambient interaction, we find that the  $O_2$  ambient causes less modification than the  $N_2$  ambient. We also described a competition between surface oxidation and nitridation, the latter of which has not been reported in the literature.

In Chapter 5, we explore the role of surface-bound  $NO_3$ , the new chemical moiety that we were the first to report on atmospheric plasma-treated surfaces. We find that it forms on surfaces after treatment by two very different sources: an atmospheric pressure plasma jet and a surface microdischarge. This species also formed on a variety of materials, indicating that its formation is generic to atmospheric plasma. Lastly, we found that  $NO_3$  on the surface correlates with biodeactivation more than oxidation that is independent of  $NO_3$ .

In Chapter 6, we conducted an in-depth investigation on the surface chemical modifications induced by the surface microdischarge, which had not been previously performed, on a variety of biomolecules and polymers. A comparison was made between the surface microdischarge and atmospheric pressure plasma jet. Both sources deactivate biomolecules effectively, but the surface microdischarge causes significantly more modifications and does not require a noble carrier gas, making it more economical. We discussed the selectivity of  $NO_3$  formation and oxidation on a variety of surfaces. These results were also compared with gas-phase characterization on the surface microdischarge and simulation results found in the literature.

In Chapter 7, conclusions are made and future directions are discussed.

## **Chapter 2: Deactivation of lipopolysaccharide by Ar and H<sub>2</sub> inductively-coupled low pressure plasma**

**E A J Bartis<sup>1,2</sup>, C Barrett<sup>1</sup>, J Seog<sup>1</sup>, G S Oehrlein<sup>1,2</sup>**

<sup>1</sup> Department of Materials Science and Engineering, University of Maryland, College Park, MD  
20742, USA

<sup>2</sup> Institute for Research in Electronics and Applied Physics, University of Maryland, College  
Park, MD 20742, USA

**T-Y Chung, N Ning, J-W Chu, D B Graves**

Department of Chemical and Biomolecular Engineering, University of California, Berkeley,  
94720, USA

## Abstract

Using an inductively-coupled plasma system, we study the effects of direct plasma, plasma-generated high energy photons in the ultraviolet and vacuum ultraviolet (UV/VUV), and radical treatments on lipopolysaccharide (LPS). LPS is a biomolecule found in the outer membrane of Gram-negative bacteria and a potent stimulator of the immune system composed of polysaccharide and lipid A, which contains 6 aliphatic chains. LPS film thickness spun on silicon was monitored by ellipsometry while the surface chemistry was characterized before and after treatments by x-ray photoelectron spectroscopy (XPS). Additionally, biological activity was measured using an enzyme-linked immunosorbent assay under a) a sensitive regime (sub- $\mu\text{M}$  concentrations of LPS) and b) a bulk regime (above  $\mu\text{M}$  concentrations of LPS) after plasma treatments. Direct plasma treatment causes rapid etching and deactivation of LPS in both Ar and  $\text{H}_2$  feed gases. To examine the effect of UV/VUV photons, a long-pass filter with a cut-off wavelength of 112 nm was placed over the sample.  $\text{H}_2$  UV/VUV treatment causes material removal and deactivation due to atomic and molecular UV/VUV emission while Ar UV/VUV treatment shows minimal effects as Ar plasma does not emit UV/VUV photons in the transmitted wavelength range explored. Interestingly, radical treatments remove negligible material but cause deactivation. Based on the amphiphilic structure of LPS, we expect a lipid A rich surface layer to form at the air-water interface during sample preparation with polysaccharide layers underneath. XPS shows that  $\text{H}_2$  plasma treatment under direct and UV/VUV conditions causes oxygen depletion through removal of C-O and O-C=O bonds in the films, which does not occur in Ar treatments. Damage to these groups can remove aliphatic chains that contribute to the pyrogenicity of LPS. Radical treatments from both Ar and  $\text{H}_2$  plasmas remove aliphatic carbon from the near-surface, demonstrating the important role of neutral species.

## 2.1. Introduction

Low temperature plasma treatment of cells and living tissue is emerging as a versatile method to alter directly the function of biological matter in desirable ways.<sup>[53]</sup> One application that has received much attention is plasma-based sterilization of bacteria and deactivation of pernicious biomolecules.<sup>[54-61]</sup> Traditional cleaning methods suffer from several disadvantages and leave harmful residues on, for example, medical instruments, which can be transferred to a patient during medical procedures.<sup>[31]</sup> Plasma treatments offer three key advantages: they operate at low temperature, which allows them to be used on heat-sensitive devices, and they consist of non-toxic gases such as argon, oxygen, hydrogen, and nitrogen. Finally, in contrast to antibiotics, bacteria cannot become resistant to the treatment. The deactivation of biomolecules has been well-demonstrated, but the mechanism, e.g. the individual roles of various plasma species and a systematic understanding of what occurs at an atomistic level has been lacking.<sup>[62]</sup>

The present work describes research aimed at improving our understanding of the plasma species responsible for deactivation as well as the chemical changes occurring in biological systems that cause deactivation. We chose lipopolysaccharide (LPS, *Escheria coli* O111:B4) as a model biomolecule. LPS is found in the outer membrane of Gram-negative bacteria and triggers a severe immune response.<sup>[39]</sup> Its presence in the body can lead to fever, changes in white blood cell count, hypotension, sepsis, multiple organ failure, and death.<sup>[46]</sup>

In this study, LPS was exposed to inert (Ar) and reactive (H<sub>2</sub>) discharges under various conditions in order to gain an atomistic understanding of how various plasma species modify its chemical structures. The effect of direct plasma treatment, plasma-generated ultraviolet and vacuum ultraviolet (UV/VUV) photons, and plasma-generated radicals on LPS films was examined. We probed the surface morphology using atomic force microscopy (AFM) and



monitored material removal using in situ and ex situ ellipsometry. Changes in biological activities of LPS were indirectly measured using biotinylated LPS in an enzyme-linked immunosorbent assay (ELISA) platform and the surface chemistry was characterized by x-ray photoelectron spectroscopy (XPS). We show that Ar and H<sub>2</sub> plasma-based deactivation of LPS occurs via very different mechanisms due to differences in reactivity of plasma-generated UV/VUV photons and radicals. We also demonstrate the spatial extent of the changes induced by various plasma species and relate these changes to the deactivation of films with different thicknesses. The results obtained in this study are compared to a complementary beam study on lipid A, the toxic portion of LPS.<sup>[1]</sup>

## **2.2. Experiments and Methods**

### *2.2.1. Description of Materials*

Lipopolysaccharide O111:B4 (Sigma-Aldrich) was chosen in this study as a model biomolecule and is shown in figure 2.1. LPS consists of a pyrogenic component, lipid A, connected to a long polysaccharide chain called an O-chain by a core oligosaccharide.<sup>[39]</sup> Changes to the lipid A structure shown in figure 2.1 decrease the molecule's endotoxicity while changes to the O-chain and core oligosaccharide decrease a bacteria cell's defenses as the purpose of the O-chain is to protect the cell.<sup>[63]</sup> For example, it has been found that monophosphorylated lipid A or lipid A with shorter and fewer aliphatic chains shows less endotoxicity than the diphosphorylated molecule consisting of six aliphatic chains made up of 12-14 carbons.<sup>[39]</sup> The core oligosaccharide and O-chain consist of cyclic carbohydrates and their derivatives some of which contain amide groups. Most of the nitrogen in the molecule is found in the amide groups on the O-chain.

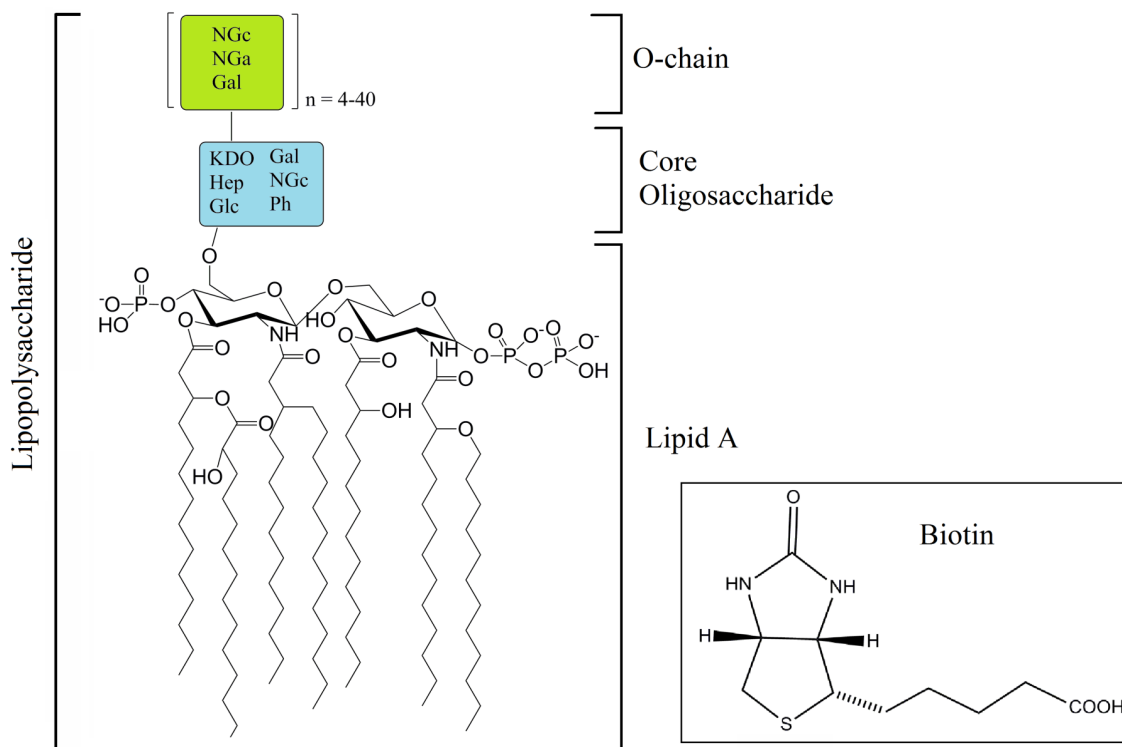


**Figure 2.1:** Schematic of lipopolysaccharide highlighting the structure of lipid A. Enclosed is the structure of biotin, which is conjugated to LPS for endotoxicity measurements. Ph = phosphate/pyrophosphate, KDO = 3-deoxy-D-manno-oct-2-ulosonic acid, Hep = heptose, Glc = glucose, Gal = galactose, NGc = N-acetyl-glucosamine, NGa = N-acetyl-galactosamine.

To prepare samples for surface analysis, LPS was dissolved in a 9:1(vol:vol) methanol:water solution and diluted to  $500 \mu\text{g ml}^{-1}$ . LPS films were prepared by spinning  $100 \mu\text{l}$  of LPS solution on piranha-cleaned silicon substrates at 100 rpm until they were dried.<sup>[64]</sup> The prepared films were about 60 nm thick. For indirect measurements of endotoxicity, biotinylated-LPS (bLPS, InvivoGen) in phosphate buffered saline solution (PBS, 0.4 M buffer, 0.15 M NaCl, pH = 7.2) was incubated in a 96-well microtiter plate for 2 hours at room temperature. The structure of biotin is shown in figure 2.1 and consists of an ureido ring fused with a tetrahydrothiophene ring containing a valeric acid substituent.<sup>[65]</sup> In these experiments, the

concentration of LPS/bLPS determines the film thickness. For LPS, decreasing the spun-on concentration below  $500 \mu\text{g ml}^{-1}$  resulted in thinner films. As discussed in detail below, after plasma treatments the bioactivity of bLPS varies depending on its concentration, demonstrating that film thickness plays a strong role in its deactivation. We use this difference to learn about the spatial extent of the changes induced by different moieties. To estimate a decrease in film thickness in the well, the well plate and a LPS-coated Si sample were treated in parallel. As material removal in the well and on the Si substrate should be the same, we correlate the loss of bioactivity with the thickness removed on the LPS-coated Si sample.

### *2.2.2 Plasma Processing*

The inductively-coupled plasma reactors used in this study have been described in detail in previous publications and will be briefly overviewed here.<sup>[47, 48]</sup> In both the 125 mm and 300 mm substrate electrode diameter reactors, a planar coil is placed on top of a quartz window and powered through an L-type matching network at 13.56 MHz with a power supply (0-2000 W). The distance between the quartz window and the substrate was 15 cm in the 125 mm reactor and 13 cm in the 300 mm reactor. The bottom electrode where the substrate is fixed was cooled at 10 °C by a chiller.  $25 \times 25 \text{ mm}^2$  samples were bonded to the substrate using thermal grease to rule out temperature effects. The base pressure achieved in the chamber was  $1.5 \times 10^{-5}$  Torr before processing and the total gas flow rate was 50 standard cubic centimeters per minute. The processing conditions used in the 125 mm reactor were 30 mTorr operating pressure with inductive power set to 300 W and 600 W for Ar and H<sub>2</sub>, respectively. In this reactor, Ar and H<sub>2</sub> plasma densities were on the order of  $10^{18} \text{ m}^{-3}$  and  $10^{16} \text{ m}^{-3}$ , respectively.<sup>[66]</sup> In the 300 mm reactor, the power was set to 150 W and the pressure was set to 10 mTorr. The ion current

density was  $1.2 \text{ mA cm}^{-2}$ . There was no external bias applied in any of the discharges, so the ion energy in direct treatments was determined by the plasma potential and floating surface potential and is estimated near  $\sim 20 \text{ eV}$ . To isolate the effect of high energy photons on LPS and enable in situ ellipsometry measurements, a stainless steel housing was placed over the sample that protects the film from ion bombardment while permitting photons to pass through a  $\text{MgF}_2$  optical filter with a cut-off wavelength of  $112 \text{ nm}$ , as shown in figure 2.2(a).<sup>[67]</sup> While the UV/VUV photon fluxes in our reactors have not been characterized, they are expected to be similar to those measured in comparable systems at  $\sim 10^{15} \text{ photons cm}^{-2}$ .<sup>[68]</sup> For UV/VUV treatment followed by XPS characterization, the  $\text{MgF}_2$  filter was placed directly on the sample. For radical treatment, a silicon roof structure with an aspect ratio of 20 to the edge of the sample was placed  $0.7 \text{ mm}$  over the sample as shown in figure 2.2(b).<sup>[69-72]</sup> As plasma is not generated within the gap and due to a long diffusion pathway to reach the sample at this high aspect ratio, the sample interacts with only radicals but minimally with other species such as ions, metastables, and photons. For XPS analysis, samples were treated by direct plasma treatment for 15 seconds and by UV/VUV-only and radical-only treatments for 15 minutes. To minimize the heating of the optical filter and roof structure, the plasma was cycled on and off every 5 minutes.

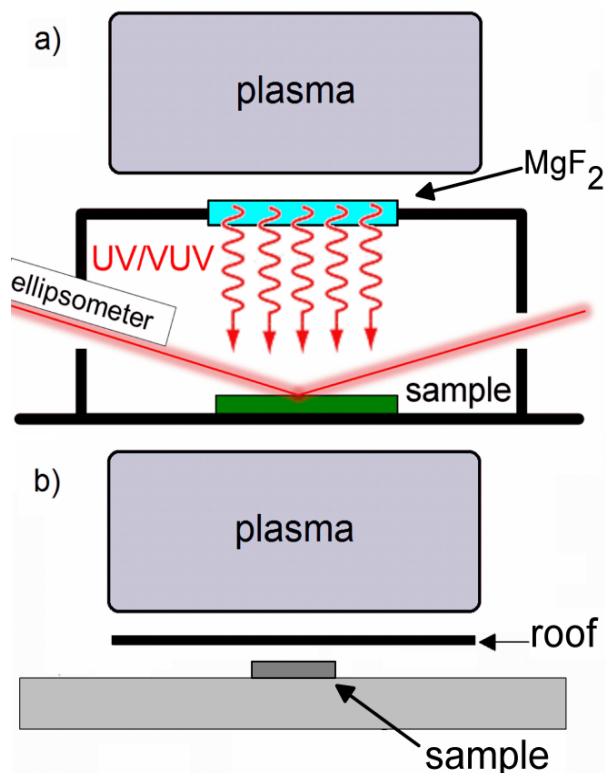


**Figure 2.2:** Schematic of the set up (not to scale) used for (a) real-time in situ ellipsometry of UV/VUV treatment and (b) radical treatment of LPS films. For UV/VUV treatment, a MgF<sub>2</sub> optical filter sits on top of a housing which prevents ion and electrons from interacting with the sample. The ellipsometer laser probed the sample through small apertures in the housing. For radical treatment, a roof structure sits 0.7 mm above the sample. Plasma is not produced within the gap, so only neutral species that diffuse under the gap (aspect ratio  $\approx 20$ ) can reach the sample.

### 2.2.3 Characterization

Material characterization was performed in real-time during processing in the 125 mm reactor by *in situ* ellipsometry or after processing in the 300 mm reactor by angle-resolved vacuum-transfer XPS. Films characterized by XPS were also characterized before and after

processing by *ex situ* ellipsometry. The ellipsometer is an automated rotating compensator ellipsometer working in the polarizer-compensator-sample-analyzer configuration at a  $\sim 72^\circ$  angle of incidence. The ellipsometric measurements were performed with a He-Ne laser ( $\lambda = 632.8$  nm). For our LPS films, multilayer modeling of the LPS layer on top of  $\sim 1.8$  nm  $\text{SiO}_2$  on a Si substrate allowed us to extract changes in film thickness.

XPS analysis provided information on chemical changes at the film surface. The analysis was performed with a Vacuum Generators ESCA Mk II surface analysis system employing a Mg-K $\alpha$  source (1253.6 eV) at electron takeoff angles of  $90^\circ$  (deep probing depth  $\approx 8$  nm) and  $20^\circ$  (shallow probing depth  $\approx 2$ -3 nm) relative to the surface at 20 eV pass energy. The film composition was calculated using the integrated peak areas of the C 1s, O 1s, N 1s, and P 2p spectra with corresponding Scofield cross sections of 1, 2.85, 1.77, and 1.25, respectively.<sup>[73]</sup> High resolution C 1s, O 1s, N 1s, and P 2p spectra were fit using a least square fit with 70/30 Gaussian-Lorentzian peaks after Shirley background subtraction and charge compensation by calibrating the binding energy position of the C-C/H peak to 285 eV. C 1s spectra were fit with six peaks corresponding to C=C (284.5 eV), C-C/H (285 eV), C-CO (285.5 eV), C-O (286.5 eV), O-C-O/N-C=O (288 eV), and O-C=O (289 eV). O 1s peaks were fit with three peaks for  $\text{PO}_x$  (531.3 eV), C-O (532.8 eV), and C=O (534 eV).<sup>[52]</sup> Intensity changes in C-C/H bonding correspond to changes in the amount of aliphatic carbon, which is predominantly found in lipid A. Intensity changes in C-O and O-C-O/N-C=O are primarily taking place in the hydrophilic core and O-chain. O-C=O groups are only found on lipid A; any decrease here would signify the loss of aliphatic chains due to cleavage of ester bonds. For XPS analysis of direct treatments, samples were treated for 15 seconds.

Surface morphology and roughness measurements were performed in a tapping mode AFM (MFP-3D, Asylum Research). The surface roughness values reported were calculated from the root mean square of the surface profile. AFM measurements reveal a uniformly-covered surface that is shown in figure 2.3. The surface roughness is less than 10 nm, which allows for the use of ellipsometry.

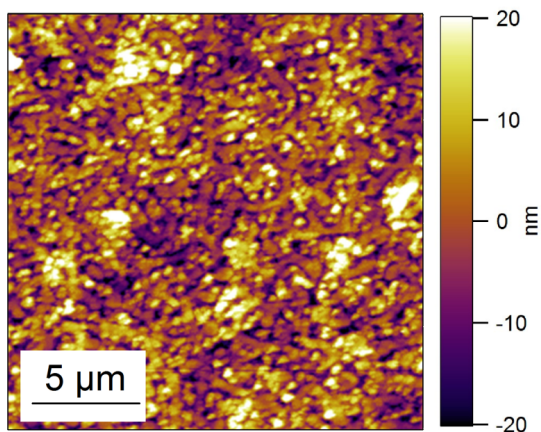


**Figure 2.3:** Representative surface morphology measured by tapping mode atomic force microscopy for untreated LPS films. The film was spin-coated on piranha treated silicon substrate at 100 rpm. Root mean square surface roughness is less than 10 nm.

#### *2.2.4 Estimation of Endotoxicity*

An enzyme-linked immunosorbent assay (ELISA) was used to estimate the endotoxicity of bLPS films after plasma treatment. Unless otherwise noted, solution volumes were 100 μl and all incubations were at room temperature. Various concentrations of bLPS in PBS were prepared and incubated in a 96-well plate (Nunc Maxisorp, EBioscience) for two hours. All wells were prepared in duplicate. The plates were washed three times with 220 μl PBS containing 0.04% Tween-20 (T-PBS) and subsequently placed inside the vacuum chamber. Placing the plates

under vacuum did not affect the bioactivity as shown in Figure 2.4. For all treatments, the wells that were used to prepare a standard curve were covered with a Si piece to prevent any plasma-well interaction. The standard curve allows for the comparison between untreated and treated wells and additionally ensures that bLPS was diluted properly. For direct treatments, the treated wells were left uncovered. For UV/VUV treatment, a MgF<sub>2</sub> filter was placed on top of the treated wells. For radical treatment, a gap structure similar to figure 2.2(b) was placed over the wells. After treatment, the wells were incubated with 150  $\mu$ l of blocking solution (StartingBlock, Thermo Scientific) for 90 minutes or overnight at 4 °C, emptied, and filled again with fresh blocking solution for another 30 minutes. Then, the wells were washed three times with T-PBS and incubated for 30 minutes with 0.25  $\mu$ g ml<sup>-1</sup> horseradish peroxidase-conjugated streptavidin in PBS (Streptavidin-HRP, Invitrogen). After washing three times with T-PBS, the wells were incubated with 3,3',5,5'-tetramethylbenzidine (1-Step Slow TMB, Thermo Scientific) for 10 minutes. Reactions were stopped by addition of 2 M H<sub>2</sub>SO<sub>4</sub> and the optical density at 450 nm was measured within 10 minutes by an automatic microplate reader (Synergy HT Multi-Mode, BioTek). Values from treated wells were then normalized to the negative control (0  $\mu$ g/mL bLPS) and compared to the untreated standard curve. We note here that this assay measures the interaction between biotinylated-LPS and streptavidin to indirectly provide information on chemical structural changes of LPS. Some functional groups (carbonyls) found in biotin are also found in LPS. We explored three different initial concentrations of bLPS. For very sensitive measurements, 0.1  $\mu$ g/ml bLPS was incubated. To study bulk deactivation, 5  $\mu$ g/ml bLPS was incubated. In the former case, the sensitive regime, a thin film is formed in the well. In the latter case, the bulk regime, a thick film is formed, which enabled us to study the impact of diffusion



and penetration of plasma generated species into the film. An intermediate concentration of 1  $\mu\text{g/ml}$  was also used.

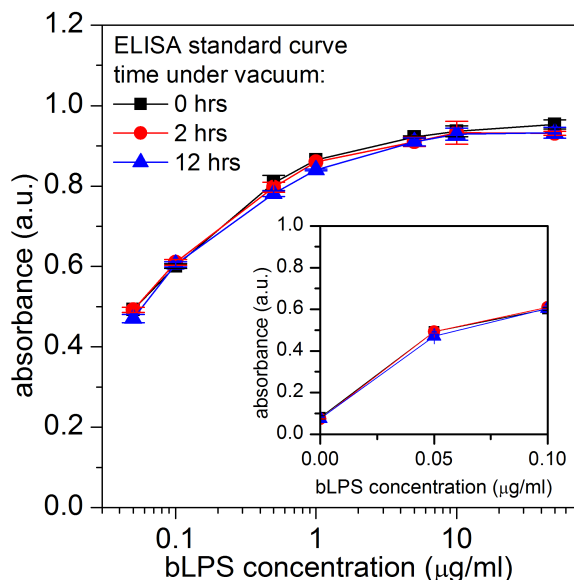


**Figure 2.4:** Absorbance as a function of bLPS concentration as measured by ELISA for various times under vacuum. The inset shows the background signal of the measurement. Vacuum conditions have a negligible effect on the biological activity of the molecule. Furthermore, absorbance begins to saturate starting at  $\sim 0.5 \mu\text{g/ml}$ .

Here we emphasize that we are comparing films prepared on different substrates from different solutions. The substrate would play a role for thin films where a monolayer or less is adsorbing. However, for thick films, the influence of the substrate would be negligible as a molecule would now see an LPS-coated surface. The polystyrene-based well plates used in these experiments were pretreated by  $\text{O}_2$  plasma by the manufacturer. This would create a hydrophilic surface comparable to the native oxide on Si wafers. Among other factors, the choice of solvent affects the aggregation of LPS molecules, but there is little agreement in the literature regarding the exact macromolecular size and structure of LPS aggregates. In fact, the macromolecular

structure can vary based on the characterization method.<sup>[40, 74]</sup> Thus, light scattering experiments performed in aqueous environments yield different results from negative staining environments performed on dry samples in an electron microscope. Given that the vacuum environment, which would cause a conformational change to the film, does not impact biological activity, we speculate that macromolecular structure in solution does not play an important role. The onset of aggregation can be inferred from the critical micelle concentration for amphiphilic molecules, which Brandenburg et al. estimate begins in the pM range based on a review of the relevant literature.<sup>[40]</sup> A key difference between the two sample preparations is the salinity; however, it has been shown that dilute salt concentrations (< 0.3 M) have negligible effects on solubility and hydrophobicity for amphiphiles.<sup>[75]</sup> In this work, we use wild-type LPS, which signifies that the O-chain varies in length, which would also impact the aggregation behavior. Richter et al. find that increasing the length of saccharide portion of various types of LPS and lipid A encourages the molecule to form bilayers or two bilayer lamellae rather than spherical particles as measured by freeze-fracture electron microscopy.<sup>[74]</sup>

## **2.3. Results and Discussion**

### *2.3.1 Correlation between Ellipsometry and Biological Activity*

*In situ* ellipsometry was used to monitor the film thickness for direct and UV/VUV treatments in real-time. For radical treatments, *ex situ* ellipsometry was used before and after treatment as the roof structure blocks the ellipsometer laser's path. Figure 2.5 shows the results of all treatments. Both Ar and H<sub>2</sub> direct treatments (solid symbols) reduce the film thickness by ~50% after about 1 minute of exposure. The high rate of material removal is expected for direct exposures where ions play a role and has been reported in several studies on bacteria cells and

protein films.<sup>[55-57]</sup> The Ar and H<sub>2</sub> plasma-generated photon emission in the 125 mm reactor has been previously characterized by Weilmboeck et al.<sup>[67]</sup> As Ar does not emit in the UV/VUV above the cut-off wavelength of the MgF<sub>2</sub> filter, they report emission corresponding to unavoidable chamber contaminations from carbon and molecular H<sub>2</sub>. This effect can be seen in the slight amount of material removal during Ar UV/VUV treatment (open squares). The slight increase in the thickness at the end of the Ar treatment is an artifact in the data and is within the uncertainty of ellipsometry measurements. Pure H<sub>2</sub> plasmas emit radiation in the UV/VUV at 121.56 nm from the Lyman- $\alpha$  line and broad molecular bands from the Lyman and Werner series above the cutoff wavelength of the filter.<sup>[76, 77]</sup> These high energy photons etch LPS films (open circles), but the etch rate is significantly slower than that of direct plasma treatments. These results agree with previous work by Bruce et al that will be briefly reviewed here.<sup>[78]</sup> They report ion dominated etching for ester-based polymers at low temperature with a decreased, but finite amount of etching for UV/VUV exposures. By comparing various ester-based polymers, they find that the oxygen content determines the etch rate of the polymer. For ester-based polymers, etch rates between subsequent exposures decrease with time, which they attribute to oxygen-depletion. As LPS is an oxygen-rich biomolecule (40-44% O), we expect it to behave similarly. In both radical treatments (half-solid symbols), the material removal is low enough that it lies within the uncertainty of the measurements. For Ar treatments, optical emission spectroscopy (not shown) was performed and trace amounts of atomic oxygen were detected at ~777 nm in Ar plasmas that originate from sputtering of the quartz window and from adsorbed O<sub>2</sub> and H<sub>2</sub>O on the chamber walls. These unavoidable oxygen contaminants are very low and are estimated at ~0.1% of equivalent flow into the chamber. H<sub>2</sub> plasma generates reactive atomic H, which, as mentioned earlier, does not etch the films. The lack of radical-induced etching is

consistent with previous work.<sup>[79]</sup> They report slow radical-induced etching of hard amorphous hydrocarbon films by deuterium atoms at 330 K. Minimal etching were also observed in the low oxygen and deuterium radical-induced etch yields on lipid A reported in our previous study using a quartz crystal microbalance.<sup>[1]</sup>

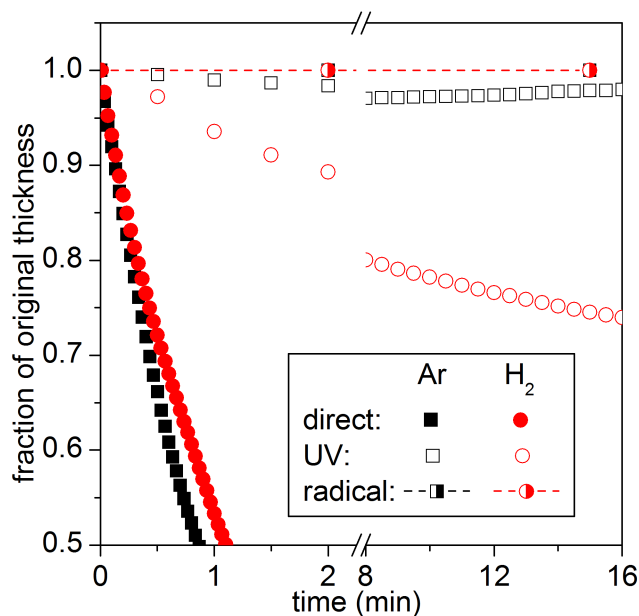


**Figure 2.5:** The fraction of the original film thickness as a function of treatment time for direct, UV/VUV, and radical treatments.

Figure 2.4 shows representative standard curves for the ELISA experiment. The inset shows the negative control i.e. background signal of the measurements. While it is clear that increasing the concentration from 0  $\mu\text{g/ml}$  up to 0.5  $\mu\text{g/ml}$  significantly increases the absorbance from  $\sim 0.08$  to  $\sim 0.8$ , increasing the concentration further even by two orders of magnitude does not significantly increase the absorbance. The impact of this saturation effect on deactivation is discussed in detail below. Figure 2.6 shows the biological activity of bLPS after Ar and H<sub>2</sub> treatments under direct, UV/VUV-only, and radical-only conditions for sensitive and bulk ELISA modes. Direct Ar treatments, shown in figure 2.6(a), deactivate the ultra-thin films

created in the sensitive mode completely after 15 seconds but only partially deactivate the thicker films formed in the bulk mode. For the highest concentration of incubated bLPS, complete deactivation was not reached until 60 seconds, after which nearly 20 nm were removed from the LPS-coated Si wafer that was treated simultaneously. Direct H<sub>2</sub> treatments, shown in figure 2.6(b), deactivate more effectively than the direct Ar with complete deactivation reached after only 6 seconds. Despite the rapid deactivation, film thickness loss is comparable to the loss after direct Ar treatments, suggesting that other plasma-generated species are playing a role through surface modifications. As H<sub>2</sub> plasmas also produce UV/VUV photons and radicals, bLPS films prepared at higher concentrations were exposed to UV/VUV-only and radical-only conditions to explore the synergistic effects that could account for the enhanced deactivation. Figure 2.6(c) shows the effect of UV/VUV-only treatment on biodeactivation. Compared to the direct treatment, the deactivation is significantly slower, which is also consistent with the reduced etch rate observed by real-time ellipsometry. Even after 45 minutes of treatment, the thicker films show only 60% deactivation. This reduction in etch rate and deactivation compared to the direct treatment is likely exaggerated as the optical filter likely attenuates the VUV emission at 121.56 nm as the cut-off wavelength is nearby at 112 nm; the VUV flux in the direct treatment is likely higher. Consistent with the lack of etching measured by real-time ellipsometry, Ar UV/VUV only treatments do not strongly deactivate the film as the plasma does not emit UV/VUV above the cut-off wavelength of the optical filter.

Interestingly, despite minimal etching of the films, plasma-generated reactive neutrals deactivate the sample, as shown in figure 2.6(d). Reactive neutrals from H<sub>2</sub> plasma deactivate about 70% and 30% after 45 minutes for 1 and 5  $\mu\text{g ml}^{-1}$  concentrations, respectively. Ar neutrals (atoms) are not reactive and cause negligible deactivation after 15 minutes. Unlike the

UV/VUV and direct treatments, the radical treatments show that material removal is not required for deactivation and that surface modifications are important. We speculate that deactivation by radicals is dependent on the flux of H atoms that are able to diffuse under the gap structure and that conditions maximizing the dissociation of H<sub>2</sub> would cause the most deactivation. The plasma density and ion mass are both significantly higher in the Ar plasma compared to the H<sub>2</sub> plasma, which demonstrates the synergy existing in H<sub>2</sub> plasma between ions, high energy photons, and chemical attack by H atoms in deactivation. The small size of H<sub>2</sub> plasma-generated reactive intermediates additionally enables these species to diffuse and penetrate into the film, enhancing deactivation. Previous works studying H and D radical effects on amorphous hydrocarbons and ultralow-k materials show that the radical-modified layer thickness depends on the density and porosity of the film. For hard amorphous hydrocarbons, D radicals create a 1.4 nm thick modified layer<sup>[79]</sup> while radicals can penetrate as far as 200 nm into porous materials.<sup>[80, 81]</sup> The thickness and surface morphology of the bLPS film in the well cannot be directly measured due to the geometry of the well plate. Tong et al used AFM to measure LPS film morphologies in both a dry and aqueous state.<sup>[82]</sup> They find that the film swells due to uptake of water, especially in the O-chain. We speculate that during the plasma treatment, where the film is in a dry state, the film is condensed, causing some biotin to be protected from the plasma by saccharide residues in LPS. After plasma treatment, the bLPS film is in an aqueous state for the subsequent ELISA steps, causing the film to expand, which exposes previously protected biotin. This effect is likely occurring especially in the direct Ar plasma treatment where the films are not deactivated completely until most of the material is removed. As the standard curve shows only small differences in absorbance between 1 µg/ml and 5 µg/ml, the difference in deactivation efficiency must also be due to a thicker film forming at higher concentrations. The

concentration-dependent deactivation established by the sensitive and bulk modes agrees with work by Kylian et al where the authors showed that deactivation efficiency decreases with increasing initial concentrations of lipid A, which they attribute to increased volume/surface area ratios.<sup>[83]</sup>

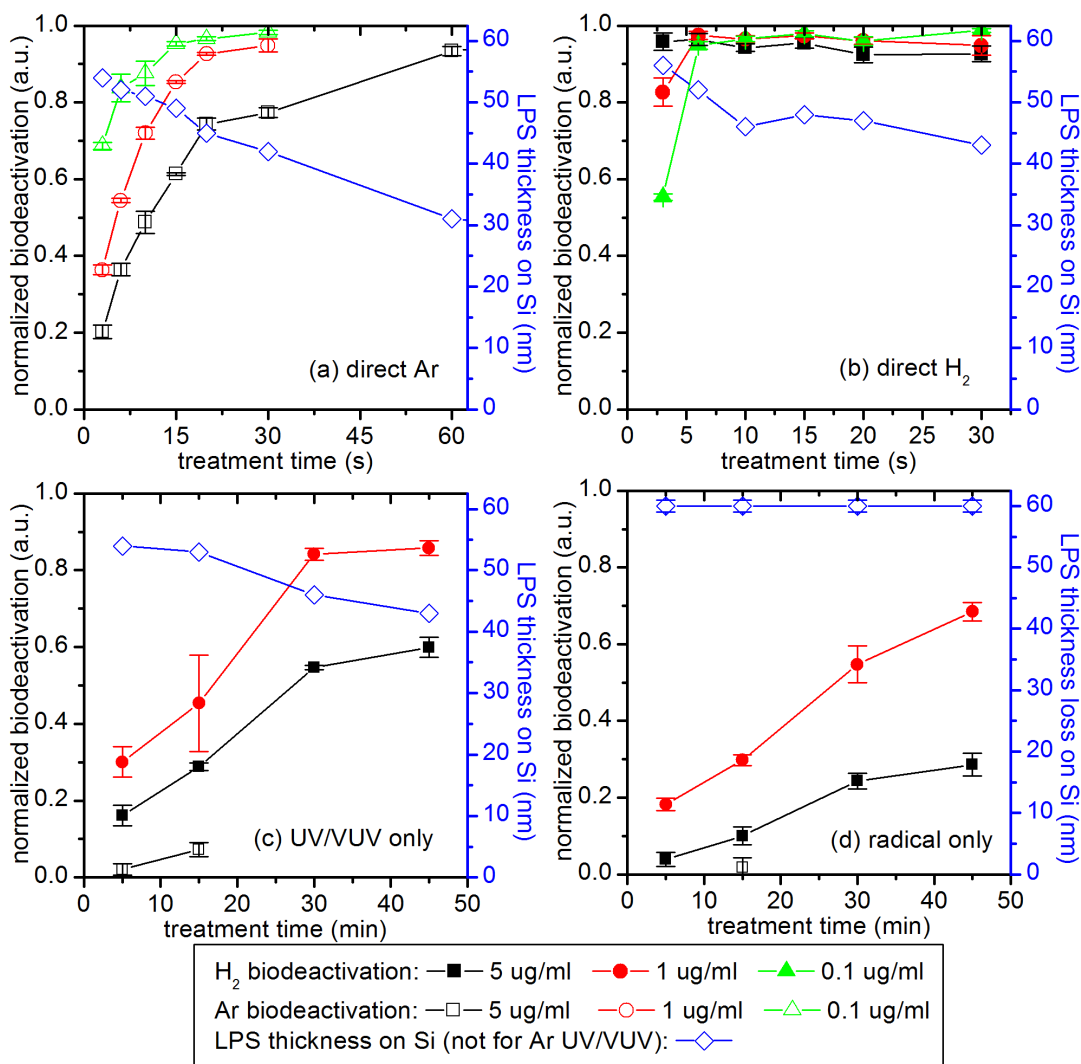


**Figure 2.6:** Normalized biodeactivation of bLPS films as a function of treatment time for direct, UV/VUV, and radical treatments. Plasma conditions: 50 sccm of feed gas, 10 mTorr operating pressure, 150 W source power, no external bias.

There is an intrinsic difficulty in measuring the biological activity of biomolecules. Interactions at the molecular level involving proteins, antigens, and antibodies are governed by non-specific interactions, which include hydrogen bonding, electrostatic interactions, van der Waals forces, hydrophobic interactions, and molecular geometric complementarity. These interactions are very sensitive to the environment; precise control of the pH, salinity, and temperature are crucial for certain interactions. For example, the amino acid histidine has an overall pKa of approximately 6.5, so small changes in pH near the physiological pH can change the amount of average charge on the molecule.<sup>[84]</sup> This sensitivity to the environment is most obvious in enzyme catalysts, which function perfectly at 37 °C, 760 Torr, and pH 6.5-7.5.<sup>[84]</sup> The biotin-streptavidin interaction is one of the strongest non-covalent interactions in nature and consists of hydrogen bonding, hydrophobic interactions, and a lock-and-key mechanism whereby the ring structure of the biotin complements the binding site on the streptavidin very well.<sup>[85]</sup> Plasma treatment can disrupt non-specific bonding in several ways. Biotin's ring structure can open, which would impact the molecular complementarity, or the ureido ring can be chemically modified, which disrupts spatially arranged hydrogen bonding.

### *3.2 XPS analysis of LPS films*

XPS spectra of untreated LPS films collected at 20° (shallow probing depth) and 90° (deep probing depth) electron take-off angles are shown in figure 2.7. More oxygen, nitrogen, and phosphorous are found deeper in the sample. Additionally, more carbon is measured as C-C/H at shallow probing depths. The broad peak in the O 1s spectra is due to CO<sub>x</sub> species and small contributions from phosphate groups. The composition of carbon and oxygen at shallow probing depths (O/C = 25.68) matches very well with what can be expected from lipid A's



structure ( $O/C = 25.52$ ). We speculate that these results originate from a lipid A layer preferentially located at the near-surface that causes increased C-C/H signals due to lipid A's aliphatic chains. The formation of this layer is known to occur at the air-water interface by hydrophobic aliphatic chains during film preparation.<sup>[86]</sup>

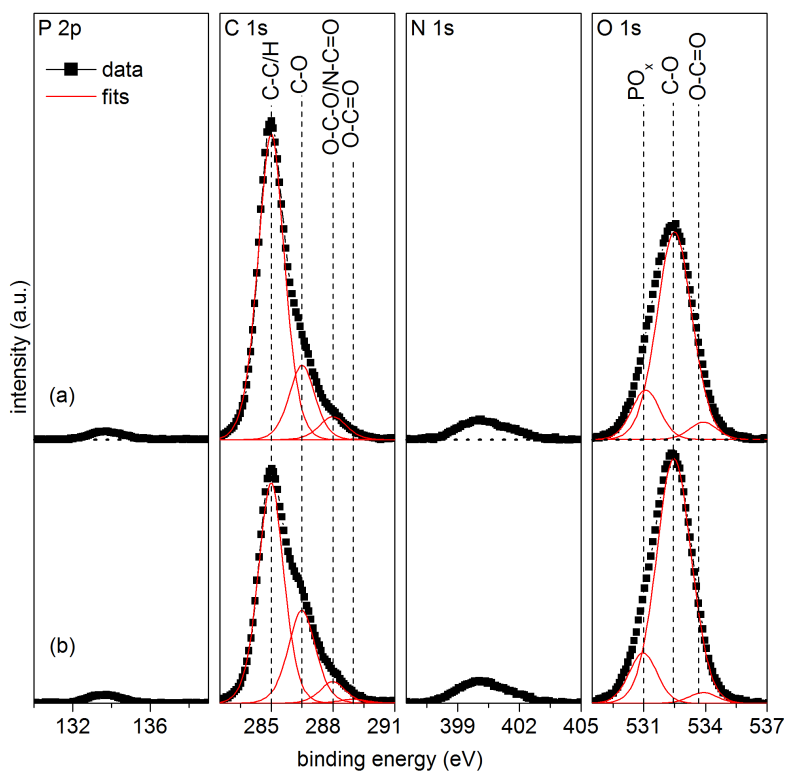


**Figure 2.7:** High resolution XPS spectra of untreated LPS at (a) shallow probing and (b) deep probing depths. Peak assignments are indicated in the figure.

XPS difference spectra obtained by subtracting untreated signal from treated signal at a shallow probing depth are shown for H<sub>2</sub> under direct, UV/VUV and radical treatments (figure 2.8). Direct (figure 2.8(a)) and UV/VUV (figure 2.8(b)) treatments have similar effects and both remove 10-12 nm of material in the treatment as measured by ellipsometry. The most prominent effects are the removal of oxygen from the molecule, mainly in the form of C-O bonds as evidenced by a decrease in peaks in the C 1s at 286.5 and O 1s at 532.8 eV, and an increase in C-

C-O at 285.5 eV. The peak at 284.5 eV is consistent with the formation of C=C bonds. Both treatments also show small increases in nitrogen and phosphorous; however, UV/VUV treatment does not change the chemical state of the phosphorous, while direct H<sub>2</sub> treatment shifts the peak toward higher binding energies. In contrast to direct and UV/VUV treatments, radical treatment (figure 2.8(c)) does not significantly affect the phosphorous and nitrogen content. O-C-O/N-C=O and oxygen slightly increase and C-C/H groups decrease. Only the near surface is modified as seen in the similar, but reduced effect in XPS measurements made at deep probing depths (not shown).

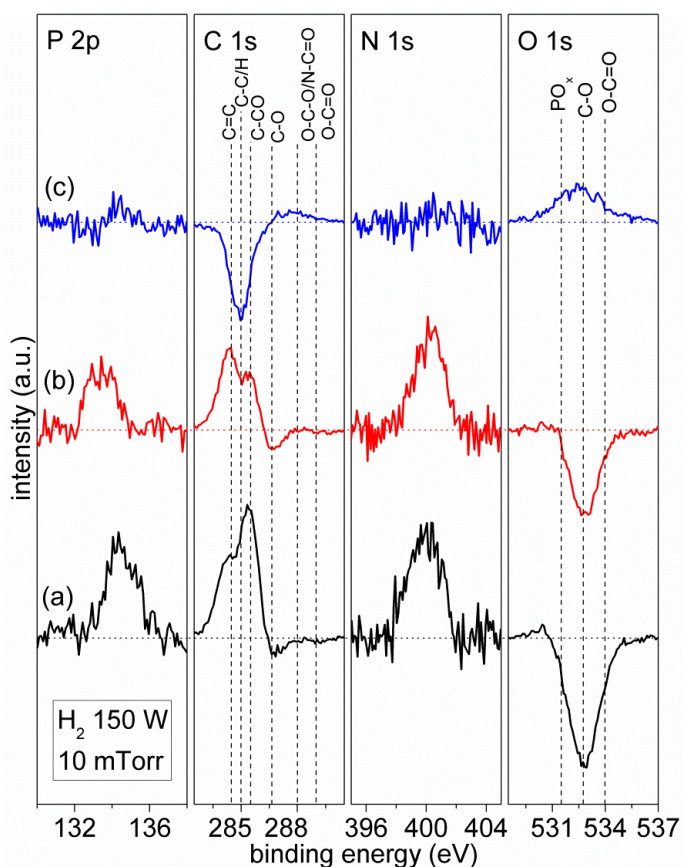


**Figure 2.8:** XPS difference plots (treated-untreated) of P 2p, C 1s, N 1s, and O 1s spectra for H<sub>2</sub> (a) direct, (b) UV/VUV, and (c) radical treatments of LPS collected at shallow probing depths. Peak assignments are indicated on the figure.

XPS difference spectra (treated minus untreated) collected at a shallow probing depth for Ar under direct, UV/VUV, and radical treatments are shown in figure 2.9. In these experiments, ex situ ellipsometry shows 10-12 nm of material removal for direct treatments and material removal within the uncertainty of our measurements for UV/VUV and radical experiments. After direct treatment (figure 2.9(a)), C-C bonding significantly decreases while O-C-O/N-C=O and O-C=O groups increase. The nitrogen content also increases significantly while the oxygen content increases mainly due to carbonyl groups, which complements the aforementioned increases in the C 1s. XPS spectra probing deeper into the sample (not shown), show similar effects with an additional loss of C-O groups. The P 2p spectrum shows a small increase in phosphorous following treatment. UV/VUV treatment, shown in figure 9(b), causes very little changes, which is consistent with Ar not emitting high energy photons above the cut-off wavelength of the MgF<sub>2</sub> optical filter. On the other hand, Ar radical treatments (figure 2.8(c)) show similar results to the H<sub>2</sub> radical treatment through a loss of C-C and an increase in O-C-O/N-C=O and oxygen. Like the H<sub>2</sub> radical treatment, these changes occur only at the near-surface and measurements probing deeper in the sample (not shown) show the same effect to a lesser extent. One possible source of reactive radicals in the case of Ar plasma is O from erosion of the quartz coupling window which produces a small oxygen background in the Ar plasma. Oxygen can be detected by its optical emission.

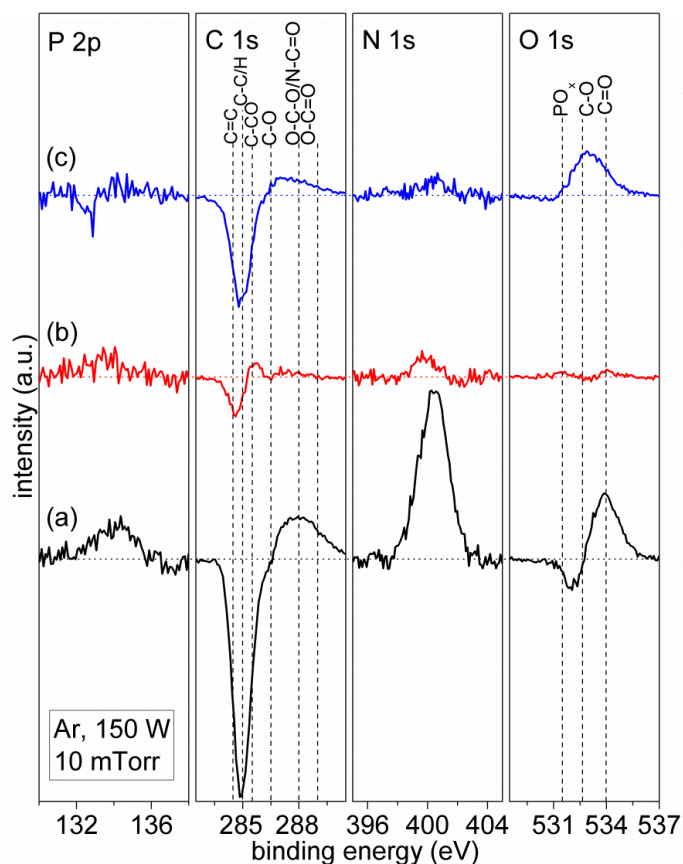


**Figure 2.9:** XPS difference plots (treated-untreated) of P 2p, C 1s, N 1s, and O 1s spectra for Ar (a) direct, (b) UV/VUV, and (c) radical treatments of LPS collected at shallow probing depths. Peak assignments are indicated on the figure.

A chemical model is presented in figure 2.10 which summarizes the different erosion/modification mechanisms for Ar and H<sub>2</sub> direct, UV/VUV, and radical treatments and is consistent with previous work by Chung et al.<sup>[1]</sup> Changes occurring on the lipid A portion of the molecule would also be observed on similar moieties that are found in the core oligosaccharide and O-chain of LPS. Direct H<sub>2</sub> plasma leaves an oxygen-poor surface as seen in the decrease in the O 1s spectrum. This oxygen decrease from direct H<sub>2</sub> plasma treatment has also been observed by Vasquez-Borucki et al where they report a decrease in oxygen content and oxygen functional

groups, mainly esters, in polyethylene terephthalate films after direct hydrogen plasma treatment under both low and high ion energy conditions.<sup>[87]</sup> Direct Ar plasma removes material primarily through physical sputtering. The removal of the surface lipid A layer is indicated by the decrease in C-C bonds and increase in O-C-O/N-C=O groups that are found in the core oligosaccharide and O-chain and is consistent with the material removal measured by ellipsometry. The C-O peak does not change in these measurements despite the exposure of the carbohydrate-rich underlayers after the carbon-rich lipid A surface layer is removed. As the near-surface of untreated LPS films contains a low amount of C-O groups, the absence of an increase of this moiety after the treatment indicates that Ar ions preferentially cleave C-O bonds over C=O bonds. This effect has been observed by Bruce et al where ester-based polymer films show an oxygen-depleted surface after low energy Ar ion bombardment.<sup>[78]</sup> The removal of the surface lipid A layer also reveals additional amide groups found predominantly in the O-chain. Figures 2.8 and 2.9 show an increase in nitrogen and phosphorous content after direct H<sub>2</sub> and Ar plasma treatments. While the nitrogen content should increase when the lipid A surface layer is removed and the O-chain is exposed, direct H<sub>2</sub> treatment causes a smaller increase than direct Ar treatment, indicating that H<sub>2</sub> plasma more effectively removes amide groups than Ar plasma. Cleaving amide bonds causes fast etching of lipid A due to removal of aliphatic chains. On the other hand, phosphorous increases more after H<sub>2</sub> plasma treatment compared to Ar plasma treatment. This suggests that bombardment by heavier Ar ions is more effective at removing phosphorous than by ions formed in H<sub>2</sub> plasma. The shift toward higher binding energies in the P 2p spectrum after direct H<sub>2</sub> treatment results from negatively charged pyrophosphates accepting a hydrogen atom to form pyrophosphoric acid. H<sub>2</sub> plasma's ability to remove oxygen and nitrogen, which create functional groups necessary for non-specific intermolecular interactions

between biotin and streptavidin, explains the increased deactivation compared to Ar plasma observed by ELISA in figure 2.6(a).

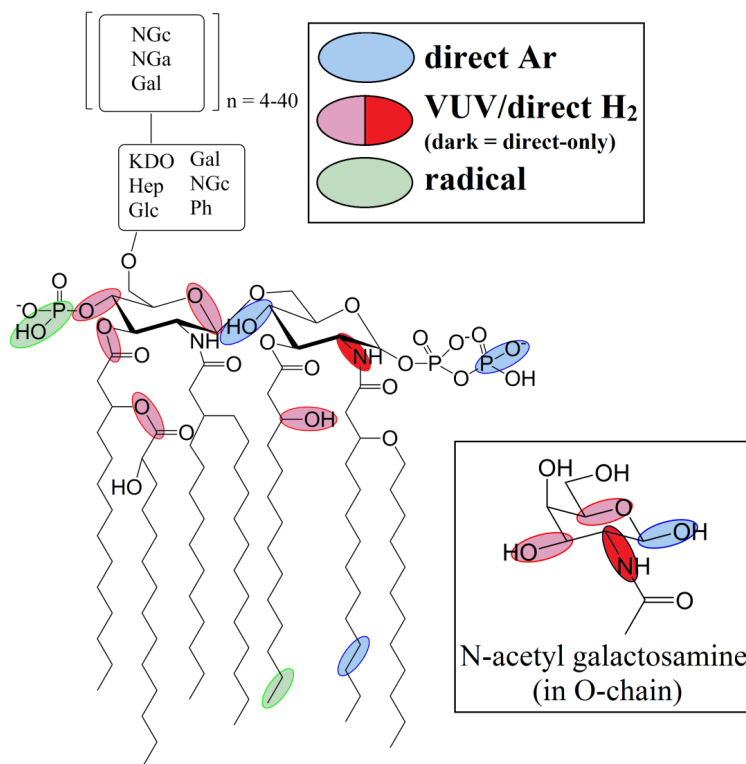


**Figure 2.10:** Schematic of the modifications to intact LPS/lipid A for the various conditions explored in this work and complementary work by Chung et al.<sup>[1]</sup> Damage to the highlighted functional groups in lipid A would also be found on similar functional groups in the core oligosaccharide and O-chain of LPS as shown for N-acetyl galactosamine.

UV/VUV modification and etching of organic materials has been extensively studied.<sup>[1, 67, 88-92]</sup> High energy photons are known to lead to loss of hydrogen from polymers and damage oxygen-containing functional groups.<sup>[92]</sup> The shift of the C-C/H peak toward lower binding energies demonstrates that C=C bonds are formed following hydrogen loss. UV/VUV degradation of oxygen-containing functional groups has been widely studied in the semiconductor industry due to the use of methacrylate-based 193 nm photoresist.<sup>[88]</sup> The

decrease in C-O bonds causes major damage to LPS due to cleavage of glycosidic C-O that link adjacent carbohydrate groups. The decrease in C-O bonds could also correspond to the opening of carbohydrate rings. Our previous work has also shown that 147 nm photons damage ester linkages and sugar groups in lipid A.<sup>[1]</sup> Breakage of ester groups causes removal of aliphatic chains on lipid A and dramatically reduces the endotoxicity of the biomolecule. UV/VUV photons can penetrate up to 200 nm into polymer films, depending on the absorption coefficient of the film.<sup>[92]</sup> Despite the enhanced penetration depth of the photons, deactivation by UV/VUV requires material removal, as the bulk ELISA experiments show more biological activity remaining after treatment than the sensitive ELISA experiments. The deactivation could be limited by the ability of fragmented groups to desorb from the surface. As direct and UV/VUV-only H<sub>2</sub> treatments remove oxygen from the films, one pathway toward deactivation of bLPS is through a breakage of C-C/H bonding and removal of heterocyclic ring structure, abolishing binding with streptavidin completely.

Radical plasma treatments and beam studies demonstrate that radicals play a significant role in deactivating and modifying LPS and lipid A films despite negligible material removal as measured in the present work by ellipsometry and in our previous work by a quartz crystal microbalance. Hydrogen and deuterium radicals can modify surfaces by chemical erosion. This mechanism has been overviewed in detail in our previous work and will be briefly discussed here.<sup>[1]</sup> H radicals can abstract bonded hydrogen from sp<sup>3</sup> CH<sub>x</sub> groups to form a radical intermediate via an Eley-Rideal mechanism. At high temperatures, the radical intermediate can de-excite by releasing a nearby CH<sub>3</sub> group or recombine with another hydrogen and cleave an adjacent C-C bond with the recombination energy.<sup>[93]</sup> The decrease in C-C bonding in the C 1s is consistent with the removal of aliphatic chains on lipid A. As this occurs at the near surface, the

increase in oxygen is due to the exposure of the underlying carbohydrate groups. Even though radical treatment by Ar plasma prevents ion bombardment of the sample, unavoidable trace chamber contaminations such as adsorbed H<sub>2</sub>O and O<sub>2</sub> originating from the walls of the reactor or from the gap structure along with oxygen from erosion of the quartz coupling window can be dissociated into reactive species and modify the film. The effect of oxygen radicals was shown in our previous study to reduce the number of intact fatty acid chains on lipid A. Although radical treatment should be limited to the surface, H radicals are small enough to diffuse into the film, depending on the density and porosity of the sample.

A key reason that H<sub>2</sub> plasma more effectively deactivates surfaces is the synergistic effects among ions, high energy photons, and radicals. This synergy is significantly reduced in inert Ar plasmas. In direct H<sub>2</sub> treatments, the UV/VUV and radical effect is much stronger due to the absence of the attenuating effects of the optical filter and high aspect ratio gap structure. For the direct Ar treatment, complete deactivation was not observed even after a nearly 20 nm decrease in film thickness. This large thickness loss suggests that the film in the well consists of multiple layers. Unlike the Ar treatment, direct H<sub>2</sub> treatments completely deactivated the films after only 8 nm was removed, demonstrating strong surface modifications and efficient penetration through the substrate due to its small size. Additionally, AFM measurements of polystyrene surfaces from a 6-well plate show surface roughness that would likely aid in adsorption of LPS and make deactivation more difficult.

## **2.4. Conclusion**

LPS films were exposed to Ar and H<sub>2</sub> plasmas under direct, UV/VUV-only, and radical-only conditions to characterize their etch behavior, biological activity, and surface chemical



composition. Direct plasma treatments under both plasma chemistries show similar etch rates. However, the mechanism of material removal is markedly different. Direct H<sub>2</sub> plasma creates an oxygen-deficient surface by removing C-O, O-C=O, and O-C-O/N-C=O groups while direct Ar plasma reduces aliphatic carbon, C-O, and phosphate groups. Direct H<sub>2</sub> plasma more effectively removes amide groups than Ar plasma, which leads to fast material removal by desorption of aliphatic chains. Fast material removal by direct plasma causes rapid deactivation as measured by ELISA. UV/VUV-induced etching is slower than direct plasma-induced etching. This slower effect is also seen in the slower reduction of biological activity. The UV/VUV treatment reduces oxygen content in the molecule, and this was due to a reduction of carbon-oxygen functional groups such as C-OH, O-C-O/N-C=O, and O-C=O. These changes are expected to alter the structure of LPS significantly, which would decrease the molecules' endotoxicity as evidenced by decreased binding of bLPS to streptavidin. Radical treatments cause negligible material removal, but deactivation still occurs. Both H<sub>2</sub> and Ar radical treatments reduce aliphatic carbon from the aliphatic chains on the near-surface and expose underlying carbohydrate layers.

Plasma sources present a promising path for sterilization and decontamination of sensitive surfaces. The results show that plasma generated UV/VUV photons and radical species play an important role in biological deactivation but are less effective than direct discharges. The lack of material removal by radicals is promising for surface treatments of sensitive medical devices as biological contaminants can be deactivated without damaging the device. This is important for future studies on low-temperature plasma interactions operating at atmospheric pressure where the effect of ions will be negligible and neutral species dominate.

## **Acknowledgements**

The authors gratefully acknowledge the financial support of this work by the US Department of Energy (DE-SC0005105 and DE-SC0001939) and National Science Foundation (PHY-1004256).

The authors thank N. Lyon, D. Metzler, F. Weirnboeck, and C. Hart for helpful discussion and contributions to this project.

# **Chapter 3: Atmospheric pressure plasma treatment of lipopolysaccharide in a controlled environment**

**E A J Bartis<sup>1,2</sup>, J Seog<sup>1</sup>, G S Oehrlein<sup>1,2</sup>**

<sup>1</sup> Department of Materials Science and Engineering, University of Maryland, College Park, MD  
20742, USA

<sup>2</sup> Institute for Research in Electronics and Applied Physics, University of Maryland, College  
Park, MD 20742, USA

**D B Graves**

Department of Chemical and Biomolecular Engineering, University of California, Berkeley,  
94720, USA

## Abstract

The atmospheric pressure plasma jet (APPJ) has been widely investigated for sterilization of surfaces, but studies on surface chemical changes of model compounds in controlled environments have been lacking. We present measurements on lipopolysaccharide (LPS) using x-ray photoelectron spectroscopy (XPS) after 1% O<sub>2</sub> in Ar APPJ treatments in controlled ambients composed of N<sub>2</sub>/Ar mixtures. By varying the N<sub>2</sub> concentration from 20% to 100%, we find that the interaction of the jet with the environment plays a major role in modifying surface reactions. This is due to the plasma exciting N<sub>2</sub>, which quenches reactive oxygen species (ROS) that would otherwise modify the film surface. By minimizing the interaction of the APPJ with the environment, e.g. by changing the APPJ geometry, we show that surface modifications increase even when the plasma itself is removed farther from the LPS surface. Measurements on the biological activity, optical emission, and ozone production of the jet using O<sub>2</sub>, N<sub>2</sub>, and O<sub>2</sub>/N<sub>2</sub> admixtures all demonstrate that ROS are readily quenched by N<sub>2</sub> species excited by the plasma. These results clearly reveal the importance of considering plasma-environment interactions for APPJ-treatments of surfaces.

### 3.1. Introduction

Atmospheric pressure plasma jets (APPJ) in noble gases with small admixtures of molecular gases ( $N_2$  and  $O_2$ ) have been the subject of a wide variety of current research due to the variety of reactive neutral species created in the discharge, e.g. metastables,<sup>[94]</sup> atomic O,<sup>[95]</sup> singlet delta oxygen,<sup>[96]</sup> ozone,<sup>[97]</sup> and  $NO_x$ .<sup>[98]</sup> Applications vary from thin film deposition<sup>[99]</sup> to medical applications such as decontamination of surfaces,<sup>[100]</sup> wound healing,<sup>[28]</sup> and cancer treatment.<sup>[10]</sup> The important role of reactive oxygen species (ROS) and reactive nitrogen species in biological systems has recently been reviewed by Graves.<sup>[29]</sup>

Nearly all the work done in this field has been done in an open environment.<sup>[101-103]</sup> It is critical to the advancement of the field to study how these plasma sources interact with the environment so that atmospheric pressure plasma sources can be properly designed to successfully impact healthcare applications. Additionally, experiments in a controlled environment allow for an advanced understanding of the fundamental processes occurring in these sources. In this letter, we describe a kHz-driven atmospheric pressure plasma jet based on the design described by Teschke where two electrodes are wrapped around a tube, made of alumina in this study, as shown in Figure 3.1(a).<sup>[49]</sup> When Ar gas flows through the tube and a high voltage is applied between the electrodes, the plasma ignites between the electrodes. The position of the electrodes along the alumina tube can be adjusted such that the plasma plume can be confined inside the alumina tube or extended into the environment. Surface chemistry of lipopolysaccharide (LPS) films before and after APPJ treatment was measured by x-ray photoelectron spectroscopy (XPS) and biological activity was studied by an enzyme-linked immunosorbent assay (ELISA). The APPJ was characterized by optical emission spectroscopy

(OES) to detect excited species in the plume and by UV-absorption spectroscopy to detect ozone concentrations.

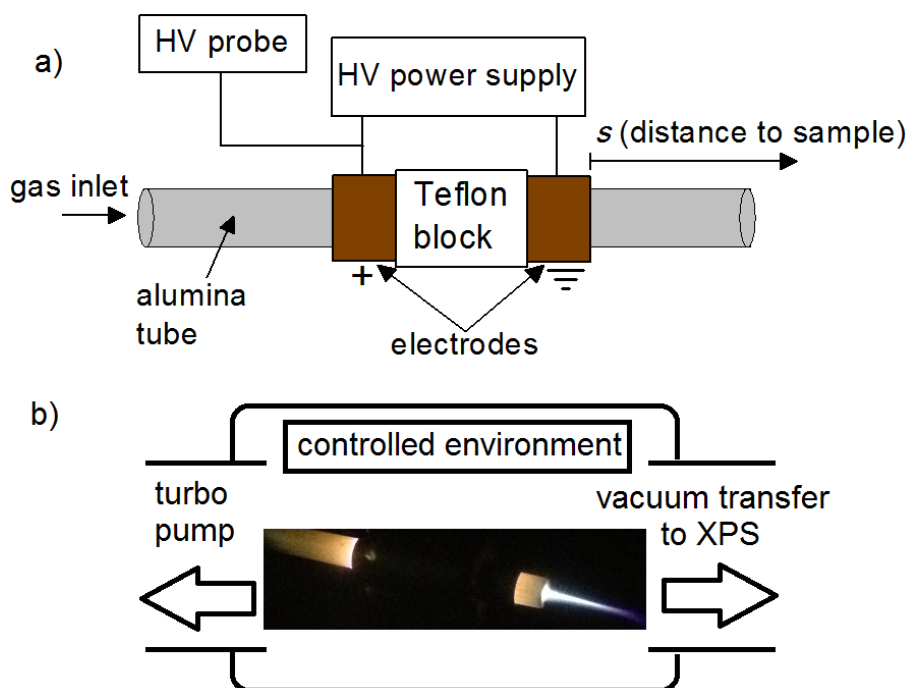


**Figure 3.1.** (a) A schematic representation of the atmospheric pressure plasma jet (APPJ). (b) The APPJ is mounted inside a vacuum chamber where the environment can be controlled during the treatment as shown. After the treatment, the samples are vacuum transferred to XPS for surface analysis.

### 3.2. Experiments and Methods

LPS from *E. coli* O111:B4 (Sigma-Aldrich) was chosen as a model molecule and is a major component of the outer membrane of Gram-negative bacteria such as *Escheria coli*. The structure of LPS is described by Erridge et al and will be briefly overviewed here.<sup>[39]</sup> Lipid A, the toxic element of LPS, consists of several aliphatic chains conjugated to a phosphorylated disaccharide backbone by ester and amide linkages. Lipid A is linked to the core oligosaccharide,

which is linked to the O-antigen. These two groups consist of carbohydrate groups, some of which contain an amide group.

To study the interaction of the jet with the environment, experiments were performed in a vacuum chamber that was evacuated to 50 mTorr and then refilled to atmospheric pressure with 20% N<sub>2</sub> in Ar, 60% N<sub>2</sub> in Ar, or 100% N<sub>2</sub> as shown in Fig. 3.1(b). Samples were vacuum transferred to XPS after APPJ treatment and subsequent pump-out of the treatment chamber, thus eliminating the exposure of surfaces to air. For XPS experiments, the plasma gas chemistry was 1% O<sub>2</sub> in Ar at a total flow of 2 liter/min, the applied voltage across the electrodes was 8 kV at 25 kHz, and samples were treated for 3 minutes. The vacuum chamber has a volume of 50 liters, so we do not expect that the gas flow from the plasma has a major impact on the environment due to the length of the treatment. Samples were treated under two conditions. In the first case, the ground electrode is 2 mm from the end of the alumina tube. With this geometry (exposed), the plasma interacts with the environment due to the source's position close to the nozzle. In the second case, the plasma was created 9 cm from the nozzle of the alumina tube. With this geometry (confined), plasma-environment interactions are minimized. In both cases, the tube nozzle was 4 cm from the sample.

LPS samples were prepared by dropping 100  $\mu$ l of 500  $\mu$ g/ml 9:1 methanol:water solution onto piranha cleaned silicon chips and spin-coating at 100 RPM.<sup>[64]</sup> Surface analysis by XPS was performed by a Vacuum Generators ESCALAB MK II surface analysis system. Narrow scan spectra of the C 1s, N 1s, and O 1s were obtained at 20 eV pass energy at an electron take-off angle of 20° with respect to the sample surface. The film composition was calculated using the integrated peak areas of the C 1s, O 1s, and N 1s spectra with Scofield cross sections of 1, 2.85, and 1.77, respectively.<sup>[73]</sup> Spectra were fit using a least square fit after Shirley

background subtraction and charge compensation by calibrating the binding energy position of the C-C/H peak to 285 eV.<sup>[52]</sup> C 1s spectra were fit with four peaks corresponding to C-C/H, C-O, O-C-O/N-C=O, and O-C=O peaks at 285 eV, 286.5 eV, 288 eV, and 289 eV, respectively. N 1s spectra were fit with three peaks corresponding to N-C, [N-R<sub>4</sub>]<sup>+</sup>, and N<sub>2</sub>O/NO<sub>3</sub> at 400.1 eV, 402 eV, and 407.9 eV, respectively. O 1s spectra were fit with four peaks corresponding to C-O/C=O, O-NO<sub>2</sub>, and O-NO<sub>2</sub> at 532.4 eV, 533.1 eV, 533.9 eV, and 534.7 eV, respectively.<sup>[52]</sup>

ELISA was used to estimate the endotoxicity of the LPS films after plasma treatment. Briefly, biotinylated LPS (bLPS) in phosphate buffered saline (PBS) was incubated in a 96-well microtiter plate. After incubating and washing away excess bLPS with 0.04% Tween-20 in PBS, wells were dried and exposed in duplicate to the APPJ. For the APPJ treatment, the confined geometry was used in open air, but the nozzle was extended into the well to further minimize environmental effects by creating a net flow out of the well. After the treatment, the wells were blocked (StartingBlock, Thermo Scientific), washed again, and then incubated with horseradish peroxidase-conjugated streptavidin in PBS (HRP-SA). If biotin on bLPS is damaged by the APPJ, then HRP-SA will not bind with it. This failure to bind is taken as evidence for LPS deactivation. After washing excess HRP-SA, 3,3',5,5'-tetramethylbenzidine (TMB) was added to the wells to react with HRP. The reaction was stopped by 2 M H<sub>2</sub>SO<sub>4</sub> and the optical density at 450 nm was measured by an automatic plate reader (Synergy HT Multi-Mode, BioTek). After background subtraction, treated wells were normalized to untreated wells. We note here that this assay measures the interaction between biotinylated-LPS and streptavidin to indirectly provide information on the biological activity of LPS because several functional groups (carbonyls, aliphatic chains, etc) found in biotin are also found in LPS.



Optical emission spectroscopy was performed with a Princeton Instruments SpectraPro 2300i with a grating of 1200 grooves/mm blazed at 300 nm. For OES measurements, an optical fiber was aligned along the jet axis such that we could probe the discharge forming between the two electrodes. For analysis, atomic O emission ( $O^*$ ) at 777 nm and the second positive system of  $N_2$  ( $N_2^*$ ,  $C\ ^3\Pi_u \rightarrow B\ ^3\Pi_g$ ) at 337 nm peaks were compared to the  $Ar^*$  emission at 750.4 nm. This widely studied Ar peak results from electron impact excitation of ground state argon atoms and therefore serves as a good indicator of the plasma density.<sup>[104]</sup>

UV absorption was used to detect ozone produced by the APPJ employing an ambient ozone analyzer (Thermo Electron UV Photometric  $O_3$  Analyzer Model 49). The outlet from the plasma source was fed into the ozone analyzer and did not interact with the ambient. The distance between the source and the ozone analyzer inlet was 20 cm.

### 3.3. Results and Discussion

Figure 3.2 shows XPS spectra of LPS before and after 1%  $O_2$  in Ar treatments in various  $N_2$ /Ar environments. For the untreated surface, we see mostly C-C bonding with small amounts of C-O, O-C-O/N-C=O, and O-C=O. These bonds are also seen in the N 1s and O 1s. Figure 3.2(a) shows spectra after treatment with the plume exposed in  $N_2$ , 60%  $N_2$  in Ar, and 20%  $N_2$  in Ar environments. Increased surface modifications occur as environmental  $N_2$  is reduced. In the C 1s, C-C bonding decreases while O-C-O/N-C=O and O-C=O slightly decrease. In the N 1s, N-C/N-C=O and  $NR_4^+$  slightly decrease while a peak at 408 eV due to  $N_2O$  or  $NO_3$  emerges. This peak is strongest in the 20%  $N_2$  in Ar environment. In the O 1s, oxygen content increases as environmental  $N_2$  decreases. Figure 3.2(b) shows spectra in the 60%  $N_2$  in Ar environment after treatment with the plume confined. Comparing the two geometries shows that the qualitative

changes are similar, but intensified. Even though the plasma is farther away from the sample, the surface is more oxidized than in the exposed case, with a substantial decrease in C-C bonding, which is chiefly found on the aliphatic chains of lipid A. The loss of C-C bonding due to atomic O is consistent with work by Chung et al. where they observed a reduction in the number of intact aliphatic chains on lipid A after exposure to O-atoms in a beam system.<sup>[1]</sup> Transferring samples to XPS through air instead of vacuum was also studied and showed that oxidation of the surface was decreased, indicating that weakly-bound surface species are removed by exposure to ambient conditions. It is apparent that the interaction of the jet with the environment plays a major role with regard to which species reach the sample and chemically interact with LPS. As the nozzle-to-sample distance remained constant for both geometries, N<sub>2</sub> in the environment is not a significant quencher of ROS, which strongly suggests that the excitation of N<sub>2</sub> species by the jet is required to reduce ROS species created by plasma.

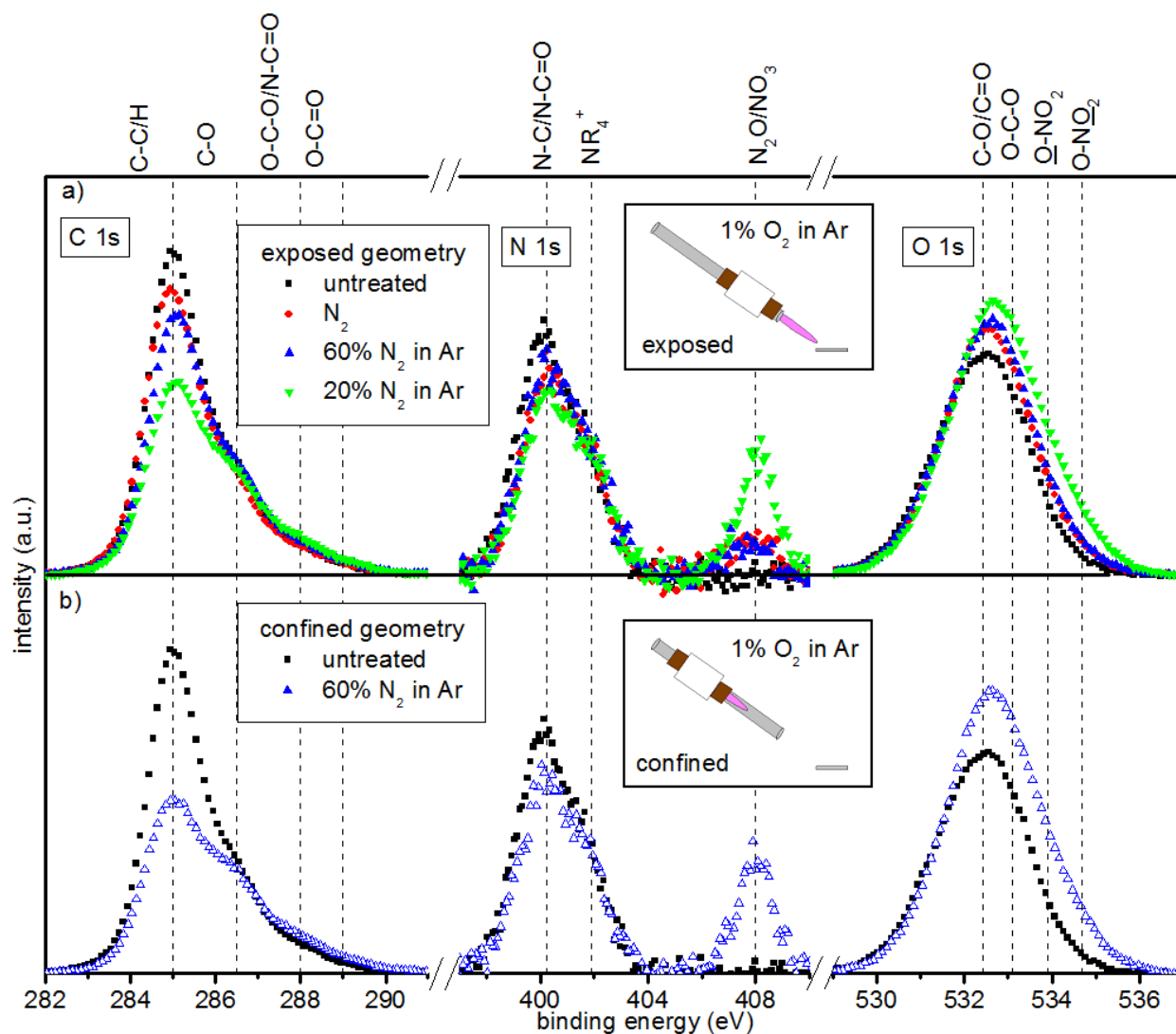


**Figure 3.2.** XPS C 1s, N 1s, and O 1s spectra of lipopolysaccharide (LPS) films after treatment in N<sub>2</sub>/Ar environments for conditions where the plasma is (a) exposed to the environment and (b) confined within the alumina tube. The distance from nozzle to the LPS coated substrate was 4 cm for both conditions.

The effect of feed gas chemistry on biological deactivation of bLPS was examined for conditions when the plume was confined, and the results are consistent with the role of nitrogen clarified in the surface analysis work. Figure 3.3 shows the differences between 1% N<sub>2</sub>, 1% and

0.2% O<sub>2</sub>, and 1% synthetic air (1:4 O<sub>2</sub>/N<sub>2</sub>) admixtures in Ar plasmas. 1% N<sub>2</sub> admixture causes very little deactivation, demonstrating that nitrogen radical species created in the plasma do not cause strong surface modifications under these conditions. As soon as O<sub>2</sub> is added to the plasma, as seen in the air admixture, stronger deactivation takes place. This demonstrates that oxygen species are required for deactivation in this APPJ. Furthermore, when 0.2% O<sub>2</sub> is added (note that this has the same O<sub>2</sub> admixture as for 1% air) deactivation increases significantly relative to air or pure N<sub>2</sub>. Nitrogen species that are excited by the plasma readily consume ROS formed in the plasma to likely create NO<sub>x</sub>.<sup>[105]</sup> 1% O<sub>2</sub> in Ar plasma shows elevated levels of deactivation compared to the 0.2% O<sub>2</sub> admixture initially, suggesting that more ROS are generated in the beginning. However, as the deactivation does not scale with the increase in O<sub>2</sub>, recombination reactions of atomic O to form O<sub>2</sub> and O<sub>3</sub> begin to play a larger role. For longer treatment times, the ELISA response saturates for both O<sub>2</sub>/Ar mixtures.

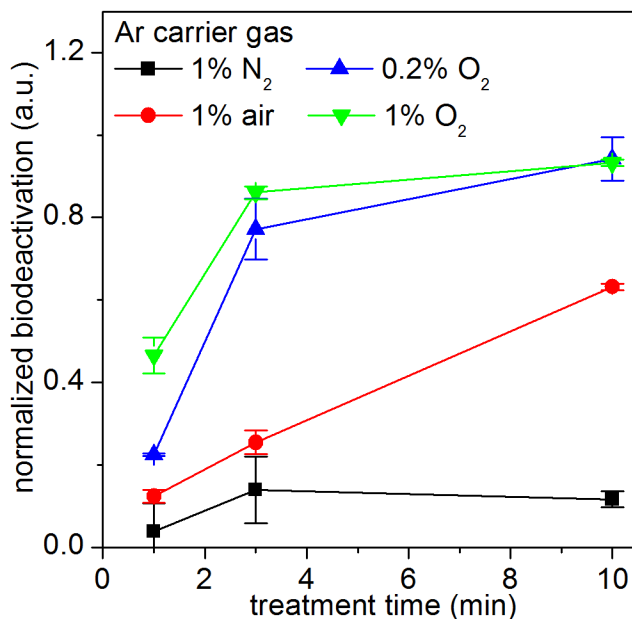


**Figure 3.3.** Normalized biodeactivation vs. treatment time for four different gas chemistries in the confined geometry. The N<sub>2</sub> admixture causes minor deactivation, while O<sub>2</sub>-based discharges show clear deactivation.

To further study the effect of nitrogen on ROS created under confined conditions, the concentration of active species ( $O^*$  and  $N_2^*$ ) in  $O_2/N_2$  admixture was measured using optical emission spectroscopy (Fig. 3.4(a)). For  $O_2$  admixtures,  $O^*$  emission increases sharply up to 0.66% admixture, after which it increases more slowly. No background  $N_2^*$  emission is detected, confirming that when the plume is confined, ambient interactions are very low. For  $N_2$  admixtures,  $N_2^*$  emission increases as the  $N_2$  admixture increases. Low  $O^*$  emission is observed, likely originating from trace contaminants from the Ar bottle as  $O^*$  emission is present at low levels without any gas admixtures. For  $O_2/N_2$  admixtures,  $O^*$  emission is lower than in the  $O_2$  admixture case, but  $N_2^*$  emission significantly drops. This drop suggests that  $N_2^*$  that builds up in the absence of  $O_2$ , reacts with ROS species formed in the plasma and reduces their effects, which is consistent with the results from the exposed plasma treatment.

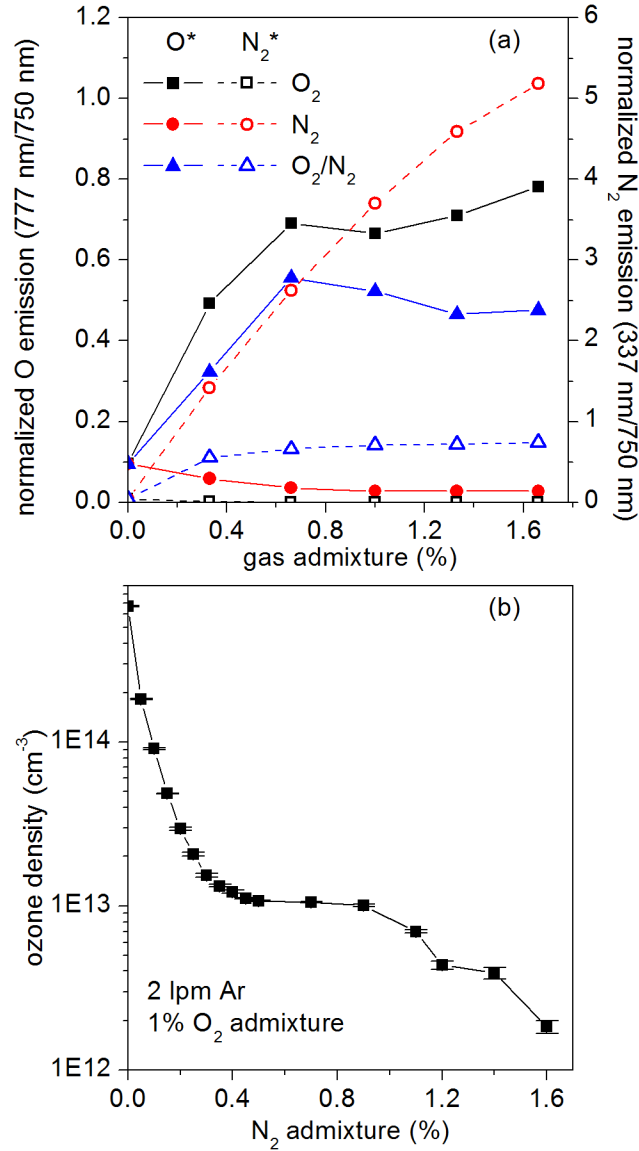


**Figure 3.4.** (a) Emission due to atomic O and the second positive system of N<sub>2</sub> normalized to the Ar emission at 750 nm for O<sub>2</sub>/N<sub>2</sub> admixtures in the confined geometry. (b) Ozone density measured using UV absorption spectroscopy for 1% O<sub>2</sub> admixture in the confined geometry was monitored as N<sub>2</sub> is added to the feed gas.

UV absorption was used to measure ozone produced by the APPJ. Ozone has known bactericidal properties and its formation is very sensitive to gas chemistry.<sup>[105]</sup> Increasing the O<sub>2</sub> admixture increases the ozone produced by the APPJ through the reaction:



where M is any species that can stabilize the reaction such as Ar, O<sub>2</sub>, or the alumina tube itself. Figure 3.4(b) shows ozone densities for 1% O<sub>2</sub> in Ar with up to 1.6% N<sub>2</sub> additionally added. Without N<sub>2</sub> addition, ozone densities reached  $7 \times 10^{14} \text{ cm}^{-3}$ . Adding less than 0.5% N<sub>2</sub> causes the ozone density to significantly drop by nearly two orders of magnitude. This effect, called discharge poisoning, has been widely studied and results from cyclic reactions where nitrogen species consume ozone and atomic O to form NO, NO<sub>2</sub>, NO<sub>3</sub>, and O<sub>2</sub>.<sup>[105]</sup>

ELISA, OES, and UV absorption measurements collectively demonstrate that when N<sub>2</sub> is purposely added to the feed gas, ROS are reduced. For the same O<sub>2</sub> admixture, biological deactivation is reduced when N<sub>2</sub> is added. O\* and N<sub>2</sub>\* emissions decrease for O<sub>2</sub>/N<sub>2</sub> admixtures as the two species react with one another. Furthermore, small admixtures of N<sub>2</sub> to ozone producing plasmas significantly decrease the ozone density. Most importantly, N<sub>2</sub> does not need to be added to the feed gas to quench ROS. XPS studies show that decreased surface oxidation occurs in the exposed geometry as N<sub>2</sub> content in the environment increases. This work demonstrates that plasma-environment interactions play a major role and demand consideration for future studies on APPJ surface treatments.

## Acknowledgements

The authors gratefully acknowledge the thoughtful insights and support of the project by N. Fox-Lyon, D. Metzler, C. Barrett, C. Hart, T.-Y. Chung, and H.-W. Chang. We also thank

Prof. R. Dickerson for generously supplying ozone measurement equipment. This work is supported by the US Department of Energy (DE-SC0005105 and DE-SC0001939) and National Science Foundation (PHY-1004256).



**Chapter 4: Polystyrene as a Model System to Probe the Impact of  
Ambient Gas Chemistry on Polymer Surface  
Modifications Using Remote Atmospheric Pressure  
Plasma under Well-Controlled Conditions**

**E. A. J. Bartis<sup>1,2</sup>, P. Luan<sup>1,2</sup>, A. J. Knoll<sup>1,2</sup>, C. Hart<sup>1,2</sup>, J. Seog<sup>1</sup> and G. S. Oehrlein<sup>1,2</sup>**

<sup>1</sup> Department of Materials Science and Engineering, University of Maryland, College Park, MD  
20742, USA

<sup>2</sup> Institute for Research in Electronics and Applied Physics, University of Maryland, College  
Park, MD 20742, USA

## Abstract

An atmospheric pressure plasma jet (APPJ) was used to treat polystyrene (PS) films under remote conditions where neither the plume nor visible afterglow interacts with the film surface. Carefully controlled conditions were achieved by mounting the APPJ inside a vacuum chamber interfaced to a UHV surface analysis system. PS was chosen as a model system as it contains neither oxygen nor nitrogen, has been extensively studied, and provides insight into how the aromatic structures widespread in biological systems are modified by atmospheric plasma. These remote treatments cause negligible etching and surface roughening, which is promising for treatment of sensitive materials. The surface chemistry was measured by X-ray photoelectron spectroscopy to evaluate how ambient chemistry, feed gas chemistry, and plasma-ambient interaction impact the formation of specific moieties. A variety of oxidized carbon species and low concentrations of  $\text{NO}_x$  species were measured after APPJ treatment. In the remote conditions used in this work, modifications are not attributed to short-lived species e.g. O atoms. It was found that  $\text{O}_3$  does not correlate with modifications, suggesting that other long-lived species such as singlet delta oxygen or  $\text{NO}_x$  are important. Indeed, surface-bound  $\text{NO}_3$  was observed after treatment, which must originate from gas phase  $\text{NO}_x$  as neither N nor O are found in the pristine film. By varying the ambient and feed gas chemistry to produce O-rich and O-poor conditions, a possible correlation between the oxygen and nitrogen composition was established. When oxygen is present in the feed gas or ambient, high levels of oxidation with low concentrations of  $\text{NO}_3$  on the surface were observed. For O-poor conditions, NO and  $\text{NO}_2$  were measured, suggesting that these species contribute to the oxidation process, but are easily oxidized when oxygen is present. That is, surface oxidation limits and competes with surface nitridation. Overall, surface oxidation takes place easily, but nitridation only occurs under

specific conditions with the overall nitrogen content never exceeding 3%. Possible mechanisms for these processes are discussed. This work demonstrates the need to control plasma-ambient interactions and indicates a potential to take advantage of plasma-ambient interactions to fine-tune the reactive species output of APP sources, which is required for specialized applications, including polymer surface modifications and plasma medicine.

## 4.1. Introduction

Low temperature atmospheric pressure plasma sources have attracted attention in the last decade due to emerging biomedical and industrial applications. These sources are applied in the field of plasma medicine<sup>[27, 106]</sup> for sterilization,<sup>[4]</sup> non-fouling coatings,<sup>[107]</sup> adhesion,<sup>[102]</sup> wound healing,<sup>[108]</sup> and cancer treatment.<sup>[10, 109]</sup> These sources are also emerging as promising tools for thin film deposition and to increase e.g. wettability of polymers.<sup>[36, 110-112]</sup> For the atmospheric pressure plasma jet (APPJ), noble gases like He or Ar are used as the primary gas since they require lower voltages to ignite and create a stable plasma compared to, for example, air. Adding low (up to a 2% percent in this work) admixtures of O<sub>2</sub>/N<sub>2</sub> to the noble gas creates a cocktail of reactive oxygen species (ROS), reactive nitrogen species (RNS), and reactive oxygen and nitrogen species (RONS), whose biological relevance has been reviewed in detail by Graves.<sup>[24, 29]</sup> These reactive species can also be generated without molecular gas admixtures by the interaction of an Ar or He plasma plume with the air environment.

An impressive effort has been made into characterizing and modeling atmospheric pressure plasma sources. A variety of gas-phase characterization techniques have been used to measure Ar metastables,<sup>[94]</sup> OH,<sup>[113, 114]</sup> NO,<sup>[98, 115]</sup> O,<sup>[116-119]</sup> N,<sup>[120]</sup> O<sub>3</sub>,<sup>[95, 97, 121, 122]</sup> and NO<sub>x</sub>.<sup>[123]</sup> This gas phase characterization has been complemented recently with simulations by Van Gaens et al. to study the production and loss processes of biomedically relevant species produced by an Ar plasma flowing into a humid open air atmosphere.<sup>[124]</sup> The aforementioned studies have demonstrated that ambient conditions (e.g. ambient humidity) are critical to determining the reactive species (RS) that will interact with a surface. Recognizing the plasma-ambient interaction has led to the development of a shielding device that encloses the effluent with a controlled gas chemistry that reduces ambient species intrusion into the effluent.<sup>[125, 126]</sup> Recent

work using high speed photography has shown that the plasma plume (the part visible to the naked eye) changes when the ambient chemistry is changed from open air to one that matches the feed gas.<sup>[127]</sup>

While the sources themselves have been widely studied, experiments aimed at uncovering how APPJ-generated reactive species interact with simple model surfaces under mild conditions are limited. Many surface studies are conducted under conditions where the visible part of the plasma plume directly interacts with the surface<sup>[128-132]</sup> or by placing the treated surface inside a dielectric barrier discharge (DBD) where microdischarge filaments strike the material.<sup>[133-137]</sup> Modeling work of a DBD interacting with polypropylene has predicted the formation of peroxy and alkoxy radicals, which result in alcohols, aldehydes, and ketones.<sup>[138]</sup> While direct treatments can possess certain advantages such as high etch rates and short exposure times, treatments that modify a target surface with minimal damage are required for sensitive materials and certain applications. In a previous study at low pressure, it was shown that plasma-generated H-atoms that were isolated from other plasma species can modify and deactivate lipopolysaccharide (LPS), a pyrogenic biomolecule, with negligible etching.<sup>[139]</sup> Another study demonstrated that the interaction of an APPJ with different N<sub>2</sub>/Ar ambients impacted the level of modification of LPS films after a remote treatment.<sup>[140]</sup> It was found that when a 1% O<sub>2</sub>/Ar plasma was exposed to N<sub>2</sub>/Ar ambients, increasing ambient N<sub>2</sub> concentrations decreased surface modifications. Furthermore, when the plasma-ambient interaction was minimized by confining the plasma plume inside an alumina tube, surface modifications were increased compared to when the plasma plume extended into the ambient.

The present work is aimed at improving the understanding of how the interactions of the plasma jet with the environment impacts surface modifications of polystyrene (PS). PS has

obvious industrial uses, and it also serves as a model to understand how aromatic structures such as those found in some amino acids (e.g. phenylalanine) react with active plasma species under a controlled environment.<sup>[141]</sup> Fricke et al. have studied how low and atmospheric pressure plasma interact modify polystyrene films and the impact of those modifications on cell growth.<sup>[142]</sup> In that study, the plasma plume touches the surface, and the authors attribute oxidation to atomic O. As shown discussed below, treatments in this study were performed under remote conditions where the plume does not touch the surface. In Sec. III A, PS films were treated by O<sub>2</sub>/Ar plasmas in N<sub>2</sub> ambient under conditions where the plasma plume is confined within an alumina tube to minimize the interaction. As a starting point, only the treatment time and oxygen admixture were varied to establish a standard condition. APPJ-induced surface modifications were evaluated by vacuum-transfer X-ray photoelectron spectroscopy (XPS). In Sec. III B-C, the ambient gas chemistry was varied. In Sec. III D, the applied voltage were varied to determine which species could be responsible for the modifications. Finally, in Sec. IV, the competition between surface oxidation and nitridation based on the availability of O<sub>2</sub> and the role of NO<sub>x</sub> species in the oxidation of the polymer are discussed.

## **4.2. Materials and Methods**

### *4.2.1. Description of Materials*

PS with an average molecular weight of 35,000 (Sigma-Aldrich, St. Louis, MO, USA) was spin-coated from a 1% solution in toluene at 2000 RPM onto Si substrates (2.54 cm x 2.54 cm) cleaned by piranha solution.<sup>[64]</sup> The resulting films were ~150 nm thick as measured by ellipsometry. Untreated PS films contained less than 1% oxygen impurities and no nitrogen impurities formed during film preparation, as measured by XPS. In the C1s spectrum,  $\pi$ - $\pi^*$

bonding, which is indicative of aromaticity, made up 4.5% of the measured signal. Pristine films had an RMS surface roughness profile of 3.5 nm as measured by atomic force microscopy (AFM).

#### *4.2.2. Plasma Processing*

The APPJ used in this study is similar to a previously described version.<sup>[140]</sup> Two copper electrodes (20 mm length, ID = 6.4 mm) wrapped around an alumina tube (ID = 4 mm, OD = 6.35 mm) and separated by a 1.6 cm thick Teflon block are driven at 24 kHz by a variable frequency power supply (PVM500, Information Unlimited, Amherst, NH, USA). The applied voltage is measured by a high voltage probe (Tektronix P6015A) connected to an oscilloscope (Hewlett-Packard 54504A) with a 400 MHz bandwidth. Unless otherwise stated, typical operating conditions were 7 minute treatments with or without a 1% molecular gas admixture to Ar (total flow rate = 2 standard liters per minute (slm)) with a 14 kV pk-pk applied voltage at 24 kHz. The gas admixture composition, APPJ geometry (i.e. electrode position along the tube), and ambient gas composition were varied. The APPJ is operated in two distinctly different geometries. In the exposed geometry, the electrodes were moved close to the nozzle to allow the plume to extend out of the tube into the ambient. The source-to-nozzle distance,  $s$ , was varied for different feed gases to ensure that the plume would extend into the environment without electrically interacting with the sample, which would cause major sample damage.<sup>[127]</sup> For Ar, N<sub>2</sub>/Ar, and O<sub>2</sub>-containing (O<sub>2</sub>/Ar and Air/Ar) plasmas in the exposed geometry,  $s$  was set to 60 mm, 20 mm, and 2 mm, respectively. These distances are the minimum distance from the source to the nozzle where the plume would extend into the environment without directly touching the sample. In the confined geometry, the electrodes were moved farther from the nozzle so that the

plume was confined within the tube and ambient interactions were limited to the far effluent where the plume is no longer visible. In the confined geometry,  $s$  was 9 cm for all feed gases unless otherwise stated. At this distance, the plasma plume does not extend past the nozzle for any gas chemistry used in this work. In all APPJ experiments, the tube nozzle was fixed at a distance of 3 cm from the sample and the APPJ was oriented at an angle of about  $70^\circ$  from the surface normal. This angle provided a good compromise between the length of the source, preventing direct interactions, and geometric constraints of the vacuum chamber. Measurements have been performed confirming a uniform surface modification. To study the impact of the ambient chemistry on APPJ-induced surface modifications, the APPJ was mounted inside a vacuum chamber that was evacuated to  $< 0.13$  Pa and then refilled to atmospheric pressure with either  $N_2$  or  $O_2$ , as shown in Fig. 4.1. This ambient flow into the chamber amounted to  $\sim 5$  slm during plasma treatments to maintain the ambient chemistry. When the chamber reached ambient pressure, an exhaust valve is opened to prevent an overpressure in the chamber. To eliminate post-treatment surface reactions from the air in the laboratory, samples were transferred under vacuum to XPS after treatment and subsequent pump-out of the treatment chamber. The vacuum chamber has a volume of 50 liters, so the ambient gas chemistry can vary slightly during the treatment. However, this change is mostly due to Ar as molecular gases account for only 1 % of the feed gas. Additionally, UV absorption at 254 nm was measured to estimate the ozone density using Beer's law.<sup>[51]</sup> In these experiments the applied voltage was kept constant for all gas chemistries so that the reduced electric field was also kept constant. The power density has been measured by the Lissajous method and is lowest at  $3.4 \text{ W cm}^{-2}$  for the Ar discharge and highest at  $3.7 \text{ W cm}^{-2}$  for the 1%  $O_2/Ar$  discharge. 1%  $N_2/Ar$  and 1% Air/Ar gas chemistries fall within this range. The focus of this article is not on the differences between gas chemistries. Rather, this



article focuses on the plasma-ambient interaction for a given gas chemistry. An exception is an O<sub>2</sub> admixture series discussed below, but the power density only increases from  $3.61 \pm 0.06 \text{ W cm}^{-2}$  to  $3.71 \pm 0.09 \text{ W cm}^{-2}$  when the O<sub>2</sub> admixture increases from 0.25% to 1%. Given that the standard deviations overlap, the changes in film composition can be attributed to the change in gas chemistry.

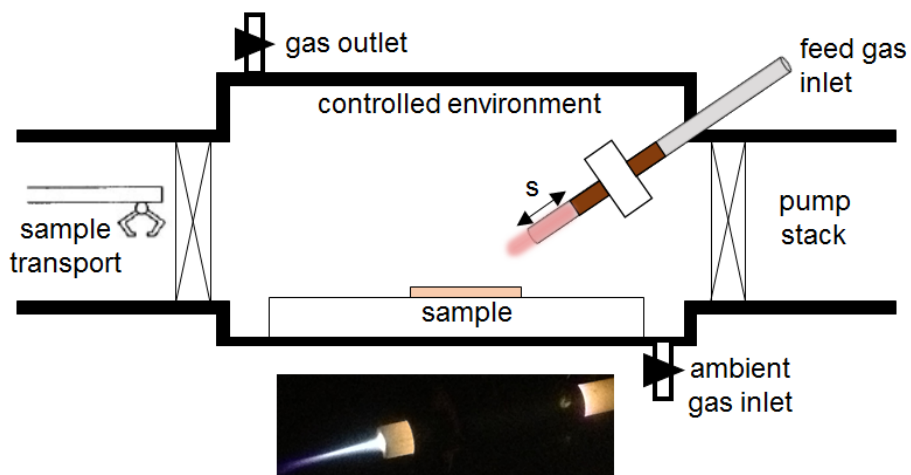


FIG. 4.1. Schematic of the atmospheric pressure plasma jet (APPJ) mounted in a vacuum chamber that can be pumped out and refilled with a controlled environment. The distance,  $s$ , between the source and the nozzle can be adjusted to regulate the interaction of the plasma plume with the environment. The photograph shows an Ar APPJ operating in the exposed geometry.

#### 4.2.3. Surface Characterization

XPS analysis provided information on chemical changes at the film surface. The analysis was performed with a Vacuum Generators ESCA Mk II surface analysis system employing a Mg-K $\alpha$  source (1253.6 eV) at electron takeoff angles of 90° (deep probing depth  $\approx 8$  nm) and 20° (shallow probing depth  $\approx 2$ -3 nm) relative to the surface at 20 eV pass energy. As the deep probing depth measurements showed similar, but attenuated effects as the shallow probing depth

measurements, only the near-surface is modified. Thus, only measurements made at a shallow probing depth are shown and analyzed below. Survey spectra were collected at a pass energy of 50 eV. The area analyzed by XPS was smaller than the area treated by the APPJ. As discussed below, a peak in the C1s spectrum due to aromatic carbon completely disappears after highly oxidizing treatments. If the XPS measured an area larger than the treated area, then one would expect this aromatic peak to show after these treatments. The treated area is estimated to be approximately 2 cm<sup>2</sup> and the measured area to be less than 1 cm<sup>2</sup>. XPS measurements were performed within 20 minutes after treatment after transferring samples under vacuum into the UHV chamber. As shown below, peaks attributed to nitrogen functionalities (NO, NO<sub>2</sub>, NO<sub>3</sub>) make up less than 1.5% of the chemical composition of the films. Great care needs to be taken when interpreting peaks with such low intensities. The presence of these peaks, even with very low intensity, and the clear binding energy shifts between them is unambiguous and highly reproducible. Taking this into consideration, reported NO<sub>x</sub> compositions can be estimated to have a maximum uncertainty of ± 0.14%. Due to the large number of experiments, not all conditions were reproduced. However, critical experiments were reproduced, and were shown to be highly reproducible. Error bars on reproduced experiments are shown where applicable.

C1s, O1s, and N1s peak assignments were taken from the literature.<sup>[52, 143, 144]</sup> Only the C1s and N1s spectra were fitted. The O1s was not fitted due to overlapping peaks. C1s spectra were fit with peaks corresponding to C=C/H at 284.7 eV, C-C/H at 285 eV, C-O at 286.5 eV, O-C-O/C=O at 287.9 eV, O-C=O at 289 eV, O-(CO)-O at 290.2 eV, and  $\pi$ - $\pi^*$  at 291.6 eV. In the N1s, peaks were fit at 401.8 eV (nitroso), 406 eV (nitrite) and 408 eV (nitrate). To calculate atomic composition of the film (excluding H), the integrated peak area was divided by its Scofield cross sections for C, O, and N of 1, 2.85, and 1.77, respectively.<sup>[73]</sup>

To monitor material removal in real-time during APPJ treatment, the APPJ was mounted in a nearly identical chamber as the one described in section 2.2 that was equipped with an ellipsometer. The main difference is that the APPJ is oriented normal to the material surface. Surface morphology was measured using tapping mode AFM (MFP-3D, Asylum Research).

### **4.3. Results**

#### *4.3.1. Time-dependent and O<sub>2</sub> Admixture-dependent Treatments*

Time-dependent and O<sub>2</sub>-admixture dependent treatments were performed. Time-dependent C1s composition and O and NO<sub>3</sub> atomic compositions are shown in figure 4.2 for a 5 cm source-to-nozzle distance. The O<sub>2</sub>/Ar plasma with a 5 cm source-to-nozzle distance is confined in the alumina tube. For this condition, all nitrogen was in the form of NO<sub>3</sub>. As treatment time increased, modifications also increased, but there was little difference between the 6 minute and 15 minute treatment. Oxidized species emerge as the treatment time increases. Although the O composition hardly changed between 6 and 15 minutes, the type of moieties did change with increased formation of ester and carbonate groups at the expense of alkoxy and carbonyl/acetal groups. As treatment time increases  $\pi$ - $\pi^*$  bonding drops dramatically.

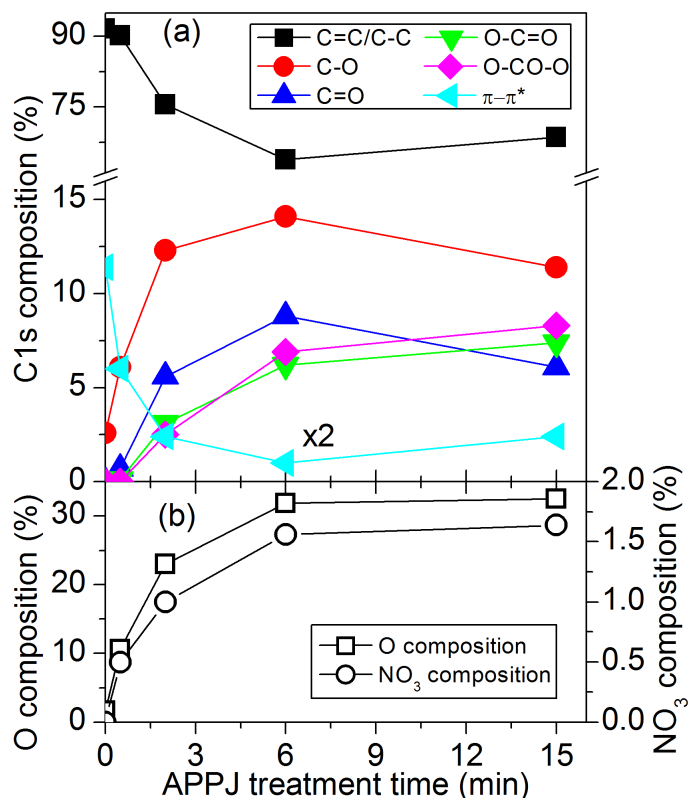


FIG. 4.2. As a function of APPJ treatment time, (a) C1s composition and (b) oxygen and NO<sub>3</sub> composition measured by XPS at shallow probing depths. Treatment conditions: 1% O<sub>2</sub>/Ar, confined geometry, N<sub>2</sub> ambient.

In addition to treatment time, reactive species flux to the surface can also be regulated by admixture. The O<sub>2</sub> admixture to Ar plasma was varied from 0.25% to 2% in a confined geometry in an N<sub>2</sub> ambient. To differentiate the admixtures more easily, samples were treated for only 3 minutes to avoid modification saturation that occurs for treatments longer than 6 minutes. Figure 4.3 shows that as the O<sub>2</sub> admixture increases, surface modifications increase with compositions and trends similar to the time-dependent treatments. However, the treatment time was not long enough for saturation to occur in any case, so carbonate and ester groups were formed less here than for the longer treatments. 1% molecular gas admixtures were used for 7 minute treatments

as a standard condition. The 1% admixture was chosen as it is commonly used in the literature and perturbs the plasma less than the 2% admixture. Samples were treated for 7 minutes instead of 6 minutes to ensure that compositional saturation was exceeded. As oxidized moieties emerged, the shake-up feature due to the  $\pi$ - $\pi^*$  transition decreased, indicating that the aromaticity of the styrene group was reduced. Despite major oxidation, real-time ellipsometry measured negligible etching, with less than 1 nm of material removed during the treatment. Similarly, the surface morphology, shown in figure 4.4, did not change with the RMS surface roughness decreasing from 3.5 nm to 3.4 nm. This decrease is insignificant.

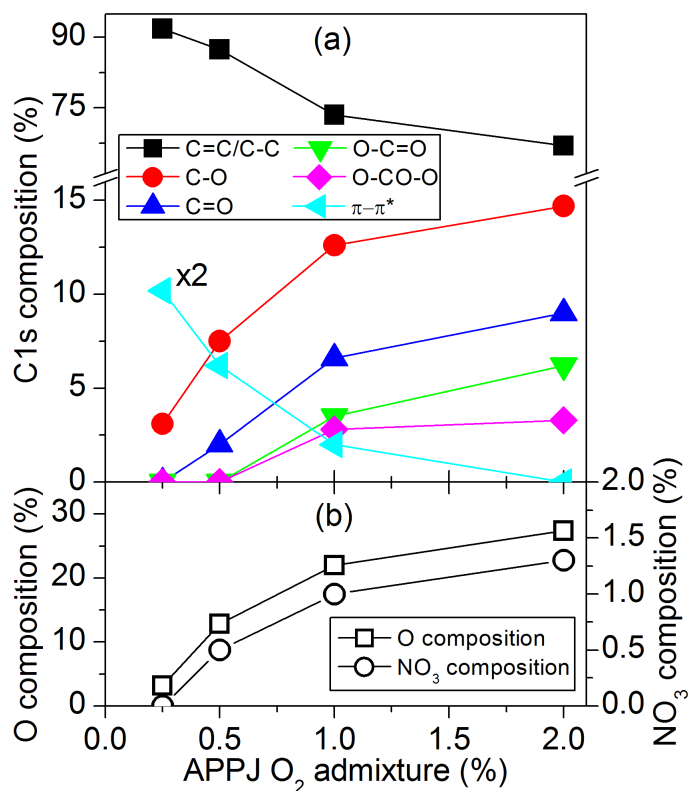


FIG. 4.3. As a function of APPJ O<sub>2</sub> admixture (a) C1s composition and (b) oxygen and nitrogen composition measured by XPS at shallow probing depths. Treatment conditions: Ar carrier gas, confined geometry, N<sub>2</sub> ambient, 3 min treatment.

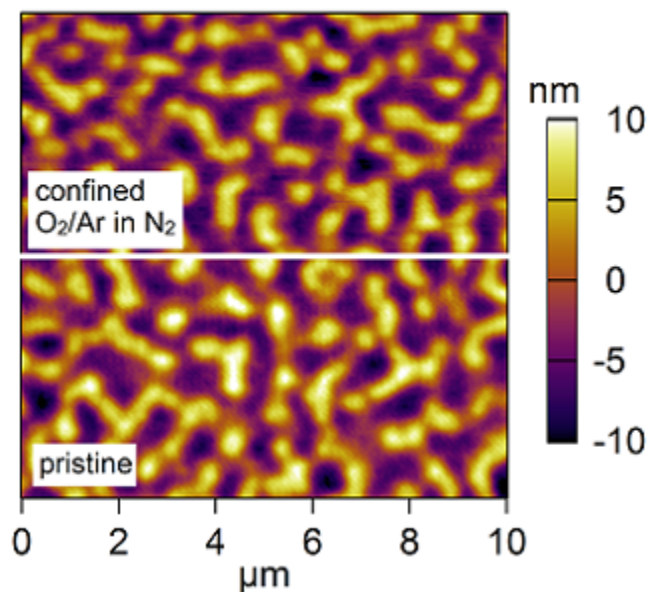


FIG. 4.4. Tapping mode AFM image of pristine PS and PS treated by 1% O<sub>2</sub> in Ar plasma in N<sub>2</sub> in the confined geometry for 7 minutes. The applied voltage and frequency were 14 kV pk-pk and 24 kHz, respectively.

#### 4.3.2. The Role of the Environment for 1% O<sub>2</sub>/Ar Feed Gas Mixture

The O<sub>2</sub>/Ar feed gas chemistry was further studied to examine the role of the environment for a highly oxidizing condition. High-resolution C1s, N1s, and O1s XPS spectra for an untreated PS film and films treated by a confined 1% O<sub>2</sub>/Ar condition for O<sub>2</sub>, air, and N<sub>2</sub> ambients are shown in figure 4.5 and highlight typical spectral changes. Untreated PS films consisted of three peaks for C=C, C-C, and  $\pi$ - $\pi^*$  shake up. As can be seen in the figure, APPJ treatment oxidized the films differently depending on the ambient gas chemistry, with decreasing ambient O<sub>2</sub> content increasing modifications. It was previously shown that O<sub>2</sub> in the feed gas is important for modifications and biodeactivation of LPS.<sup>[140]</sup> Interestingly, the O<sub>2</sub> ambient reduced surface modifications, with minimal formation of both ester (O-C=O) and carbonate (O-

CO-O) groups. In the N1s spectrum, plasma treatment formed a new feature at 408 eV due to NO<sub>3</sub>. This low intensity peak was reported previously in LPS.<sup>[140]</sup> However, it was uncertain if this species originated from nitrogen and oxygen already found in LPS or from plasma-generated species. As PS contains neither nitrogen nor oxygen, it is clear that this species requires both ROS and RNS or RONS to interact with the surface of the sample. This species decays quickly due to X-rays, as discussed in the literature, so the N1s spectrum was measured first in all experiments.<sup>[145]</sup>

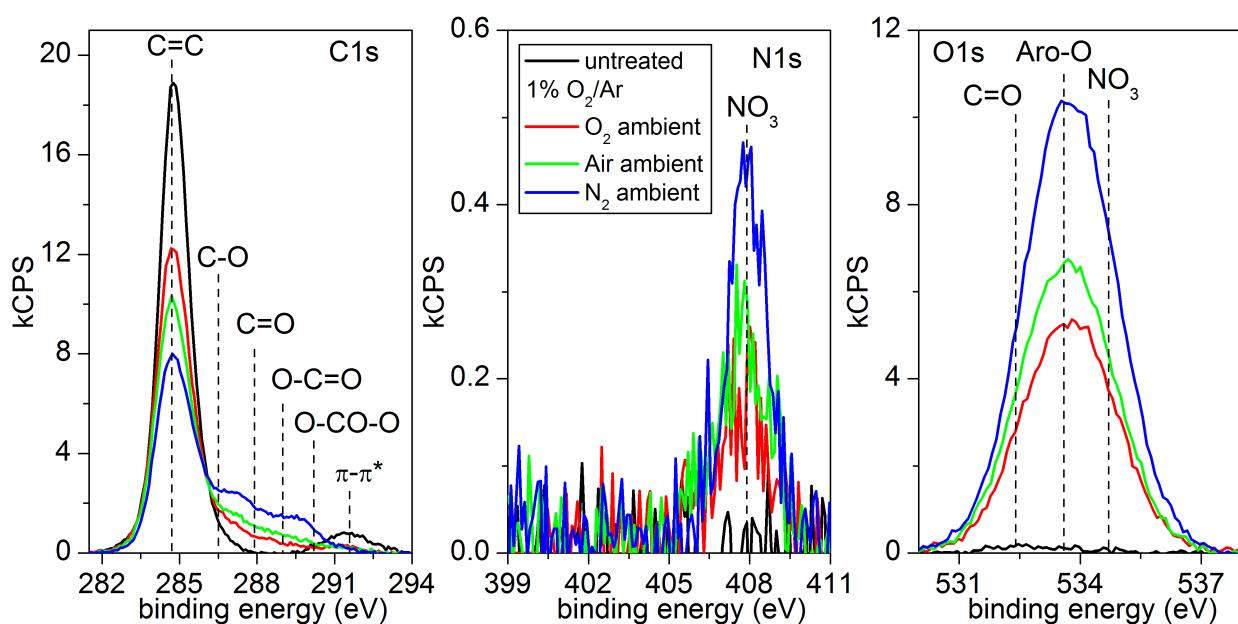


FIG. 4.5. High resolution XPS C1s, N1s, and O1s spectra of PS films before and after the confined 1% O<sub>2</sub>/Ar treatment in O<sub>2</sub>, air, and N<sub>2</sub> environments.

#### 4.3.3. The Role of the Environment and Source Geometry for Various Feed Gas Mixtures

O<sub>2</sub>/N<sub>2</sub>/Ar and Ar feed gases were also studied to evaluate which specific surface moieties are impacted. Figure 4.6 shows C1s difference plots (treated – untreated) for PS after Ar, 1%

N<sub>2</sub>/Ar, 1% air/Ar, and 1% O<sub>2</sub>/Ar plasma treatments were performed either in the confined or exposed geometry using either O<sub>2</sub> (Fig. 4.6(a)) or N<sub>2</sub> (Fig. 4.6(b)) ambient, respectively. The film atomic composition is summarized in table 4.1 after treatments performed.

		Atomic percent (%)					
		confined			exposed		
feed gas	ambient	C	O	N	C	O	N
Ar	O <sub>2</sub>	86.0 ± 0.1	13.2 ± 0.1	0.8 ± 0.0	74.2 ± 0.2	24.3 ± 0.1	1.5 ± 0.1
	N <sub>2</sub>	91.7 ± 0.0	7.3 ± 0.1	1.0 ± 0.1	87	11.7	1.3
1% O <sub>2</sub> /Ar	O <sub>2</sub>	81.6 ± 2.5	17.7 ± 2.3	0.8 ± 0.2	74.8 ± 0.4	24.3 ± 0.5	0.8 ± 0.1
	N <sub>2</sub>	67.2 ± 0.3	31.4 ± 0.7	1.4 ± 0.1	69 ± 0.2	29.9 ± 0.3	1.1 ± 0.2
1% Air/Ar	O <sub>2</sub>	91.9	8.1	0	89.7	10.3	0
	N <sub>2</sub>	96.6	3.1	0.3	85.1	13.6	1.4
1% N <sub>2</sub> /Ar	O <sub>2</sub>	97 ± 0.3	2.9 ± 0.5	0.1 ± 0.1	85.6	13.5	0.9
	N <sub>2</sub>	95.5 ± 0.4	4.2 ± 0.4	0.3 ± 0.1	88.8	9.9	1.3

TABLE 4.1. XPS measured composition of PS films after various APPJ treatments for the standard conditions used in this work.

Overall, for O<sub>2</sub>/Ar plasma, the geometry and environment did not make a large difference as plenty of ROS were produced. For all other gases, ROS were either reduced by excited N<sub>2</sub> or simply not present. This section starts with results from the confined geometry and then notes major differences when the APPJ is changed to the exposed geometry. At the end, key differences in NO<sub>x</sub> surface chemistry are described.



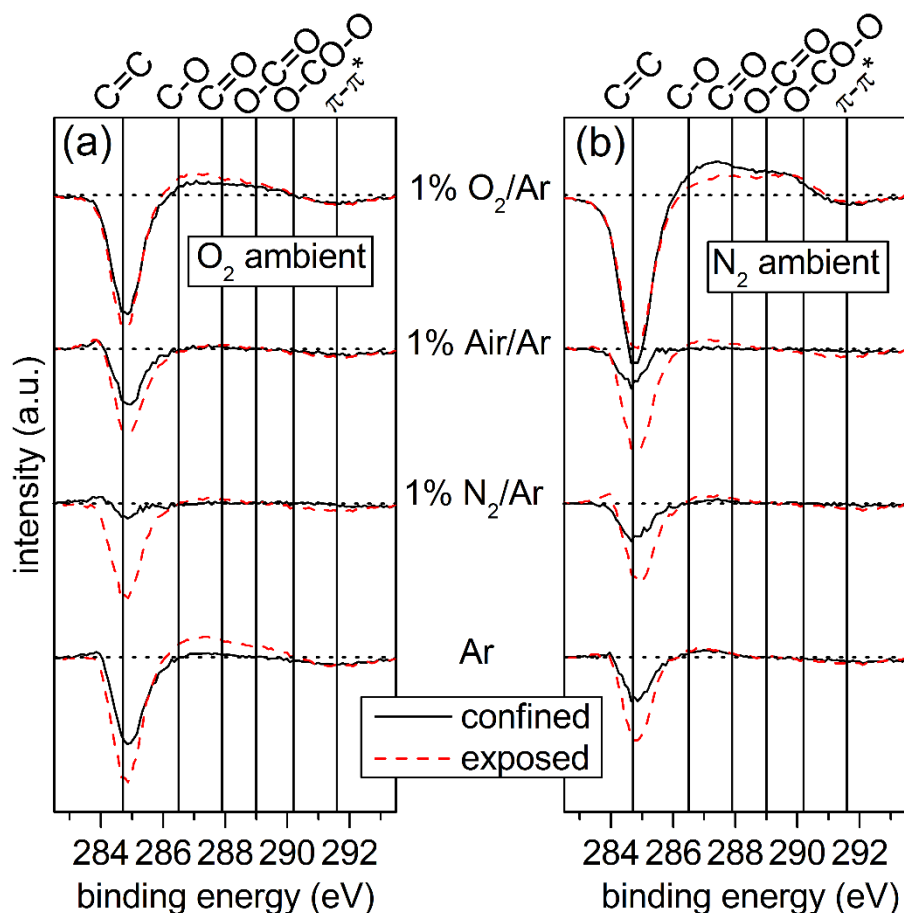


FIG. 4.6. C1s difference plots (treated-untreated) for Ar and 1% admixtures of N<sub>2</sub>, Air, and O<sub>2</sub> to Ar in O<sub>2</sub> and N<sub>2</sub> ambients. The confined geometry (black solid line) was compared with the exposed geometry (red dashed line) to study how the environment interacts with long-lived and short-lived species.

**O<sub>2</sub>/Ar, Air/Ar, and N<sub>2</sub>/Ar in O<sub>2</sub> or N<sub>2</sub>.** As previously mentioned, the 1% O<sub>2</sub>/Ar plasma treatment oxidized the surface for both ambients, but the effect was greater in the N<sub>2</sub> ambient. C-O, C=O, and O-C=O are all higher after treatment in N<sub>2</sub>. Highly oxidized carbonate groups, O-CO-O, only form in the N<sub>2</sub> ambient. This difference suggests that there is a different type of quenching occurring by the O<sub>2</sub> ambient, as discussed in Sec. IV. For the air admixture to Ar, only slight drops in C=C/C-C bonding and slight increases in oxidized species were observed in

the confined geometry. For the N<sub>2</sub> admixture to Ar, neither ambient causes substantial modifications in the confined geometry with only slight drops in C=C/C-C bonding.

**Ar in O<sub>2</sub> or N<sub>2</sub>.** For the Ar plasma, stronger modifications occurred for the O<sub>2</sub> ambient. This resulted in slight formation of C-O and C=O at the expense of C=C/H and aromaticity, and can be explained by ROS being generated close to the sample by both Ar metastables and electrons in the plasma jet, which can dissociate, excite, and ionize ambient O<sub>2</sub> molecules and O atoms. After treatment, the atomic composition of oxygen was 13.2% ± 0.1%, but C-O bonding made up only 6.5% ± 0.4% of the C1s. In the N<sub>2</sub> ambient, minimal surface modifications occur. However, there is still a decrease in C=C and increase in C-O, indicating that trace O<sub>2</sub> in the system can still play a large role. In N<sub>2</sub>, oxygen uptake comparable to the oxygen composition seen in the C1s is observed. This difference in the oxidation in the C1s and O1s is due to formation of peroxy radicals or hydroperoxide and will be discussed in Sec. IV.

The C1s composition was further analyzed to compare how the feed gas and plasma-ambient interaction impact the formation of specific moieties. The integrated peak area is shown in figure 4.7 for each moiety. In this plot, each individual panel represents a particular moiety. The left side of a given panel corresponds to the exposed configuration and the right side corresponds to the confined geometry. O<sub>2</sub> (red) and N<sub>2</sub> (green) ambients are vertically adjacent to each other. For C=C/C-C bonding (Fig. 4.7(a)), O<sub>2</sub>/Ar has a greater effect in N<sub>2</sub>. For other gas chemistries, the ambient does not play a strong role when confined. For C-O bonding (Fig. 4.7(b)), O<sub>2</sub>/Ar in N<sub>2</sub> shows much more formation than in O<sub>2</sub>. For N<sub>2</sub>/Ar and Air/Ar, C-O is the only oxidized species formed in appreciable amounts, though it is still low. Changing the ambient gas chemistry for N<sub>2</sub>/Ar, Air/Ar, and Ar plasmas does not impact the surface modifications much. The more highly oxidized groups only form in the O<sub>2</sub>/Ar plasma. The most

highly oxidized group, O-CO-O, only forms when the O<sub>2</sub>/Ar plasma is operated in the N<sub>2</sub> ambient. Aromatic  $\pi$ - $\pi^*$  (Fig. 4.7(f)) shows similar behavior as the C=C/C-C bonding.

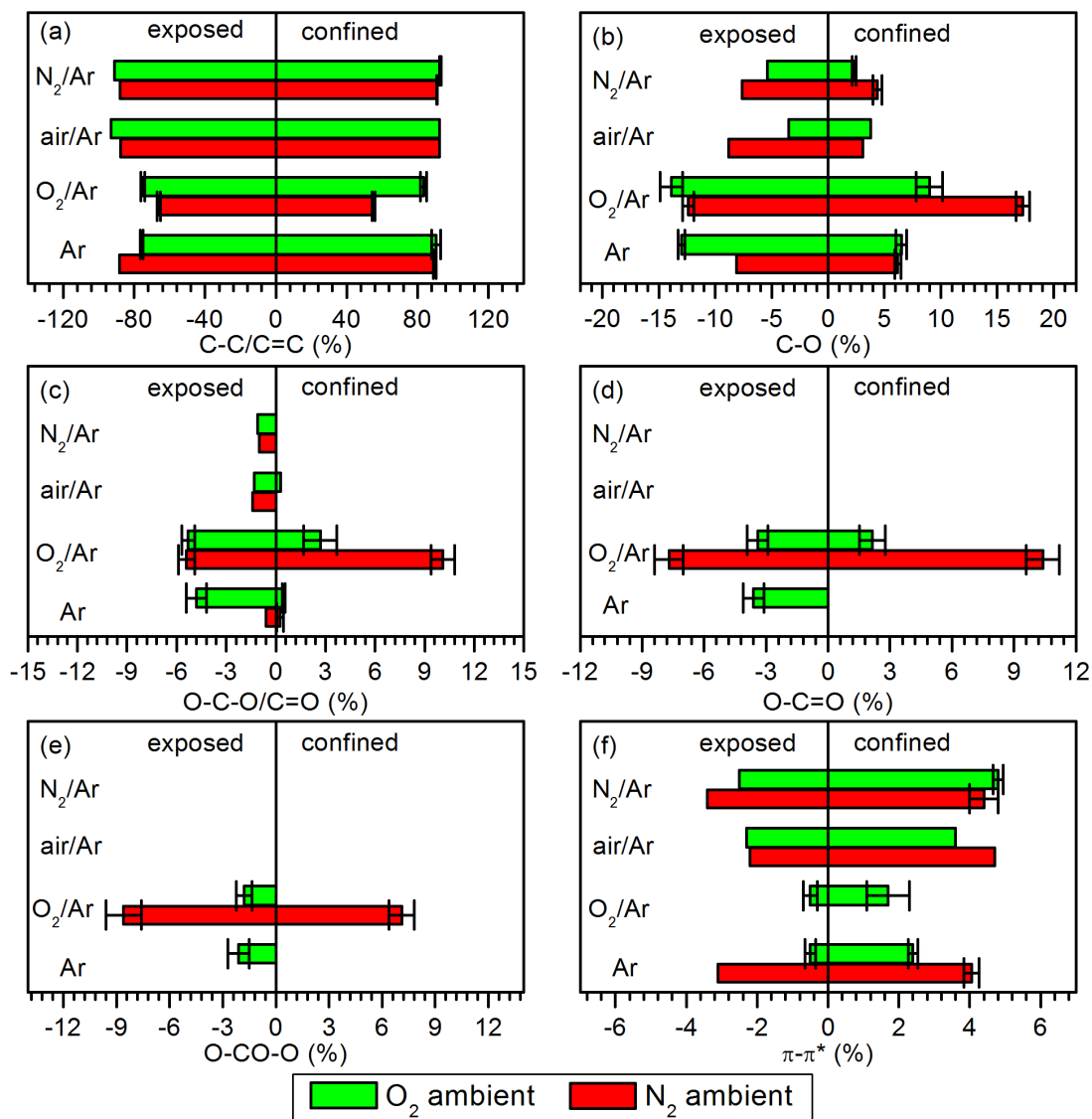


FIG. 4.7. Integrated peak areas corresponding to (a) C=C/C-C, (b) C-O, (c) O-C-O/C=O, (d) O-C=O, (e) O-CO-O, and (f)  $\pi$ - $\pi^*$  for APPJ treatments in the exposed (left side) and confined (right side) configurations for Ar and 1% O<sub>2</sub>, air, and N<sub>2</sub> admixture to Ar feed gases in the N<sub>2</sub> (red) and O<sub>2</sub> (green) ambients.

**Key differences when exposed.** As expected, plasma-ambient interactions played a larger role in the exposed geometry, and the major differences between the confined and exposed will be highlighted here. The largest difference was observed for the Ar plasma. When exposed in O<sub>2</sub>, C-O density increases to levels comparable to the O<sub>2</sub>/Ar plasma and high binding energy groups such as O-C-O/C=O, O-C=O, and O-CO-O emerge. O-C=O and O-CO-O only appeared for O<sub>2</sub>/Ar and Ar exposed in O<sub>2</sub>. In the N<sub>2</sub> ambient, O<sub>2</sub>/Ar plasma changed the composition of the oxidized groups with increased carbonate functionality at the expense of C-O, O-C-O/C=O, and O-C=O. However, the oxygen composition was similar for both geometries. In O<sub>2</sub>, O<sub>2</sub>/Ar modifications are stronger when exposed. N<sub>2</sub>/Ar and Air/Ar behave similarly: C-O is larger in N<sub>2</sub> and low concentrations of O-C-O/C=O form in both ambients.

**Surface-bound NO<sub>x</sub>.** In addition to changes in the C and O content in the films, the ambient gas chemistry also introduced nitrogen functionalities on the surface. Figure 4.8 shows N1s spectra after treatment comparing N<sub>2</sub>/Ar and O<sub>2</sub>/Ar plasma exposed in N<sub>2</sub>. The O<sub>2</sub>/Ar treatment shows a single peak at 408 eV due to NO<sub>3</sub> while the N<sub>2</sub>/Ar treatment shows three peaks due to NO<sub>3</sub>, NO<sub>2</sub>, and NO due to trace oxygen or water impurities in the system. The authors emphasize that NO<sub>2</sub> and NO only formed in the N<sub>2</sub> ambient and never formed for the O<sub>2</sub>/Ar feed gas. This is consistent with the O-deficient conditions as fewer ROS were available to further oxidize NO<sub>2</sub> to NO<sub>3</sub>. The N<sub>2</sub>/Ar plasma produced NO (0.8% ± 0.2%), NO<sub>2</sub> (1.1% ± 0.1%), and NO<sub>3</sub> (0.6% ± 0.1%). The Air/Ar plasma produced NO<sub>2</sub> (0.6%) and NO<sub>3</sub> (0.7%). The Ar plasma produced NO<sub>2</sub> and NO<sub>3</sub> equally on the surface at 0.7%. As noted in the introduction, NO<sub>x</sub> species have been measured and modeled in the effluent and far effluent of atmospheric plasma sources; it is clear that these species can also interact with surfaces. Atmospheric

pressure plasma-surface interactions have been evaluated for a variety of polymers by XPS and water contact angle measurements,<sup>[130]</sup> but, to the best of our knowledge, only CO<sub>x</sub> species were reported, not NO<sub>3</sub>. Nitrogen functionalities between 397 and 403 eV have been reported and assumed to be contaminants.<sup>[111]</sup>

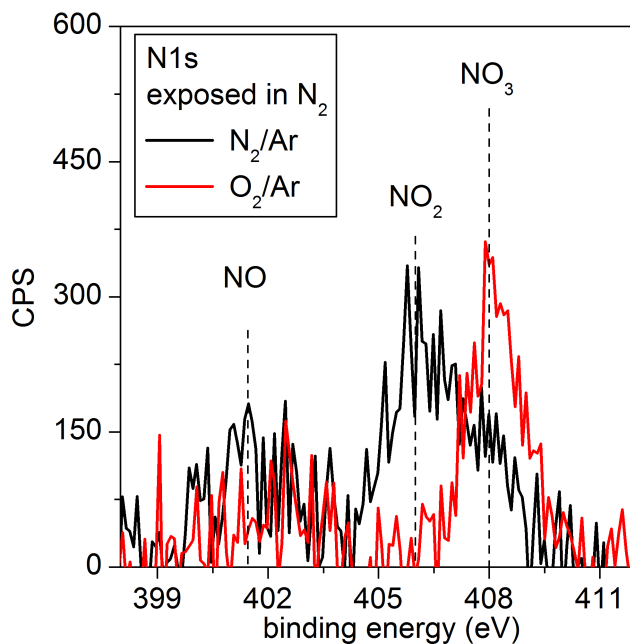


FIG. 4.8. High resolution XPS N1s spectrum of PS comparing exposed N<sub>2</sub>/Ar and O<sub>2</sub>/Ar treatments in an N<sub>2</sub> environment.

#### 4.3.4. The Role of Ozone

To further understand the role of O<sub>3</sub>, the O<sub>3</sub> density was also measured for the APPJ for varying applied voltages. Ozone production in DBDs has been extensively studied. When the applied power reaches a certain level, ozone production breaks down completely in a process known as discharge poisoning.<sup>[146]</sup> This effect has also been observed with gas-phase FTIR by Pavlovich et al. for an air-operated surface microdischarge where the absorbance due to O<sub>3</sub> was diminished and absorbance due to NO<sub>2</sub> and N<sub>2</sub>O increased when the power density was increased

from  $0.10 \text{ W cm}^{-2}$  to  $0.30 \text{ W cm}^{-2}$ .<sup>[121]</sup> Figure 4.9 shows ozone densities produced by the APPJ for peak-to-peak voltages ranging from 12 kV to 18 kV. Two effects are observed when the voltage is increased. Higher voltages not only led to decreased ozone generation, but the time at which destructive processes dominate happened earlier as well. The 12 kV experiment showed the  $\text{O}_3$  density increasing over the first 3 minutes and then reaching a constant density of  $\sim 6.7 \times 10^{14} \text{ cm}^{-3}$ . In contrast, at 14 kV, 16 kV, and 18 kV, destructive processes dominated after 150 s, 90 s, and 60 s, respectively, leading to  $\text{O}_3$  densities below the detection limit of the setup,  $10^{13} \text{ cm}^{-3}$ . For higher applied voltages, the temperature of the alumina tube and source increase dramatically. As the temperature increases, the rate constants for the formation of  $\text{O}_3$  (see reaction 1 below) and its destruction by associative collision with O atoms to form  $\text{O}_2$  and  $\text{O}_2(\text{a})$  increase.<sup>[124]</sup> If  $\text{O}_3$  was a key species for the surface modification of PS, then one would expect the 18 kV treatment to modify the PS surface much less than the 12 kV treatment. XPS analysis supports that  $\text{O}_3$  is not a key player as the 18 kV treatment results in an O/C ratio of  $0.42 \pm 0.04$ , but the 12 kV treatment results in an O/C ratio of  $0.37 \pm 0.02$  despite significantly decreased  $\text{O}_3$  production over the course of the treatment.

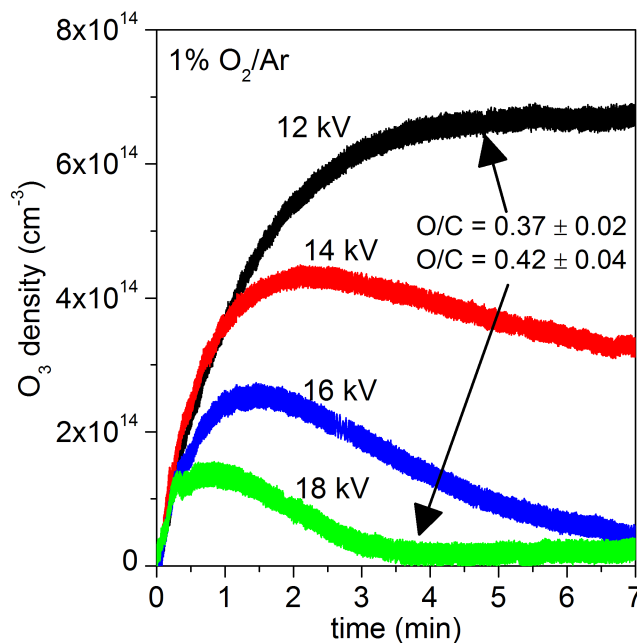


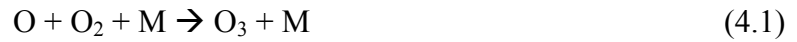
FIG. 4.9. The  $O_3$  density measured by UV absorption at 254 nm as a function of treatment time for a 1%  $O_2/Ar$  plasma operated at peak-peak voltages of 12 kV, 14 kV, 16 kV, and 18 kV. O/C ratios extracted from XPS analysis are shown for the 12 kV and 18 kV condition.

#### 4.4. Discussion

Extra oxygen was measured in the O1s compared to the C1s after Ar treatment in  $O_2$  ambient. It has been shown that H-abstraction from surfaces leads to the formation of surface bound  $O_2$  in the form of a peroxy radical or hydroperoxide group.<sup>[147]</sup> This would lead to roughly double the  $O_2$  composition in the O1s compared to the C1s, which is consistent with the observations of  $6.5\% \pm 0.4\%$  and  $13.2\% \pm 0.1\%$  in the C1s and O1s, respectively. For Ar treatment in  $N_2$ , the O1s and C1s oxygen contents agree, which is consistent with the  $O_2$ -deficient environmental conditions preventing the formation of peroxy radicals and hydroperoxide. The lack of modifications by air/Ar plasma agrees with the role of  $N_2$  in the feed

gas which becomes excited and quenches the most reactive species to form less reactive species such as N<sub>2</sub>O and N<sub>2</sub>O<sub>3</sub>.

One of the most reactive species produced by atmospheric plasma sources is atomic oxygen. A two-photon absorption laser induced fluorescence and molecular beam mass spectrometry study by Ellerweg et al. found that O atom densities in an O<sub>2</sub>/He APPJ reached a maximum at ~0.6% O<sub>2</sub> admixture.<sup>[148]</sup> This maximum is reached due to the increased production of O<sub>3</sub> at higher O<sub>2</sub> concentrations. Similar behavior is expected for this APPJ. Assuming that [O] << [O<sub>2</sub>], which is reasonable as O atom densities have been measured in the 10<sup>15</sup> cm<sup>-1</sup> range, O atoms are only quenched by forming O<sub>3</sub> through a collision with O<sub>2</sub> by:



where M is any third body that can stabilize the formation of O<sub>3</sub>. Under this assumption, the mean free path of an O atom can be estimated. The collision cross section,  $\sigma$ , is given by:

$$\sigma = \pi(r_{\text{O}} + r_{\text{O}_2})^2 \quad (4.2)$$

where  $r_{\text{O}}$  and  $r_{\text{O}_2}$  are the radius of O and O<sub>2</sub>, respectively with radii 1.3 x 10<sup>-10</sup> m and 1.81 x 10<sup>-10</sup> m, respectively. The mean free path,  $\lambda$ , is given by:

$$\lambda = kT/\sqrt{2}\sigma p \quad (4.3)$$

where  $k$  is Boltzmann's constant,  $T$  is the temperature, and  $p$  is the partial pressure of O<sub>2</sub>, which is 1013.3 Pa for a 1% admixture. This results in an approximate mean free path of 10  $\mu\text{m}$  between collisions of O atoms and O<sub>2</sub> molecules. Thus, O atoms produced in the plasma source and effluent would not be able to travel from the source to the sample as the total distance in the confined geometry is 12 cm (9 cm from source to nozzle and 3 cm from nozzle to sample). The inability of O atoms generated in the source and effluent to reach the sample marks a key difference in surface reactions between other types of treatments. Gonzalez and Hicks have



studied remote plasma treatment of various polymers by O<sub>2</sub>/He atmospheric pressure plasma where the sample is placed in the plasma afterglow 5 mm from the nozzle.<sup>[103]</sup> Plasma generated O atoms were proposed to attack methyl and methylene groups in high density polyethylene and poly(methyl methacrylate), resulting in chain scission. For polyethersulfone, O atoms induced ring-opening and insertion of carboxylic acid. Other studies on oxygen plasma treatment at low and atmospheric pressure treatment have reported carbonate formation on PS.<sup>[130, 142, 149]</sup> It has not been observed or modeled in other polymers such as polyethylene,<sup>[130]</sup> polypropylene,<sup>[135, 138]</sup> and poly(methyl methacrylate),<sup>[150-152]</sup> suggesting that this species is unique to the styrene ring or aromatic groups. Due to the short lifetime of an O atom and the large source-sample distances here, O atoms are unlikely responsible for the formation of these groups.

Studies on photodegradation of polymers have concluded that singlet oxygen, O<sub>2</sub>(a), in the presence of sunlight is a potent oxidant, pointing towards the importance of this metastable species.<sup>[147]</sup> This species is mainly generated by electron-impact excitation of O<sub>2</sub> and destroyed in the far effluent by reactions with O<sub>3</sub>.<sup>[124]</sup> In the voltage series described above, increased O<sub>2</sub>(a) formation by electron impact and decreased O<sub>2</sub>(a) destruction by O<sub>3</sub> can be expected due to lower O<sub>3</sub> densities at 18 kV compared to 12 kV. In the results section, decreased modifications in O<sub>2</sub> compared to N<sub>2</sub> ambients were observed. This could be due to absorption of high energy photons, which is enhanced in O<sub>2</sub>. In the UV range, emission down to 240 nm due to NO has been measured, consistent with other groups.<sup>[123]</sup> Higher energy photons due to Ar<sub>2</sub><sup>\*</sup>, which emits in the 120-135 nm range, have also been detected in APPJs.<sup>[119]</sup> It is well known that O<sub>2</sub> absorbs high energy photons in the upper atmosphere, contributing to the O<sub>3</sub> layer. One possibility is the ability of O<sub>2</sub> to more effectively absorb plasma-generated ultraviolet/vacuum ultraviolet (UV/VUV) photons than N<sub>2</sub>, resulting in decreased modifications in the O<sub>2</sub> ambient.

High energy photons are known to abstract hydrogen from polymers, leading to radical sites on the polymer.<sup>[89, 90, 92]</sup> This extra pathway for hydrogen abstraction is likely responsible for the increased modifications in N<sub>2</sub> ambient. Another possibility involves the ambient-dependent length of the plasma plume for exposed treatments.<sup>[127]</sup> The plume length will decrease in the O<sub>2</sub> ambient similarly to how O<sub>2</sub> admixtures to the feed gas shorten the plume length. Based on this work and the previous study on LPS with N<sub>2</sub>/Ar environments, ambient quenching of reactive species for confined treatments proceeds as O<sub>2</sub> > N<sub>2</sub> > Ar.

#### *4.4.1. Mechanism and the Role of NO<sub>x</sub>*

As the procedure for establishing well-controlled pure gas environments was developed and improved, a possible correlation between oxygen composition and nitrogen composition of PS surfaces was observed. This is shown in figure 4.10. The variability in the data for identical conditions results from experiments performed as we were improving the experimental set up, which resulted in various degrees of ambient purity. This data also includes results from the time, voltage, and O<sub>2</sub>-admixture series. When O<sub>2</sub> is added to the feed gas (blue diamonds), enough ROS are generated so that gas-phase NO<sub>x</sub> species do not dominate modifications regardless of the geometry, environment, treatment time, or O<sub>2</sub> admixture, which only impact the level of oxidation. For Ar, N<sub>2</sub>/Ar, and Air/Ar APPJ treatments, this correlation depends on whether the ambient is composed of O<sub>2</sub> or N<sub>2</sub>. For the O<sub>2</sub> ambient, more NO<sub>3</sub> can build up on the surface for a given oxidation level compared to the O<sub>2</sub>/Ar plasma. Oxidation is still rapid since ambient O<sub>2</sub> can interact with plasma-generated species as well as radical sites on the surface to form peroxy radicals and hydroperoxide groups, which are known to result in a variety of oxygenated species.<sup>[147]</sup> For the oxygen-deficient treatment conditions in the N<sub>2</sub> ambient,

enhanced nitridation due to NO and NO<sub>2</sub> was measured, as previously shown in figure 4.8. This results in a competition between surface nitridation and oxidation. NO and NO<sub>2</sub> are strong oxidizers and are known to lead to nitrosative stress in biological systems.<sup>[29]</sup> Abou Rich et al. measured gas-phase NO (formed by gaseous N<sub>2</sub> contaminants) in an O<sub>2</sub>/Ar post discharge and measured low concentrations of nitrogen on the surface between 397 – 403 eV, which they attribute to amides, nitriles, and imines.<sup>[110]</sup> While the role of NO in surface modification mechanisms was not discussed, in their ageing study, no nitrogen-containing species were present on the surface after 10 days. Based on this ageing effect and the present work, it is clear that, while NO<sub>x</sub> species participate in surface oxidation, they are transient species that are easily oxidized and removed from the surface by ROS and possibly O<sub>2</sub>.

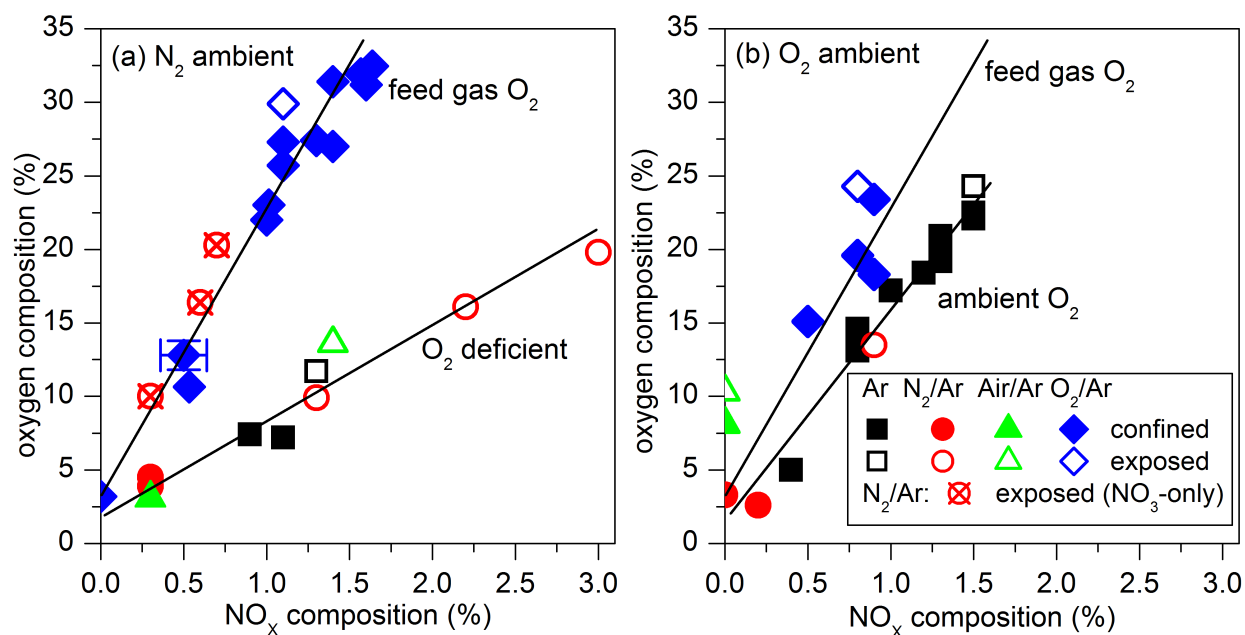


FIG. 4.10. XPS measured oxygen composition as a function of NO<sub>x</sub> composition for the various experimental conditions used in this work in (a) N<sub>2</sub> ambient and (b) O<sub>2</sub> ambient. Surface nitration is limited by the availability of O<sub>2</sub> to oxidize the surface via NO<sub>x</sub>. For O<sub>2</sub>-deficient situations, if the oxygen composition is plotted against NO<sub>3</sub> instead of NO<sub>x</sub>, the modifications follow an O<sub>2</sub>-

rich condition, demonstrating that  $\text{NO}_3$  is a key species for feed gases other than  $\text{O}_2/\text{Ar}$ . A typical error bar is shown in Fig. 10 (a).

This effect is highlighted in figure 4.11, where one can see that nearly all experiments show  $\text{NO}_3$ , only a handful show  $\text{NO}_2$  and only two show  $\text{NO}$ . For the highest oxidation levels, only  $\text{NO}_3$  is seen. The overall picture for PS is that oxidation is preferred whereas nitridation is hard and only seen for specific conditions. Even though these species are covalently bound to the surface, nitrogen is not found without a bond to oxygen. That is, amine ( $\text{C-NR}_2$ ) and amide ( $\text{R-NH-C=O}$ ) moieties are absent. If the oxygen composition is plotted against only  $\text{NO}_3$  instead of  $\text{NO}_x$  for the  $\text{N}_2/\text{Ar}$  plasma exposed in  $\text{N}_2$  ambient, then the trend follows that of the  $\text{O}_2/\text{Ar}$  treatment (see Fig. 10(a), exposed  $\text{NO}_3^-$  only). This indicates that  $\text{NO}_3$  is a key species related to surface oxidation and that if ROS are not produced directly in the discharge, then oxidation relies on  $\text{NO}_x$  species in the far effluent and ultimately to surface-bound  $\text{NO}_3$ . A number of mechanisms are possible for this, including formation of  $\text{NO}_3$  in the gas phase and direct interaction with the surface.<sup>[153]</sup>

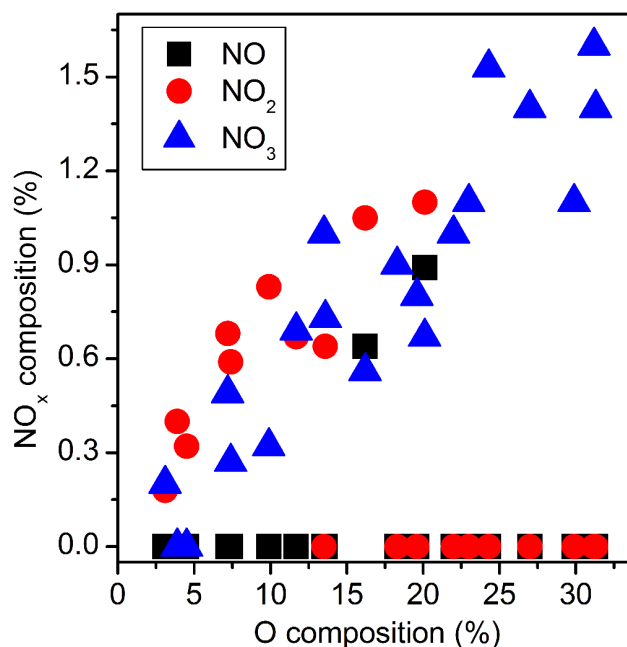


FIG. 4.11. The dependence of surface bound NO, NO<sub>2</sub>, and NO<sub>3</sub> on the O composition of PS treated films under a wide range of experimental conditions explored in this work. For the most highly oxidized films, NO and NO<sub>2</sub> are not present.

The reactive uptake of various gas phase reactive species including NO<sub>2</sub>, NO<sub>3</sub>, HNO<sub>3</sub>, N<sub>2</sub>O<sub>5</sub>, and O<sub>3</sub> by polycyclic aromatic hydrocarbon (PAH) surfaces has been studied by Gross et al.<sup>[153]</sup> They report that reactive uptake by NO<sub>3</sub> was very fast for the three PAHs studied and very slow for the other species. The NO<sub>3</sub> reactive uptake coefficient, defined as the fraction of collisions between gas-phase reactant with the surface that leads to reactive uptake, reached as high as 0.79 +0.21/-0.67, but was at or below the detection limit of 6.6 x 10<sup>-5</sup> for the other gas-phase species. The NO<sub>3</sub> reactive uptake coefficient was measured in the presence of NO<sub>2</sub> and O<sub>2</sub>, but the authors found that these species did not change the surface chemistry on their own.<sup>[145]</sup> The aromatic ring in styrene is expected to behave similarly. Gross et al.<sup>[145]</sup> and Zhang et al.<sup>[154]</sup> conducted a study on nitrate radicals interacting with vinyl-terminated self-assembled

monolayers. Consistent with this work, both groups found that surface-bound nitrates decompose during XPS measurements. However, Gross et al. do not observe organonitro (R-NO<sub>2</sub>) moieties by IR spectroscopy, which demonstrates that the formation of this species must result from another gas-phase species.

Despite the variety of NO<sub>x</sub> species that have been modeled and measured in the effluent of Ar APPJs, the nitrogen atomic composition never exceeds 1.6% for the most highly oxidized conditions. For O-deficient conditions, oxidation proceeds based on the availability of NO<sub>x</sub>. A proposed mechanism is schematically shown in figure 4.12 that is consistent with the O deficient conditions preventing the formation of ROS in the plasma jet and peroxy radicals on the surface. The mechanism also follows the formation of C-O and O-C-O/C=O and reduction of aromatic groups shown in Fig. 4.6(b) for Ar, N<sub>2</sub>/Ar, and Air/Ar plasma in N<sub>2</sub> ambients. Furthermore, under O<sub>2</sub> deficient conditions, NO<sub>3</sub> should not form in high concentrations as it is mainly generated by:



In a first step, reactive species generated in the plasma abstract hydrogen from the aromatic ring to form an aryl radical. This initiation step could result from plasma generated high energy photons, trace atomic O, or NO<sub>x</sub> species. In Fig. 4.12(a), NO adds onto the radical site, which subsequently reacts with additional NO molecules to form nitrate and nitrite groups and lose molecular nitrogen and oxygen, as proposed by Wilken et al.<sup>[143]</sup> NO has been simulated<sup>[124]</sup> and measured at densities as high as 10<sup>15</sup> cm<sup>-3</sup> in MHz driven APPJs, and significant densities can be expected in this kHz driven jet.<sup>[98]</sup> This radical species has been previously studied for etching of silicon nitride films.<sup>[155, 156]</sup> The authors report that NO enhances the removal of N from the Si<sub>3</sub>N<sub>4</sub> surface by the formation of gaseous N<sub>2</sub> and a surface-bound Si-O. A similar

mechanism may be occurring here as nitrogen is not found on the surface at high densities. After  $\text{NO}_3$  has formed on the surface, subsequent reactions take place as shown in Fig. 4.12(b),  $\text{NO}_2$  desorbs, leaving an alkoxy radical. This alkoxy radical results in ring opening that reduces aromaticity and creates aldehyde and ketones.<sup>[138]</sup> Alternatively, the alkoxy group can react with  $\text{NO}$  to form  $\text{NO}_2$ , which is the dominant peak in the N1s spectrum under O-deficient conditions (see Fig. 4.8).

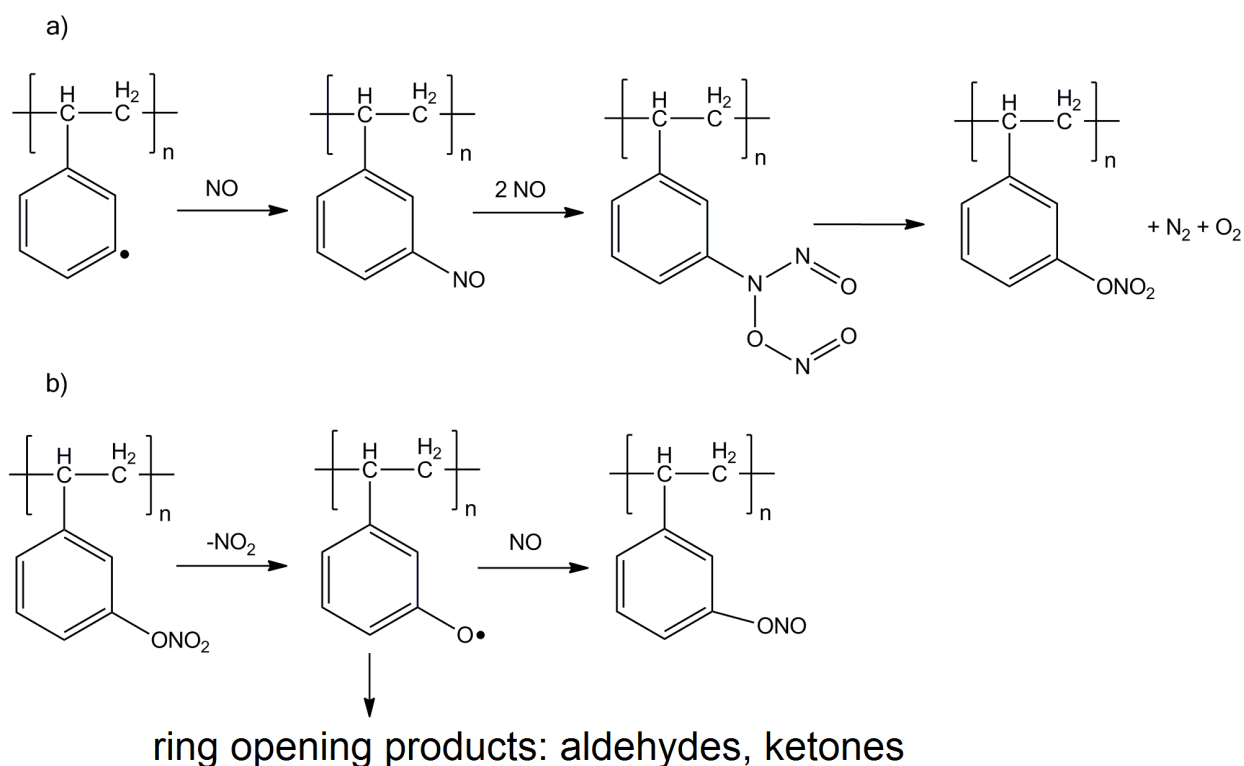
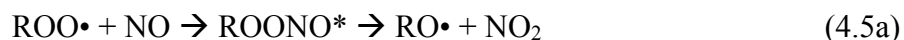


FIG. 4.12. Possible mechanism for the surface reaction of PS with  $\text{NO}$  to oxidize the styrene ring and eliminate aromaticity.

The presence of oxygen opens up a number of mechanisms by which  $\text{NO}_x$  species can oxidize the surface.<sup>[157-159]</sup>  $\text{NO}$  radicals can attack peroxy radical sites to form an unstable

intermediate, resulting in cleavage to form an alkoxy radical and NO<sub>2</sub> or rearrangement to form nitrate:



where the asterisk denotes a vibrationally excited state and M denotes a third species that can collisionally stabilize the formation of RONO<sub>2</sub>. The overall formation of nitrate formation (reaction 5b) is exothermic by ~57 kcal mol<sup>-1</sup>.<sup>[159]</sup> Several authors report that reaction 5b is much less common and that reaction 5a dominates, which agrees with the low concentration of NO<sub>3</sub> observed in this work.<sup>[160]</sup> NO<sub>2</sub> has been modeled<sup>[124]</sup> and measured<sup>[123]</sup> in the APPJ effluent, but the reaction:



is inconsequential as the back-decomposition is rapid.<sup>[159]</sup>

The polymer backbone is also subject to oxidation. Modeling work by Dorai and Kushner on the plasma modification of polypropylene using atmospheric pressure discharges found that H abstraction at the tertiary carbon is most probable due to the stability of substituted radicals.<sup>[138]</sup> The resulting radical can crosslink, chain scission, or bind to gaseous O<sub>2</sub> (O-rich conditions) or NO<sub>2</sub> (O-deficient conditions), which is consistent with the NO<sub>2</sub> peak seen in Fig. 4.8. The tertiary carbon in PS is even more susceptible to attack as the resulting radical site can be distributed throughout the styrene ring through resonance.

#### 4.5. Conclusion

The interaction of the plasma with the environment strongly impacts the modification of PS, a model polymer system, under remote interaction conditions where negligible surface



etching and roughening occurs. Overall oxidation of the surface at the expense of aromaticity was observed. In addition,  $\text{NO}_x$  groups were measured and made up no more than 3% of the film composition. For surface modification, O atoms and  $\text{O}_3$  did not seem to be key reactants; rather, these results suggest that singlet delta oxygen, high energy photons, and  $\text{NO}_x$  are important. A possible correlation between oxygen composition and nitrogen composition based on the availability of oxygen either in the feed gas or ambient was proposed. Depending on ambient conditions, NO and  $\text{NO}_2$  species can either aid in or compete with surface oxidation as they are easily oxidized and removed during the oxidation process. This work has shown that unless ROS are created in the discharge,  $\text{NO}_3$  is a key species in surface modifications. Overall oxidation of PS takes place easily for many conditions, whereas formation of a nitrogen is difficult and requires very specific interaction conditions. A possible mechanism for  $\text{NO}_x$ -based surface oxidation is shown, but complementary simulations are required to confirm this. This study is particularly relevant to treatment of sensitive devices or in specialized applications in plasma medicine since treatments where the plasma plume or afterglow directly contact the sample can result in surface damage.

### **Acknowledgements**

The authors gratefully acknowledge the financial support of this work by the US Department of Energy (DE-SC0005105 and DE-SC0001939) and National Science Foundation (PHY-1004256 and PHY-1415353), and thank Prof. D.B. Graves for collaboration on cold plasma-biomolecule interactions. The authors thank D. Metzler, C. Li, and B. Crump for helpful discussion and contributions to this project.

# **Chapter 5: Biodeactivation of Lipopolysaccharide Correlates with NO<sub>3</sub> Formation after Cold Atmospheric Plasma Treatment**

**E A J Bartis<sup>1,2</sup>, P. Luan<sup>1,2</sup>, A. J. Knoll<sup>1,2</sup>, J Seog<sup>1</sup>, G S Oehrlein<sup>1,2</sup>**

<sup>1</sup> Department of Materials Science and Engineering, University of Maryland, College Park, MD  
20742, USA

<sup>2</sup> Institute for Research in Electronics and Applied Physics, University of Maryland, College  
Park, MD 20742, USA

**D B Graves**

Department of Chemical and Biomolecular Engineering, University of California, Berkeley,  
94720, USA

**Plasma Processes and Polymers, submitted**

## Abstract

Cold atmospheric plasma (CAP) treatment of biological surfaces results in a variety of important changes of biological functions, but little knowledge on specific atomistic surface-chemical changes is available. We present measurements of surface-bound  $\text{NO}_3$  formation for polymer and biomolecular films of different molecular structure and chemical composition following exposure to CAP. Studying before and after treatments showed that this moiety can result from  $\text{NO}_x$  produced in the gas phase as films containing neither oxygen nor nitrogen, e.g. polystyrene, show  $\text{NO}_3$  formation. Furthermore, we confirmed the same effect after treatment by two very different sources, an atmospheric pressure plasma jet operating with an Ar carrier gas and a surface microdischarge operating with  $\text{N}_2/\text{O}_2$  mixtures. Thus,  $\text{NO}_3$  formation is a generic chemical modification of materials by CAP sources. The surface microdischarge was used to deactivate lipopolysaccharide (LPS), an immune-stimulating biomolecule found in Gram negative bacteria such as *E. coli*. We find that LPS biodeactivation is highest for low  $\text{N}_2$  concentrations in  $\text{O}_2$ . The observed biodeactivation varies roughly linearly with surface  $\text{NO}_3$  signal intensity, which is consistent with a Langmuir adsorption model of biodeactivation. A fixed number of binding sites for antibody attachment to LPS exist, and the CAP treatment modifies a fraction of these sites, inhibiting binding and causing biodeactivation. In contrast, LPS biodeactivation does not correlate as well with other oxidized components.

## 5.1. Introduction

Cold atmospheric plasma (CAP) sources are used in a variety of applications ranging from thin film deposition<sup>[36, 161, 162]</sup> to treatment of biological tissue for disinfection<sup>[26, 140, 163, 164]</sup> or cancer treatment.<sup>[9, 24, 165, 166]</sup> CAP produces reactive species including atomic O,<sup>[119]</sup> NO<sub>x</sub>,<sup>[123, 167, 168]</sup> singlet delta oxygen,<sup>[96]</sup> and O<sub>3</sub>,<sup>[95, 121]</sup> to name just a few. Many different sources exist in the literature, each creating different concentrations of plasma-generated species. Similarly, small changes in operating conditions such as gas chemistry and applied power can have major impacts on the reactive species concentrations. For example, Pavlovich et al. distinguished a low power ozone mode and a high power NO<sub>x</sub> mode in a surface microdischarge (SMD) separated by an unstable, transition region.<sup>[168]</sup> Gas-phase CAP-generated reactive species have been characterized and modeled for many different sources.<sup>[124, 169]</sup> The reaction pathways for the formation of these species in the gas phase are generally well understood, but an atomistic understanding of how these species interact with surfaces is lacking. For example, O atoms and OH radicals have been measured in the gas phase but their lifetimes are very short (typically not more than microseconds) due to their high reactivity. For treatments under mild conditions where the visible plasma does not directly touch the surface, these species are unlikely to be responsible for surface chemical modification. Thus, other reactive gaseous species, photons, and so forth must be at work. Reactive oxygen and nitrogen species (RONS) have attracted a great deal of attention for applications in plasma medicine.<sup>[29, 170]</sup>

In the first part of this study, we show by X-ray photoelectron spectroscopy (XPS) that surface-bound NO<sub>3</sub> forms on a variety of different polymers and biomolecules using two different CAP sources, a rare gas/trace O<sub>2</sub> atmospheric pressure plasma jet (APPJ) and an O<sub>2</sub>/N<sub>2</sub>-based SMD. We subsequently evaluate the ability of the SMD-generated reactive species to

deactivate a pernicious biomolecule, lipopolysaccharide (LPS), as measured by an enzyme linked immunosorbent assay (ELISA). Lastly, we evaluate a possible correlation between the biodeactivation and surface modifications, which may be suggestive of a Langmuir adsorption model. NO<sub>x</sub> species have well-established roles in many physiological systems including the mammalian immune and cardiovascular systems.<sup>[29, 171]</sup>

## 5.2. Materials and Methods

Biomolecular and polymeric films were treated by CAP. As a model biomolecule, LPS from *E. coli* O111:B4 (Sigma-Aldrich) was chosen. This pyrogenic biomolecule is a major component of the outer membrane of Gram-negative bacteria. Its presence in sterile tissue can lead to generalized sepsis syndrome resulting in fever, hypotension, multiple organ failure, and even death.<sup>[46]</sup> LPS' ability to activate the innate immune system is directly related to its structure.<sup>[39]</sup> LPS films were prepared as described previously.<sup>[139, 140]</sup> To simplify the complex molecular structure of LPS to specific functional groups, model polymers were studied. This also allows one to distinguish nitrogen and oxygen species created by the CAP treatment from those originating in the film. Polystyrene (PS) and poly(methyl methacrylate) (PMMA) were purchased from Sigma Aldrich and spin-coated at 2000 RPM onto pirhana-cleaned Si substrates from a 1% solution in toluene (PS only) or propylene glycol monomethyl ether acetate (PMMA only).<sup>[64]</sup> Polypropylene (PP) films were purchased from Goodfellow Corporation and cut into 25 mm x 25 mm substrates before treatment.

All CAP treatments were performed in a vacuum chamber that is interfaced to XPS, which enables rapid sample transfer under vacuum and avoids contamination or surface oxidation that would occur if the sample were transferred through air (e.g. exposure to moisture).

The APPJ is similar to a previously reported design and will be overviewed here.<sup>[127, 140]</sup> Two electrodes (length = 2 cm) are wrapped around an alumina tube (ID = 4 mm, OD = 6.35 mm) and separated by a 1.6 cm Teflon block. In this work, 2 standard liters per minute of Ar with 1% O<sub>2</sub> admixture is flowed through the tube into an air environment. The APPJ treatment was performed at 14 kV<sub>pp</sub> at 24 kHz with a gap of 9 cm between the downstream, grounded electrode and the tube nozzle. An additional 3 cm separates the nozzle from the sample. The APPJ operates in an air environment. The SMD is similar to one reported in the literature.<sup>[169, 172-175]</sup> A 1 mm-thick quartz sheet (8.9 cm x 8.9 cm) separates a copper electrode (5 cm x 5 cm) from a grounded mesh (#12, opening size ~ 1.8 mm, 8.9 cm x 8.9 cm). When a 6 kV<sub>pp</sub> high voltage driven at 41.5 kHz is connected to the copper electrode, a discharge forms around the mesh. The mesh-sample gap was 3 mm for all XPS experiments. For ELISA, the mesh was 3 mm from the top of the well plate. An individual well is 11.3 mm deep, so the mesh was 14.3 mm from the bottom of the well. To vary the gas composition of the SMD, the vacuum chamber was evacuated and refilled with N<sub>2</sub>/O<sub>2</sub> mixtures. All treatments were performed for 7 min. For both of these sources, the visible glow does not touch the surface.

XPS was performed by a Vacuum Generators ESCALAB MK II surface analysis system. C1s, N1s, and O1s narrow scan spectra were measured at 20 eV pass energy at an electron take-off angle of 20° (shallow probing depth) and 90° (deep probing depth) with respect to the sample surface. Unless otherwise noted, data in this article is from the 20° take-off angle. The fitting procedure and estimation of atomic composition have been described previously.<sup>[139, 140]</sup> N1s spectra were fit with three peaks corresponding to N-C, [N-R<sub>4</sub>]<sup>+</sup>, and NO<sub>3</sub> at 400.1 eV, 402 eV, and 408 eV, respectively. O1s spectra were fit with peaks corresponding to C=O, C-O, O-C-O, O-C=O, O-NO<sub>2</sub>, and O-NO<sub>2</sub> at 532.1 eV, 532.6 eV, 533.1 eV, and 533.6 eV, 533.9 eV, and

534.7 eV, respectively.<sup>[52]</sup> As has been previously reported,<sup>[145]</sup> we observed that NO<sub>3</sub> peaks decay during X-ray exposure. Thus, the N1s spectrum was measured first in all experiments. Average film composition values (two samples per condition) with error taken as the mean absolute deviation are reported.

ELISA was used to estimate the biological activity of LPS after SMD treatment. The ELISA is based on a protocol provided by the primary antibody manufacturer and will be overviewed here. Various concentrations of LPS in DOCA buffer (formulation: 2.28 g monobasic sodium phosphate, 11.5 g dibasic sodium phosphate, 0.163 g NaCl, and 0.882 g deoxycholic acid brought to one liter with distilled/deionized water) were incubated in duplicate overnight in a 96-well plate (Nunc Maxisorp, EBioscience) to form a standard curve and the to-be-treated wells. The plates were then washed three times with phosphate buffered saline containing 0.0375% Tween-20 (PBS-T) and dried under vacuum for 30 minutes at a pressure of  $2 \times 10^{-3}$  Pa. A plasma treatment was then performed on the dried wells. After plasma treatment, blocking solution of 1% bovine serum albumin (BSA) in PBS-T (BSA-PBS-T) was added for 30 min. The primary antibody (purified endotoxin monoclonal antibody, mouse host, clone 15303, QED Bioscience) was dissolved in BSA-PBS-T and incubated for 30 min on a rocking platform. After another washing with BSA-PBS-T, an enzyme-labeled secondary antibody in BSA-PBS-T was added and incubated for 30 min on a rocking platform. The enzyme, horseradish peroxidase, is light sensitive, so the wells were covered during this step. The wells were washed again and then incubated with substrate solution (1-Step Slow TMB, ThermoFisher) for 15 minutes in the dark. Reactions were stopped by addition of 2 M sulfuric acid and the optical density at 450 nm was measured within 10 min by an automatic microplate reader (Synergy HT Multi-Mode, BioTek). In ELISA, the concentration of LPS is directly proportional to the concentration of the

enzyme-labeled antibody, which is only present if the primary antibody can bind to LPS. The thorough washing between each incubation step ensures that excess biomolecules or biomolecules that are weakly bound are removed. To analyze the results, the optical density for the negative control (0  $\mu\text{g/ml}$  of antigen) was subtracted from all the wells. Treated wells were then compared to untreated wells from the standard curve of the same pretreatment concentration. The biological activity is defined as a ratio of the absorbance of the treated well to the absorbance of the untreated well in the standard curve of the same initial concentration. We consider this the normalized biological activity (BA):

$$BA = \frac{A_p}{A_0} \quad (5.1)$$

where  $A_p$  is the absorbance of the plasma treated well and  $A_0$  is the absorbance of the untreated well. The normalized biodeactivation (BDA) is unity minus this value:

$$BDA = 1 - BA \quad (5.2)$$

Thus, a normalized biodeactivation of unity would correspond to complete biodeactivation and zero would correspond to zero biodeactivation. To ensure a proper comparison between the LPS film in the well and the LPS film on the Si, the well plate surface was measured by XPS after the plasma treatment by the SMD. This LPS film was prepared in the same manner as for ELISA but in a 6-well plate (culture treated polystyrene, BD Bioscience) so that it was compatible with XPS measurements. To compensate for the larger volume of the well, 650  $\mu\text{l}$  of LPS in DOCA were incubated. An individual well was removed from the plate after films were washed and dried using a chisel. As will be discussed in detail below, a key result of the plasma treatment is the formation of surface-bound  $\text{NO}_3$ . We find that this species forms on LPS films deposited both in the well and on the Si, as shown in Figure 5.1. Based on this information, it is assumed that the



film in the well is comparable to the film on the Si surface even though they are prepared differently. In the rest of this work, XPS analysis is based on LPS films spin coated onto Si.

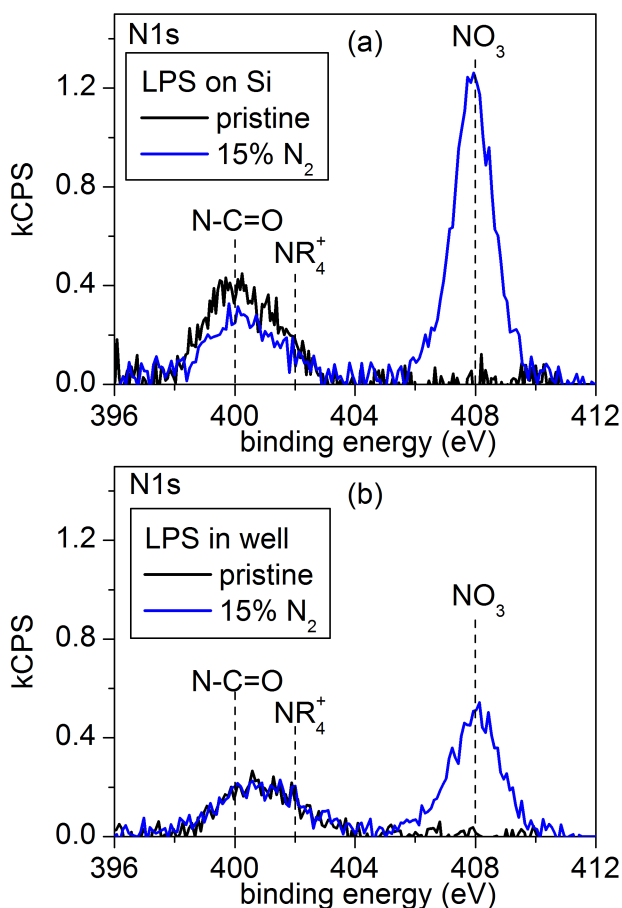


**Figure 5.1.** N1s spectra of pristine LPS and LPS after SMD treatment (a) on Si and (b) in the well. NO<sub>3</sub> forms on both surfaces.

Angle-resolved spectra were collected to determine how NO<sub>3</sub> is distributed in the film. The N1s spectrum is shown in Figure 5.2 and compares measurements made at a shallow probing depth (~ 2 nm into the film) and a deep probing depth (~ 8 nm into the film). The signal intensity is much larger at the shallow probing depth, indicating that NO<sub>3</sub> formation only occurs at the near surface. Previous work using angle-resolved XPS showed that lipid A self-organizes at the air-film interface during LPS film preparation.<sup>[139]</sup> Considering that the film in the well and

the film on Si show similar effects, lipid A is present at the surface, and  $\text{NO}_3$  forms at the near surface, modifications to lipid A can explain the biodeactivation data discussed below. Biodeactivation as a surface modification process was also observed by Chung et al. The authors concluded that biodeactivation occurred at the film surface by using the human whole blood test since lipid A was not readily soluble in human whole blood and because radicals only modified the film surface, as confirmed by Fourier transform infrared (FTIR) spectroscopy and time of flight secondary ion mass spectroscopy (ToF-SIMS).<sup>[1]</sup>

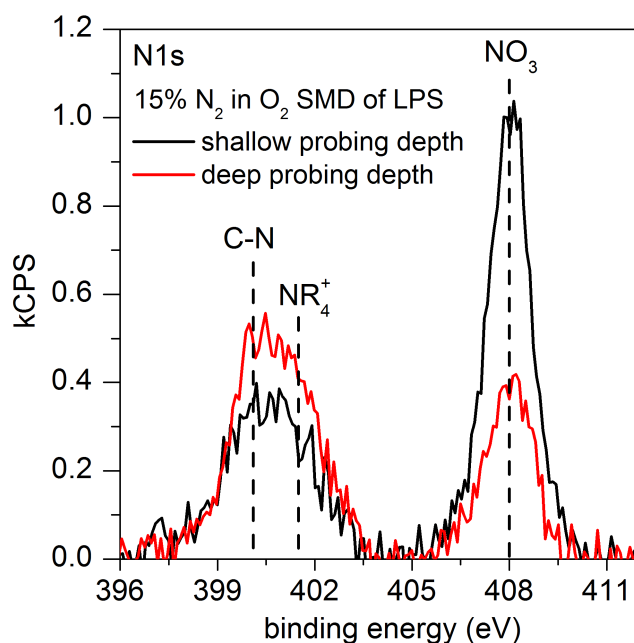


**Figure 5.2.** Angle-resolved XPS N1s spectrum of LPS after treatment by 15%  $\text{N}_2$  in  $\text{O}_2$  SMD. More  $\text{NO}_3$  is found at the surface than in the bulk. Treatment conditions: 7 min, 6  $\text{kV}_{\text{pp}}$ , 41.5 kHz, 3 mm mesh-sample gap.

### 5.3. Results and Discussion

Figure 5.3 shows C1s, N1s, and O1s spectra before and after 1%  $\text{O}_2$  in Ar treatments for LPS, PMMA, PP, and PS (materials are noted on the right of the figure). In the C1s, the largest

modifications are observed for LPS and PS, where C-C/H or C=C/H (for LPS and PS, respectively) decrease and high binding energy groups such as C=O and O-C=O appear. PP shows a slight decrease in C-C/H bonding and PMMA shows negligible differences. Before treatment, only LPS has nitrogen in its molecular structure, which is reflected in the peaks in the N1s at 400.1 eV and 402 eV. Only LPS and PMMA have oxygen in the molecular structure, as seen in the O1s. LPS shows a peak mainly resulting from C-O bonding in the biomolecules carbohydrate groups while PMMA shows a double peak due to the ester group. As previously reported, LPS shows NO<sub>3</sub> after plasma treatment, but it was unclear whether this nitrogen and oxygen originated from gas phase species or from oxygen and nitrogen naturally found in LPS.<sup>[140]</sup> After APPJ treatment, PS, PMMA, and PP all show low concentrations of NO<sub>3</sub> on the surface. While NO<sub>3</sub> formation is generic to all these materials, the overall oxygen uptake is not. LPS and PS show major oxygen uptake resulting from a variety of carbon-oxygen moieties, but also from the NO<sub>3</sub>, as shown in the high binding energy shoulder. PMMA and PP show very little oxygen uptake. Based on NO<sub>3</sub> formation occurring in a variety of materials, we conclude that this behavior is generic, at least to polymers. A more in-depth study is in preparation regarding the surface modifications induced by CAP sources under a variety of conditions.

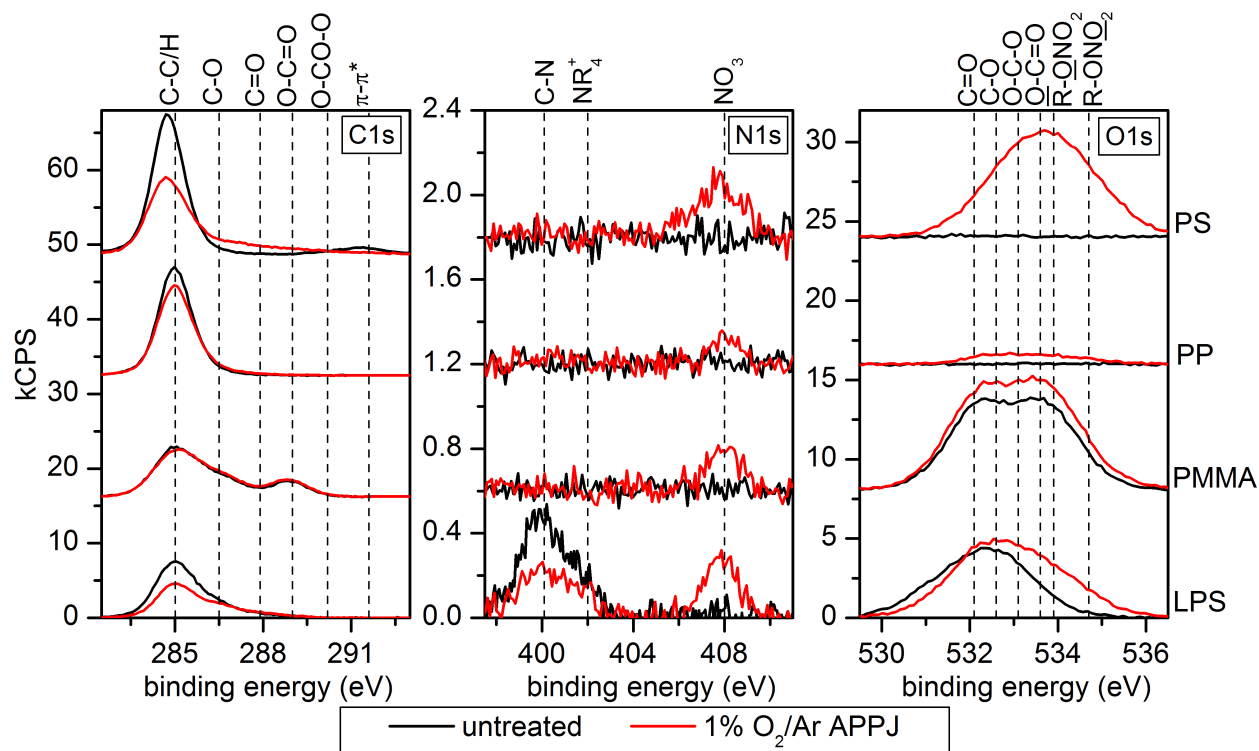


**Figure 5.3.** XPS C1s, N1s, O1s spectra taken before and after APPJ treatment of LPS, PMMA, PP, and PS.  $\text{NO}_3$  forms on all the materials, but the accompanying oxygen uptake is material dependent. Treatment conditions: 7 min, 1%  $\text{O}_2$  in Ar, 14  $\text{kV}_{\text{pp}}$ , 24 kHz, 9 cm source-to-nozzle gap, 3 cm nozzle-sample gap.

The SMD device was subsequently used to determine whether  $\text{NO}_3$  formation was unique to the APPJ and to explore the role of gas composition. Representative C1s, N1s, and O1s spectra of SMD-treated (15%  $\text{N}_2$  in  $\text{O}_2$ ) and untreated LPS are shown in Figure 5.4. After treatment, there is a clear drop in C-C/H bonding and an increase in peaks associated with C- $\text{ONO}_2$ , O-C-O/C=O/N-C=O, and O-C=O. In the N1s, a strong  $\text{NO}_3$  peak is measured. The O1s shows a major increase in oxygen, with a double peak forming due to increased C-O/C=O at lower binding energies and new peaks at higher binding energy due to  $\text{NO}_3$ . While both the APPJ and SMD introduce  $\text{NO}_3$  on the LPS surface, the  $\text{NO}_3$  composition is much higher after

SMD treatment than after APPJ treatment. This difference likely results from a combination of the higher  $N_2/O_2$  density for the SMD as well as the fact that the mesh is much closer to the sample compared the APPJ ground electrode. Despite the major differences between the two sources, both sources produce reactive species that directly interact with the sample, resulting in  $NO_3$ .

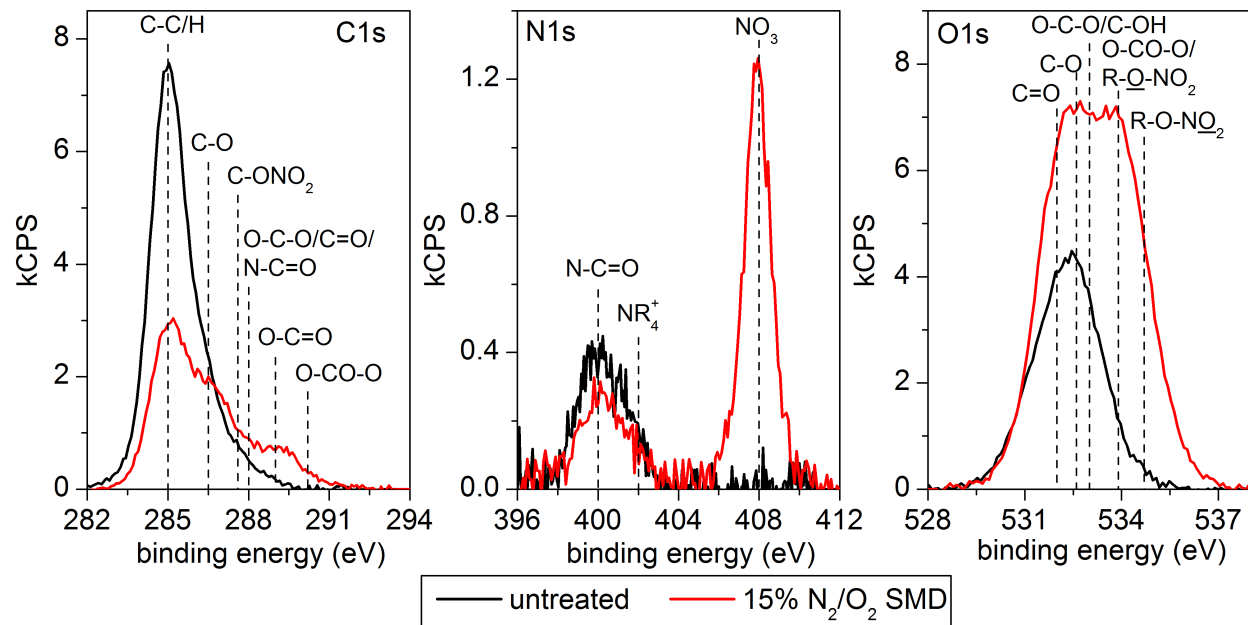


**Figure 5.4.** XPS spectra of LPS before and after treatment by the SMD. Treatment conditions: 15%  $N_2$  in  $O_2$ , 7 min, 6 kV<sub>pp</sub>, 41.5 kHz, 3 mm mesh-sample gap.

Figure 5.5 shows the  $NO_3$  and O composition of LPS films as a function of the  $N_2$  fraction in the  $O_2$  ambient. The total oxygen composition (closed circles) increases from 42.6% to a maximum of 44.6% when the  $N_2$  gas composition is increased from 0 to 10%. For higher  $N_2$  admixtures, the oxygen uptake on the surface drops. At the highest  $N_2$  gas composition, 50%, the oxygen composition was 23.6%, which is only slightly higher than the measured oxygen composition of pristine LPS at ~19.6%. The  $NO_3$  composition increases from 1.9% to 5.3% when the  $N_2$  admixture is increased from 0% to 20%. Similarly to the O composition, the  $NO_3$

composition decreases when additional  $N_2$  is added. If the  $NO_3$  contribution to the O composition is subtracted out (open circles), which is indicative of “pure” oxidation, then we see that increasing  $N_2$  gas compositions decrease this kind of oxidation.

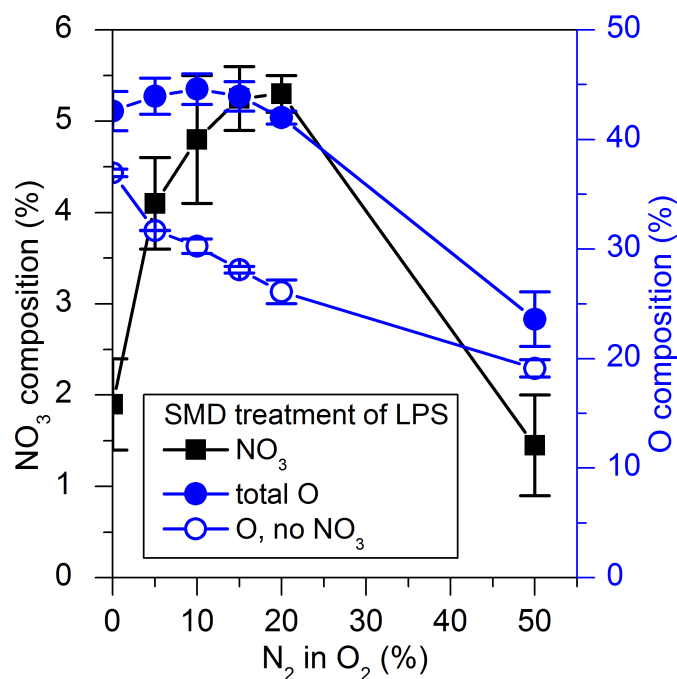


**Figure 5.5.**  $NO_3$  and O composition derived from XPS analysis of SMD-treated LPS for various  $N_2/O_2$  gas chemistries. For the open circles, the  $NO_3$  contribution to the O composition has been subtracted out. Treatment conditions: 7 min, 6 kV<sub>pp</sub>, 41.5 kHz, 3 mm mesh-sample gap.

ELISA was used to determine the impact of the SMD gas chemistry and role of surface-bound  $NO_3$  on the biological activity of LPS. Figure 5.6 shows the normalized biodeactivation as a function of the SMD ambient gas chemistry. When the SMD operates with just  $O_2$ , biodeactivation is 0.61. As  $N_2$  is added to the  $O_2$  ambient, biodeactivation increases. When the  $N_2$  admixture is 5%, biodeactivation increases up to 0.75. Biodeactivation reaches a maximum of 0.81 when the  $N_2$  admixture is 15%. Further increasing the  $N_2/O_2$  ratio reduces biodeactivation. At the highest  $N_2$  admixture, 50%, biodeactivation drops to 0.30. Superimposed on Figure 5.6(a)

and 5.6(b) are the  $\text{NO}_3$  composition and O compositions shown in Figure 5.5. The biodeactivation trend much more closely matches with the  $\text{NO}_3$  composition rather than the O composition if the O bound to  $\text{NO}_3$  (open triangles) is removed.

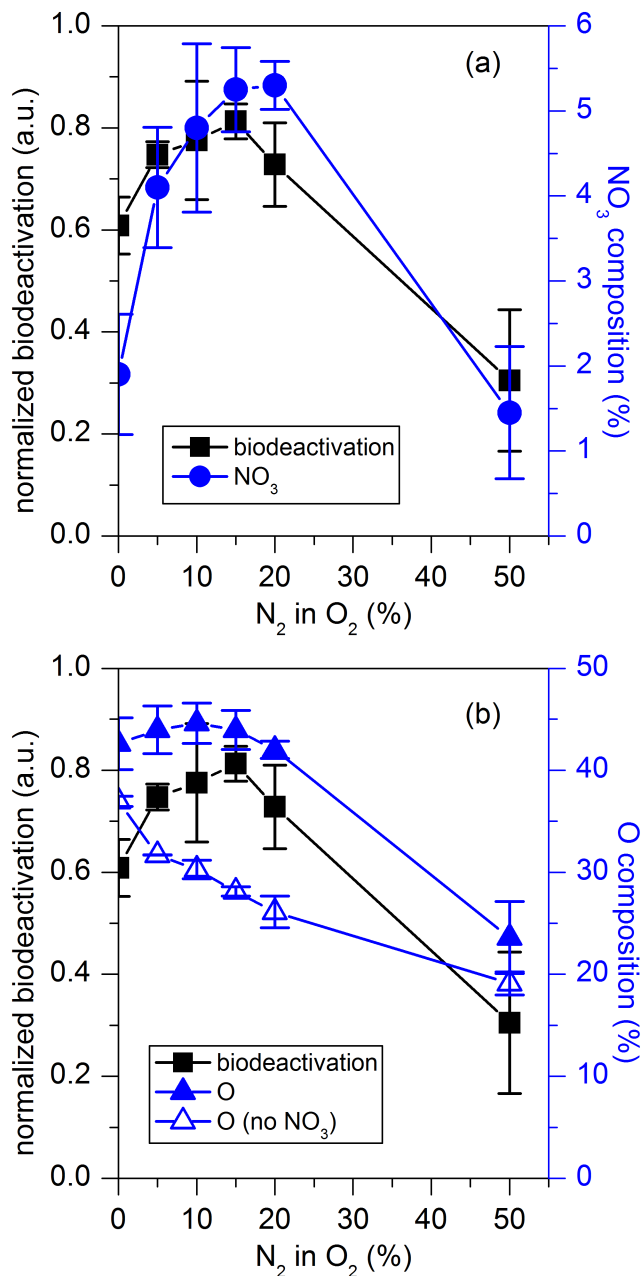


**Figure 5.6.** Normalized LPS biodeactivation vs.  $\text{N}_2/\text{O}_2$  ratio as measured by ELISA compared with (a)  $\text{NO}_3$  composition and (b) O composition with and without  $\text{NO}_3$  considered. Treatment conditions: 6 kV<sub>pp</sub>, 41.5 kHz, 7 min.

Figure 5.7 demonstrates this effect by showing how the biodeactivation changes with  $\text{NO}_3$  and O (without  $\text{NO}_3$  contributions) compositions. A key message from this figure is that the highest biodeactivation occurs when  $\text{NO}_3$  is highest (Figure 5.7(a)), not oxidation by other species. In fact, only intermediate oxidation is measured for the highest biodeactivation condition (Figure 5.7(b)). Similarly, biodeactivation vs.  $\text{NO}_3$  composition forms a loop, which demonstrates its importance.



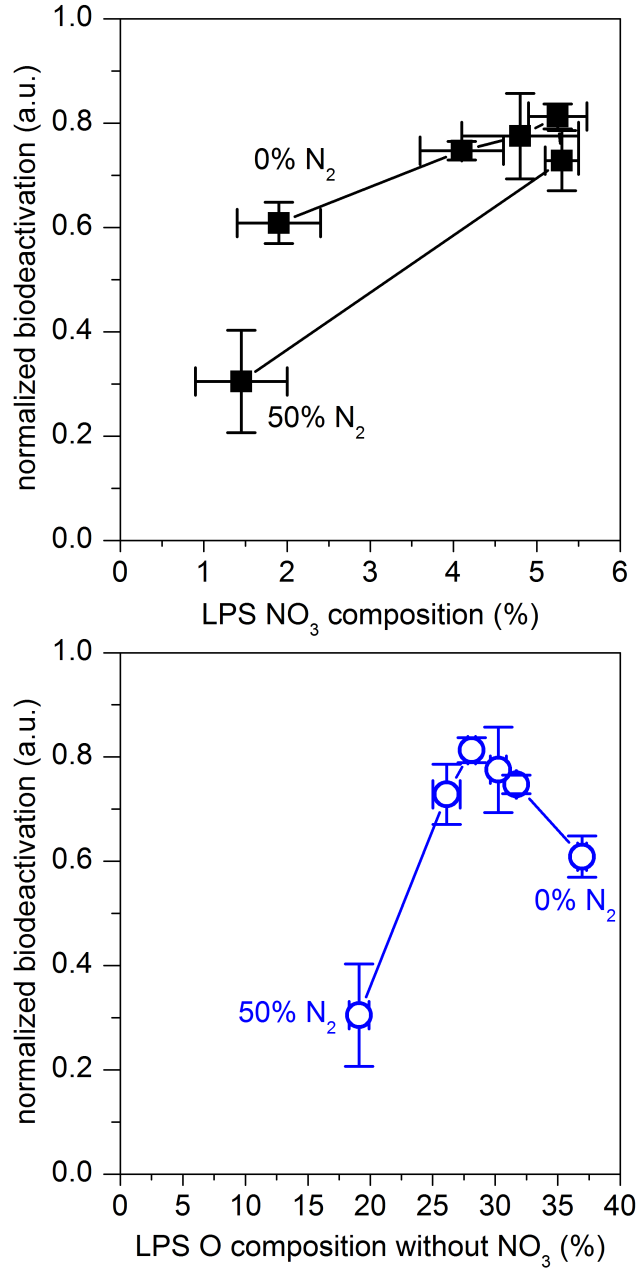


**Figure 5.7.** Normalized LPS biodeactivation vs (a) NO<sub>3</sub> and (b) O (without NO<sub>3</sub>) composition of SMD-treated LPS films.

A possible explanation of the dependence of observed LPS biodeactivation on NO<sub>3</sub> signal intensity is a Langmuir adsorption model. We assume that the LPS film surface has a fixed number of binding sites  $n$  (cm<sup>-2</sup>) on which antibodies can adsorb with equal probabilities, and

that Langmuir's model of adsorption can describe this, consistent with lipid A placement on surface. A Langmuir adsorption model has been used previously in a related application where plasma polymerized films were deposited on stainless steel surfaces to prevent adsorption of *Enterobacter sakazakii*.<sup>[176]</sup> This model has also been used to evaluate adsorption of metal ions after introduction of acidic groups onto an adsorbent by dielectric barrier discharge treatment.<sup>[177]</sup> The number of sites with antibodies is assumed to be at most equal to  $n$ , i.e. the coverage of antibodies is limited to a single monolayer. The ELISA method follows this model as the untreated standard curve shows absorbance saturation at high LPS concentrations.<sup>[139]</sup>

During plasma treatment some of the sites  $n$  are modified, and adsorption of antibodies is no longer possible. The fractional surface coverage  $\theta$  for which adsorption of antibodies is no longer possible is defined as the ratio of modified sites  $n_m$  to the total number of sites  $n$ .

$$\theta = \frac{n_m}{n} \quad (5.3)$$

Without plasma treatment,  $\theta$  is assumed to be zero. As the plasma treatment takes place, some of the adsorption sites are chemically modified by NO<sub>3</sub> chemisorption and the saturation coverage of antibodies will decrease, as shown schematically in Figure 5.8. The authors emphasize that this is a highly simplified schematic; for example, the primary antibody may not need to stand up. This corresponds to biodeactivation (*BDA*). In the simplest case, *BDA* can be written as

$$BDA = BDA_0\theta \quad (5.4)$$

with  $BDA_0$  the value measured for no plasma treatment. By comparing the measured *BDA* with the intensity of surface-bound NO<sub>3</sub> we find that the intensity of NO<sub>3</sub> modified LPS corresponds qualitatively to a Langmuir adsorption model of *BDA*. On the other hand, the behavior of *BDA* versus other oxidized LPS components (not involving NO<sub>3</sub>, such as C-O, C=O, etc) is not qualitatively consistent with a Langmuir adsorption model. Additionally, *BDA* is strongly

reduced in this case for conditions when the amount of oxidized LPS components is still significant.

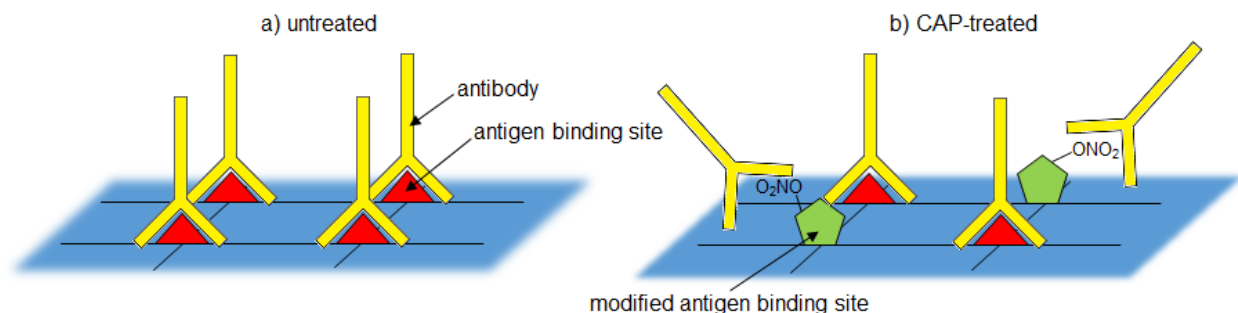


**Figure 5.8.** A Langmuir model of adsorption for LPS biodeactivation following CAP treatment demonstrating the modification of LPS (the antigen) binding sites inhibiting antibody binding.

As previously mentioned, the structure of LPS, and biomolecules in general, govern the interactions occurring on a molecular level. Intermolecular interactions involving proteins, nucleic acids, antigens, and antibodies are specific and include hydrogen bonding, electrostatic interactions, hydrophobic interactions, and geometric complementarity. The formation of nitrate on surfaces either as alkyl nitrate, or peroxyacyl nitrates would disrupt the above-mentioned specific interactions. Yusupov et al. have modeled the interaction of reactive oxygen species such as O atoms and OH radicals with biomolecules.<sup>[178, 179]</sup> They report cleavage of glycosidic bonds and desorption of aliphatic chains in lipid A, the toxic component of LPS. If similar destructive processes occur during NO<sub>3</sub> incorporation, this could account for the enhanced biodeactivation. In addition to enhancing biodeactivation, surface-bound NO<sub>3</sub> has medical applications. For example, R-ONO<sub>2</sub>, in the form of glyceryl trinitrate, is used to treat angina and heart failure.<sup>[29]</sup> This treatment is based on NO<sub>3</sub> acting as a reservoir for NO. The physiological mechanism of action is widely disputed and is thought to rely on enzymes. Nevertheless, it is

possible that modifications to CAP-treated LPS continue even after the plasma treatment ends when NO is released at the film surface.

The sensitivity of surface processes with regard to the N<sub>2</sub> fraction in N<sub>2</sub>/O<sub>2</sub> containing gas mixtures in low temperature plasma may indicate a possible role of NO formation, e.g. similar to that seen in the work by Kastenmeier et al.<sup>[180]</sup> They found that adding up to 10% N<sub>2</sub> to a CF<sub>4</sub>/O<sub>2</sub> low pressure plasma enhanced the etch rate of Si<sub>3</sub>N<sub>4</sub> by a factor of 7. If the N<sub>2</sub> admixture was increased above 10%, the etch rate dropped again. Using mass spectrometry, they observed that the NO concentration in the reaction chamber closely correlated with the etch rate. The decreased etch rate at higher N<sub>2</sub> concentrations results from NO being lost by reaction with gas phase atomic N:



At the high O<sub>2</sub> concentrations used in this work, we expect the resulting O atom to rapidly form O<sub>3</sub> by:



where M is any species that stabilizes the formation of the O<sub>3</sub> molecule.<sup>[181]</sup> We believe that a similar mechanism occurs with the SMD. Sakiyama et al. modeled the plasma chemistry of a surface microdischarge.<sup>[169]</sup> They find that long lived NO<sub>x</sub> species such as NO<sub>2</sub> and NO<sub>3</sub> build up in the afterglow with densities higher by a factor of 100 during 1000 s of SMD operation. Shorter lived species such as NO are converted to more stable species in less than ~100 s. Consistent results showing a strong time dependence for NO<sub>x</sub> densities were experimentally obtained by Pavlovich et al.<sup>[168]</sup>

The nitrate radical has been widely studied in atmospheric science. It is one of the most important oxidizing gases in the atmosphere due to its ability to degrade volatile organic

compounds and facilitate the formation of HO<sub>x</sub> ( $x = 1, 2$ ). The nitrate radical has been modeled in CAP sources, but, to the best of our knowledge, it has not been measured in the effluent of CAP devices.<sup>[124, 169]</sup> However, related species such as NO<sub>2</sub><sup>[123]</sup> and HNO<sub>3</sub><sup>[121]</sup> have been measured. The importance of NO<sub>3</sub> and NO in surface processes has been observed in atmospheric science<sup>[153]</sup> and lipid peroxidation<sup>[182]</sup> and seems to be consistent with our work. However, we do not yet have a complete understanding between existing mechanisms and our observations, which is a subject of future study.

The role of NO<sub>x</sub> and O<sub>3</sub> has been studied for similar SMDs operated in air or pure O<sub>2</sub>. Pavlovich et al. found that bacterial inactivation was much higher in the NO<sub>x</sub> mode than in the O<sub>3</sub> mode for their air SMD. For their study, they additionally concluded ‘that disinfection under these conditions is not purely diffusion-controlled, and reactions between gaseous RONS and bacteria might be the kinetically limiting step.’<sup>[168]</sup> Inactivation by O<sub>3</sub> has also been studied and was reported to be much more effective under wet conditions.<sup>[183]</sup> Mahfoud et al. exposed polystyrene petri dishes to 4000 ppm O<sub>3</sub> for 60 minutes and observed major oxidation of the surface. NO<sub>3</sub> was not reported on the surfaces, though the operating conditions and treatment time were quite different.<sup>[183]</sup> NO<sub>2</sub> has also been reported to play a key role in bacterial disinfection.<sup>[184]</sup> Based on the surface analysis shown in this article, surface-bound NO<sub>3</sub> is likely important for the underlying mechanism of bactericidal effects.

In this work, we distinguished NO<sub>3</sub>-related oxidation from oxidation not involving NO<sub>3</sub> i.e. the O composition that is independent of the O atoms found in NO<sub>3</sub> (open symbols in Figs. 5.5, 5.6, and 5.7). This can occur via a number of reaction pathways that open up after H abstraction from the film occurs. Due to the high density of O<sub>2</sub> in the processing chamber, formation of peroxy radicals and hydroperoxide is likely. These surface species are not stable

and will result in alcohols, aldehydes, and ketones.<sup>[147]</sup> O<sub>3</sub> is produced by the APPJ<sup>[140]</sup> and SMD<sup>[174]</sup> and can react with alkyl radicals to form alkoxy radicals, which can also result in oxygenated species.<sup>[147]</sup> LPS C1s spectra show a peak appearing at 289 eV, indicating that ester groups are formed as well. The introduction of these groups does change the surface of the biomolecule, but the biodeactivation does not correlate with these changes as strongly as it does with NO<sub>3</sub>. One possibility is that these groups are naturally found in biological systems, whereas R-ONO<sub>2</sub> is not. As previously mentioned, antibody binding is very specific, but the degree of specificity can differ. For example, changing an R-OH group on the LPS disaccharide backbone to an aldehyde may not impact e.g. geometric complementarity or H-bonding. However, changing an R-OH group to R-ONO<sub>2</sub> would introduce a bulkier, charged group.

#### **5.4. Conclusions**

We report the presence of NO<sub>3</sub> on plasma-treated biomolecular and polymeric surfaces. The modified films indicate that the precursors for this moiety originate in the gas phase. In addition to being generic to different surfaces, this species also forms after treatment by two very different CAP sources. For the surface microdischarge, low N<sub>2</sub> admixtures to the O<sub>2</sub> ambient gas resulted in higher NO<sub>3</sub> content on the surface of biomolecular films. However, oxidation independent of NO<sub>3</sub> decreased with N<sub>2</sub> admixtures. The observed LPS biodeactivation varied roughly linearly with surface NO<sub>3</sub> signal intensity, consistent with a Langmuir adsorption model of biodeactivation where surface-bound NO<sub>3</sub> disrupts antibody-LPS binding by modifying the LPS binding site. The role of NO and NO<sub>3</sub> in surface modifications has been addressed in other work at low pressures or in atmospheric science and seems to be consistent with our observations. While the specific mechanism by which NO<sub>x</sub> species may cause and/or assist in

biodeactivation and surface modifications for O<sub>2</sub>/N<sub>2</sub> mixtures compared to pure O<sub>2</sub> remains unclear at this time, the present surface chemical observations provide compelling evidence that NO<sub>x</sub> are important for a variety of surface processes when CAP sources interact with polymer surfaces and/or biomolecules. A detailed study is in progress as an atomistic understanding of CAP-induced surface modifications is required for advancing surface functionalizations for polymers, plasma medicine, and other applications.

Acknowledgements: The authors gratefully acknowledge the thoughtful insights and support of the project by D. Metzler, C. Li, A. Pranda, and C. Hart. This work is supported by the US Department of Energy (DE-SC0005105 and DE-SC0001939) and National Science Foundation (PHY-1004256 and PHY-1415353).

Keywords: ESCA/XPS; plasma jet; sterilization; surface discharges; surface modification

# **Chapter 6: A Comparative Study of Biomolecule and Polymer Surface Modifications by a Surface Microdischarge and Atmospheric Pressure Plasma Jet**

**E. A. J. Bartis<sup>1,2</sup>, P. Luan<sup>1,2</sup>, A. J. Knoll<sup>1,2</sup>, J. Seog<sup>1</sup> and G. S. Oehrlein<sup>1,2</sup>**

<sup>1</sup> Department of Materials Science and Engineering, University of Maryland, College Park, MD 20742, USA

<sup>2</sup> Institute for Research in Electronics and Applied Physics, University of Maryland, College Park, MD 20742, USA

**D. B. Graves**

Department of Chemical and Biomolecular Engineering, University of California, Berkeley, 94720, USA

**Draft of an article to be submitted to Plasma Chemistry and Plasma Processing**



**Abstract:**

Cold atmospheric plasma (CAP) sources are economical and environmentally friendly sources of reactive species with promising industrial and biomedical applications. Many different sources are studied in the literature for advanced applications including surface disinfection, wound healing, and cancer treatment, but the underlying mechanisms for these applications are not well-understood. In this paper, two very different CAP sources are used under mild, remote conditions to study the biological deactivation of two immune-stimulating biomolecules: lipopolysaccharide, found in bacteria such as *Escherichia coli*, and peptidoglycan, found in bacteria such as *Staphylococcus aureus*. The surface chemistry was measured to understand which plasma-generated species and surface modifications are important for biological deactivation. The overall goal of this work is to determine which effects of CAP treatment are generic and which bonds are susceptible to attack. The kHz-powered atmospheric pressure plasma jet (APPJ) used in this study operates with 1% N<sub>2</sub>/O<sub>2</sub> admixtures to an Ar feed gas. The kHz-powered surface microdischarge (SMD) used in this study operates with N<sub>2</sub>/O<sub>2</sub> mixtures where the N<sub>2</sub> fraction is varied from 0 to 0.5. The applied voltage was also varied. These parameters effectively regulate changes in biological activity and the amount of surface-bound NO<sub>3</sub> and overall modification both on biomolecular and polymeric surfaces. NO<sub>3</sub> forms most strongly for low N<sub>2</sub> mixtures (5-20%) in O<sub>2</sub>. Model polymers were also studied to isolate specific moieties. It is shown that NO<sub>3</sub> formation is most favorable on surfaces containing alcohol (R-OH) groups. Furthermore, polymers containing  $\alpha$ -hydrogen side groups were more susceptible to modifications compared to a polymer containing a  $\alpha$ -methyl side group. Overall, the SMD showed much higher surface modifications and surface chemistry tunability compared to the APPJ. Results are compared with recent computational investigations. Our results demonstrate

the importance of long-lived plasma-generated species and advance an atomistic understanding of CAP-surface interactions.

## 6.1. Introduction

Cold atmospheric plasma (CAP) sources are commonly used as economical and environmentally friendly sources of reactive species. These CAP sources have applications in several fields. They can be used for polymer surface modification to create antimicrobial surfaces or to increase, for example, adhesion or biocompatibility.<sup>[185-189]</sup> Biomedical applications such as surface disinfection,<sup>[121, 140, 164, 170, 190-192]</sup> wound healing,<sup>[24, 166, 193]</sup> and cancer treatment<sup>[9, 10, 194-196]</sup> have been shown. The promising role in healthcare has been attributed to plasma-generated reactive oxygen and nitrogen species (RONS), as described in a recent review by Graves.<sup>[29]</sup> There is also interest in environmental applications to degrade harmful pollutants.<sup>[197-200]</sup> A wide variety of sources have been reported with completely different geometries, though sometimes the same name is used. For medical uses, these sources have been reviewed by Isbary et al.<sup>[26]</sup> and include gliding arc, corona, electrospray, plasma jets, and dielectric barrier discharge. The underlying physics and chemistry of these sources has been reviewed by Bruggeman and Brandenburg.<sup>[201]</sup>

In this article, we compare two drastically different sources, a surface microdischarge (SMD) and an atmospheric pressure plasma jet (APPJ). The SMD is gaining increased attention since a key feature is that it operates without noble gas admixture. Several studies have been performed measuring and modeling gas-phase species and antimicrobial activity has been well-demonstrated.<sup>[163, 169, 172, 174, 202]</sup> Furthermore, treated surfaces are electrically isolated from the discharge and high voltage electrode. Some of the antimicrobial work has studied aqueous solutions, where the roles of nitrate ( $\text{NO}_3^-$ ), nitrite ( $\text{NO}_2^-$ ), hydrogen peroxide, peroxyxynitrite ( $\text{ONOO}^-$ ) and hydroxyl radicals are very important, especially under acidic conditions.<sup>[203, 204]</sup> This same level of understanding is lacking for dry conditions and surfaces. In a recent report,

Pavlovich et al. distinguish a low-power “ozone mode” and high-power “NO<sub>x</sub> mode” based on the plasma power density with the former being less effective at bacterial decontamination than the latter.<sup>[121, 168]</sup>

The APPJ has been used to study plasma bullets,<sup>[49]</sup> reactive oxygen species (ROS),<sup>[96]</sup> and surface disinfection,<sup>[100, 140]</sup> among other applications. Both MHz- and kHz-powered sources have been used for surface studies. A large amount of information is available in the literature, and only a sample will be reviewed here. MHz sources are commonly used as they create more homogeneous plasmas that require lower operating voltages to ignite and sustain. Film deposition by atmospheric plasma has been reviewed by Merche et al.<sup>[36]</sup> Nisol et al. used atmospheric plasma to deposit polymer films including poly(ethylene glycol), allyl methacrylate, and acrylic acid.<sup>[107, 205]</sup> The same source was also used to modify polyethylene and polytetrafluoroethylene.<sup>[110, 206, 207]</sup> Ruegner et al. have conducted fundamental studies on the reaction mechanisms occurring during film deposition.<sup>[208, 209]</sup> They describe how O, O<sub>3</sub>, and N impact film properties during the growth of SiO<sub>2</sub>-like films on a rotating substrate using two APPJs. One APPJ is used for the deposition and contains the precursor in He, while the other APPJ, operating with O<sub>2</sub>/N<sub>2</sub>/He, removes carbon, creating the SiO<sub>2</sub>-like film. The surface analysis work is complemented by gas-phase characterization using molecular beam mass spectrometry.<sup>[210]</sup> Plasma-material interactions have also been studied extensively by Fricke et al. using a MHz APPJ in contact with polymer and biofilm surfaces.<sup>[128-131, 142]</sup> In their work, they studied changes in surface chemistry, morphology and impact of cell growth. APPJ etching was correlated with the O atom emission and density.<sup>[128, 129]</sup> Reuter et al. modified this source to introduce a gas curtain around the effluent, which acts as a shielding gas.<sup>[126, 211]</sup> They showed that this gas curtain effectively allows for regulation of reactive species in water. They measured

VUV emission from Ar<sub>2</sub> excimers to show that ambient air (specifically O<sub>2</sub> which absorbs the radiation) diffusion into the effluent is minimized. Kilohertz-powered sources are also used and have the advantage of using inexpensive power supplies without the need for a matching network. Van Deynse et al. have performed in-depth studies on the surface activation and aging of polyethylene surfaces.<sup>[133, 134, 212]</sup> Work in our group demonstrated that the plasma-ambient interaction can be used to regulate the surface modifications of lipopolysaccharide (LPS), a harmful biomolecule, and polystyrene (PS).<sup>[140, 213]</sup> Increasing N<sub>2</sub> concentrations in an N<sub>2</sub>/Ar ambient decreased surface modifications, likely by quenching reactive oxygen species. However, the O<sub>2</sub> ambient reduced modifications even more, which was suggested to originate from absorption of VUV photons. Many studies using kHz power sources use a parallel plate dielectric barrier discharge rather than the jet set up. There is also interest in plasma-activated water by both MHz- and kHz-powered sources.<sup>[121, 203, 204, 214-220]</sup>

Even though the APPJ and SMD are very different (e.g. gas chemistry, volume vs surface discharge), both of these sources are configured in the present work to operate under conditions where the visible glow does not touch the surface. These treatments represent mild, remote conditions where minimal surface damage occurs and reactions with long-lived species dominate. Previous work in our group has shown that treatments under these remote conditions result in surface-bound NO<sub>3</sub>.<sup>[140, 213]</sup> Unpublished work in our group has shown that LPS biodeactivation by CAP correlates better with NO<sub>3</sub> formation than with general surface oxidation. Biodeactivation was associated with a Langmuir adsorption model. In this work, the biological activity of various biomolecules is correlated with surface modifications and gas phase species. In addition, model polymers were treated to evaluate which CAP-surface interactions are generic and which key bonds are susceptible to attack.

This paper is organized as follows. After describing the experimental setup, results are shown in section 6.3. In Sec. 6.3.1 and 6.3.2, surface analysis and biodeactivation of biomolecules and polymers after SMD treatment is shown. In Sec. 6.3.3 and 6.3.4, similar experiments are performed with the APPJ. Finally, in section 6.4, we compare key differences between the SMD and APPJ, discuss polymer modification mechanisms, and compare our results with molecular dynamics simulations.

## 6.2. Materials and Methods

### 6.2.1 Description of Materials

Smooth LPS from *Escherichia coli* O111:B4 (Sigma-Aldrich) was chosen in this study as a model biomolecule and was described previously.<sup>[39, 139]</sup> LPS is found in the outer membrane of Gram-negative bacteria and consists of three distinct regions: the O-antigen, core oligosaccharide, and lipid A. The O-antigen is made up of a long polysaccharide chain that determines the strain of the LPS, the core oligosaccharide links the O-antigen to lipid A and has a similar composition as the O-antigen. Lipid A, also called endotoxin, is the component of LPS that causes an immune response in mammals and can lead to sepsis, multiple organ failure, and even death. It is composed of several aliphatic chains linked to a disaccharide backbone by ester and amide linkages. The backbone also contains two phosphate groups. Peptidoglycan from *Staphylococcus aureus* (cell wall component, Sigma-Aldrich) was also studied and consists of a network of repeating disaccharide backbones that are cross-linked by a peptide chain.<sup>[221]</sup> In Gram positive bacteria, the outermost layer consists of a thick peptidoglycan matrix that provides structural rigidity to the cell wall. LPS and PGN both cause an immune response based on molecular pattern recognition.<sup>[39, 41]</sup> Biomolecules in the blood recognize motifs that are

characteristic of bacteria cells. Thus, there is a strong relationship between the biomolecular structure and its toxicity. In fact, it has been reported that monophosphorylated lipid A with shorter and/or fewer aliphatic chains shows less endotoxicity than the diphosphorylated molecule with six aliphatic chains of 12-14 carbons each.<sup>[39]</sup> A key advantage of studying these biomolecules is that a complex bacteria cell can be simplified to just its surface.

For the enzyme-linked immunosorbent assay (ELISA), rough LPS (*Escherchia coli* J5 (Rc mutant), Sigma-Aldrich) was used instead of the smooth form described above. Rough LPS does not contain the O-chain. A purified Gram negative endotoxin monoclonal antibody (clone 15303, QED Bioscience Inc.) was used to detect LPS and a purified *Staphylococcus aureus* monoclonal antibody (clone 15702, QED Bioscience Inc.) was used to detect PGN. These antibodies were detected by a horseradish peroxidase (HRP) conjugated goat anti-mouse antibody (Goat anti-Mouse IgG (H+L) secondary antibody, HRP conjugate, Thermo Scientific). These antibodies were diluted in 1% bovine serum albumin (BSA, Thermo Scientific) in phosphate buffered saline (PBS) containing 0.04% Tween-20 (BSA-PBS-T). To detect HRP, 3,3',5,5'-tetramethylbenzidine (TMB, 1-Step Slow TMB, Thermo Scientific) was used as a substrate. Biotinylated-LPS (bLPS) was also treated and the ELISA protocol was discussed previously.<sup>[139]</sup>

In addition to the toxic biomolecules, model polymers including polyvinyl alcohol (PVA, molecular weight 89,000 – 98,000, Sigma-Aldrich), polystyrene (PS, average molecular weight ~35,000, Sigma-Aldrich), polypropylene (PP, Goodfellow USA), and poly(methyl methacrylate) (PMMA, average molecular weight ~15,000, Sigma-Aldrich) were studied. These polymers simplify the complex molecular structure of the biomolecules. PS was chosen to study aromatic

rings, PMMA to study ester groups, PP to study aliphatic carbon, and PVA to study alcohol groups. The chemical structure of these polymers is shown in Fig. 6.1.

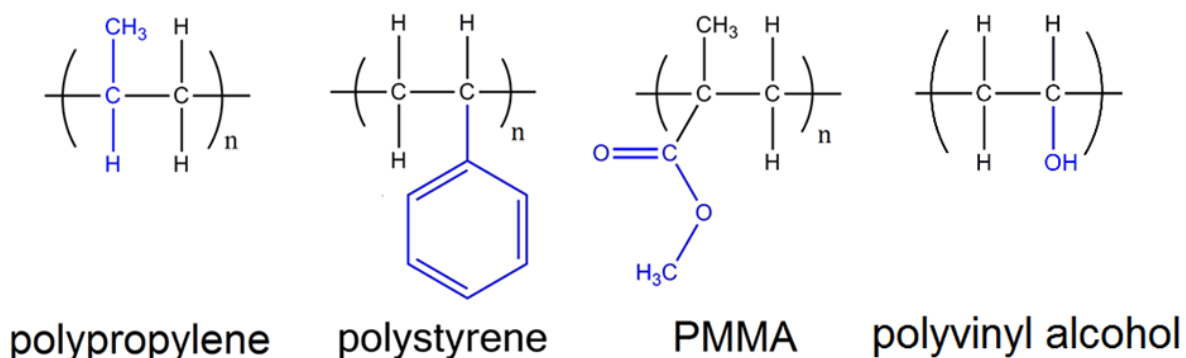


**Figure 6.1:** Chemical structures of the polymers studied in this work. PMMA = poly(methyl methacrylate).

LPS samples for surface analysis were prepared as described previously by dissolving LPS in a 9:1 (vol:vol) methanol:water solution diluted to 500  $\mu\text{g/ml}$  and spin coating at 100 RPM onto Si substrates.<sup>[139, 140]</sup> PGN was dissolved in a 17:2:1 methanol:chloroform:water solution diluted to 500  $\mu\text{g/ml}$  and subsequently spotted onto Si substrates. PS and PMMA films were dissolved in propylene glycol monomethyl ether acetate and spin coated onto Si substrates at 2000 RPM. PP films were used as received and cut into 2.54 cm x 2.54 cm pieces. PVA powder was dissolved in water and brought to 90 °C. A 2% PVA solution was spin coated onto Si substrates by ramping over 10 s to 3000 RPM. Prior to use, all Si substrates were cleaned by piranha solution, copiously rinsed with distilled water, and dried on the spin coater at 4000 RPM for 10 s.<sup>[64]</sup>



### 6.2.2 Cold Atmospheric Plasma (CAP) Treatments

The APPJ used in this study has been described in detail in previous publications, to which we refer the reader.<sup>[127, 140, 213]</sup> Briefly, the APPJ consists of two copper electrodes (20 mm length, ID = 6.4 mm) wrapped around an alumina tube (ID = 4 mm, OD = 6.35 mm) and separated by a 1.6 cm thick Teflon block. Power is supplied at 24 kHz by a variable frequency power supply (PVM500, Information Unlimited, Amherst, NH, USA). Ar gas containing 1% O<sub>2</sub>/N<sub>2</sub> admixtures (2 standard liter/min total gas flow rate) was used as a feed gas. The source is mounted inside a stainless steel vacuum chamber that is filled with compressed laboratory air as shown in Figure 6.2(a). When the chamber reaches ambient pressure, an exhaust valve is opened to prevent an overpressure in the chamber. For X-ray photoelectron spectroscopy (XPS) experiments, the source-nozzle distance,  $s$ , was 9 cm and the nozzle-sample distance was 3 cm. This distance was chosen to be comparable with previous work and to ensure that we have a remote treatment for all conditions without any electrical interaction with the substrate, which can cause major damage to the films in the form of pinholes.<sup>[127]</sup> XPS experiments were performed for 7 minutes with a 1% molecular gas admixture with 14 kV<sub>pp</sub> applied voltage at 24 kHz. The vacuum chamber has a volume of 50 liters, so we can expect the ambient gas to vary slightly during the treatment due to the Ar feed gas.

The SMD used in this study is similar to those reported in the literature.<sup>[169, 172, 174, 175]</sup> A 1 mm-thick quartz sheet separates a copper electrode (5 cm x 5 cm) from a grounded mesh (#12, opening size ~ 1.8 mm). A 6 kV<sub>pp</sub> high voltage AC input at ~41 kHz was used to ignite the discharge, which forms around the grounded mesh. SMD treatments were performed in the same vacuum chamber as APPJ experiments. The chamber was evacuated and refilled with N<sub>2</sub>/O<sub>2</sub> mixtures to study the impact of different gas chemistries. Unless otherwise stated, SMD

experiments were performed for 7 minutes with a 5-8 kV<sub>pp</sub> applied voltage at ~41 kHz. Unless otherwise noted, the applied voltage was 6 kV<sub>pp</sub>. For XPS and ellipsometry measurements, the grounded mesh was 0.3 cm above the sample surface. The experimental setup is schematically shown in figure 6.2(b). One key difference between this work and SMD studies by Pavlovich et al. is the chamber volume.<sup>[168]</sup> The measurement cell used in that study was ~0.09 l, whereas the chamber is 50 l in this work. An air-operated SMD was used in their work, whereas dry N<sub>2</sub>/O<sub>2</sub> mixtures are used in this work.

To eliminate post-treatment surface reactions from the air in the laboratory and to enable rapid transfer to surface analysis, samples were vacuum transferred to XPS after treatment and subsequent pump-out of the treatment chamber.

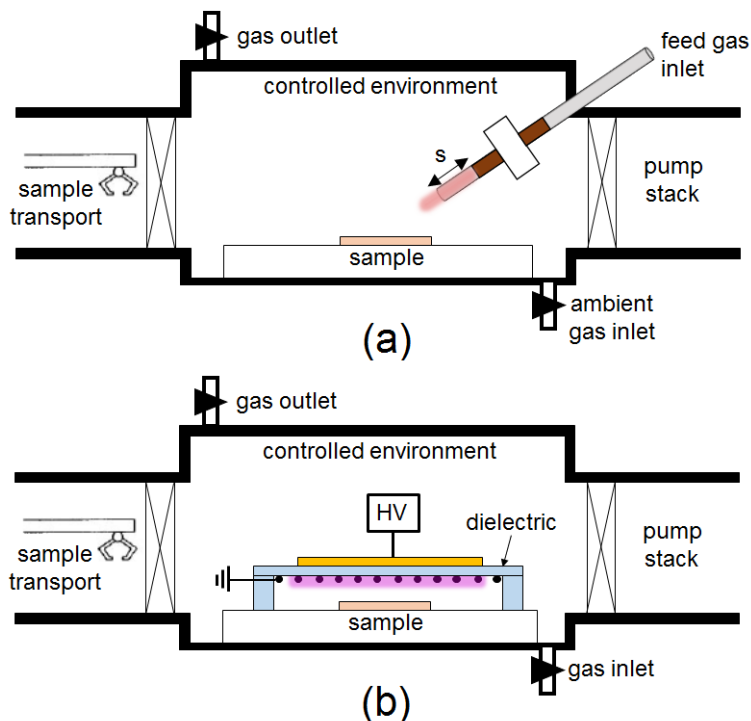


**Figure 6.2:** SMD experimental setup enabling controlled environments and sample transport under vacuum to surface analysis for (a) the APPJ and (b) the SMD.

### 6.2.3 Estimation of Biodeactivation

An enzyme-linked immunosorbent assay (ELISA) was used to estimate the biological activity of LPS and PGN after plasma treatment by the APPJ or SMD. The ELISA proceeds as follows and is based on a protocol provided by the primary antibody manufacturer. Unless otherwise noted, all incubation steps were performed at room temperature and solution volumes were 100  $\mu$ l. For LPS, various concentrations of LPS in DOCA buffer (formulation: 2.28 g monobasic sodium phosphate, 11.5 g dibasic sodium phosphate, 0.163 g NaCl, and 0.882 g deoxycholic acid brought to one liter with distilled/deionized water) were incubated overnight in a 96-well plate (Nunc Maxisorp, EBioscience) to form a standard curve and the to-be-treated wells. The only difference for PGN was that the solvent was 0.1 M carbonate-bicarbonate (pH 9.6). All wells were prepared in duplicate. The plates were then washed three times with 220  $\mu$ l PBS containing 0.04% Tween-20 (PBS-T) and dried under vacuum for 30 minutes at a pressure of  $2 \times 10^{-3}$  Pa. After plasma treatment, 150  $\mu$ l of 1% BSA in PBS-T (BSA-PBS-T) was added for 30 minutes as a blocking step. For the primary antibodies, 80  $\mu$ l was added at a concentration of 1  $\mu$ g/ml and 10  $\mu$ g/ml in BSA-PBS-T for LPS and PGN, respectively, and incubated for 30 minutes on a rocking platform. After washing three times with PBS-T, 80  $\mu$ l of 3  $\mu$ g/ml of HRP-conjugated goat anti-mouse secondary antibody in BSA-PBS-T was added and incubated for 30 minutes on a rocking platform. HRP is light sensitive, so the well plate was covered during this incubation. The wells were washed another three times and then incubated with TMB for 15 minutes. Reactions were stopped by addition of 2 M  $\text{H}_2\text{SO}_4$  and the optical density at 450 nm was measured within 10 minutes by an automatic microplate reader (Synergy HT Multi-Mode, BioTek). The ELISA protocol for measuring the bioactivity of biotinylated LPS has been

described previously.<sup>[139]</sup> To analyze the results, the optical density for the negative control (0 mg/ml of antigen) was subtracted from all the wells and compared to the untreated standard curve. The biological activity is measured as a ratio of the treated well to the untreated well in the standard curve of the same initial concentration, as discussed in Chapter 5. We consider this the normalized biological activity. The normalized biodeactivation is reported as unity minus this value. Thus, a normalized biodeactivation of unity would correspond to complete biodeactivation and zero would correspond to zero biodeactivation. Error was taken as the mean absolute deviation.

For the APPJ ELISA, the grounded electrode was 11 cm from the nozzle and 12 cm from the bottom of the well. The nozzle entered the wells by 1 mm to obtain a net gas flow out of the well, as described previously.<sup>[140]</sup> The plasma was operated at 12 kV pk-pk for N<sub>2</sub>/Ar and 14 kV pk-pk for all other gas chemistries. The voltage was lowered for the N<sub>2</sub>/Ar plasma due to the visible effluent extending from the source into the well, which allows charged species to contribute. O<sub>2</sub>-containing discharges have dramatically decreased plume lengths due to O<sub>2</sub> being an electronegative gas, so this was not an issue. The APPJ treatment was performed for 7 minutes.

For the SMD ELISA, the SMD sat on top of the well plate with a 3 mm gap between the top of the well and the grounded mesh, giving a total mesh-sample distance of 1.43 cm. The interaction of the SMD with the standard curve was minimized by covering the wells with Parafilm M and a Si piece. A vacuum-only standard curve was also measured to ensure that the SMD did not impact the standard curve. The SMD treatment was performed for 7 minutes.

#### *6.2.4. Characterization*

The film's surface chemistry was measured by X-ray photoelectron spectroscopy (XPS). The experimental and fitting procedure have been described in great detail in previous work and will be summarized here.<sup>[139, 140, 213]</sup> The analysis was performed with a Vacuum Generators ESCA Mk II surface analysis system employing a Mg-K $\alpha$  source (1253.6 eV) at pass energies of 50 eV and 20 eV for survey and narrow scans, respectively. As previously described, measurements probing deeper (up to 8 nm for 90° electron takeoff angle) into the sample showed similar, but reduced effects as the measurements probing the near surface (up to 3 nm for 20° electron takeoff angle). Thus, only measurements taken at the 20° electron takeoff angle are shown here. XPS measurements were performed within 20 minutes after treatment after transferring samples under vacuum into the UHV chamber.

C1s, O1s, and N1s peak assignments were taken from the literature.<sup>[52]</sup> As the O1s spectrum of polymers is difficult to deconvolve due to overlapping peaks, we grouped together O1s peaks with binding energy between 532.2 eV and 533.1 to a single peak at 532.7 eV and 533.6 and 535.3 eV to a single peak at 534.6 eV. Nitrate peaks were fit separately as the exact areas could be extracted from the single peak in the N1s spectrum. A 1:2 doublet at 533.9 and 534.7 eV was fit for R-O-NO<sub>2</sub> and RON-O<sub>2</sub>, respectively. To calculate atomic composition of the film (excluding H), the integrated peak area was divided by its Scofield cross sections for C, O, N, and P of 1, 2.85, 1.77, and 1.25, respectively.<sup>[73]</sup> Spectra were calibrated to the C-C/H peak at 285 eV after Shirley background subtraction. Average film composition values with error taken as the mean absolute deviation are reported. Due to the large number of experiments, only critical conditions were reproduced, which showed low error.

Film thickness changes were evaluated in real-time for the APPJ treatment and pre- and post-processing for the SMD treatment. A nearly identical chamber as the one described in

section 6.2.2 was equipped with an ellipsometer oriented  $\sim 70^\circ$  from the surface normal. The APPJ was mounted normal to the sample surface for APPJ treatments, in contrast to those performed for XPS analysis where the APPJ is oriented at  $\sim 70^\circ$  to the surface normal.

Gaseous  $O_3$  was measured by UV absorption at 254 nm using Beer's law with an absorption cross section of  $1.14 \times 10^{-21} \text{ m}^2$ .<sup>[168]</sup> 254 nm light was generated by an Ar/Hg pen lamp and measured by a photodiode after passing a narrow band pass filter centered at  $254 \pm 10$  nm.

## 6.3. Results

### 6.3.1. Biodeactivation and Surface Analysis of Biomolecules

**Biodeactivation of LPS, bLPS, and PGN.** The biodeactivation after SMD treatment by  $N_2/O_2$  mixtures was measured for biotinylated-LPS, LPS, and PGN and is shown in figure 6.3. Each biomolecule behaves somewhat differently. Biotinylated-LPS and LPS both show lower biodeactivation for pure  $O_2$  treatment that increases as  $N_2$  is added. However, bLPS biodeactivation remains high for all  $N_2/O_2$  mixtures while LPS biodeactivation decreases for  $N_2$  admixtures greater than 15%. On the other hand, PGN is easy to biodeactivate for all the gas chemistries.

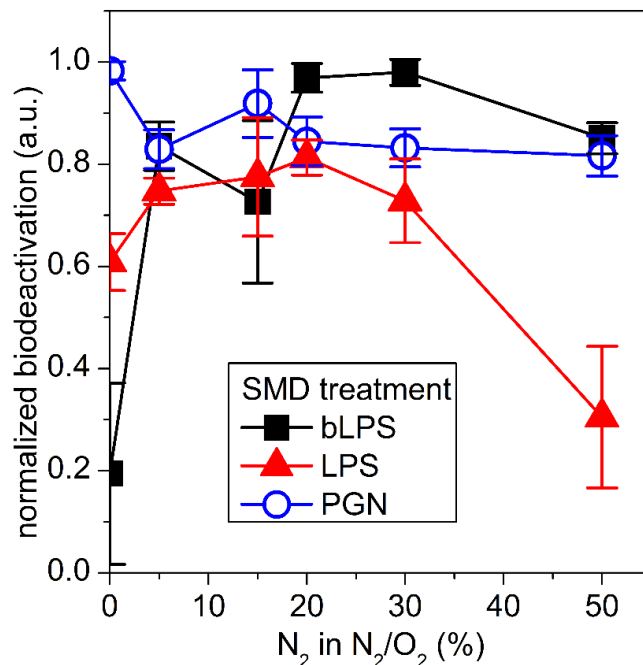


**Figure 6.3:** Normalized biodeactivation by the SMD as a function of N<sub>2</sub>/O<sub>2</sub> mixture for biotinylated-LPS (bLPS), LPS, and PGN.

**Negligible etching after treatments.** Real-time ellipsometry cannot be accomplished with the SMD as the source blocks the path of the laser. To overcome this, ellipsometry measurements were made before and after treatment. The SMD was then removed and the system was evacuated for 20 minutes before another measurement, which is approximately the time it takes to transfer CAP-treated samples to XPS. Material removal was not observed. Interestingly, the thickness increased  $\sim 5$  nm. This thickness increase is the subject of future study. Preliminary results show that the increase depends on the film thickness, suggesting a swelling effect. The authors conclude that biodeactivation does not require an etching mechanism and that changes in surface chemistry, shown below, can dominate.

**XPS analysis of LPS.** XPS spectra (Fig. 6.4(a-c)) highlight the key differences between pristine LPS, and LPS after O<sub>2</sub> and 15% N<sub>2</sub>/O<sub>2</sub> SMD treatment. After treatment, the C1s is not very different between the two treatments, though there is more C-O bonding with pure O<sub>2</sub>. The N1s shows the largest changes. After treatment in O<sub>2</sub>, a small amount of NO<sub>3</sub> forms, but amide groups are unaffected. After 15% N<sub>2</sub>/O<sub>2</sub> treatment, the NO<sub>3</sub> peak dramatically increases and the amide peak slightly drops. These changes can also be seen in the O1s, where we see an overall increase in O composition after both treatments, with the O<sub>2</sub> treatment creating mostly C-O<sub>x</sub> moieties and the 15% N<sub>2</sub>/O<sub>2</sub> treatment showing a double peak due to the high binding energy for electrons from the oxygen atoms in NO<sub>3</sub>. The NO<sub>3</sub> and O composition as a function of N<sub>2</sub>/O<sub>2</sub> mixture are shown in figure 6.4(d). For pure O<sub>2</sub>, NO<sub>3</sub> and O account for ~1.9% and 42.6% of the film composition. As N<sub>2</sub> is added, NO<sub>3</sub> increases dramatically to 5.3% at 20% N<sub>2</sub>/O<sub>2</sub>. The O composition hardly changes in this region and actually peaks earlier, at 10% N<sub>2</sub>. For the highest N<sub>2</sub> admixture explored, 50%, NO<sub>3</sub> falls dramatically to less than 1% and the O composition approaches that of the pristine film at 19.6%. If oxidation unrelated to NO<sub>3</sub> moieties is considered (Fig. 6.4(d), open circles), then the O composition falls as N<sub>2</sub> is added. It is clear that gas chemistry is a major knob for controlling NO<sub>3</sub>.



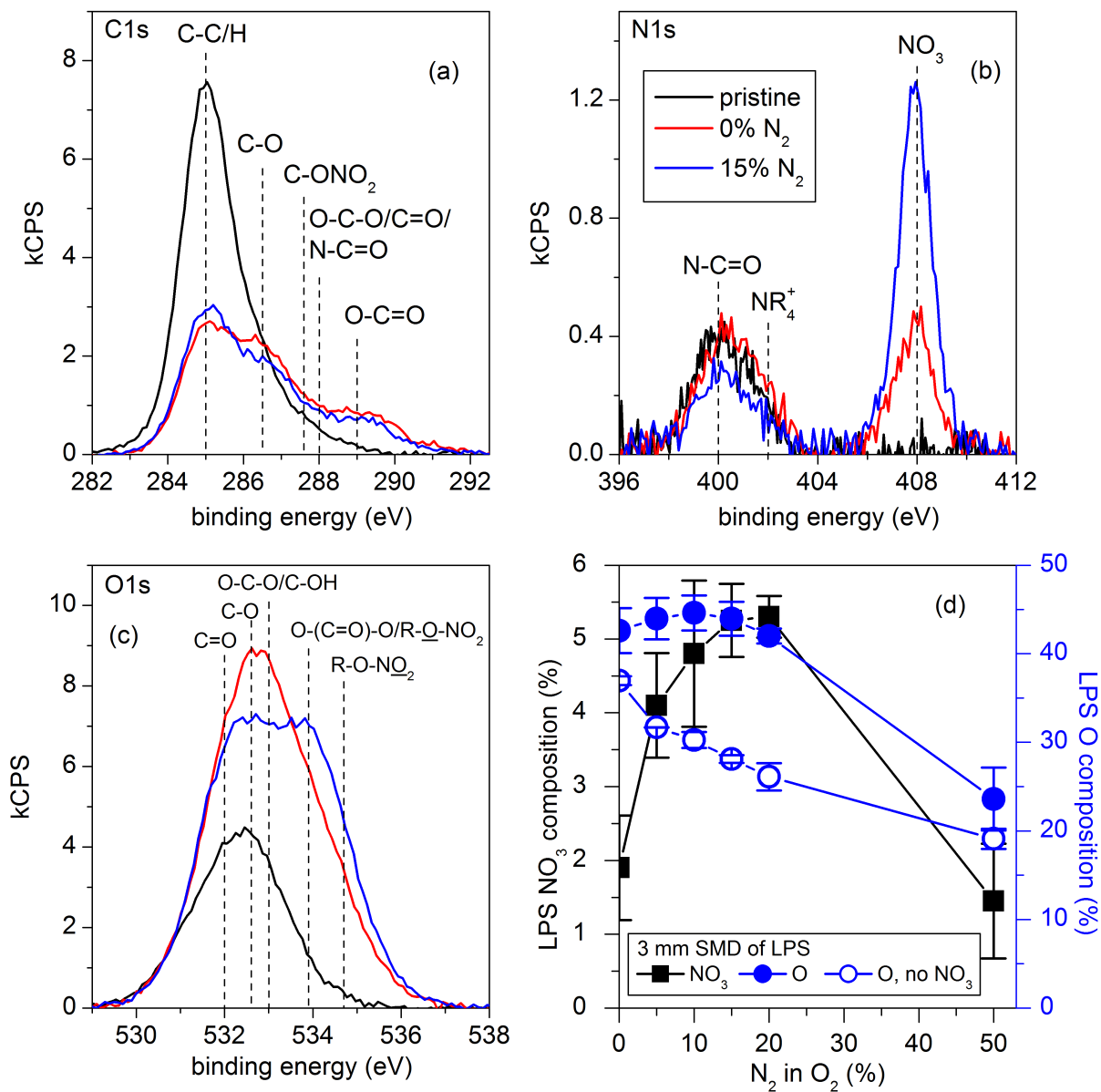


**Figure 6.4:** After SMD treatment, (a) C1s, (b) N1s, and (c) O1s XPS spectra of LPS. In (d), the NO<sub>3</sub> and O composition vs N<sub>2</sub>/O<sub>2</sub> mixture are shown.

Changing the gas chemistry also changes the power density, measured by the Lissajous method, as shown in Figure 6.5(a). For pure O<sub>2</sub>, the power density was 0.24 W cm<sup>-2</sup>. The power density increases with N<sub>2</sub> admixture up to 20% N<sub>2</sub> in O<sub>2</sub>, where it reaches a maximum of 0.40 W

cm<sup>-2</sup>. The power density then decreases as the N<sub>2</sub> fraction increases to 0.35 W cm<sup>-2</sup> for the 50% condition. The film NO<sub>3</sub> and O compositions shown in Figure 6.4(d) can also be plotted against this measured power to test whether the observed behavior is due to power dissipation rather than gas chemistry. As shown in Figure 6.5(b), similar gas chemistry-dependent power densities provide similar levels of modification. We conclude that the gas chemistry dominates over changes in dissipated power.

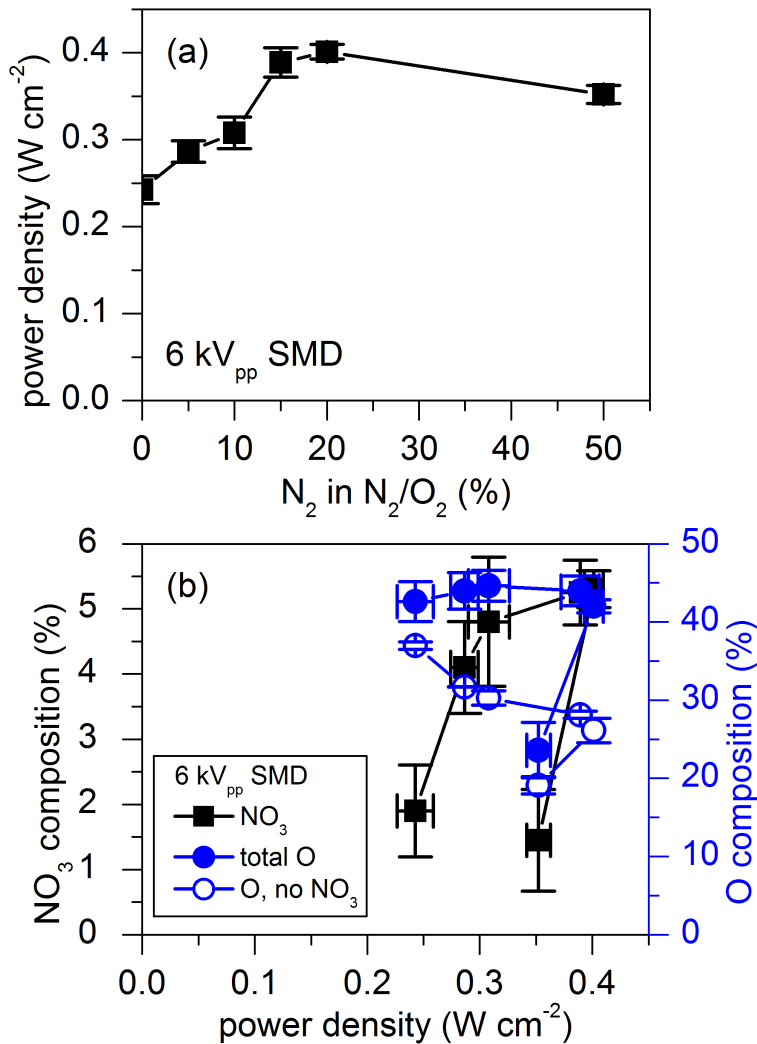


**Figure 6.5:** (a) Power density vs N<sub>2</sub>/O<sub>2</sub> mixture for the surface microdischarge at constant applied voltage and (b) film composition vs power density for the investigated gas chemistries.

In addition to changing the gas chemistry, the applied voltage was varied, as this is known to impact the reactive species output. Figure 6.6(a) shows the  $\text{NO}_3$  and O composition of LPS films after a 15%  $\text{N}_2/\text{O}_2$  SMD treatment at applied voltages ranging from 5  $\text{kV}_{\text{pp}}$  to 8  $\text{kV}_{\text{pp}}$ . Both the  $\text{NO}_3$  and O composition follow the same trend. Increasing from 5  $\text{kV}_{\text{pp}}$  to 6  $\text{kV}_{\text{pp}}$  slightly increases both  $\text{NO}_3$  and O. Further increasing the voltage decreases surface modifications.  $\text{NO}_3$  drops from its maximum of 5.3% down to 1.7% when the voltage is increased from 6  $\text{kV}_{\text{pp}}$  to 8  $\text{kV}_{\text{pp}}$ . Similarly, the O composition drops from 42.1% to 23.7%, which is close to the pristine LPS O composition of 19.6%. By examining oxidation that does not directly result from  $\text{NO}_3$ , the O composition at 8  $\text{kV}_{\text{pp}}$  is actually slightly less than that of the pristine film, indicating the  $\text{NO}_3$  forms at  $\text{C-O}_x$  groups naturally found in the film. By plotting the O composition without  $\text{NO}_3$  against the applied voltage, we see that this “pure” oxidation still decreases as the voltage is increased, but the drop is much less.

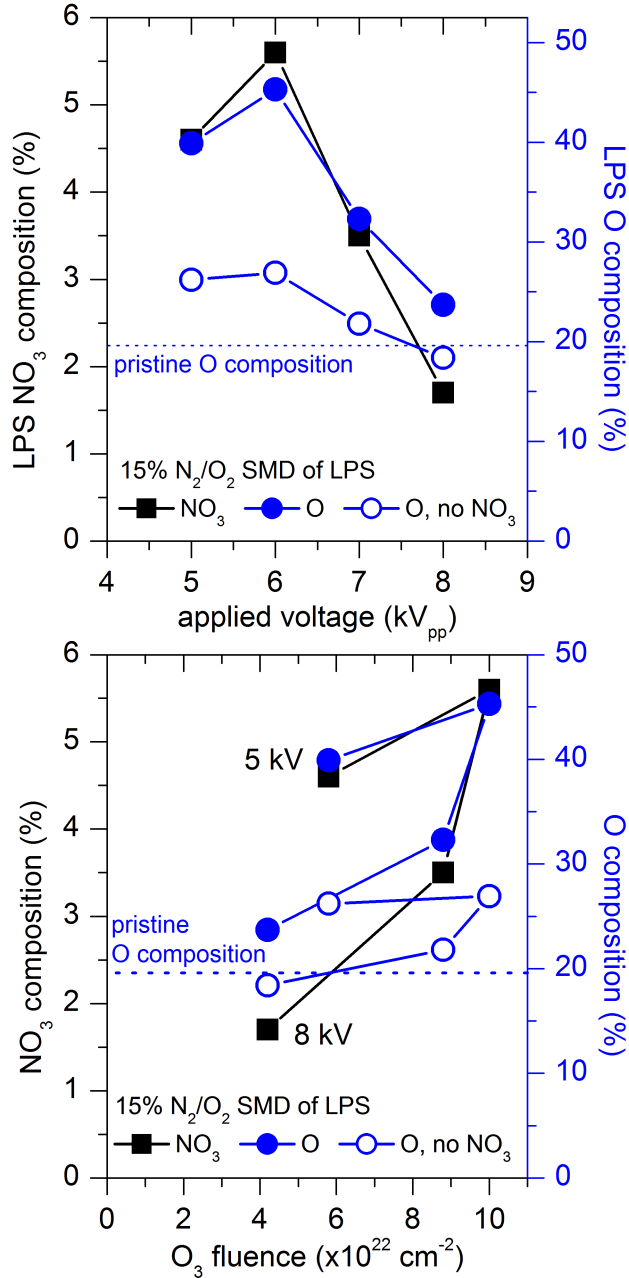


**Figure 6.6:** (a) LPS NO<sub>3</sub> and O composition of LPS for varying applied voltages after SMD treatment in 15% N<sub>2</sub> in O<sub>2</sub>. (b) LPS NO<sub>3</sub> and O composition after SMD treatment as a function of O<sub>3</sub> fluence. The O composition is divided into total O composition (solid circles) and O composition independent of NO<sub>3</sub> (open circles). The dotted line indicates the O composition of the pristine film.

The O<sub>3</sub> density produced in the APPJ was previously reported and is highest in the mid-10<sup>14</sup> cm<sup>-3</sup> range for O<sub>2</sub>/Ar plasma without N<sub>2</sub> admixture.<sup>[140]</sup> The SMD produces significantly more O<sub>3</sub> than the APPJ. The O<sub>3</sub> density was measured over 7 min as this was the treatment time chosen for surface studies. As shown in figure 6.7(a), at a constant applied voltage of 6 kV<sub>pp</sub>, the O<sub>3</sub> density increases over ~ 4 min before saturating regardless of the O<sub>2</sub>/N<sub>2</sub> mixture. An exception is for pure O<sub>2</sub>, where the O<sub>3</sub> density does not completely saturates and reaches a maximum of 4.1 x 10<sup>16</sup> cm<sup>-3</sup>. For 5% N<sub>2</sub> in O<sub>2</sub>, the O<sub>3</sub> density reaches a maximum of 6.7 x 10<sup>16</sup> cm<sup>-3</sup>. As the N<sub>2</sub> fraction is further increased, the O<sub>3</sub> density drops. The O<sub>3</sub> density was also measured for applied voltages ranging from 5 kV<sub>pp</sub> to 8 kV<sub>pp</sub> for 15% N<sub>2</sub> in O<sub>2</sub> as shown in Figure 6.7(b). This gas chemistry was chosen because this feed gas condition caused both high oxidation and nitridation of biomolecular and polymeric films. At 5 kV<sub>pp</sub> and 6 kV<sub>pp</sub>, the O<sub>3</sub> density increases over the length of the treatment. The maximum O<sub>3</sub> density at 6 kV<sub>pp</sub> was 3.4 x 10<sup>16</sup> cm<sup>-3</sup>. At 5 kV<sub>pp</sub>, saturation is not reached. For the higher applied voltages, destructive processes begin to dominate and O<sub>3</sub> density drops after 3 minutes and 2 minutes for 7 kV<sub>pp</sub> and 8 kV<sub>pp</sub>, respectively.

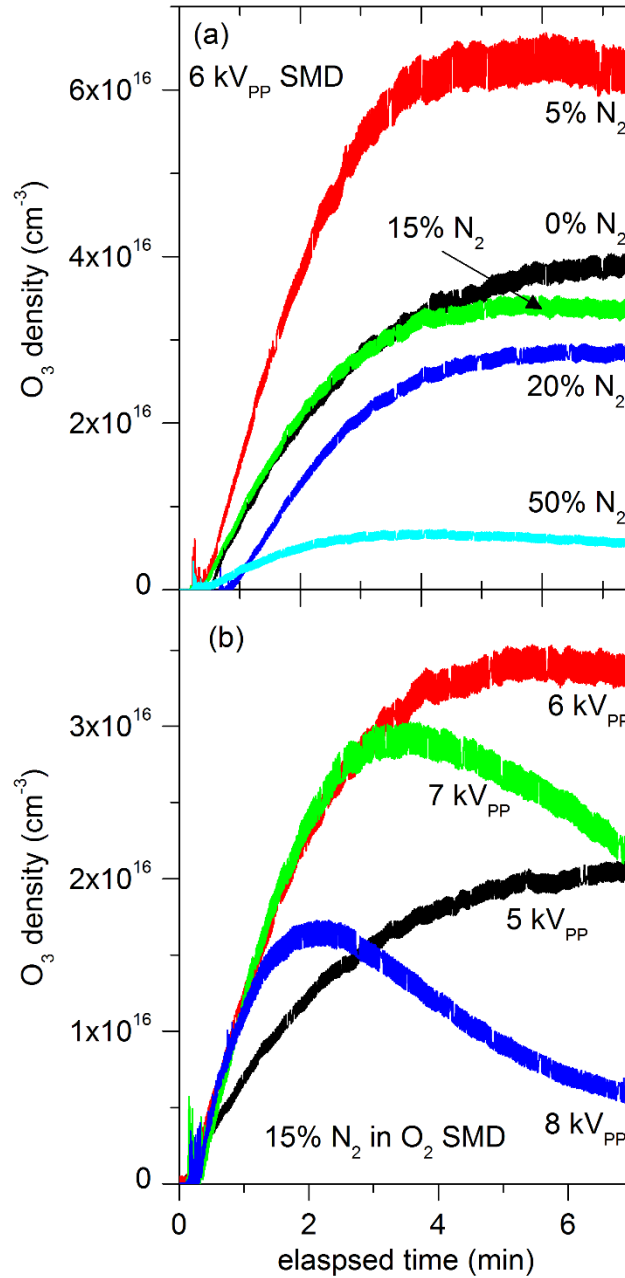


**Figure 6.7:**  $O_3$  density produced by the SMD vs time for (a) varying  $N_2/O_2$  mixtures at constant applied voltage (6 kV) and (b) varying applied voltage for 15%  $N_2$  in  $O_2$  environment.

The  $O_3$  density measurements and surface modifications for the voltage series were compared for the 15%  $N_2/O_2$  condition. The results are shown in figure 6.6(b). The  $O_3$  fluence

was calculated by integrating the O<sub>3</sub> flux,  $\Gamma$ , over time. The flux was calculated from the O<sub>3</sub> density by:

$$\Gamma = \frac{n_{O_3}\bar{v}}{4} \quad (6.1)$$

where  $n_{O_3}$  is the density of O<sub>3</sub> and  $\bar{v}$  is the average velocity calculated from the temperature (assumed to be 320 K). The NO<sub>3</sub> and O composition both show similar behavior, with the highest modifications occurring when O<sub>3</sub> is highest. This result suggests that O<sub>3</sub> is important for surface modifications. Previous work in our group using an atmospheric pressure plasma jet has shown that polystyrene surface modifications are not solely determined by O<sub>3</sub>.<sup>[213]</sup> This was shown by comparing different applied voltages. The higher voltage produced higher surface oxygen uptake, but produced less O<sub>3</sub>, indicating that other plasma-generated species were at work. If NO<sub>3</sub> is important for surface modifications, then conditions that produce O<sub>3</sub> are beneficial, since one pathway for NO<sub>3</sub> is reaction of NO<sub>2</sub> with O<sub>3</sub>. Similarly, as discussed below, O<sub>3</sub> can create alkoxy radicals, which react with NO<sub>2</sub> to form NO<sub>3</sub>.

**XPS analysis of PGN.** PGN surface modifications are similar to LPS. Figure 6.8(a) compares the C1s of pristine PGN and PGN after SMD treatment in O<sub>2</sub> and 15% N<sub>2</sub>/O<sub>2</sub>. The C1s shows major oxidation after treatment, but the spectra look nearly identical. The oxidation and nitridation of the surface shown in figure 6.8(b) can be seen in the C1s through the drop in C-H bonding and increase in higher binding energy groups. The O and NO<sub>3</sub> composition reached a maximum at 5% and 15% N<sub>2</sub> in O<sub>2</sub>, respectively. The maximum NO<sub>3</sub> composition was higher in PGN than in LPS at 6.4%. When oxidation that does not directly originate from NO<sub>3</sub> is plotted (open circles), then we see a decrease in oxidation as N<sub>2</sub> is added. For LPS, both the NO<sub>3</sub> composition and biodeactivation drop significantly for high N<sub>2</sub> admixtures. For PGN,

biodeactivation is high and the  $\text{NO}_3$  content remains relatively high at 4.4% for the 50%  $\text{N}_2/\text{O}_2$  gas chemistry. The possible correlation between  $\text{NO}_3$  and biodeactivation also appears to hold for PGN.

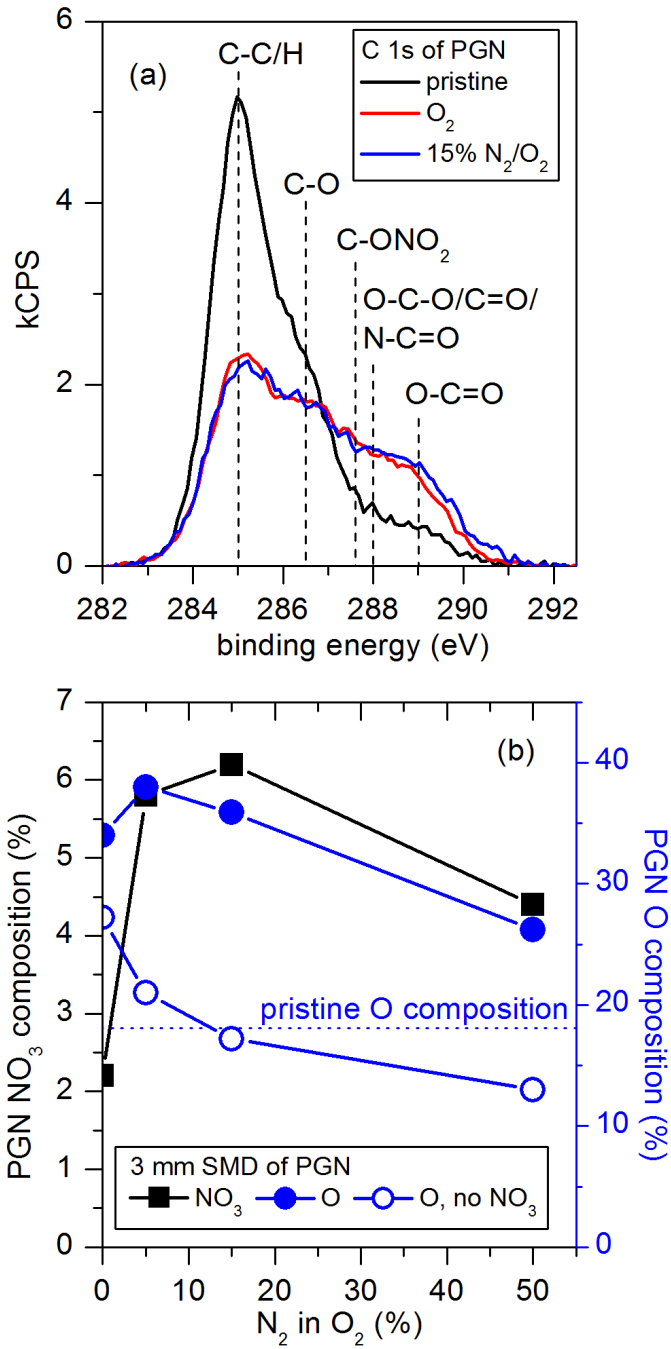




**Figure 6.8:** (a) C 1s XPS spectra of PGN after SMD treatment and (b) PGN NO<sub>3</sub> and O composition as a function of N<sub>2</sub>/O<sub>2</sub> mixture. In (b), the dotted line indicates the pristine PGN film O composition.

### 3.2. SMD Treatment: Surface Analysis of Model Polymers

PVA, PP, PS, and PMMA were studied to gain insights into how SMD treatments modify specific functional groups. PP and PS also do not contain oxygen, so any resulting oxidation must result from plasma-surface interactions. These polymers all contain functional groups that are commonly found in biopolymers such as peptides and carbohydrates. By isolating specific functional groups, the selectivity of CAP treatment toward different chemical moieties can be evaluated. XPS spectra are shown below for pristine films and after 0% and 15% N<sub>2</sub> in O<sub>2</sub> SMD treatments.

N1s spectra for the polymers are shown in Figure 6.9. All the films show NO<sub>3</sub>, but the amount varies for each of the polymers. This demonstrates that NO<sub>3</sub> formation depends on the molecular structure. PVA (Fig. 6.9(a)) shows the most NO<sub>3</sub> while PMMA (Fig. 6.9(d)) shows the least. When N<sub>2</sub> is removed, NO<sub>3</sub> drops.

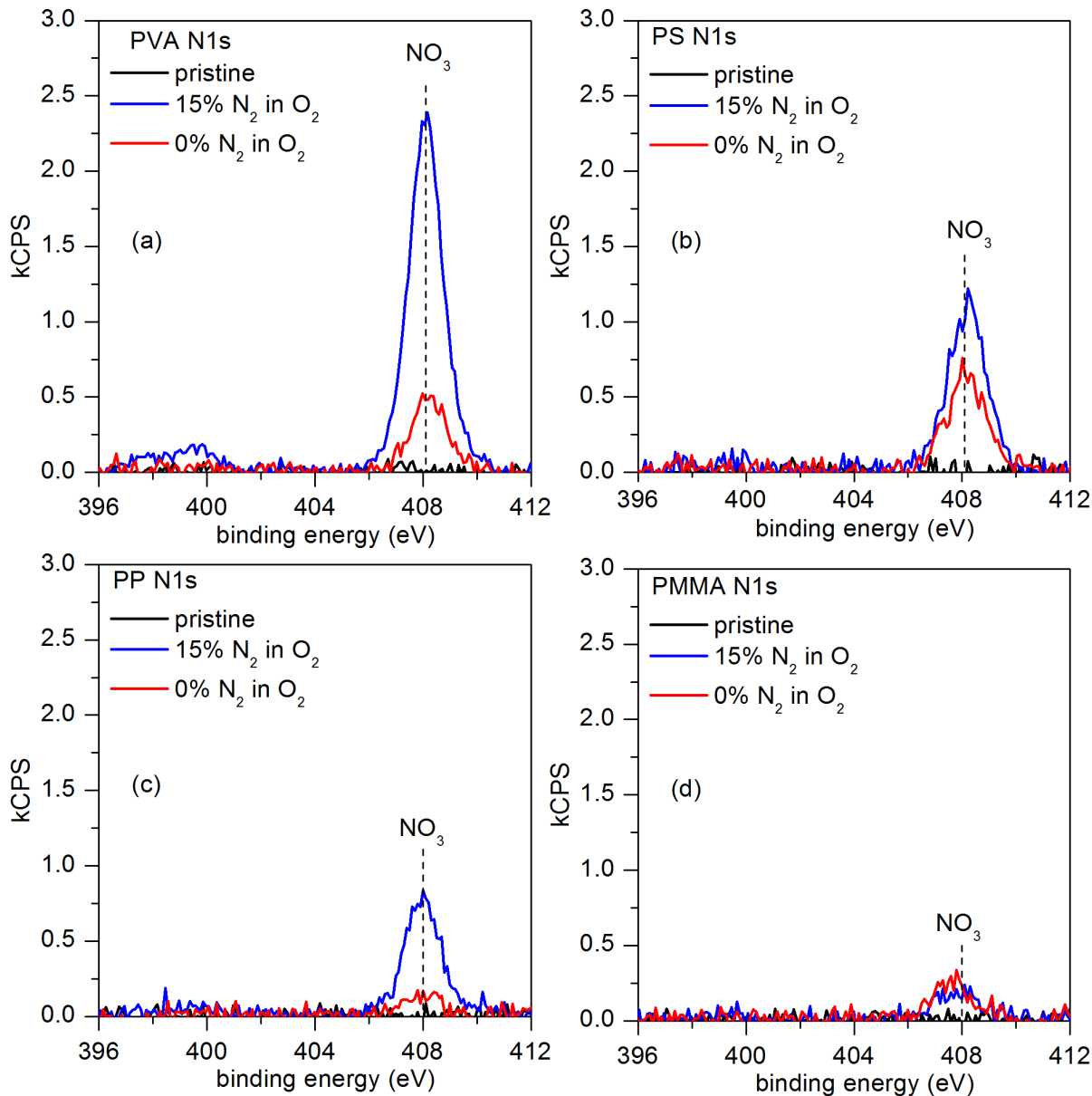


Figure 6.9. N1s spectra of (a) PVA, (b) PS, (c) PP, and (d) PMMA before and after SMD treatment. Treatment conditions: 7 min, 6 kV<sub>pp</sub>, 41.5 kHz.

The C1s spectra are shown in Figure 6.10. For PVA in Fig. 6.10(a), the pristine film shows a double peak due to C-OH and C-C/H bonding. After SMD treatment, both the C-C/H and C-O peaks decrease and peaks emerge at higher binding energies due to ester, orthoester, and carbonate moieties. We also observe C-ONO<sub>2</sub> at 287.6 eV. The C-C/H bond shifts to higher

binding energies due to the greater secondary shift by the nitro group, which is more apparent after the 15% N<sub>2</sub>/O<sub>2</sub> treatment. Comparing the 15% N<sub>2</sub> and 0% N<sub>2</sub> in O<sub>2</sub> treatments, more C-O, O-C=O, O-(C-O)-O, and O-(C=O)-O was measured after O<sub>2</sub> treatment and more C-ONO<sub>2</sub> after 15% N<sub>2</sub>/O<sub>2</sub>. While the binding energy of O-C-ONO<sub>2</sub> has not been reported in the literature, it may be approximately equal to the sum of the individual chemical shifts i.e. 1.5 eV + 2.6 eV = 4.1 eV. Thus, the higher binding energy shoulder could partially result from this type of group. Both PS (Fig. 6.10(b)) and PP (Fig. 6.10(c)) show similar modifications with an increase in higher binding energy groups. For PS, more higher binding energy groups such as orthoesters and carbonates form after the 0% N<sub>2</sub> in O<sub>2</sub> treatment than after the 15% N<sub>2</sub> in O<sub>2</sub> treatment. In PP, there is more oxidation after the 15% N<sub>2</sub>/O<sub>2</sub> treatment. Lastly, PMMA shows minimal modifications after both treatments with a slight decrease in C-C/H bonding. There is a very weak shoulder at the highest binding energy, indicating that orthoesters are forming.

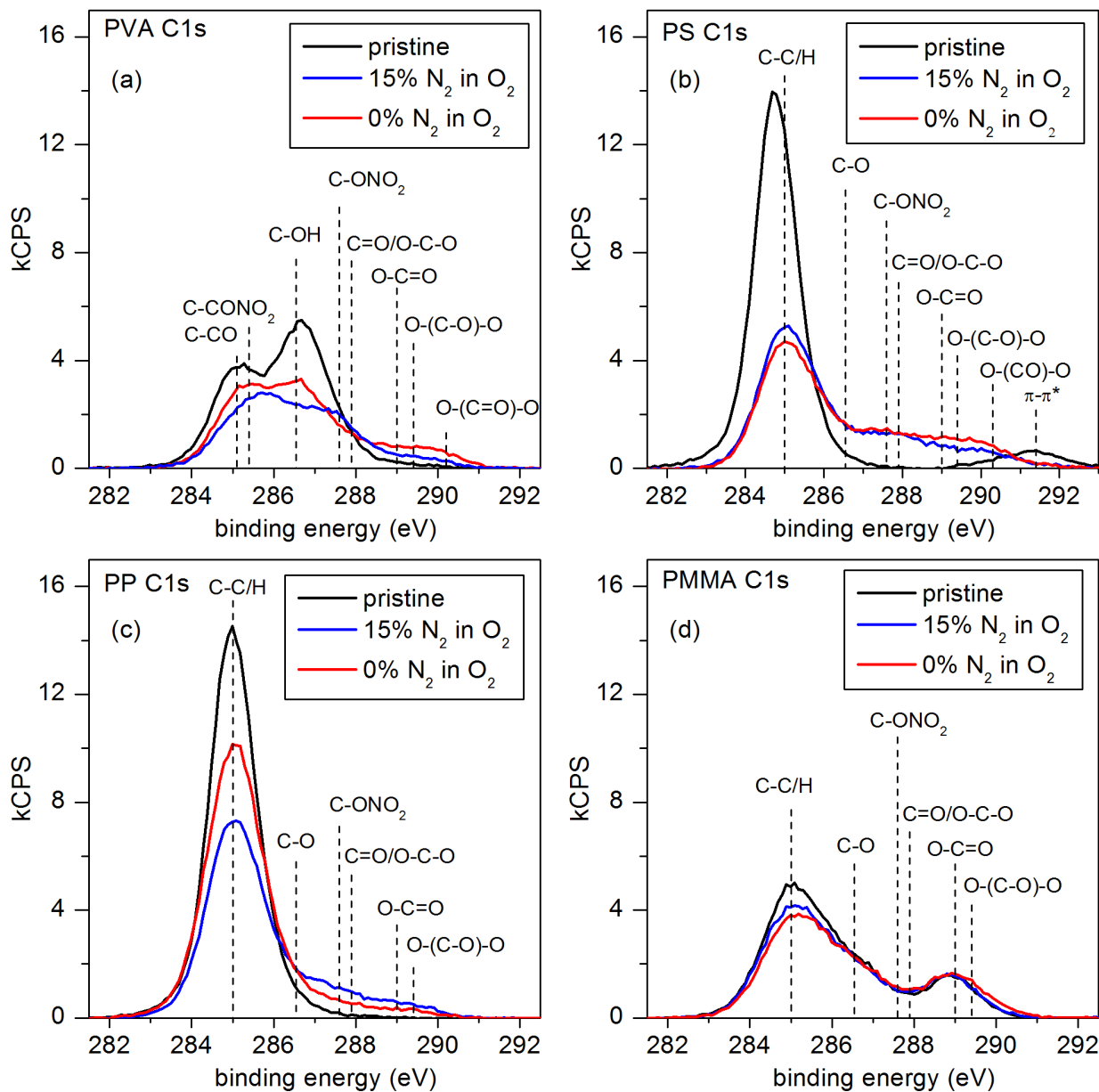


Figure 6.10. C1s spectra of (a) PVA, (b) PS, (c) PP, and (d) PMMA before and after SMD treatment. Treatment conditions: 7 min, 6 kV<sub>pp</sub>, 41.5 kHz. Peak positions are indicated in the figure.

The O1s spectra are shown in Figure 6.11 and are consistent with the N1s and C1s. When strong amounts of NO<sub>3</sub> are present, the O1s peak shifts to higher binding energies due to the two

types of oxygen atoms in  $\text{NO}_3$ , which have binding energies at 533.9 eV and 534.7 eV. For PVA and PS, carbon-oxygen species are more prevalent when  $\text{N}_2$  is removed. PMMA shows modifications resulting from  $\text{NO}_3$ .

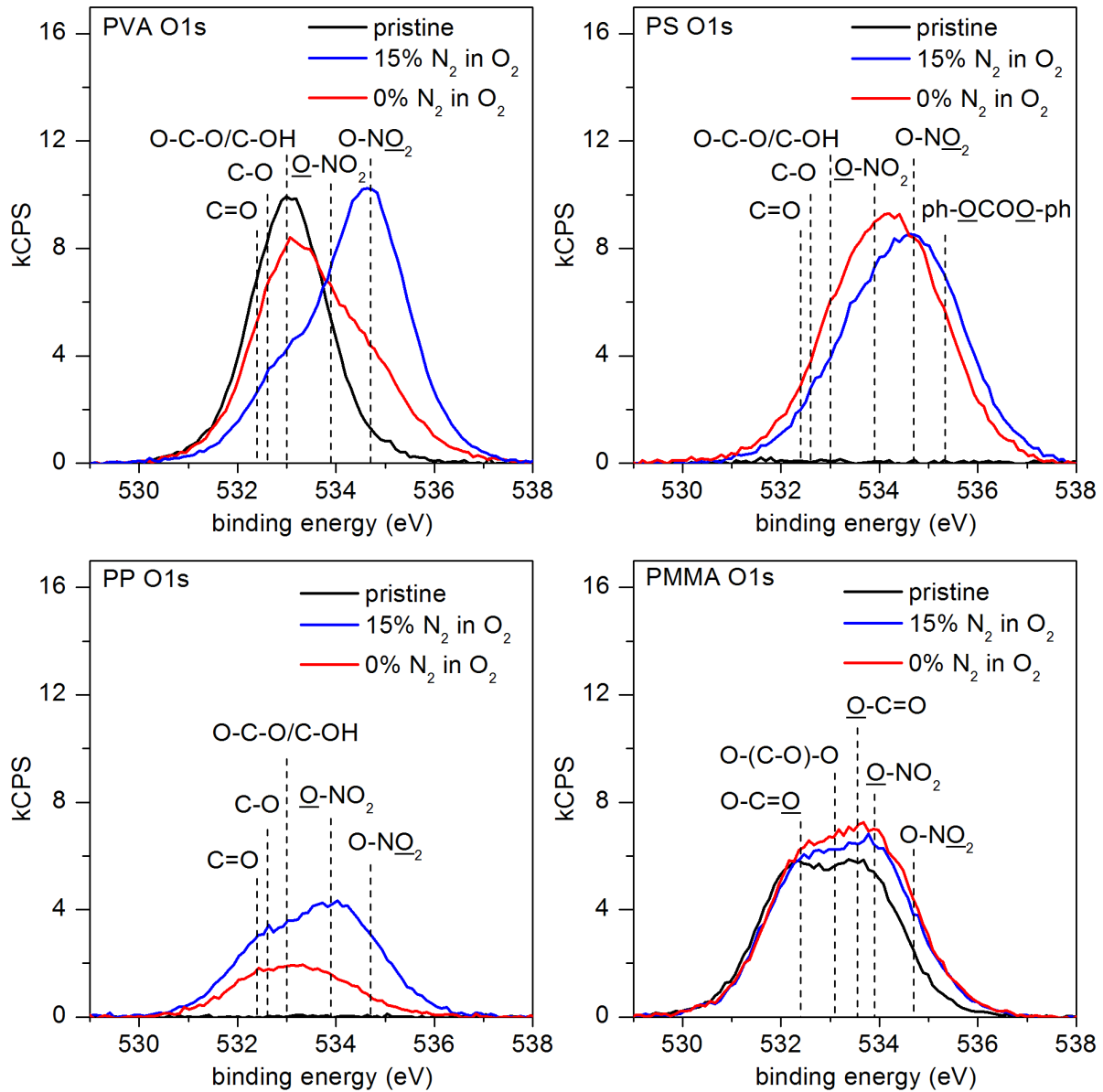


Figure 6.11. O1s spectra of (a) PVA, (b) PS, (c) PP, and (d) PMMA before and after SMD treatment. Treatment conditions: 7 min, 6 kV<sub>pp</sub>, 41.5 kHz. Peak positions are indicated in the figure.

Figure 6.12 summarizes the changes in NO<sub>3</sub> composition and O composition for each of the polymers studied for N<sub>2</sub> admixtures ranging from 0-50% in O<sub>2</sub>. In these plots, the total O composition (solid circles) is distinguished from O independent from NO<sub>3</sub> (open circles). That is, the NO<sub>3</sub> contribution to the O composition is subtracted from the total O composition. For PMMA and PVA, the dotted lines indicate the O composition of the pristine film. For all of these materials, only NO<sub>3</sub> was measured, not NO or NO<sub>2</sub>.

For PP (Fig. 6.12(a)) after O<sub>2</sub> treatment, 9.1% and 0.7% of the film surface is due to oxygen and nitrate, respectively. As N<sub>2</sub> is added up to 15%, the oxygen and NO<sub>3</sub> content increase to 21.4% and 3.6%, respectively. Further increasing the N<sub>2</sub> fraction decreases modifications with oxygen and nitrogen dropping to 8.8% and 1.5%, respectively, for 50% N<sub>2</sub>/O<sub>2</sub> gas. The oxidation unrelated to NO<sub>3</sub> is relatively unchanged, but also maximizes at 15% N<sub>2</sub>/O<sub>2</sub> at 10.8%. As will be shown, PP shows low oxidation and nitridation compared to the other materials.

The NO<sub>3</sub> and O composition is shown in Fig. 6.12(b) for PMMA. NO<sub>3</sub> formation is low and less than 1% for most chemistries. There is no trend with the gas chemistry. Overall oxidation slightly increases, but most of this is due to the NO<sub>3</sub> as the O composition that is independent of NO<sub>3</sub> is just barely above that of the pristine film.

PS (Fig. 6.12(c)) is consistent with the biomolecules and PP: the NO<sub>3</sub> content is highest for N<sub>2</sub>/O<sub>2</sub> mixtures compared to pure O<sub>2</sub>. Overall, the total oxidation does not change much among the different gas chemistries, which is consistent with the previous study showing that PS oxidation is easy.<sup>[213]</sup> Even when NO<sub>3</sub> is subtracted from the O composition, “pure” oxidation accounts for at least 15% of the composition.

PVA (Fig. 6.12(d)) shows very strong surface modifications after plasma treatment and shows the strongest preference for NO<sub>3</sub> formation of all the treated films. The NO<sub>3</sub> composition

is lowest for the pure O<sub>2</sub> treatment, reaches a maximum at 15% N<sub>2</sub>/O<sub>2</sub>, and remains relatively stable up to 50% N<sub>2</sub>/O<sub>2</sub>. The overall oxidation of the film is relatively constant at ~ 41%, though it is slightly lower for pure O<sub>2</sub> than N<sub>2</sub>/O<sub>2</sub> mixtures. When NO<sub>3</sub> contributions are subtracted from the total O composition (open circles), we see that the O composition is less than that of the pristine film. As discussed in detail in Sec. 6.4, this demonstrates that the –OH group is very susceptible to attack by gas-phase NO<sub>x</sub>.

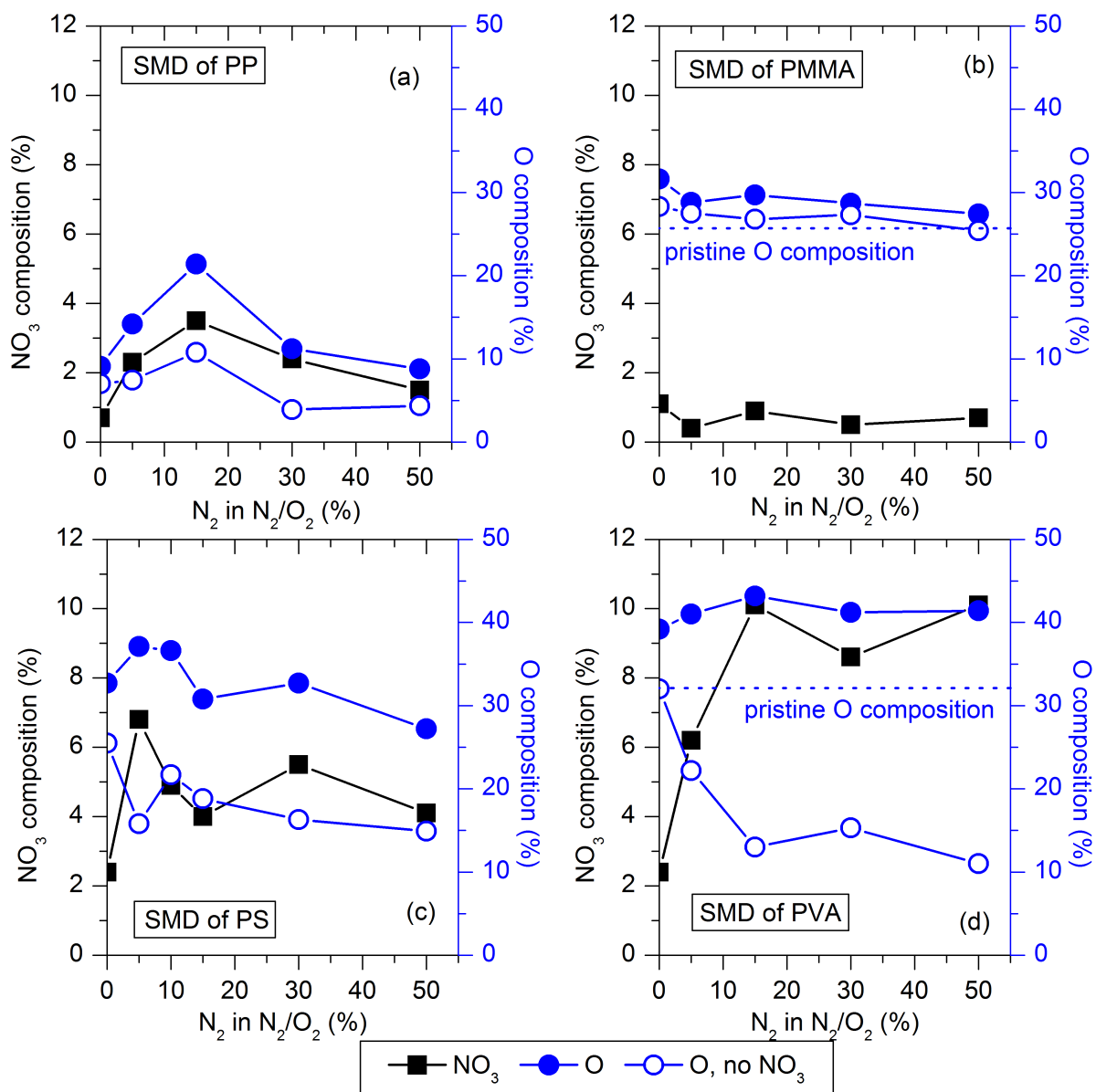


**Figure 6.12:** NO<sub>3</sub> and O compositions vs N<sub>2</sub>/O<sub>2</sub> mixture for a) PP, b) PMMA, c) PS, and d) PVA. For PMMA and PVA after SMD treatments. The dotted line shows the O composition of the pristine film. Open circles show the O composition if contributions due to NO<sub>3</sub> are subtracted.

### 3.3. APPJ Treatment: Biodeactivation and Surface Analysis of Biomolecules

**Biodeactivation of LPS, bLPS, and PGN.** Biodeactivation by the APPJ was measured for 1% ((1-x)N<sub>2</sub>/xO<sub>2</sub>) admixtures to Ar. Figure 6.13 shows the normalized biodeactivation as a function of the O<sub>2</sub> fraction in the 1% N<sub>2</sub>/O<sub>2</sub> molecular gas admixture to Ar for the three biomolecules. For each biomolecule, biodeactivation increases with the O<sub>2</sub> fraction. No N<sub>2</sub>/O<sub>2</sub> mixture is more effective than the pure O<sub>2</sub>/Ar plasma. In contrast to PGN and biotin-LPS, LPS is relatively easy to deactivate with deactivation occurring even for N<sub>2</sub>/Ar plasma.



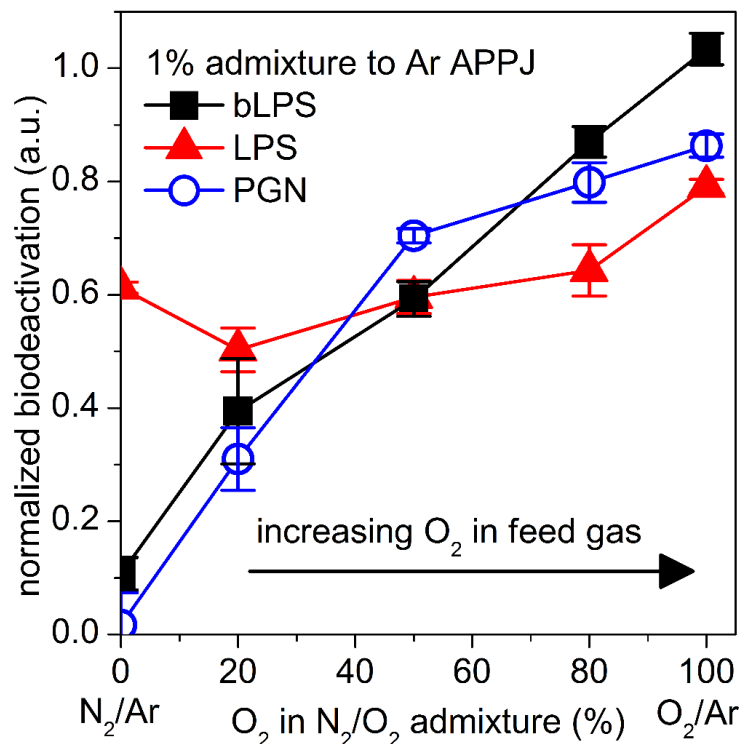


**Figure 6.13:** Normalized biodeactivation by the APPJ as a function of the 1% N<sub>2</sub>/O<sub>2</sub> admixture chemistry for biotinylated-LPS (bLPS), LPS, and PGN.

**XPS analysis of APPJ-treated LPS.** XPS was used to measure the APPJ-induced surface modifications for a variety of N<sub>2</sub>/O<sub>2</sub> molecular gas admixtures with a source-nozzle gap of 9 cm and a nozzle-sample gap of 3 cm. Figure 6.14(a) shows the C1s composition of LPS films. As O<sub>2</sub> is added to the admixture, surface modifications increase, with a decrease in C-C/H bonding and increase in C-O bonding. O-C-O/C=O/N-C=O slightly increase and O-C=O is hardly present. When N<sub>2</sub> is removed from the feed gas, surface modifications dramatically increase. Compared to the 1:4 N<sub>2</sub>/O<sub>2</sub> ratio, C-C/H composition drops from 76.5% to 62.1%, C-O increases from 18.7% to 27.3%, O-C-O/C=O/N-C=O increases from 4.6% to 6.9%, and O-C=O emerges from 0.2% to 3.7%. Figure 6.14(b) shows the NO<sub>3</sub> and O composition (with and without NO<sub>3</sub>) as a function of the 1% N<sub>2</sub>/O<sub>2</sub> admixture chemistry. For the most weakly oxidizing

conditions,  $\text{NO}_3$  was the only modification. Similar to the SMD-treated materials, the O composition independent of  $\text{NO}_3$  was lower than that of the pristine material, indicating that  $\text{NO}_3$  forms at O-containing groups in the biomolecule. As the  $\text{O}_2$  admixture increases, both the O and  $\text{NO}_3$  composition increase. A significant fraction of the overall oxidation is due to  $\text{NO}_3$ , but pure oxidation is also present, which is consistent with the SMD treatment of the biomolecules. As the pure  $\text{O}_2$  admixture most effectively biodeactivated and modified the biomolecular films, we chose this gas chemistry for subsequent experiments. The overall  $\text{NO}_3$  composition after APPJ treatment is much lower than after SMD treatment. This suggests that different mechanisms are at work with an emphasis on RONS for the SMD and ROS for the APPJ.

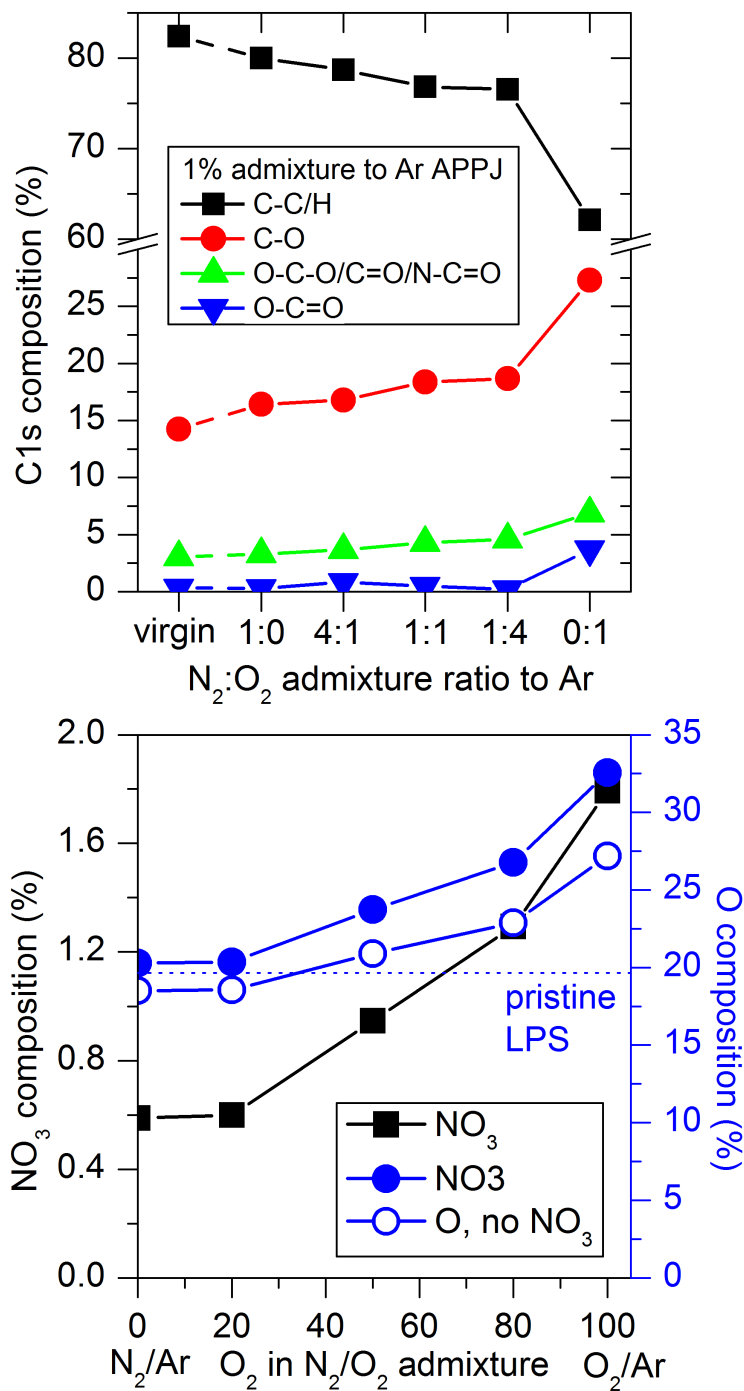


**Figure 6.14:** (a) LPS C1s composition for the virgin LPS film and after various 1% molecular gas admixtures to Ar APPJ treatments. In (b) the LPS NO<sub>3</sub> and O compositions as a function of the 1% N<sub>2</sub>/O<sub>2</sub> gas admixture chemistry. Mention APPJ

**Negligible etching after treatments.** Real-time *in situ* ellipsometry was used to determine if biodeactivation and surface modifications were accompanied by etching. The LPS film thickness was measured for 1% O<sub>2</sub> in Ar feed gas when the source was 9 cm from the nozzle and the nozzle is 3 cm from the sample. Previous work demonstrated that polystyrene surface modifications were highest in a pure N<sub>2</sub> ambient compared to O<sub>2</sub>-containing ambients. Thus, an N<sub>2</sub> ambient was used to simulate the more strongly modifying conditions. The LPS film thickness was unchanged over the course of the treatment. Similar to the SMD, etching is not required for changes in biological activity.

## 6.4. Discussion

### 4.1. Comparison of APPJ and SMD

APPJ treatments of model polymers are not shown here, but are consistent with the LPS work and previous PS work.<sup>[213]</sup> That is, modifications were much less and NO<sub>3</sub> formation was very low (< 1.5%). There are several key differences between the two sources. The SMD is much closer to the sample surface (3 mm) compared to the APPJ nozzle (3 cm). This proximity difference is likely the strongest contributor to the difference in modification. While the APPJ experiments in this work were performed with O<sub>2</sub>/N<sub>2</sub>/Ar mixtures, many studies in the literature use He or Ar without molecular gas admixtures. The reactive species required for these modifications are produced through the interaction of the plasma with the ambient environment. Unfortunately, these gases are quite expensive. Furthermore, noble gas APPJs sustained with low frequency power at close nozzle-sample distances can electrically interact with the sample, which can create spots or pinholes, and have discharge properties (e.g. plume length) changing during the treatment.<sup>[127]</sup> The 3 cm nozzle-sample distance used in this study is ideal for studying

remote treatments. However, an Ar or N<sub>2</sub>/Ar APPJ will electrically interact with the sample if the ground electrode is too close to the nozzle, in the author's experience. This gap also allowed for sufficient plasma-ambient interactions to occur, which we have shown can serve as another knob to regulate surface modifications. On the other hand, the SMD grounded mesh can be very close to the sample without any electrical interaction. As there is no gas flow or noble gas, the plasma is confined to the area around the mesh. Provided that the grounded mesh is flat, the SMD is very uniform and easily scalable. The excitation processes are very different in the two systems. Ar metastables have a relatively high energy of 11.5 and 11.7 eV, which could contribute to dissociation and excitation of O<sub>2</sub> and N<sub>2</sub>. The SMD is also most efficient for ~15% N<sub>2</sub>/O<sub>2</sub> gas. In contrast, the APPJ was shown to be most effective at biodeactivation and surface modifications for O<sub>2</sub>/Ar plasma without any N<sub>2</sub>. This marks a major difference in the reactive output of the two sources and demonstrates that the SMD likely relies on NO<sub>x</sub> chemistry while the APPJ relies on reactive oxygen species such as SDO. SDO has been measured in APPJs and is mainly produced by electron impact excitation of O<sub>2</sub> molecules.<sup>[222]</sup> Increasing the applied voltage of the APPJ decreased O<sub>3</sub> production but increased surface modifications of polystyrene, possibly due to increased formation of SDO.<sup>[213]</sup>

Increasing the applied voltage of the SMD decreased surface modifications. We additionally observed evidence that O<sub>3</sub> was important for surface modifications. This is inconsistent with the work by Pavlovich et al., but can be explained by the difference in chamber volumes and gas chemistry.<sup>[168]</sup> In their work, the measurement cell was 0.09 l without any air flow. Due to the small volume, SMD-generated O<sub>3</sub> can easily react again with the SMD to dissociate and form NO<sub>x</sub>. In this work, O<sub>3</sub> can remain in the chamber due to the large volume and interact with the gas to form additional NO<sub>2</sub>/NO<sub>3</sub> or the sample to form alkoxy radicals, as

described above. In the high-power “NO<sub>x</sub> mode,” Pavlovich et al. observed negligible O<sub>3</sub> formation. Given the higher concentrations of O<sub>2</sub> in this work, we expect and continue to measure O<sub>3</sub> formation still at higher powers. The fact that the surface modifications decrease when the peak-peak voltage is increased from 6 kV<sub>pp</sub> to 8 kV<sub>pp</sub> is similar to the weakest bacterial decontamination being observed in the unstable, transitional region between the two modes observed by Pavlovich et al. We speculate that increasing the applied voltage above 8 kV would result in higher surface modifications as the transition to “NO<sub>x</sub> mode” is completed.

The APPJ also emits high energy photons in the ultraviolet/vacuum ultraviolet (UV/VUV) range, which unpublished work in our group has shown to modify polymer films over long treatment times. VUV surface interactions at atmospheric pressure have also been studied with He/O<sub>2</sub> with a modified μ-APPJ, called the X-jet.<sup>[191, 223, 224]</sup> VUV emission by Ar APPJs has also been measured by Reuter et al. and results from the Ar<sub>2</sub>\*-eximer second continuum in the region between 120-135 nm.<sup>[126]</sup> This source was a MHz-powered APPJ consisting of a powered centered rod electrode in a ceramic tube and a grounded ring electrode. While the APPJ-generated VUV-induced etching of the films is very slow, H-abstraction by VUV radiation is widely accepted.<sup>[1, 88-90, 92, 139]</sup> Similarly, C-C bond cleavage can occur by UV photons having energies > 4-5 eV to form surface alkyl radical sites.<sup>[225]</sup> In an O<sub>2</sub>-containing environment, the resulting surface radicals will form peroxy radicals, which decompose into a variety of oxidized surface species. Incident photons with wavelengths below ~160 nm can be absorbed by hydrocarbons due to dipole transitions and electronic excitations of C-H and C-C σ bonds.<sup>[147]</sup> The SMD can generate UV radiation from the NO γ system (200 nm < λ < 300 nm).<sup>[172]</sup> Photoabsorption in this region results from chromophores such as C=C and oxygen containing groups. However, VUV effects are not dominating as polypropylene, which contains

only C-C/H bonds, shows much less oxidation after APPJ treatment compared to the SMD treatment.

Despite these differences, we see that both sources are able to biodeactivate films effectively. This highlights the sensitivity of the biomolecules' biological activity to small structural changes. That is, major modifications are not required. Given that monoclonal antibodies can be made specific to a particular species of a given biomolecule i.e. peptidoglycan from *Staphylococcus* vs. *Streptoloccus*, it is not surprising that small modifications can destroy the biological activity. The mammalian innate immune system works through molecular pattern recognition whereby structural motifs common to several classes of bacterium e.g. the aliphatic chains and diphosphate groups on lipid A.<sup>[226]</sup> As noted above, small changes to these conserved structures can greatly reduce the immune response.

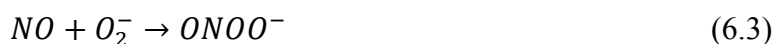
#### 4.2 Polymer Modification Mechanisms

Polymer surface modifications have been extensively studied at low<sup>[67, 78, 88, 227-229]</sup> and atmospheric<sup>[127, 151, 186, 187, 213, 230-235]</sup> pressure. Comparison with the literature is difficult given the remote conditions used in this work; a majority of studies place the sample between the electrodes (for dielectric barrier discharges) or in direct contact with a visible plasma plume. Thus, extremely short-lived species e.g. charged species and OH/O radicals dominate. For polymers, high energy photons will play a role in creating radical sites. The photochemistry can proceed via elimination of H<sub>2</sub> to form adjacent alkyl radical sites, which can undergo chain scission or recombine to form an alkene, of which the latter is less likely.<sup>[225]</sup> Additionally, high energy photons can break C-C bonds or C-H bonds. Given the remote nature of these treatments and the lifetime of reactive neutrals such as O and OH, initiation of radical chain reactions may

occur via high energy photons. Lipid peroxidation studies have shown that NO is not a strong enough oxidant to initiate lipid peroxidation, but NO<sub>2</sub> is.<sup>[182, 236, 237]</sup> NO<sub>3</sub> also has been reported to abstract H from aromatics, which is relevant for PS, and has been modeled in the SMD.<sup>[145, 153, 169]</sup> However, the role of gas phase NO<sub>3</sub> is uncertain as it has not been directly measured in the effluent of CAP sources. NO<sub>3</sub> has been measured in DBDs at low concentrations, but reacts quickly with NO to form NO<sub>2</sub>.<sup>[105, 238]</sup> However, it may be present since NO<sub>2</sub><sup>[123]</sup> and O<sub>3</sub><sup>[140]</sup> have both been measured, which react to form NO<sub>3</sub> by:



Even though NO cannot by itself abstract H, it has been well-established as a key species in the effluent of CAP sources with densities in the 10<sup>14</sup>-10<sup>15</sup> cm<sup>-3</sup> range for MHz jets and in the low 10<sup>16</sup> cm<sup>-3</sup> for the SMD.<sup>[98, 167, 168]</sup> NO may indirectly contribute to H-abstraction by forming the peroxy nitrite anion, which has been widely studied in physiological conditions and has well-established roles in biological systems. This species forms through reaction of superoxide and NO:<sup>[203, 236, 239]</sup>



After H-abstraction, a variety of reactions can occur, some of which have been discussed in a previous publication.<sup>[213]</sup> The abundant O<sub>2</sub> present during treatment can add to a radical site to form peroxy radicals and hydroperoxide, which result in alcohols, aldehydes, and ketones.<sup>[147]</sup> O<sub>3</sub> is also present, which can react with alkyl radicals to form alkoxy radicals and O<sub>2</sub>. Similar to peroxy radicals and hydroperoxide, alkoxy radicals can result in a variety of oxygenated species. NO<sub>x</sub> species can also interact with alkoxy and peroxy radicals and is likely a key species for the formation of surface-bound NO<sub>3</sub>. For example, NO can react with peroxy radicals to form an unstable intermediate that a) isomerizes to R-ONO<sub>2</sub> or b) results in an alkoxy radical. Alkoxy



radicals can react with  $\text{NO}_2$  to form  $\text{R-ONO}_2$ .<sup>[145]</sup> Given that only  $\text{NO}_3$  is observed on CAP treated surfaces, direct addition of  $\text{NO}_2$  to alkyl radical sites is not a final product. NO can also add onto a radical site, but this is not a final product as N-O bonds are not measured by XPS. Wilken et al. describe additional NO radicals interacting with  $\text{R-N=O}$  sites in polyolefins to form nitrate groups by losing  $\text{N}_2$  and  $\text{O}_2$ .<sup>[143, 240]</sup> The sensitivity of SMD surface modifications with regard to  $\text{N}_2$  admixture is similar to work by Kastenmeier et al. and supports the importance of NO.<sup>[155, 180]</sup> They found that silicon nitride etch rates were enhanced by a factor of 7 when 10%  $\text{N}_2$  was added to a  $\text{CF}_4/\text{O}_2$  low pressure plasma. Further increasing the  $\text{N}_2$  admixture above 10% caused the etch rate to drop again. The measured etch rate was correlated with the NO concentration in the reaction chamber.

This work demonstrates material-dependent modifications and selectivity for modifications at certain moieties. SMD treatment of PVA showed that most of the oxidation after  $\text{N}_2/\text{O}_2$  treatment resulted from  $\text{R-ONO}_2$  at the expense of  $\text{R-OH}$ . This indicates that nitrate formation occurs at the  $-\text{OH}$  site more selectively than the methylene bridge. One possible mechanism for this is  $\text{NO}_2$  addition to an alkoxy radical after H-abstraction from the alcohol group, which was reported as an initiation step in a recent computational study by van der Paal et al.<sup>[241]</sup> Other mechanisms are possible, but this observation suggests that the introduction of nitrate groups could originate from  $\text{R-OH}$  groups. In fact, the highest  $\text{R-ONO}_2$  content is found on the  $-\text{OH}$  containing materials i.e. PVA (10%  $\text{NO}_3$ ), PGN (6.4%  $\text{NO}_3$ ), and LPS (5.3%  $\text{NO}_3$ ). Further work is needed to determine whether the C-OH bond or the CO-H bond is broken. In previous work, we have described a competition between oxidation and nitridation of polystyrene films. This competition also occurs for PVA, PS, and LPS as well since more carbon-oxygen groups are observed in the C1s after  $\text{O}_2$  SMD treatment.

We measured the least amount of oxidation and NO<sub>3</sub> formation by CAP treatment for PMMA. This indicates that ester bonds are very stable, which is reasonable as they are formed after plasma treatment of other materials. H-abstraction at the  $\alpha$  carbon on the polymer backbone cannot occur as there are no C-H bonds there, so H-abstraction would most likely occur at the secondary carbon. As secondary alkyl radicals are less stable than tertiary radicals, they are formed less easily. H-abstraction from polystyrene is particularly stable since the resulting radical can be stabilized through the aromatic ring. Indeed, aromatic groups appear to be very susceptible to oxidation.

#### *4.3 Comparison to Simulations*

Computer simulations are complementary to experimental work and can be very valuable toward achieving an atomistic understanding of plasma-material interactions. A number of recent reactive molecular dynamics (MD) simulations have modeled the interaction of atmospheric plasma-generated reactive neutrals with biomolecules including PGN<sup>[179, 242]</sup>, lipid A<sup>[178]</sup>, and lipids present in human skin.<sup>[243]</sup> Atmospheric plasma-surface interaction modeling has been recently reviewed by Bogaerts et al.<sup>[244]</sup> These works focus on reactive oxygen species including O atoms, OH, H<sub>2</sub>O<sub>2</sub>, O<sub>3</sub>, and HO<sub>2</sub>. While RONS and RNS are known to have bactericidal effects and, as we have shown via XPS, interact with surfaces, the force fields required for ReaxFF do not accurately describe these reactions. Additionally, the force field parameter for O<sub>3</sub> is also uncertain. While we do not believe that the mean free paths of O and OH are long enough to directly interact with our samples, some effects could be generic. Furthermore, the functional groups resulting from these simulations could react further. For example, Yusupov et al. report that OH, HO<sub>2</sub>, and H<sub>2</sub>O<sub>2</sub> impacts on lipid A create alkene, aldehyde groups, and also desorbed

aliphatic chains with a radical end group. Alkenes are known to react with  $O_3$  and  $NO_3$  to form a variety of oxidized species.<sup>[145, 154, 245]</sup> Aldehyde groups can also be further oxidized to acids.<sup>[246]</sup> Desorbed aliphatic chains with a radical at the carboxyl head group can further react within the film. Most reactions occurred in the disaccharide backbone, with events at the aliphatic chains only occurring 1.7% of the time. For both lipid A and peptidoglycan, our experiments measure major oxidation of the surface. For lipid A, simulations show the formation of C=O bonds, indicative of cleavage of the glycosidic bond on lipid A's disaccharide backbone. Presumably, similar glycosidic bond cleavages could occur on the O-chain and core oligosaccharide as well.

The simulated mechanisms for bond-breaking processes for ROS interacting with peptidoglycan are similar to lipid A with initiation by H-abstraction by O atoms, OH, and  $H_2O_2$  (via  $HO_2$ ).<sup>[179, 242]</sup> Most of the bond-breaking processes occur in the disaccharides rather than the peptide crosslinks and resulted in cleavage of ether bonds: one on MurNAc, one on GlcNAc, and one between them. These bond-breaking events are followed by the formation of C=C and C=O bonds. This is promising for decontamination applications since the disaccharide backbone in PGN is widely conserved compared to the peptide chains, indicating that the backbone is involved in the molecular pattern recognition by the innate immune system.<sup>[41]</sup> As the backbone is easily modified, biodeactivation is easier. Even though H-abstraction takes place, Yusupov et al. attributed the lack of modifications to the pentaglycine bridge to stabilization via resonance.<sup>[179, 242]</sup>

Dorai and Kushner conducted a computational investigation on dielectric barrier discharge treatments of polypropylene.<sup>[138]</sup> They report increased energy deposition causing increased production of alcohol, carbonyl, acid, and peroxy radicals on the PP surface and increased  $O_3$  and  $NO_x$  production in the gas phase. Increasing the relative humidity and gas

temperature decreased alcohol, carbonyl, and acid groups and increased peroxy radicals on the surface. Similar to the work by Yusupov et al., the main species interacting with the surfaces were O atoms and OH radicals, which abstracted H, leading to peroxy radical formation.<sup>[178, 179, 242]</sup> The initiating reactions for H abstraction at the tertiary carbon have a rate that is 150 times larger than those at the secondary carbon. While we cannot distinguish the attack site on PP by XPS, we do observe replacement of the alcohol group in PVA with  $\text{ONO}_2$ , indicating that reactions at the tertiary carbon are more common in PVA. Another possibility observed in a recent study by van der Paal et al. found that H-abstraction of ceramides by OH radicals occurs most often at the H atom in alcohol groups.<sup>[241]</sup> Favorable attack at the tertiary carbon is supported by the lack of modifications on PMMA since a C-H bond on a tertiary carbon is not available.

The aforementioned results, discussion, and comparison with other work can provide insights into why PGN and LPS show different biodeactivation behavior, as shown in Fig. 6.3. PGN was able to deactivate under all conditions, but LPS required higher  $\text{NO}_3$  producing conditions. There are two possibilities. Both LPS and PGN have disaccharide backbones, where the dominant reactions have been simulated. This layer also contains more  $-\text{OH}$  groups, which this work has shown are more susceptible to  $\text{NO}_3$  modification and where H-abstraction has been simulated. We previously reported angle-resolved XPS measurements demonstrating that lipid A forms favorably at the air-film interface.<sup>[139]</sup> This layer of aliphatic chains is not present in PGN and only 1.7% of bond-breaking reactions were simulated in lipid A's aliphatic chains. This layer of aliphatic chains may act as a barrier to modifications in lipid A and could partly explain why PGN is easier to deactivate. Furthermore, PGN has more  $-\text{OH}$  sites on the disaccharide backbone to react with reactive species.

## 5. Conclusion

In conclusion, we have compared two drastically different CAP sources, an APPJ operating with low N<sub>2</sub>/O<sub>2</sub> admixtures to Ar and an SMD operating with N<sub>2</sub>/O<sub>2</sub> mixtures, in their ability to deactivate biomolecules and modify a variety of surfaces under remote conditions where charged species do not interact with the sample. Despite the differences between the two sources, both sources can effectively deactivate the biomolecules. Given that neither source etched the films, surface modifications are sufficient to change biological function. However, the surface modifications are very different for the two sources: NO<sub>x</sub> species dominate for the SMD while ROS and NO<sub>x</sub> dominate for the APPJ. Overall, surface modifications are much stronger after SMD treatment using only O<sub>2</sub>/N<sub>2</sub> gas mixtures with more oxidation and surface-bound NO<sub>3</sub> than after APPJ treatment. By varying the gas chemistry of the SMD, we find that surface-bound NO<sub>3</sub> is a dominant and generic surface modifications to a variety of materials, but forms at different amounts depending on the surface. The competition between oxidation and nitridation first reported in APPJ-treated PS was also observed with the SMD and some of the material studied here. Biodeactivation of both LPS and PGN correlated with NO<sub>3</sub>. By studying model polymers with different molecular structures, we saw that reactions occur more likely at tertiary carbons. NO<sub>3</sub> formation also occurs most strongly on materials containing alcohol groups, with the most NO<sub>3</sub> forming on PVA, which contains the highest OH density of all the materials studied. In contrast, APPJ treated surfaces showed much less NO<sub>3</sub> formation with N<sub>2</sub>/O<sub>2</sub> admixtures to Ar causing less modification than O<sub>2</sub>-only admixtures. This study provides valuable information on surface modifications by surface microdischarges currently used for

surface disinfection and provides insights into fundamental understandings of how CAP sources interact with surfaces, which is crucial to the advancement of plasma medicine.

### **Acknowledgements**

The authors gratefully acknowledge helpful discussions and support of the project by D. Metzler, C. Li, A. Pranda, and C. Hart. This work is supported by the US Department of Energy (DE-SC0005105 and DE-SC0001939) and National Science Foundation (PHY-1004256 and PHY-1415353).

## Chapter 7: Conclusions and Future Work

The investigations presented in this dissertation are relevant to the rapidly expanding variety of applications for atmospheric pressure plasma on a variety of materials, including living tissue and polymer surfaces. This work advanced the fundamental, atomistic understanding of plasma-surface interactions with biological tissues at low and atmospheric pressure by 1) identifying the individual contributions of plasma-generated species toward biodeactivation, 2) demonstrating the impact of plasma-ambient interactions with model biomolecules and polymers, 3) for the first time, correlating a specific surface moiety with biological function, and 4) demonstrating the impact of material structure and composition on plasma-induced surface modifications.

In Chapter 2, we studied the individual contributions of ions, high energy photons, and radicals to lipopolysaccharide (LPS) etching, biodeactivation, and surface modifications by using an optical filter approach and a gap structure to isolate UV/VUV photons and radicals, respectively. Direct H<sub>2</sub> and Ar plasmas lead to relatively high etch rates and rapid biodeactivation, but the surface modifications were very different. Direct H<sub>2</sub> plasma created an oxygen-deficient surface more selectively targeted amide groups than the direct Ar plasma. UV/VUV-only treatments also created an oxygen-deficient surface, but the etch rate and biodeactivation were slower. In contrast, radical-only treatments did not etch the films, but still caused biodeactivation. Plasma-generated radicals reduced the amount of aliphatic carbon on the near-surface, and exposed the underlying carbohydrate layers.

The fact that radicals can induce changes in biodeactivation without damaging the target surface motivated studies at atmospheric pressure where the role of charged species and high energy photons will drop dramatically due to the high pressure. Negligible material removal is

also critical for plasma-based disinfection of sensitive medical devices as they can be cleaned without damaging the device.

In Chapter 3, an atmospheric pressure plasma jet (APPJ) was described and used to modify and deactivate LPS films. ELISA, OES, and UV absorption measurements corroborated that when  $N_2$  is purposely added to the feed gas, ROS are reduced. No  $N_2/O_2$  mixture to the Ar feed gas more effectively deactivated the films than the  $O_2$ -only admixture. OES showed that  $O^*$  and  $N_2^*$  emissions decrease for  $O_2/N_2$  admixtures, which we attribute to the two species reacting with one another. By measuring the ozone density, we saw that small admixtures of  $N_2$  to ozone producing plasmas significantly decrease the ozone density. The interaction of the plasma with varying  $N_2/Ar$  ambients showed that ambient  $N_2$  can also quench plasma-generated reactive oxygen species. We observed decreased surface oxidation by XPS when the ambient  $N_2$  content was increased. This work demonstrates that plasma-environment interactions play a major role and demand consideration for future studies on APPJ surface treatments.

In Chapter 4, the impact of the plasma-ambient interaction on surface modifications was further studied using polystyrene as a model system. We used remote interaction conditions where negligible surface etching and roughening occurs. Overall, polystyrene surfaces were oxidized with a loss of aromaticity. We measured  $NO_x$  groups at low concentrations ( $< 3\%$ ) on the film surface, which had not previously been studied or reported in the literature after atmospheric pressure plasma treatment. As polystyrene contains neither oxygen nor nitrogen, the precursors for this species must originate in the gas phase. We found that oxygen atoms and ozone do not play a large role, and suggested that singlet delta oxygen, high energy photons, and  $NO_x$  are important. We also described a competition between surface oxidation and nitridation by varying the availability of oxygen in the feed gas and ambient. Unless reactive oxygen species



are created in the discharge,  $\text{NO}_x$  plays a key role. Polystyrene oxidation was very easy and occurred under a variety of conditions, but formation of  $\text{NO}$ ,  $\text{NO}_2$ , and  $\text{NO}_3$  on the surface is difficult and only occurs under specific conditions (for  $\text{NO}$  and  $\text{NO}_2$ ). We proposed a possible mechanism for gas-phase  $\text{NO}_x$ -based modifications that require additional work to confirm, especially from simulations.

In Chapter 5, the role of  $\text{NO}_3$  was further explored. We found that it forms on a variety of biomolecular and polymeric surface after treatment by two very different sources, the APPJ and surface microdischarge (SMD). For the APPJ,  $\text{NO}_3$  concentrations were highest for  $\text{O}_2/\text{Ar}$  plasma. In contrast, the SMD showed the highest  $\text{NO}_3$  concentrations for low admixtures of  $\text{N}_2$  to  $\text{O}_2$ . However, as  $\text{N}_2$  is added to the  $\text{O}_2$  feed gas, oxidation independent of  $\text{NO}_3$  decreases. To explain the surface modifications, we introduced a Langmuir adsorption model where surface-bound  $\text{NO}_3$  disrupts the non-specific interactions required for effective antibody-LPS binding by modifying the LPS binding site. By comparing surface modifications with biodeactivation, we found that surface  $\text{NO}_3$  composition, not oxidation independent of  $\text{NO}_3$ , correlated better with biodeactivation. The specific mechanism by which  $\text{NO}_x$  species contribute to biodeactivation is not completely clear, but this work presented compelling evidence that  $\text{NO}_x$  species are important for surface processes at atmospheric pressure. This work represents the first effort in the literature toward correlating a specific surface moiety with biological functions.

In Chapter 6, we continued surface chemical analysis after treatments using the surface microdischarge. Biomolecules and model polymers were treated and comparisons were made with the APPJ. Despite the differences between the two sources, both can biodeactivate biomolecules effectively, but the SMD caused dramatically more modifications with significantly more surface-bound  $\text{NO}_3$ . Indeed, the SMD relies on RONS while the APPJ relies

on ROS. Consistent with the previous work,  $\text{NO}_3$  formed on a variety of surfaces and was a dominant feature, depending on the gas chemistry and molecular structure of the target surface. We showed that surfaces containing C-H bonds at a tertiary carbon show the strongest modifications. Furthermore, the highest  $\text{NO}_3$  compositions were found on materials containing alcohol groups.

Overall, the ideas and analysis presented here, i.e. identifying which plasma-generated species are responsible for modifications that lead to changes in biological activity, are critical to advancing the cutting edge of the emerging field of plasma medicine. The approaches described above can be used for many different biomolecules. The selectivity observed for different molecular structures may explain the observed sensitivities of CAP treatment of cancer cells and may even be used to functionalize specific domains such as carbohydrates.<sup>[196]</sup> RONS have well-established roles in biological systems. This work shows for the first time that these RONS can directly interact with CAP-treated surfaces. Further, quantitative gas-phase characterization techniques need to be used, especially for the SMD, to confirm which species are dominating. A key missing piece of information is the flux of reactive species striking the surface. In the next steps, the impact of water vapor, both in the feed gas and in the ambient, needs to be explored. On a similar note, CAP-treated water has antimicrobial properties that need to be tailored for specific applications. Other well-studied, model intermolecular interactions, such as the biotin-streptavidin bond, can be investigated too. The polymer treatments performed in this research can also be correlated with biological effects e.g. antimicrobial surfaces or patterned surfaces to promote cell adhesion. Lastly, the role of  $\text{NO}_x$  species needs to be incorporated into computational investigations.

## Appendix A: ELISA Protocol

An enzyme-linked immunosorbent assay (ELISA) was used to estimate the biological activity of LPS and PGN after plasma treatment by the APPJ or SMD. The ELISA proceeds as follows and is based on a protocol provided by the primary antibody manufacturer. Unless otherwise noted, all incubation steps were performed at room temperature and solution volumes were 100  $\mu\text{l}$ . For LPS, various concentrations of LPS (0.01 – 10  $\mu\text{g/ml}$ ) in DOCA buffer (formulation: 2.28 g monobasic sodium phosphate, 11.5 g dibasic sodium phosphate, 0.163 g NaCl, and 0.882 g deoxycholic acid brought to one liter with distilled/deionized water) were incubated overnight in a 96-well plate (Nunc Maxisorp, EBioscience) to form a standard curve and the to-be-treated wells. The only difference for PGN was that the solvent was 0.1 M carbonate-bicarbonate (pH 9.6). All wells were prepared in duplicate. The plates were then washed three times with 220  $\mu\text{l}$  PBS containing 0.04% Tween-20 (PBS-T). Before plasma treatment, the wellplates were placed under vacuum at  $2 \times 10^{-3}$  Pa for at least 30 minutes to dry the wells. The wells were then treated by the plasma under specific conditions. Untreated wells were covered by a Parafilm M. To prevent the Parafilm M from damage when the well is pumped down, a tiny hole was pierced into the Parafilm M over each well using a needle. These wells were then additionally covered with a Si piece that was secured with Kapton tape. The wells were then treated by the plasma. After plasma treatment, 150  $\mu\text{l}$  of 1% BSA in PBS-T (BSA-PBS-T) was added for 30 minutes as a blocking step. For the primary antibodies, 80  $\mu\text{l}$  was added at a concentration of 1  $\mu\text{g/ml}$  and 10  $\mu\text{g/ml}$  in BSA-PBS-T for LPS and PGN, respectively, and incubated for 30 minutes on a rocking platform. After washing three times with PBS-T, 80  $\mu\text{l}$  of 3  $\mu\text{g/ml}$  of HRP-conjugated goat anti-mouse secondary antibody in BSA-PBS-T was added and incubated for 30 minutes on a rocking platform. HRP is light sensitive, so the

well plate was covered during this incubation. The wells were washed another three times and then incubated with 3,3',5,5'-tetramethylbenzidine (TMB, 1-Step Slow TMB, Thermo Scientific) for 15 minutes. Reactions were stopped by addition of 2 M H<sub>2</sub>SO<sub>4</sub> and the optical density at 450 nm was measured within 10 minutes by an automatic microplate reader (Synergy HT Multi-Mode, BioTek).

The protocol for measuring biotinylated-LPS (bLPS) is similar. Various concentrations of bLPS in PBS (0.01 – 5 µg/ml) were prepared and incubated in a 96-well plate for two hours. All wells were prepared in duplicate. The plates were washed three times with 220 µl PBS-T and subsequently placed inside the vacuum chamber at  $2 \times 10^{-3}$  Pa for at least 30 minutes. Placing the plates under vacuum did not affect the bioactivity as shown in Figure 2.4. After treatment, the wells were incubated with 150 µl of blocking solution (StartingBlock, Thermo Scientific) for 90 minutes or overnight at 4 °C, emptied, and filled again with fresh blocking solution for another 30 minutes. Then, the wells were washed three times with T-PBS and incubated for 30 minutes with 0.25 µg ml<sup>-1</sup> horseradish peroxidase-conjugated streptavidin in PBS (Streptavidin-HRP, Invitrogen). After washing three times with T-PBS, the wells were incubated with TMB for 10 minutes. Reactions were stopped by addition of 2 M H<sub>2</sub>SO<sub>4</sub> and the optical density at 450 nm was measured within 10 minutes by an automatic microplate reader (Synergy HT Multi-Mode, BioTek).

To analyze the results, the optical density for the negative control (0 µg/ml of antigen) was subtracted from all the wells. Treated wells were then compared to untreated wells from the standard curve of the same pretreatment concentration. The biological activity is defined as a ratio of the absorbance of the treated well to the absorbance of the untreated well in the standard curve of the same initial concentration. We consider this the normalized biological activity (BA):

$$BA = \frac{A_p}{A_0} \quad (\text{A.1})$$

where  $A_p$  is the absorbance of the plasma treated well and  $A_0$  is the absorbance of the untreated well. The normalized biodeactivation (BDA) is unity minus this value:

$$BDA = 1 - BA \quad (\text{A.2})$$

Thus, a normalized biodeactivation of unity would correspond to complete biodeactivation and zero would correspond to zero biodeactivation.

## References

- [1] T.-Y. Chung, N. Ning, J.-W. Chu, D. B. Graves, E. Bartis, J. Seog, and G. S. Oehrlein, *Plasma Processes and Polymers*, **2013**, *10*, 2.
- [2] N. Andreeva, T. Ishizaki, P. Baroch, and N. Saito, *Japanese Journal of Applied Physics*, **2012**, *51*, 12.
- [3] H. S. Uhm, E. H. Choi, G. S. Cho, and Y. C. Hong, *Journal of the Korean Physical Society*, **2012**, *60*, 6.
- [4] Y.-F. Li, T. Shimizu, J. L. Zimmermann, and G. E. Morfill, *Plasma Processes and Polymers*, **2012**, *9*, 6.
- [5] N. N. Misra, B. K. Tiwari, K. S. M. S. Raghavarao, and P. J. Cullen, *Food Engineering Reviews*, **2011**, *3*, 3-4.
- [6] G. Fridman, M. Peddinghaus, H. Ayan, A. Fridman, M. Balasubramanian, A. Gutsol, A. Brooks, and G. Friedman, *Plasma Chemistry and Plasma Processing*, **2006**, *26*, 4.
- [7] M. Laroussi, *Plasma Processes and Polymers*, **2005**, *2*, 5.
- [8] K.-D. Weltmann, K. Fricke, M. Stieber, R. Brandenburg, T. von Woedtke, and U. Schnabel, *Ieee Transactions on Plasma Science*, **2012**, *40*, 11.
- [9] A. M. Hirst, F. M. Frame, N. J. Maitland, and D. O'Connell, *BioMed research international*, **2014**, *2014*.
- [10] N. K. Kaushik, Y. H. Kim, Y. G. Han, and E. H. Choi, *Current Applied Physics*, **2013**, *13*, 3.
- [11] X. Han, M. Klas, Y. Y. Liu, M. S. Stack, and S. Ptasinska, *Applied Physics Letters*, **2013**, *102*, 23.
- [12] S. Arndt, E. Wacker, Y.-F. Li, T. Shimizu, H. M. Thomas, G. E. Morfill, S. Karrer, J. L. Zimmermann, and A.-K. Bosserhoff, *Experimental Dermatology*, **2013**, *22*, 4.
- [13] N. Barekzi and M. Laroussi, *Plasma Processes and Polymers*, **2013**, *10*, 12.
- [14] M. Vandamme, E. Robert, S. Lerondel, V. Sarron, D. Ries, S. Dozias, J. Sobilo, D. Gosset, C. Kieda, B. Legrain, J.-M. Pouvesle, and A. Le Pape, *International Journal of Cancer*, **2012**, *130*, 9.
- [15] K. Kim, J. D. Choi, Y. C. Hong, G. Kim, E. J. Noh, J.-S. Lee, and S. S. Yang, *Applied Physics Letters*, **2011**, *98*, 7.
- [16] S. U. Kalghatgi, G. Fridman, M. Cooper, G. Nagaraj, M. Peddinghaus, M. Balasubramanian, V. N. Vasilets, A. F. Gutsol, A. Fridman, and G. Friedman, *Ieee Transactions on Plasma Science*, **2007**, *35*, 5.
- [17] S. Arndt, P. Unger, E. Wacker, T. Shimizu, J. Heinlin, Y.-F. Li, H. M. Thomas, G. E. Morfill, J. L. Zimmermann, A.-K. Bosserhoff, and S. Karrer, *Plos One*, **2013**, *8*, 11.
- [18] K. P. Arjunan, G. Friedman, A. Fridman, and A. M. Clyne, *Journal of the Royal Society Interface*, **2012**, *9*, 66.
- [19] K. P. Arjunan and A. M. Clyne, *Plasma Processes and Polymers*, **2011**, *8*, 12.
- [20] S. Kalghatgi, G. Friedman, A. Fridman, and A. M. Clyne, *Annals of Biomedical Engineering*, **2010**, *38*, 3.
- [21] G. Lloyd, G. Friedman, S. Jafri, G. Schultz, A. Fridman, and K. Harding, *Plasma Processes and Polymers*, **2010**, *7*, 3-4.
- [22] X. P. Lu, Y. G. Cao, P. Yang, Q. Xiong, Z. L. Xiong, Y. B. Xian, and Y. Pan, *Ieee Transactions on Plasma Science*, **2009**, *37*, 5.

- [23] M. Laroussi and X. Lu, *Applied Physics Letters*, **2005**, *87*, 11.
- [24] D. B. Graves, *Physics of Plasmas*, **2014**, *21*, 8.
- [25] E. C. Neyts, M. Yusupov, C. C. Verlaack, and A. Bogaerts, *Journal of Physics D-Applied Physics*, **2014**, *47*, 29.
- [26] G. Isbary, T. Shimizu, Y. F. Li, W. Stolz, H. M. Thomas, G. E. Morfill, and J. L. Zimmermann, *Expert Review of Medical Devices*, **2013**, *10*, 3.
- [27] M. G. Kong, G. Kroesen, G. Morfill, T. Nosenko, T. Shimizu, J. van Dijk, and J. L. Zimmermann, *New Journal of Physics*, **2009**, *11*.
- [28] G. Fridman, G. Friedman, A. Gutsol, A. B. Shekhter, V. N. Vasilets, and A. Fridman, *Plasma Processes and Polymers*, **2008**, *5*, 6.
- [29] D. B. Graves, *Journal of Physics D-Applied Physics*, **2012**, *45*, 26.
- [30] J. Friedrich, W. Unger, and A. Lippitz, *Macromolecular Symposia*, **1995**, *100*.
- [31] L. Moesby, E. W. Hansen, J. D. Christensen, C. H. Hoyer, G. L. Juhl, and H. B. Olsen, *European Journal of Pharmaceutical Sciences*, **2005**, *26*, 3-4.
- [32] C. R. Arciola, Y. H. An, D. Campoccia, M. E. Donati, and L. Montanaro, *International Journal of Artificial Organs*, **2005**, *28*, 11.
- [33] L. G. Glance, P. W. Stone, D. B. Mukamel, and A. W. Dick, *Archives of Surgery*, **2011**, *146*, 7.
- [34] H. Grundmann, M. Aires-de-Sousa, J. Boyce, and E. Tiemersma, *Lancet*, **2006**, *368*, 9538.
- [35] J. L. Zimmermann, T. Shimizu, H. U. Schmidt, Y. F. Li, G. E. Morfill, and G. Isbary, *New Journal of Physics*, **2012**, *14*.
- [36] D. Merche, N. Vandencastele, and F. Reniers, *Thin Solid Films*, **2012**, *520*, 13.
- [37] T. Belmonte, G. Arnoult, G. Henrion, and T. Gries, *Journal of Physics D-Applied Physics*, **2011**, *44*, 36.
- [38] D. Mariotti and R. M. Sankaran, *Journal of Physics D-Applied Physics*, **2010**, *43*, 32.
- [39] C. Erridge, E. Bennett-Guerrero, and I. R. Poxton, *Microbes and Infection*, **2002**, *4*, 8.
- [40] K. Brandenburg and A. Wiese, *Current Topics in Medicinal Chemistry*, **2004**, *4*, 11.
- [41] B. Fournier and D. J. Philpott, *Clinical Microbiology Reviews*, **2005**, *18*, 3.
- [42] K. Takeda and S. Akira, *International Immunology*, **2005**, *17*, 1.
- [43] S. E. Girardin and D. J. Philpott, *European Journal of Immunology*, **2004**, *34*, 7.
- [44] R. Dziarski, *Cellular and Molecular Life Sciences*, **2003**, *60*, 9.
- [45] B. Beutler and E. T. Rietschel, *Nature Reviews Immunology*, **2003**, *3*, 2.
- [46] J. Cohen, *Nature*, **2002**, *420*, 6917.
- [47] X. F. Hua, X. Wang, D. Fuentevilla, G. S. Oehrlein, F. G. Celii, and K. H. R. Kirmse, *Journal of Vacuum Science & Technology A*, **2003**, *21*, 5.
- [48] T. Standaert, M. Schaepkens, N. R. Rueger, P. G. M. Sebel, G. S. Oehrlein, and J. M. Cook, *Journal of Vacuum Science & Technology a-Vacuum Surfaces and Films*, **1998**, *16*, 1.
- [49] M. Teschke, J. Kedzierski, E. G. Finantu-Dinu, D. Korzec, and J. Engemann, *Ieee Transactions on Plasma Science*, **2005**, *33*, 2.
- [50] G. E. Morfill, T. Shimizu, B. Steffes, and H. U. Schmidt, *New Journal of Physics*, **2009**, *11*.
- [51] J. M. Williamson, D. Trump, P. Bletzinger, and B. N. Ganguly, *Journal of Physics D-Applied Physics*, **2006**, *39*, 20.

- [52] D. Briggs, *Surface Analysis of Polymers by XPS and Static SIMS*. Cambridge, England: Cambridge University Press, 1998.
- [53] E. Stoffels, Y. Sakiyama, and D. B. Graves, *Ieee Transactions on Plasma Science*, **2008**, 36, 4.
- [54] M. Hasiwa, O. Kylian, T. Hartung, and F. Rossi, *Innate Immunity*, **2008**, 14, 2.
- [55] O. Kylian, J. Benedikt, L. Sirghi, R. Reuter, H. Rauscher, A. von Keudell, and F. Rossi, *Plasma Processes and Polymers*, **2009**, 6, 4.
- [56] H. Rauscher, O. Kylian, J. Benedikt, A. von Keudell, and F. Rossi, *Chemphyschem*, **2010**, 11, 7.
- [57] F. Rossi, O. Kylian, and M. Hasiwa, *Plasma Processes and Polymers*, **2006**, 3, 6-7.
- [58] J. Pollak, M. Moisan, D. Keroack, and M. K. Boudam, *Journal of Physics D-Applied Physics*, **2008**, 41, 13.
- [59] J. Seguin, P. Levif, J. Pollak, M. Moisan, and J. Barbeau, *Abstracts of the General Meeting of the American Society for Microbiology*, **2009**, 109.
- [60] P. Levif, J. Seguin, M. Moisan, and J. Barbeau, *Plasma Processes and Polymers*, **2011**, 8, 7.
- [61] B. Elmoualij, O. Thellin, S. Gofflot, E. Heinen, P. Levif, J. Seguin, M. Moisan, A. Leduc, J. Barbeau, and W. Zorzi, *Plasma Processes and Polymers*, **2012**, 9, 6.
- [62] F. Bretagnol, H. Rauscher, M. Hasiwa, O. Kylian, G. Ceccone, L. Hazell, A. J. Paul, O. Lefranc, and F. Rossi, *Acta Biomaterialia*, **2008**, 4, 6.
- [63] H. Nikaido, *Science*, **1994**, 264, 5157.
- [64] Y. S. Lo, N. D. Huefner, W. S. Chan, P. Dryden, B. Hagenhoff, and T. P. Beebe, *Langmuir*, **1999**, 15, 19.
- [65] V. du Vigneaud, *Science (New York, N.Y.)*, **1942**, 96, 2499.
- [66] N. Fox-Lyon, G. S. Oehrlein, N. Ning, and D. B. Graves, *Journal of Applied Physics*, **2011**, 110, 10.
- [67] F. Weilmboeck, N. Kumar, G. S. Oehrlein, T. Y. Chung, D. Graves, M. Li, E. A. Hudson, and E. C. Benck, *Journal of Vacuum Science & Technology B*, **2012**, 30, 3.
- [68] J. R. Woodworth, M. E. Riley, V. A. Arnatucci, T. W. Hamilton, and B. P. Aragon, *Journal of Vacuum Science & Technology a-Vacuum Surfaces and Films*, **2001**, 19, 1.
- [69] L. Zheng, L. Ling, X. F. Hua, G. S. Oehrlein, and E. A. Hudson, *Journal of Vacuum Science & Technology A*, **2005**, 23, 4.
- [70] M. Sumiya, R. Bruce, S. Engelmann, F. Weilmboeck, and G. S. Oehrlein, *Journal of Vacuum Science & Technology B*, **2008**, 26, 6.
- [71] M. Sumiya, R. Bruce, S. Engelmann, F. Weilmboeck, and G. S. Oehrlein, *Journal of Vacuum Science & Technology B*, **2008**, 26, 5.
- [72] M. Sumiya, R. Bruce, S. Engelmann, F. Weilmboeck, and G. S. Oehrlein, *Journal of Vacuum Science & Technology B*, **2008**, 26, 5.
- [73] J. H. Scofield, *Journal of Electron Spectroscopy and Related Phenomena*, **1976**, 8, 2.
- [74] W. Richter, V. Vogel, J. Howe, F. Steiniger, A. Brauser, M. H. J. Koch, M. Roessle, T. Gutschmann, P. Garidel, W. Maentele, and K. Brandenburg, *Innate Immunity*, **2011**, 17, 5.
- [75] C. A. Aurell and A. O. Wistrom, *Biochemical and Biophysical Research Communications*, **1998**, 253, 1.
- [76] B. R. LaFreniere, D. R. Wiederin, V. A. Fassel, and R. S. Houk, *Spectrochimica Acta Part B-Atomic Spectroscopy*, **1996**, 51, 1.



- [77] A. C. Fozza, M. Moisan, and M. R. Wertheimer, *Journal of Applied Physics*, **2000**, *88*, 1.
- [78] R. L. Bruce, S. Engelmann, T. Lin, T. Kwon, R. J. Phaneuf, G. S. Oehrlein, B. K. Long, C. G. Willson, J. J. Vegh, D. Nest, D. B. Graves, and A. Alizadeh, *Journal of Vacuum Science & Technology B*, **2009**, *27*, 3.
- [79] G. S. Oehrlein, T. Schwarz-Selinger, K. Schmid, M. Schluter, and W. Jacob, *Journal of Applied Physics*, **2010**, *108*, 4.
- [80] P. Lazzeri, G. J. Stueber, G. S. Oehrlein, R. McGowan, and E. Busch, *Journal of Vacuum Science & Technology B*, **2006**, *24*, 6.
- [81] G. J. Stueber, G. S. Oehrlein, P. Lazzeri, M. Bersani, M. Anderle, E. Busch, and R. McGowan, *Journal of Vacuum Science & Technology B*, **2007**, *25*, 5.
- [82] J. H. Tong and T. J. McIntosh, *Biophysical Journal*, **2004**, *86*, 6.
- [83] O. Kylian, M. Hasiwa, D. Gilliland, and F. Rossi, *Plasma Processes and Polymers*, **2008**, *5*, 1.
- [84] H. Lodish, A. Berk, P. Matsudaira, C. A. Kaiser, M. Krieger, M. P. Scott, S. L. Zipursky, J. Darnell, *Molecular Cell Biology*, Fifth ed. New York: W. H. Freeman and Company, 2004.
- [85] O. H. Laitinen, V. P. Hytonen, H. R. Nordlund, and M. S. Kulomaa, *Cellular and Molecular Life Sciences*, **2006**, *63*, 24.
- [86] S. Roes, U. Seydel, and T. Gutschmann, *Langmuir*, **2005**, *21*, 15.
- [87] S. Vasquez-Borucki, C. A. Achete, and W. Jacob, *Surface & Coatings Technology*, **2001**, *138*, 2-3.
- [88] F. Weilnboeck, R. L. Bruce, S. Engelmann, G. S. Oehrlein, D. Nest, T. Y. Chung, D. Graves, M. Li, D. Wang, C. Andes, and E. A. Hudson, *Journal of Vacuum Science & Technology B*, **2010**, *28*, 5.
- [89] R. Wilken, A. Hollander, and J. Behnisch, *Plasmas and Polymers*, **2002**, *7*, 2.
- [90] A. Hollander and J. Behnisch, *Surface & Coatings Technology*, **1998**, *98*, 1-3.
- [91] D. Nest, D. B. Graves, S. Engelmann, R. L. Bruce, F. Weilnboeck, G. S. Oehrlein, C. Andes, and E. A. Hudson, *Applied Physics Letters*, **2008**, *92*, 15.
- [92] F. E. Truica-Marasescu and M. R. Wertheimer, *Macromolecular Chemistry and Physics*, **2005**, *206*, 7.
- [93] W. Jacob, *Thin Solid Films*, **1998**, *326*, 1-2.
- [94] B. Niermann, R. Reuter, T. Kuschel, J. Benedikt, M. Boeke, and J. Winter, *Plasma Sources Science & Technology*, **2012**, *21*, 3.
- [95] D. Ellerweg, A. von Keudell, and J. Benedikt, *Plasma Sources Science & Technology*, **2012**, *21*, 3.
- [96] J. S. Sousa, K. Niemi, L. J. Cox, Q. T. Algwari, T. Gans, and D. O'Connell, *Journal of Applied Physics*, **2011**, *109*, 12.
- [97] S. Reuter, J. Winter, S. Iseni, S. Peters, A. Schmidt-Bleker, M. Dunnbier, J. Schafer, R. Foest, and K. D. Weltmann, *Plasma Sources Science & Technology*, **2012**, *21*, 3.
- [98] A. F. H. van Gessel, B. Hrycak, M. Jasinski, J. Mizeraczyk, J. J. A. M. van der Mullen, and P. J. Bruggeman, *Journal of Physics D-Applied Physics*, **2013**, *46*, 9.
- [99] S. Bornholdt, M. Wolter, and H. Kersten, *European Physical Journal D*, **2010**, *60*, 3.
- [100] M. Y. Alkawareek, Q. T. Algwari, G. Laverty, S. P. Gorman, W. G. Graham, D. O'Connell, and B. F. Gilmore, *Plos One*, **2012**, *7*, 8.
- [101] J. Xu, C. Zhang, T. Shao, Z. Fang, and P. Yan, *Journal of Electrostatics*, **2013**, *71*, 3.

- [102] D. Duday, C. Vreuls, M. Moreno, G. Frache, N. D. Boscher, G. Zocchi, C. Archambeau, C. Van de Weerd, J. Martial, and P. Choquet, *Surface & Coatings Technology*, **2013**, 218.
- [103] E. Gonzalez, II and R. F. Hicks, *Langmuir*, **2010**, 26, 5.
- [104] J. P. Booth, O. Joubert, J. Pelletier, and N. Sadeghi, *Journal of Applied Physics*, **1991**, 69, 2.
- [105] U. Kogelschatz, *Plasma Chemistry and Plasma Processing*, **2003**, 23, 1.
- [106] K. D. Weltmann, E. Kindel, T. von Woedtke, M. Haehnel, M. Stieber, and R. Brandenburg, *Pure and Applied Chemistry*, **2010**, 82, 6.
- [107] B. Nisol, G. Oldenhove, N. Preyat, D. Monteyne, M. Moser, D. Perez-Morga, and F. Reniers, *Surface & Coatings Technology*, **2014**, 252.
- [108] A. S. Wu, S. Kalghatgi, D. Dobrynin, R. Sensenig, E. Cerchar, E. Podolsky, E. Dulaimi, M. Paff, K. Wasko, K. P. Arjunan, K. Garcia, G. Fridman, M. Balasubramanian, R. Ownbey, K. A. Barbee, A. Fridman, G. Friedman, S. G. Joshi, and A. D. Brooks, *Journal of Surgical Research*, **2013**, 179, 1.
- [109] G. Fridman, A. Shereshevsky, M. M. Jost, A. D. Brooks, A. Fridman, A. Gutsol, V. Vasilets, and G. Friedman, *Plasma Chemistry and Plasma Processing*, **2007**, 27, 2.
- [110] S. Abou Rich, T. Dufour, P. Leroy, L. Nittler, J. J. Pireaux, and F. Reniers, *Journal of Physics D-Applied Physics*, **2014**, 47, 6.
- [111] T. Dufour, J. Hubert, N. Vandencastele, P. Viville, R. Lazzaroni, and F. Reniers, *Journal of Physics D-Applied Physics*, **2013**, 46, 31.
- [112] J. Hubert, C. Poleunis, A. Delcorte, P. Laha, J. Bossert, S. Lambeets, A. Ozkan, P. Bertrand, H. Terryn, and F. Reniers, *Polymer*, **2013**, 54, 16.
- [113] J. Vorac, P. Dvorak, V. Prochazka, J. Ehlbeck, and S. Reuter, *Plasma Sources Science & Technology*, **2013**, 22, 2.
- [114] R. Ono and T. Oda, *Ieee Transactions on Industry Applications*, **2000**, 36, 1.
- [115] A. V. Pipa, T. Bindemann, R. Foest, E. Kindel, J. Roepcke, and K. D. Weltmann, *Journal of Physics D-Applied Physics*, **2008**, 41, 19.
- [116] K. Niemi, V. Schulz-von der Gathen, and H. F. Dobeles, *Plasma Sources Science & Technology*, **2005**, 14, 2.
- [117] N. Knake, S. Reuter, K. Niemi, V. Schulz-von der Gathen, and J. Winter, *Journal of Physics D-Applied Physics*, **2008**, 41, 19.
- [118] G. D. Stancu, F. Kaddouri, D. A. Lacoste, and C. O. Laux, *Journal of Physics D-Applied Physics*, **2010**, 43, 12.
- [119] S. Reuter, J. Winter, A. Schmidt-Bleker, D. Schroeder, H. Lange, N. Knake, V. Schulz-von der Gathen, and K. D. Weltmann, *Plasma Sources Science & Technology*, **2012**, 21, 2.
- [120] E. Wagenaars, T. Gans, D. O'Connell, and K. Niemi, *Plasma Sources Science & Technology*, **2012**, 21, 4.
- [121] M. J. Pavlovich, H.-W. Chang, Y. Sakiyama, D. S. Clark, and D. B. Graves, *Journal of Physics D-Applied Physics*, **2013**, 46, 14.
- [122] J. Winter, M. Dunnbier, A. Schmidt-Bleker, A. Meshchanov, S. Reuter, and K. D. Weltmann, *Journal of Physics D-Applied Physics*, **2012**, 45, 38.
- [123] S. Iseni, S. Reuter, and K.-D. Weltmann, *Journal of Physics D-Applied Physics*, **2014**, 47, 7.
- [124] W. Van Gaens and A. Bogaerts, *Plasma Sources Science & Technology*, **2014**, 23, 3.

- [125] A. Schmidt-Bleker, J. Winter, S. Iseni, M. Duennbier, K. D. Weltmann, and S. Reuter, *Journal of Physics D-Applied Physics*, **2014**, *47*, 14.
- [126] S. Reuter, J. Winter, A. Schmidt-Bleker, H. Tresp, M. U. Hammer, and K.-D. Weltmann, *Ieee Transactions on Plasma Science*, **2012**, *40*, 11.
- [127] A. J. Knoll, P. Luan, E. A. J. Bartis, C. Hart, Y. Raitses, and G. S. Oehrlein, *Applied Physics Letters*, **2014**, *105*, 17.
- [128] K. Fricke, S. Reuter, D. Schroeder, V. Schulz-von der Gathen, K.-D. Weltmann, and T. von Woedtke, *Ieee Transactions on Plasma Science*, **2012**, *40*, 11.
- [129] K. Fricke, I. Koban, H. Tresp, L. Jablonowski, K. Schroeder, A. Kramer, K.-D. Weltmann, T. von Woedtke, and T. Kocher, *Plos One*, **2012**, *7*, 8.
- [130] K. Fricke, H. Tresp, R. Bussiahn, K. Schroeder, T. von Woedtke, and K. D. Weltmann, *Plasma Chemistry and Plasma Processing*, **2012**, *32*, 4.
- [131] K. Fricke, H. Steffen, T. von Woedtke, K. Schroeder, and K.-D. Weltmann, *Plasma Processes and Polymers*, **2011**, *8*, 1.
- [132] Q. T. Algwari and D. O'Connell, *Ieee Transactions on Plasma Science*, **2011**, *39*, 11.
- [133] A. Van Deynse, P. Cools, C. Leys, R. Morent, and N. De Geyter, *Surface & Coatings Technology*, **2014**, *258*.
- [134] A. Van Deynse, N. De Geyter, C. Leys, and R. Morent, *Plasma Processes and Polymers*, **2014**, *11*, 2.
- [135] K. G. Kostov, T. M. C. Nishime, L. R. O. Hein, and A. Toth, *Surface & Coatings Technology*, **2013**, *234*.
- [136] D. Dixon and B. J. Meenan, *Journal of Adhesion Science and Technology*, **2012**, *26*, 20-21.
- [137] R. Morent, N. De Geyter, C. Leys, L. Gengembre, and E. Payen, *Surface & Coatings Technology*, **2007**, *201*, 18.
- [138] R. Dorai and M. J. Kushner, *Journal of Physics D-Applied Physics*, **2003**, *36*, 6.
- [139] E. A. J. Bartis, C. Barrett, T. Y. Chung, N. Ning, J. W. Chu, D. B. Graves, J. Seog, and G. S. Oehrlein, *Journal of Physics D-Applied Physics*, **2014**, *47*, 4.
- [140] E. A. J. Bartis, D. B. Graves, J. Seog, and G. S. Oehrlein, *Journal of Physics D-Applied Physics*, **2013**, *46*, 31.
- [141] [http://en.wikipedia.org/wiki/Amino\\_acid](http://en.wikipedia.org/wiki/Amino_acid).
- [142] K. Fricke, K. Duske, A. Quade, B. Nebe, K. Schroeder, K.-D. Weltmann, and T. von Woedtke, *Ieee Transactions on Plasma Science*, **2012**, *40*, 11.
- [143] R. Wilken, A. Hollander, and J. Behnisch, *Surface & Coatings Technology*, **1999**, *116*.
- [144] D. T. Clark and H. R. Thomas, *Journal of Polymer Science Part a-Polymer Chemistry*, **1978**, *16*, 4.
- [145] S. Gross and A. K. Bertram, *Journal of Geophysical Research-Atmospheres*, **2009**, *114*.
- [146] B. Eliasson, M. Hirth, and U. Kogelschatz, *Journal of Physics D-Applied Physics*, **1987**, *20*, 11.
- [147] J. F. Rabek, *Photodegradation of Polymers*. New York: Springer-Verlag, 1996.
- [148] D. Ellerweg, J. Benedikt, A. von Keudell, N. Knake, and V. Schulz-von der Gathen, *New Journal of Physics*, **2010**, *12*.
- [149] A. Vesel, *Surface & Coatings Technology*, **2010**, *205*, 2.
- [150] A. Vesel and M. Mozetic, *Vacuum*, **2012**, *86*, 6.
- [151] T. Homola, J. Matousek, B. Hergelova, M. Kormunda, L. Y. L. Wu, and M. Cernak, *Polymer Degradation and Stability*, **2012**, *97*, 6.

- [152] E. Gonzalez, II, M. D. Barankin, P. C. Guschl, and R. F. Hicks, *Plasma Processes and Polymers*, **2010**, 7, 6.
- [153] S. Gross and A. K. Bertram, *Journal of Physical Chemistry A*, **2008**, 112, 14.
- [154] Y. Zhang, R. C. Chapleski, J. W. Lu, T. H. Rockhold, D. Troya, and J. R. Morris, *Physical chemistry chemical physics : PCCP*, **2014**, 16, 31.
- [155] B. E. E. Kastenmeier, P. J. Matsuo, G. S. Oehrlein, R. E. Ellefson, and L. C. Frees, *Journal of Vacuum Science & Technology a-Vacuum Surfaces and Films*, **2001**, 19, 1.
- [156] B. E. E. Kastenmeier, P. J. Matsuo, G. S. Oehrlein, and J. G. Langan, *Journal of Vacuum Science & Technology a-Vacuum Surfaces and Films*, **1998**, 16, 4.
- [157] R. Atkinson and J. Arey, *Chemical Reviews*, **2003**, 103, 12.
- [158] R. Atkinson, S. M. Aschmann, W. P. L. Carter, A. M. Winer, and J. N. Pitts, *International Journal of Chemical Kinetics*, **1984**, 16, 9.
- [159] R. Atkinson, S. M. Aschmann, W. P. L. Carter, A. M. Winer, and J. N. Pitts, *Journal of Physical Chemistry*, **1982**, 86, 23.
- [160] I. C. Plumb, K. R. Ryan, J. R. Steven, and M. F. R. Mulcahy, *International Journal of Chemical Kinetics*, **1982**, 14, 2.
- [161] X. Zheng, G. Chen, Z. Zhang, G. Lv, J. Beem, S. Massey, and M. Tatoulian, *Plasma Processes and Polymers*, **2013**, 10, 4.
- [162] R. Reuter, D. Ellerweg, A. von Keudell, and J. Benedikt, *Applied Physics Letters*, **2011**, 98, 11.
- [163] S. Shimizu, S. Barczyk, P. Rettberg, T. Shimizu, T. Klaempfl, J. L. Zimmermann, T. Hoeschen, C. Linsmeier, P. Weber, G. E. Morfill, and H. M. Thomas, *Planetary and Space Science*, **2014**, 90.
- [164] T. G. Klaempfl, G. Isbary, T. Shimizu, Y.-F. Li, J. L. Zimmermann, W. Stolz, J. Schlegel, G. E. Morfill, and H.-U. Schmidt, *Applied and Environmental Microbiology*, **2012**, 78, 15.
- [165] T. von Woedtke, H. R. Metelmann, and K. D. Weltmann, *Contributions to Plasma Physics*, **2014**, 54, 2.
- [166] T. von Woedtke, S. Reuter, K. Masur, and K. D. Weltmann, *Physics Reports-Review Section of Physics Letters*, **2013**, 530, 4.
- [167] B. T. J. van Ham, S. Hofmann, R. Brandenburg, and P. J. Bruggeman, *Journal of Physics D-Applied Physics*, **2014**, 47, 22.
- [168] M. J. Pavlovich, D. S. Clark, and D. B. Graves, *Plasma Sources Science & Technology*, **2014**, 23, 6.
- [169] Y. Sakiyama, D. B. Graves, H.-W. Chang, T. Shimizu, and G. E. Morfill, *Journal of Physics D-Applied Physics*, **2012**, 45, 42.
- [170] M. J. Pavlovich, T. Ono, C. Galleher, B. Curtis, D. S. Clark, Z. Machala, and D. B. Graves, *Journal of Physics D-Applied Physics*, **2014**, 47, 50.
- [171] S. Moncada, R. M. J. Palmer, and E. A. Higgs, *Pharmacological Reviews*, **1991**, 43, 2.
- [172] J. Jeon, T. M. Rosentreter, Y. Li, G. Isbary, H. M. Thomas, J. L. Zimmermann, G. E. Morfill, and T. Shimizu, *Plasma Processes and Polymers*, **2014**, 11, 5.
- [173] Y.-F. Li, J. L. Zimmermann, and G. E. Morfill, *New Journal of Physics*, **2012**, 14.
- [174] T. Shimizu, Y. Sakiyama, D. B. Graves, J. L. Zimmermann, and G. E. Morfill, *New Journal of Physics*, **2012**, 14.
- [175] T. Shimizu, J. L. Zimmermann, and G. E. Morfill, *New Journal of Physics*, **2011**, 13.
- [176] Y. Sen, U. Bagci, H. A. Gulec, and M. Mutlu, *Food and Bioprocess Technology*, **2012**, 5, 1.

- [177] S. Kodama, H. Habaki, H. Sekiguchi, and J. Kawasaki, *Thin Solid Films*, **2002**, *407*, 1-2.
- [178] M. Yusupov, E. C. Neyts, C. C. Verlaack, U. Khalilov, A. C. T. van Duin, and A. Bogaerts, *Plasma Processes and Polymers*, **2014**.
- [179] M. Yusupov, A. Bogaerts, S. Huygh, R. Snoeckx, A. C. T. van Duin, and E. C. Neyts, *Journal of Physical Chemistry C*, **2013**, *117*, 11.
- [180] B. E. E. Kastenmeier, P. J. Matsuo, J. J. Beulens, and G. S. Oehrlein, *Journal of Vacuum Science & Technology a-Vacuum Surfaces and Films*, **1996**, *14*, 5.
- [181] U. Kogelschatz, B. Eliasson, and M. Hirth, *Ozone-Science & Engineering*, **1988**, *10*, 4.
- [182] V. M. Darleyusmar, N. Hogg, V. J. O'leary, M. T. Wilson, and S. Moncada, *Free Radical Research Communications*, **1992**, *17*, 1.
- [183] A. Mahfoudh, M. Moisan, J. Seguin, J. Barbeau, Y. Kabouzi, and D. Keroack, *Ozone-Science & Engineering*, **2010**, *32*, 3.
- [184] R. Ehrlich and S. Miller, *Applied Microbiology*, **1972**, *23*, 3.
- [185] V. Fombuena, D. Garcia-Sanoguera, L. Sanchez-Nacher, R. Balart, and T. Boronat, *Journal of Adhesion Science and Technology*, **2014**, *28*, 1.
- [186] G. B. Rusu, M. Asandulesa, I. Topala, V. Pohoata, N. Dumitrascu, and M. Barboiu, *Biosensors & bioelectronics*, **2014**, *53*.
- [187] Y. Kusano, *Journal of Adhesion*, **2014**, *90*, 9.
- [188] Z. Liu, P. Chen, D. Han, F. Lu, Q. Yu, and Z. Ding, *Vacuum*, **2013**, *92*.
- [189] T. Desmet, R. Morent, N. De Geyter, C. Leys, E. Schacht, and P. Dubruel, *Biomacromolecules*, **2009**, *10*, 9.
- [190] M. J. Pavlovich, Z. Chen, Y. Sakiyama, D. S. Clark, and D. B. Graves, *Plasma Processes and Polymers*, **2013**, *10*, 1.
- [191] J.-W. Lackmann, S. Schneider, E. Edengeiser, F. Jarzina, S. Brinckmann, E. Steinborn, M. Havenith, J. Benedikt, and J. E. Bandow, *Journal of the Royal Society, Interface / the Royal Society*, **2013**, *10*, 89.
- [192] M. J. Pavlovich, Y. Sakiyama, D. S. Clark, and D. B. Graves, *Plasma Processes and Polymers*, **2013**, *10*, 12.
- [193] B. Haertel, T. von Woedtke, K.-D. Weltmann, and U. Lindequist, *Biomolecules & Therapeutics*, **2014**, *22*, 6.
- [194] B. B. Choi, M. S. Kim, K. W. Song, U. K. Kim, J. W. Hong, H. J. Lee, and G. C. Kim, *Journal of Biomedical Nanotechnology*, **2015**, *11*, 5.
- [195] E. A. Ratovitski, X. Cheng, D. Yan, J. H. Sherman, J. Canady, B. Trink, and M. Keidar, *Plasma Processes and Polymers*, **2014**, *11*, 12.
- [196] D. B. Graves, *Plasma Processes and Polymers*, **2014**, *11*, 12.
- [197] R. Brandenburg, V. V. Kovacevic, M. Schmidt, R. Basner, M. Kettlitz, G. B. Sretenovic, B. M. Obradovic, M. M. Kuraica, and K. D. Weltmann, *Contributions to Plasma Physics*, **2014**, *54*, 2.
- [198] P. Talebizadeh, M. Babaie, R. Brown, H. Rahimzadeh, Z. Ristovski, and M. Arai, *Renewable & Sustainable Energy Reviews*, **2014**, *40*.
- [199] R. Rudolph, K. P. Francke, and H. Miessner, *Plasmas and Polymers*, **2003**, *8*, 2.
- [200] R. Hackam and H. Akiyama, *Ieee Transactions on Dielectrics and Electrical Insulation*, **2000**, *7*, 5.
- [201] P. Bruggeman and R. Brandenburg, *Journal of Physics D-Applied Physics*, **2013**, *46*, 46.

- [202] J. Heinlin, T. Maisch, J. L. Zimmermann, T. Shimizu, T. Holzmann, M. Simon, J. Heider, M. Landthaler, G. Morfill, and S. Karrer, *Future Microbiology*, **2013**, *8*, 9.
- [203] K. Oehmigen, J. Winter, M. Haehnel, C. Wilke, R. Brandenburg, K.-D. Weltmann, and T. von Woedtke, *Plasma Processes and Polymers*, **2011**, *8*, 10.
- [204] K. Oehmigen, M. Haehnel, R. Brandenburg, C. Wilke, K. D. Weltmann, and T. von Woedtke, *Plasma Processes and Polymers*, **2010**, *7*, 3-4.
- [205] B. Nisol, A. Batan, F. Dabeux, A. Kakaroglou, I. De Graeve, G. Van Assche, B. Van Mele, H. Terry, and F. Reniers, *Plasma Processes and Polymers*, **2013**, *10*, 6.
- [206] S. Abou Rich, P. Leroy, T. Dufour, N. Wehbe, L. Houssiau, and F. Reniers, *Surface and Interface Analysis*, **2014**, *46*, 3.
- [207] A. Sarani, N. De Geyter, A. Y. Nikiforov, R. Morent, C. Leys, J. Hubert, and F. Reniers, *Surface & Coatings Technology*, **2012**, *206*, 8-9.
- [208] K. Ruegner, R. Reuter, D. Ellerweg, T. de los Arcos, A. von Keudell, and J. Benedikt, *Plasma Processes and Polymers*, **2013**, *10*, 12.
- [209] K. Ruegner, R. Reuter, A. von Keudell, and J. Benedikt, *Journal of Physics D-Applied Physics*, **2014**, *47*, 22.
- [210] J. Benedikt, D. Ellerweg, S. Schneider, K. Ruegner, R. Reuter, H. Kersten, and T. Benter, *Journal of Physics D-Applied Physics*, **2013**, *46*, 46.
- [211] S. Reuter, H. Tresp, K. Wende, M. U. Hammer, J. Winter, K. Masur, A. Schmidt-Bleker, and K.-D. Weltmann, *Ieee Transactions on Plasma Science*, **2012**, *40*, 11.
- [212] A. Van Deynse, P. Cools, C. Leys, N. De Geyter, and R. Morent, *Applied Surface Science*, **2015**, *328*.
- [213] E. A. J. Bartis, P. Luan, A. J. Knoll, C. Hart, J. Seog, and G. S. Oehrlein, *Biointerphases*, **2015**, *10*, 2.
- [214] W. Tian and M. J. Kushner, *Journal of Physics D-Applied Physics*, **2014**, *47*, 16.
- [215] J. Winter, H. Tresp, M. U. Hammer, S. Iseni, S. Kupsch, A. Schmidt-Bleker, K. Wende, M. Duennbier, K. Masur, K. D. Weltmann, and S. Reuter, *Journal of Physics D-Applied Physics*, **2014**, *47*, 28.
- [216] K. Y. Baik, Y. H. Kim, Y. H. Ryu, H. S. Kwon, G. Park, H. S. Uhm, and E. H. Choi, *Plasma Processes and Polymers*, **2013**, *10*, 3.
- [217] C. A. J. van Gils, S. Hofmann, B. K. H. L. Boekema, R. Brandenburg, and P. J. Bruggeman, *Journal of Physics D-Applied Physics*, **2013**, *46*, 17.
- [218] D. Dobrynin, A. Fridman, and A. Y. Starikovskiy, *Ieee Transactions on Plasma Science*, **2012**, *40*, 9.
- [219] A. Starikovskiy, Y. Yang, Y. I. Cho, and A. Fridman, *Plasma Sources Science & Technology*, **2011**, *20*, 2.
- [220] P. Bruggeman and C. Leys, *Journal of Physics D-Applied Physics*, **2009**, *42*, 5.
- [221] W. Vollmer, D. Blanot, and M. A. de Pedro, *Fems Microbiology Reviews*, **2008**, *32*, 2.
- [222] J. S. Sousa, G. Bauville, B. Lacour, V. Puech, and M. Touzeau, *European Physical Journal-Applied Physics*, **2009**, *47*, 2.
- [223] S. Schneider, J.-W. Lackmann, D. Ellerweg, B. Denis, F. Narberhaus, J. E. Bandow, and J. Benedikt, *Plasma Processes and Polymers*, **2012**, *9*, 6.
- [224] S. Schneider, J. W. Lackmann, F. Narberhaus, J. E. Bandow, B. Denis, and J. Benedikt, *Journal of Physics D-Applied Physics*, **2011**, *44*, 29.
- [225] A. N. Bhoj and M. J. Kushner, *Journal of Physics D-Applied Physics*, **2007**, *40*, 22.

- [226] B. S. Park, D. H. Song, H. M. Kim, B.-S. Choi, H. Lee, and J.-O. Lee, *Nature*, **2009**, *458*, 7242.
- [227] E. Vogli, D. Metzler, and G. S. Oehrlein, *Applied Physics Letters*, **2013**, *102*, 25.
- [228] G. S. Oehrlein, R. J. Phaneuf, and D. B. Graves, *Journal of Vacuum Science & Technology B*, **2011**, *29*, 1.
- [229] R. L. Bruce, F. Weilmboeck, T. Lin, R. J. Phaneuf, G. S. Oehrlein, B. K. Long, C. G. Willson, J. J. Vegh, D. Nest, and D. B. Graves, *Journal of Applied Physics*, **2010**, *107*, 8.
- [230] G. Fauland, F. Constantin, H. Gaffar, and T. Bechtold, *Journal of Applied Polymer Science*, **2015**, *132*, 3.
- [231] A. Chipper and G. Borcia, *Plasma Chemistry and Plasma Processing*, **2013**, *33*, 3.
- [232] M. Donegan, V. Milosavljevic, and D. P. Dowling, *Plasma Chemistry and Plasma Processing*, **2013**, *33*, 5.
- [233] K. G. Doherty, J.-S. Oh, P. Unsworth, A. Bowfield, C. M. Sheridan, P. Weightman, J. W. Bradley, and R. L. Williams, *Plasma Processes and Polymers*, **2013**, *10*, 11.
- [234] G.-L. Chen, X. Zheng, J. Huang, X.-L. Si, Z.-L. Chen, F. Xue, and S. Massey, *Chinese Physics B*, **2013**, *22*, 11.
- [235] D. Pappas, *Journal of Vacuum Science & Technology A*, **2011**, *29*, 2.
- [236] N. Hogg and B. Kalyanaraman, *Biochimica Et Biophysica Acta-Bioenergetics*, **1999**, *1411*, 2-3.
- [237] D. F. Church and W. A. Pryor, *Environmental Health Perspectives*, **1985**, *64*.
- [238] I. Stefanovic, N. K. Bibinov, A. A. Deryugin, I. P. Vinogradov, A. P. Napartovich, and K. Wiesemann, *Plasma Sources Science & Technology*, **2001**, *10*, 3.
- [239] W. A. Pryor and G. L. Squadrito, *American Journal of Physiology-Lung Cellular and Molecular Physiology*, **1995**, *268*, 5.
- [240] R. Wilken, A. Hollander, and J. Behnisch, *Macromolecules*, **1998**, *31*, 22.
- [241] J. V. d. Paal, C. C. Verlackt, M. Yusupov, E. C. Neyts, and A. Bogaerts, *Journal of Physics D: Applied Physics*, **2015**, *48*, 15.
- [242] M. Yusupov, E. C. Neyts, U. Khalilov, R. Snoeckx, A. C. T. van Duin, and A. Bogaerts, *New Journal of Physics*, **2012**, *14*.
- [243] J. Van der Paal, S. Aernouts, A. C. T. van Duin, E. C. Neyts, and A. Bogaerts, *Journal of Physics D-Applied Physics*, **2013**, *46*, 39.
- [244] A. Bogaerts, M. Yusupov, J. Van der Paal, C. C. W. Verlackt, and E. C. Neyts, *Plasma Processes and Polymers*, **2014**.
- [245] E. Grosjean, D. Grosjean, and J. H. Seinfeld, *Environmental Science & Technology*, **1996**, *30*, 3.
- [246] I. J. George and J. P. D. Abbatt, *Nature Chemistry*, **2010**, *2*, 9.